

Novel Catalytic Systems for Carbon Dioxide Activation

Andreas Weilhard

Thesis submitted to the University of Nottingham for the degree of Doctor of Philosophy

September 2019

"Chemistry itself knows altogether too well that - given the real fear that the scarcity of global resources and energy might threaten the unity of mankind - chemistry is in a position to make a contribution towards securing a true peace on earth."

Kenichi Fukui

Abstract

This work has developed a series of strategies for the efficient hydrogenation of CO_2 to different products with applications as chemicals and fuels. The main focus has been on the synthesis of formic acid (FA). Thermodynamic and kinetic barriers imposed in the hydrogenation of CO_2 to formic acid have been overcome by utilizing ionic liquids as additives in the reaction. In the first part the beneficial thermodynamic role of ionic liquids acting as a buffer is described. The buffering properties of ionic liquids are afterwards utilized to develop a structure-activity relationship for a range of catalysts including homogeneous and heterogeneous examples. This enables for the development of highly efficient catalysts in the hydrogenation of CO_2 to FA.

When CO_2 is used as feedstock for carbon-based material, the reduction of the oxidation state at the carbon is critical in order to generate a highly diversified product portfolio. Formic acid is, beneath carbon monoxide, the first product with a reduced oxidation state at the carbon atom. Consequently, formic acid represents a perfect starting point for the development of decarbonised chemical value chains. Furthermore, it is both industrially relevant and has potential to be implemented in future technologies including hydrogen storage schemes, thus underlining the importance for the development for new processes for the synthesis of formic acid.

However, the catalytic transformation of CO_2 with hydrogen is thermodynamically and kinetically challenging. On the one hand, the formation of formic acid is thermodynamically uphill in gas phase and consequently the

equilibrium is commonly shifted to the product side by the addition of stoichiometric amounts of bases. The key here is the formation of formate salts and adducts which would inevitably lead to tedious purifications and to the generation of large amounts of waste. Alternatively, the reaction is carried out in liquid phase which results in an acidic reaction media. On the other hand, CO_2 is a kinetically inert molecule, thus necessitating highly nucleophilic, basic metal hydride complexes in order to activate CO_2. If no bases are employed, the basicity of the active metal hydride complexes leads inevitably to a fast deactivation of the catalysts.

This work addresses the thermodynamic challenges by utilizing ionic liquids (ILs) as additives in the reaction. The ILs act as a buffer during the reaction, thus stabilising the pH of the solution at higher values than that expected by the concentration of FA generated, whilst avoiding the formation of formate salts and adducts. Indeed, the additional stabilisation of formic acid falls into the range of an additional H-bond, compared to the pure solvent system.

The buffering properties of ILs allowed also for the screening of different catalysts, including heterogeneous RuFe-nanoalloys. These nanoalloys displayed low activity and selectivity towards the formation of formic acid in comparison to the homogeneous counterparts. One major issue is the preferred formation of carbon monoxide under elevated temperatures, prohibiting efficient transformation rates.

Consequently, a wide range of Ru complexes with pyridylideneamide ligands were screened for the hydrogenation of CO_2 to formic acid. It was found that the rate of reaction can be enhanced by a) an increased electron density at

the metal centre and b) by changing the dominant mechanism for the CO_2 insertion into the metal hydride bond. The catalyst durability can be increased by increasing the resistance of the active hydride towards protonation. This is achieved by using pyridinium carbenes as coordinating sites. The catalyst stability and activity with pyridylideneamide ligands is in general good, in line with the literature reports.

Based on the experience learned from the pyridylideneamide-based catalysts, a guideline for a highly robust, active and stable catalysts was created. The first example synthesised is a Ru-pincer complexes with N-heterocyclic (NHC) side arms as coordinating sides. Here, the NHC groups, mimic the strong electron donation observed with pyridylideneamides, whilst avoiding side reactions such as electrophilic attacks onto the ligand scaffold. This scaffold allows the performance of the catalyst at demanding reaction conditions without a loss in catalytic activity *via* the formation of heterogeneous nanoparticles. Furthermore, the structural design of the catalyst avoids the poisoning of the catalyst by the reagents, product or lewis acids. Consequently, the here developed catalyst achieved a TON of 833,800 with an initial turnover frequency (TOF) of 22,000 h^{-1}. These results represent the best catalytic performance reported to date by a factor of 50 (TON) and 22 (TOF), compared to the best performing catalysts reported to date under base free conditions.[1]

Statutory declaration

I hereby declare that this thesis with the title "***Novel Catalytic Systems for Carbon Dioxide Activation***" has been written by myself without any external unauthorised help, that it has been neither presented to any institution for evaluation nor previously published in its entirety. Any parts, words or ideas, of the thesis, however limited, and including tables, graphs and schemes, which are quoted from or based on other sources have been acknowledged as such without exception.

(Andreas Weilhard) (01/04/2019, Nottingham, UK)

Acknowledgements

I wish to express my deepest gratitude to my academic supervisors Dr. Victor Sans Sangorrin and Prof. Jairton Dupont. Their guidance and patience over the years have been invaluable. Without their academic knowledge and insights this thesis would not have been possible.

My gratitude goes also to Dr. Israel Cano, Dr. Maria Martin-Gandul, Dr. Jesum Alves Fernandes, Dr. Aitor Gual, Dr. Isabel Vincente Valverde and Dr. Jamie Cameron. Without their hands on knowledge and guidance in the laboratory, the experimental outcome of this thesis would not have been possible.

I would also like to thank all the current and former members of the Graham Newton group, Peter Licence Group, Jairton Dupont Group, Darren Walsh Group and Victor Sans Group for sharing the laboratory with me over the years.

I also thank Obinna Okafor, Dr. Irfan Quadir, Kevin Salzmann, Prof. Martin Albrecht, Dr Christof Jaeger, Dr. Martin Prechtl, Dr. Gabriel Abarca, Janine Viscardi, Prof. Antonino La Rocca, Annalisa Ferrante and Dr. Erno Karjalainen with whom I had the great opportunity to work on several projects.

Special thanks to my PhD colleagues Sharad Amin, Astrid Delorme, Meike Leu, Lorenzo Maggi, Mark Jurat, Grace Lowe, Daniel Smith and Tom Barber for being my weekend/ late night buddies.

Thanks also to the technician team in Nottingham. Without Mark Guyler, Kevin Butler, Ben Pointer-Gleadhill, Tom Clayton and Zoe Dislay the laboratories would not be nearly as functional as they are.

Furthermore, I would like to thank all my friends in Nottingham and Germany for keeping me good company. Without their support this work would not have been possible. May the fourth be with you!

At least but not last I would like to thank my parents, Franz Josef Weilhard and Marja-Liisa Lindholm-Weilhard. Without your condition less support and love throughout my life I would never have been able to fulfil my dreams and be where I am now.

Table of Content

ABSTRACT I

STATUTORY DECLARATION IV

ACKNOWLEDGEMENTS V

TABLE OF CONTENT 1

LIST OF PUBLICATIONS 5

ABBREVIATIONS AND SYMBOLS 8

CHAPTER 1: INTRODUCTION 10

1.1. Formic acid 15

1.1.1. Physical and chemical properties formic acid 15

1.1.2. Industrial application of formic acid 16

1.1.3. Chemical reactivity of formic acid 18

1.1.4. Current production 20

1.2. Formic acid from CO_2 27

1.2.1. Thermodynamic consideration 27

1.2.2. Kinetic considerations and catalyst design 30

1.3. Catalysts under basic conditions 39

1.3.1. Catalysts with phospine based ligand architectures 39

1.3.2. Catalysts with pincer-based ligand architectures 42

1.3.3. Catalysts with NHC-carbene based ligand architectures 46

1.3.4. Half sandwich complexes as catalysts for the hydrogenation for CO_2 46

1.4. Catalyst under acidic conditions 48

1.5. Existing processes for the transformation of CO_2 to formic acid 54

1.5.1. Connection to processes upstream 55

1.5.2. Connection to downstream processing 57

1.6. General Overview over ILs **61**

1.6.1. Interaction of ILs with CO_2 65

1.7 References **68**

CHAPTER 2: MOTIVATION AND OBJECTIVES 79

CHAPTER 3: METHODOLOGY 82

3.1. Chemical Syntheses **82**

3.1.1. Ionic liquid synthesis 82

3.1.2. Pincer ligand synthesis 84

3.1.3. Pincer complex synthesis 85

3.2. Equipment **87**

3.2.1. 5512 50.0 cm^3 stirred Parr batch reactor 87

3.2.2. High pressure NMR-tube 89

3.3 References **91**

CHAPTER 4: ILS AS ADDITIVES FOR CO_2 HYDROGENATION 92

4.1. Publication I: Selective CO_2 hydrogenation to formic acid with Multifunctional Ionic Liquids. **92**

4.2. Results and Discussion **100**

4.2.1. Thermodynamic effect of ionic liquids onto the hydrogenation of CO_2 to formic acid 100

4.2.2. Kinetic and mechanistic implications of BMMI.OAc as an additive in the hydrogenation of CO_2 to formic acid 106

4.3. Concluding remarks on the utilization of ionic liquids as additives for the hydrogenation of CO_2 to formic acid 110

4.4. Experimental **111**

4.4.1. Synthesis of IL immobilized onto a Merrifield resin 111

4.5. Publication I Supporting Information: Selective CO_2 hydrogenation to formic acid with Multifunctional Ionic Liquids. **113**

4.4. References **130**

CHAPTER 5: RUFE NANOPARTICLES FOR CO_2 HYDROGENATION 131

5.1. Introduction **131**

5.2. Publication II: Selective Carbon Dioxide Hydrogenation Driven by Ferromagnetic RuFe Nanoparticles in Ionic Liquids. **133**

5.3. Results and Discussion **141**

5.3.1. Catalytic activity of RuFe nanoparticles in the hydrogenation of CO_2 to formic acid 141

5.4. Concluding remarks on the utilization of heterogeneous catalyst for the hydrogenation of CO_2 to formic acid **144**

5.5 Publication II Supporting Information: Selective Carbon Dioxide Hydrogenation Driven by Ferromagnetic RuFe Nanoparticles in Ionic Liquid **147**

5.6 References **166**

CHAPTER 6: RU-PYRIDYLAMIDE COMPLEXES FOR CO_2 HYDROGENATION 168

6.1. Introduction **168**

6.2. Initial screening of homogeneous catalysts **172**

6.3. Publication III: Catalyst design for highly efficient base-free carbon dioxide hydrogenation to formic acid **174**

6.4. Results and Discussion **207**

6.4.1. Different turnover limiting steps 211

6.4.2. Parameters influencing the rate of catalytic transformation 217

6.4.3. Parameters influencing the resistance towards acidic conditions 223

6.5. Elucidating catalytic intermediates for the hydrogenation of CO_2 **225**

6.6. Concluding remarks on the utilization of homogeneous catalysts **230**

6.7. Experimental **232**

6.7.1. General Information 232

6.7.2. Investigating hydride formation with 3 232

6.8. Publication III, Supporting Information: Catalyst design for highly efficient base-free carbon dioxide hydrogenation to formic acid **235**

6.9. References **272**

CHAPTER 7: RU-CNC PINCER FOR CO_2 HYDROGENATION 275

7.1 Introduction **275**

7.2. Publicaiton IV: Highly efficient base-free synthesis of formic acid from carbon dioxide **278**

7.3. Results and Discussion **292**

7.4. Concluding remarks about Ru-CNC pincer complexes in the hydrogenation of CO_2 to formic acid **295**

7.5. Publicaiton IV Supporting Information: Highly efficient base-free synthesis of formic acid from carbon dioxide **297**

7.6. References **319**

8. CONCLUSIONS AND OUTLOOK 321

List of publications

This thesis resulted in the following publications:

I Andreas Weilhard, Muhammad I. Qadir, Victor Sans, and Jairton Dupont **Selective CO2 Hydrogenation to Formic Acid with Multifunctional Ionic Liquids,** *ACS Catalysis* **2018** *8* (3), 1628-1634.

II Muhammad I. Qadir, Andreas Weilhard, Jesum A. Fernandes, Imanol de Pedro, Bruno J. C. Vieira, João C. Waerenborgh, and Jairton Dupont **Selective Carbon Dioxide Hydrogenation Driven by Ferromagnetic RuFe Nanoparticles in Ionic Liquids**, *ACS Catalysis* **2018** *8* (2), 1621-1627.

III Andreas Weilhard, Kevin Salzmann, Christoff Jaeger, Jairton Dupont, Martin Albrecht, Victor Sans **Catalyst Design for Base-Free hydrogenation of CO_2 to formic acid,** manuscript in preparation **2019**.

IV Andreas Weilhard, Stephen Argen, Victor Sans **Highly efficient base-free synthesis of formic acid from carbon dioxide,** manuscript in preparation **2019**.

V Andreas Weilhard, Jairton Dupont, Victor Sans **Carbon dioxide hydrogenation to formic acid** in Carbon Dioxide Utilisation: From fundamental discoveries to production processes; Eds: Michael North and Peter Styring. De Gruyter. **2019**

The publications are referred to in the text by their roman numerals.

The author's contribution to publications:

The author drew the research plan and synthesized all the ionic liquids and planned and conducted all the experimental work in publication I. In publication II the author drew the research plan for the hydrogenation of CO_2 to formic acid. In publication III the author drew the research plan, synthesized all ionic liquids and performed all the catalytic tests for the CO_2 hydrogenation to formic acid, whilst the complexes presented in publication III were synthesized by collaborators. In publication IV the author conducted all the catalytic experiments, synthesized all ionic liquids and drew the research plan. In all publications the author prepared the manuscripts in collaboration with the co-authors. Furthermore, parts of the introduction (**section 1.1**, **1.2** and **1.3**) are being published as book chapter, see publication V.

In addition to this thesis, the author has contributed to several other publications:

VI A. Weilhard, G. Abarca, J. Viscardi, M. H. G. Prechtl, J. D. Scholten, F. Bernardi, D. L. Baptista, J. Dupont, **Challenging Thermodynamics: Hydrogenation of Benzene to 1,3-Cyclohexadiene by Ru@Pt Nanoparticles** *ChemCatChem* **2017**, *9*, 204.

VII Okafor, Obinna; Weilhard, Andreas; Fernandes, Jesum A.; Karjalainen, Erno; Goodridge, Ruth; Sans, Victor **Advanced reactor engineering with 3D printing for the continuous-flow synthesis of silver nanoparticles**, *Reaction Chemistry & Engineering* **2017**, *2 (2)*, 129-136.

VIII Linda Jütten, Karla Ramírez-Gualito, Andreas Weilhard, Benjamin Albrecht, Gabriel Cuevas, María del Carmen Fernández-Alonso, Jesús Jiménez-Barbero, Nils E. Schlörer, and Dolores Diaz **Exploring the Role of Solvent on Carbohydrate–Aryl Interactions by Diffusion NMR-Based Studies**, *ACS Omega* **2018** *3* (1), 536-543.

IX Antonino La Rocca; Annalisa Ferrante; Ephraim Haffner-Staton; Alasdair Cairns; Andreas Weilhard; Victor Sans; Antonio P Carlucci; Domenico Laforgia **Investigating the impact of copper leaching on combustion characteristics and particulate emissions in HPCR diesel engines**, *Fuel*, submitted **2019.**

Abbreviations and Symbols

Acriphos	4,5-bis(diphenylphosphino)acridine
ATR	Attenuated total reflectance
BD	back donation
C	Concentration
COD	cycloocatdiene
dcpm	dicyclohexylphosphinomethane
DFT	Density Functional Theory
DLVO	Derjaguin, Landau, Verwey, Overbeek
dmpe	dimethylphosphine ethane
DN	donor number
dppe	diphenylphosphine ethane
dppm	diphenylphosphine methane
Et_2O	diethylether
FA	Formic acid
ΔG	Change in Gibb's Free Energy
ΔH	Change in Enthalpy
HR-TEM	High Resolution Transmission Electron Microscopy
ICP-OES	Inductively Coupled Plasma - Optical Emission Spectrometry
IL	ionic liquid
IPA	isopropanol
IR	infrared
k	Constant
K_{eq}	Equilibrium constant
MEA	monoethanolamine
MeCN	acetonitrile
MeOH	methanol
MeTHF	methyl tetrahydrofurane
MIBC	methyl isobutylcarbonol
MNP	metal nanoparticles
mtppms	3,3'3''-phosphanetriyl(benzenosulfonic acid) sodium

NEt_3	triethylamine
*n*Bu	Butyl
*n*BuOH	*n*-butanol
nDecyl	Decyl
$NHex_3$	trihexylamine
NOE	Nuclear Overhauser Effect
NP	nanoparticle
NTf_2	bis(trifluoromethylsulfonyl)imide
OAc	acetate
OMe	methoxy
OTf	triflate
PEI	polyethyleneimie
pH	Logarithmic concentration of hydroxonium ions
ph	phenyl
pKa	Logarithmic acid dissociation constant
$PnBu_3$	tributylphosphine
PPh_3	triphenylphosphine
ppm	part per million
PTA	1,3,5-triaza-7-phospha adamantine
P_x	Partial pressure
PYA	pyridinylidene amide
PYE	pyridinylidene amine
R	Ideal gas contant
rWGS	reverse water gas shift
ΔS	Change in Entropy
sc	super critical
SD	sigma donation
T	Temperature
tppts	tris(3-sulfonatophenyl)phosphine
Vkd	Verkade's base
XPS	X-Ray Photoelectron Spectroscopy

Chapter 1: Introduction

In our daily life we encounter a wide variety of synthesized chemicals such as polymers, pharmaceuticals, lubricants etc. The main raw materials for these chemicals are natural resources such as fossil fuels, water and air.[2] By far the most predominant source for carbon based synthetic materials are fossil fuels.[3] As an example, crude oil constitutes a mixture of hydrocarbons of various chain lengths which can be separated into its components by fractional distillation. These are then further functionalised to yield basic precursor materials or are directly used as fuels.[2, 4]

Inevitably, the price of these chemicals and fuels is linked to the price of crude oil. A stable oil price is therefore vital for long term business strategies.[5] Since the 70's however, the price of crude oil has undergone remarkable fluctuations and prices have steadily increased. Consequently, an alternative feedstock for carbon based chemicals would be highly desirable to ensure future economic prosperity.[6] Changing our raw material for carbon based materials from fossil fuels to renewable alternatives – such as CO_2 - would not only stabilize the price development in long term but also facilitate the decarbonisation of the productive chains for chemicals and fuels.[7]

An inspiration for future processes can be found in nature. The majority of life on Earth is underpinned by the utilisation of CO_2 as a carbon source and sunlight as the energy source.[8] In this way plant life is capable of transforming CO_2 into highly complex molecules such as sugars, which can be used as an energy storage material or further transformed into products with an enormous

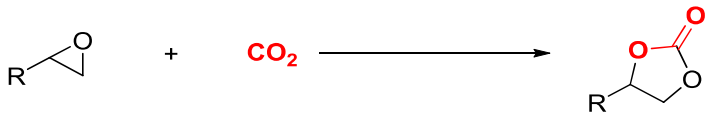
variety of uses and functions, ultimately leading to the high biodiversity we observe on Earth.[9-10]

Indeed human kind has started to use solar energy directly (photovoltaic) or indirectly (wind energy, bio refineries) for economical purposes as a source of renewable energy.[11] Using renewable sources as such as CO_2 as a chemical precursor is highly desirable to drive the transformation of our current economic model to a more sustainable one.[12] Transitioning from a fossil fuel based economy to a CO_2 harvesting economy would be encompassed by a high availability of the raw material (CO_2) which has surpassed a concentration of 400 ppm in the atmosphere by 2017.[13] In this fashion processes utilizing CO_2 as a raw material could be connected to process lines with high CO_2 output, giving raw material streams in acceptable concentrations. This would ultimately lead to beneficial economic effects on carbon capture and storage schemes.[14-16]

CO_2 as a resource or starting point of chemical processes can theoretically be transformed into various chemicals, such as formic acid, carbon monoxide, methanol and others.[14-15] In principle, each of the aforementioned groups can be defined by their oxidation state and the amount of hydrogen (electrons and protons in the case of electrochemical processes) needed to form the compound of interest. Furthermore, each of these compounds can be further functionalised in consecutive chemical transformations.[12, 14, 17]

For instance, CO_2 has an oxidation state of +IV on the carbon atom and can be transformed into organic carbonates in the presence of epoxides, diols and alkenes/alkynes. The transformation of CO_2 into organic carbonates is already

a transformation performed in multi-ton-scale. A good example would be the Shell-Omega process for the synthesis of propylene carbonate and ethylene carbonate from CO_2 and propylene oxide/ethylene oxide, see **figure 1.1**.[18-20]



R = H, CH_3

Figure 1.1 Chemical transformation of CO_2 into cyclic carbonates in the Shell-Omega process.

Alternatively, CO_2 can be reduced with molecular hydrogen, i.e. the oxidation state is reduced by 2, to yield carbon monoxide or formic acid. Carbon monoxide can be fed into the Fischer-Tropsch synthesis to produce traditional fuels (hydrocarbons)[21] or be transformed into formamides and formate esters.[22] A similar reactivity can also be observed for formic acid, although formic acid reacts with alcohols and amines in the absence of catalysts to yield the corresponding formate esters or formamide. Alternatively, formic acid can be converted into carbon monoxide[23] under dehydration conditions, which in turn can be fed into the Fischer Tropsch synthesis.[21]

Upon addition of another hydrogen-molecule the oxidation state is further reduced by 2, yielding formaldehyde (oxidation state O), which represents the same oxidation state as is present in conventional sugars. Another addition of hydrogen gives methanol (oxidation state –II), which is an important starting material for the synthesis of formaldehyde and can be used as a fuel additive.[24-25] Methanol can also be transformed into methane and hydrocarbons, thus can be converted into conventional fuels.[26] **Figure 1.2** depicts the main transformation which can be performed with CO_2.

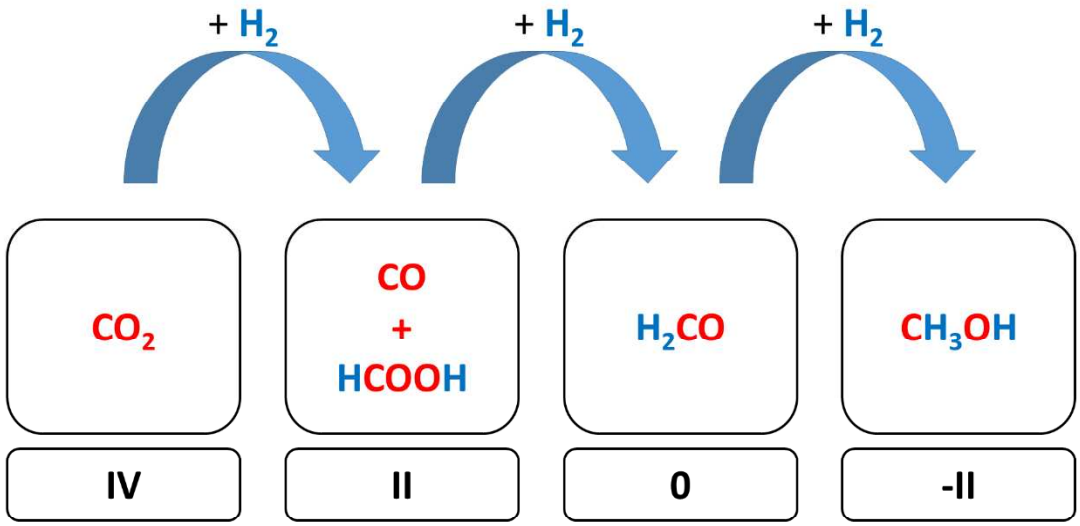


Figure 1.2 Overview of C_1 products theoretically accessible by hydrogenation of CO_2. Roman letters indicate the oxidation state at the carbon.

As shown in **figure 1.2** each of the chemical transformation of CO_2 to lower oxidation state involves hydrogen. Therefore it is important to know how hydrogen is produced today, which is mainly through the oxidation of fossil fuels. The most important process here is steam reforming – the oxidation of methane to CO, CO_2 and H_2.[26-27] Without doubt, replacement of this process by green alternatives, e.g. water splitting – connected to renewable energies - is desirable. However, the production of hydrogen from renewable sources is still in development, thus hydrogen is expected to limit the sustainability of these processes in near future. Therefore, a high consumption of hydrogen for chemical transformations in terms of sustainability is not to be expected to be feasible in foreseeable time.[27] This fact sheds light on the prospects of CO_2 transformations depicted in the figure above.[28] For instance, the transformation of CO_2 to methanol consumes three equivalents of hydrogen.

If, chemicals on the oxidation state II are desired, methanol produced with hydrogen must be oxidised, inevitably leading to waste amounts of H_2.[28]

Although, the equivalents of consumed hydrogen in any transformation do not impact hydrogen storage schemes, i.e. with lower oxidation states larger quantities of hydrogen can be stored and released, compounds with the oxidation state II (CO and formic acid) still represent an attractive area for academic and industrial research. Here, the synthesis of CO and formic acid can be regarded as the entry point for the decarbonisation of current value chains, because only one equivalent of hydrogen is consumed and are thus less impacted by the price and availability of renewable hydrogen.[28] If compounds with lower oxidation states are desired, CO and formic acid can theoretically be further reduced with molecular hydrogen to the desired molecule.

Compared to CO, formic acid holds major advantages. On the one hand, formic acid is a non-toxic liquid whilst CO is a highly toxic gas. This inherently eases the means of handling and transportation of formic acid, when compared to CO. On the other hand formic acid can be transformed easily into H_2 and CO_2 streams, which could be usable for fuel cells and with the added advantage of having no CO impurities (a fuel cell poison).[29-30] Finally, formic acid can be transformed into CO under acidic conditions representing a possibility to store CO in a relatively non-hazardous precursor material.[22, 31]

1.1. Formic acid

Note: Parts of this section are being published separately as a book chapter, see publication V.

Formic acid (FA) was first isolated from the strongly corroding venom of red ants by distillation.[22, 32-33] It is the smallest carboxylic acid with a high boiling point of 100.8°C and a low pKa of 3.74.[32] The global market share of FA was $517M in 2016 and is expected to increase to $879M by the end of 2027, because of the rapid market growth in Asia.[34-35]

1.1.1. Physical and chemical properties formic acid

Physically, FA is a colourless liquid with highly pungent odour, soluble in organic solvents such as alcohols, ethers and acetone. It has a melting point of 8.3°C and a boiling point of 100.3°C at atmospheric pressures. It forms eutectic mixtures with water, with an eutectic point at -48.5°C (41 mol% formic acid in H_2O), see **Figure 1.3a**. The vapour pressure curve deviates considerably from an ideal gas behaviour due to the thermodynamically favourable dimerization (ΔH = -63.8 kJ mol^{-1}) of formic acid in the gas phase, see **Figure 1.3b**. Furthermore, FA and water form azeotropes with a boiling point of 107.6°C at atmospheric pressures (77.6 wt% formic acid and 22.4 wt% water). Higher concentrations (up to 85 wt%) can be obtained under increased pressures, see **Figure 1.3c**. However increased pressure leads to increased boiling points as depicted in **Figure 1.3d**.[22]

The unfavourable physical properties of formic acid and water mixtures (Figure 3) necessitate tedious and energy intensive purification requirements of formic acid water mixtures. This will be further elaborated in ***section 1.1.4***.

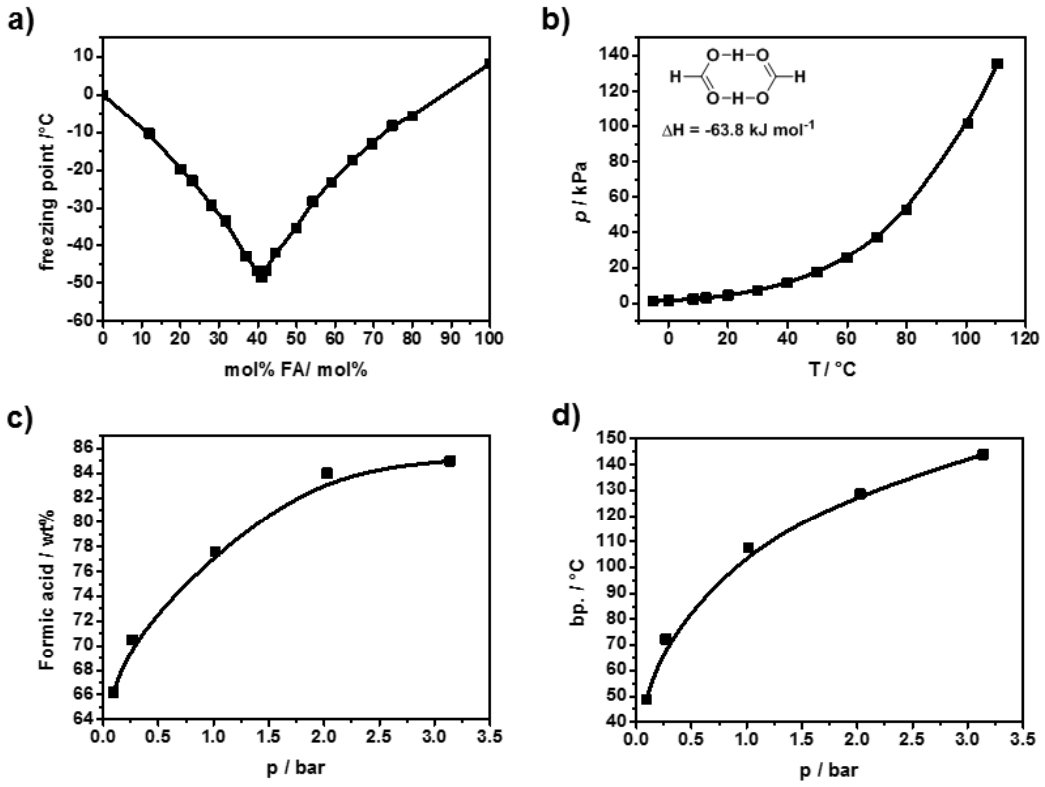


Figure 1.3 Physical properties of formic acid; a) freezing point of water formic acid mixture, b) vapour pressure of formic acid, c) concentrations of formic acid obtainable under increased pressures, d) boiling point of formic acid under differing pressures (data adapted from reference 20).

1.1.2. Industrial application of formic acid

Formic acid is mainly used in silage and animal feed (27%), in the leather and tanning industry (22%) and in pharmaceutical and food chemicals (14%). Other applications include the textile industry (9%), natural rubber production

(7%) and its utilisation as a drilling fluid (4%). The table below gives the market share of formic acid per economical sector.[22]

Table 1.1 Industrial applications of formic acid by sector and share

Entry	Application	Share / %
1	Silage and animal feed	27
2	Leather and tanning	22
3	Pharmaceuticals and food chemicals	14
4	Textile	9
5	Natural rubber	7
6	Drilling fluids	4
7	Miscellaneous	17

Formic acid in silage

Ensiling is based on fermentation under anaerobic conditions. Lactic acid produced by bacteria lowers the pH and prevents unwanted microbiological growth. Upon addition of formic acid the unwanted growth of microbiological organisms can be further prevented, by the rapid drop of pH.[22, 36]

Leather and tanning

Pre-treatment of hides leaves the hides in a slightly alkaline condition. However, common tanning agents require slightly acidic conditions. Therefore, the hides are treated with formic acid which penetrates the collagen fibres in the hides rapidly and homogeneously. This ensures the subsequent penetration of the tanning agent throughout the entire thickness of the hides.[22, 37]

Pharmaceuticals and food chemicals

Formic acid is used in various processes as an important intermediate in the synthesis of pharmaceuticals and food chemicals. Examples include synthetic insulin (purification of recombinant insulin), caffeine, aspartame and vitamin B1. Other applications include the decontamination of *salmonella*, as a preservative and as a flavouring agent.[22]

1.1.3. Chemical reactivity of formic acid

Formic acid can form CO and water in the presence of oxide catalysts or strong acids. Alternatively, formic acid can be dehydrogenated to yield hydrogen and CO_2 in the presence of metal catalysts. These properties give rise to plausible future applications of formic acid as a hydrogen vector. Because the hydrogen generated from formic acid can be obtained free of CO contamination, this reaction pathway becomes especially attractive for fuel cell technologies.[38-40] Alternatively, FA might be considered as a feedstock for carbon monoxide, which can be liberated on demand under formation of water as the sole side product.[41] This would avoid the storage of high amounts of toxic carbon monoxide replacing carbon monoxide by a relatively non-toxic liquid, ultimately easing the storage demands.[22] In general the reactivity of FA can be summarized in the FA triangle (**figure 1.4**).[14] Here, CO_2 represents the highest oxidation state of the carbon atom and can be converted either in the endothermic reverse water gas shift reaction to CO or alternatively exothermically to formic acid.

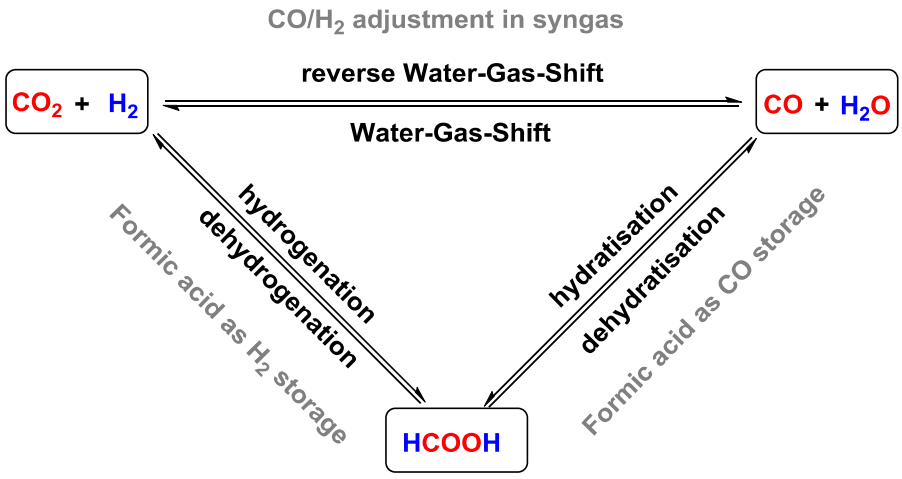


Figure 1.4 Main reactivity pathways of HCOOH described via the FA triangle.[14]

The reducing properties of formic acid are already used in the reduction of imines (Schiff bases).[42] A notable synthetic reaction is the Leuckardt reaction for the formylation of primary amines from ammonia, ketones and formic acid.[42] Dehydration of formic acid is a key step in the Koch carboxylic acid synthesis to branched carboxylic acids.[34, 42]

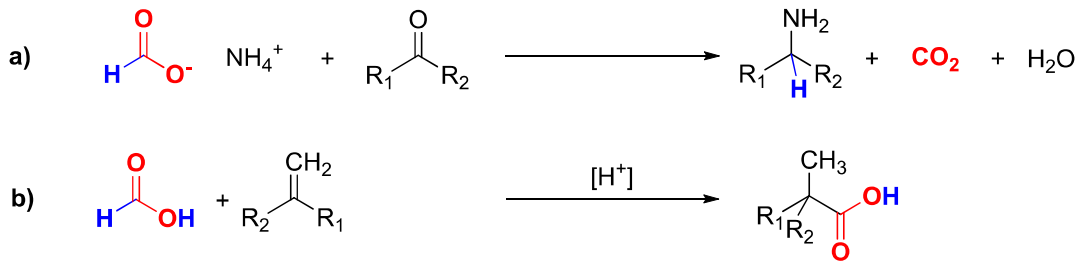


Figure 1. 5 a) Leuckardt reaction; b) Koch carboxylic acid synthesis.

Other important transformations of formic acid involve esterification with alcohols. Notably, due to the low pKa of formic acid, no mineral acids are needed to catalyse the ester formation. Furthermore, formic acid adds to double bonds in alkenes and alkynes to yield the corresponding alkyl esters. For example, ethylene reacts with formic acid to yield the corresponding ethyl

formate. In the vapour phase acetylene can be transformed into vinyl formates, as depicted in figure below.[22]

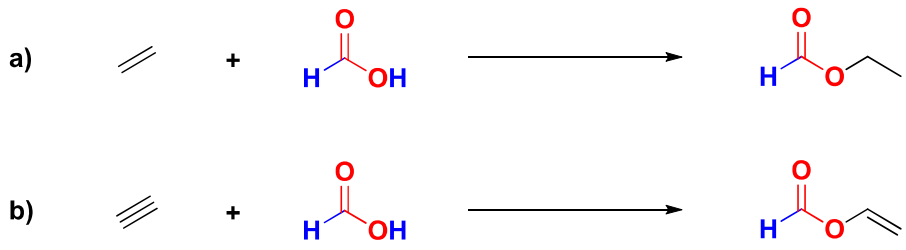


Figure 1.6 a) Reaction of formic acid and ethylene to ethylformate and b) with acetylene to vinylformate.

Formic acid reacts with most amines to form formamido compounds. Of major interest here is the formation of dimethylformamide in the presence of dimethylamine.[22, 43]



Figure 1.7 Reaction of formic acid with dimethylamine to dimethylformamide.

1.1.4. Current production

Currently the main process for the synthesis of formic acid involves the indirect carbonylation of water. Theoretically, the direct carbonylation of water is possible, although the unfavourable reaction parameters make this pathway economically unfavourable. For instance, below 150°C reaction rates are low and although the reaction rate can be increased by increased temperatures, this leads to highly elevated pressures in order to reach suitable formic acid concentrations.[22]

The thermodynamic hurdles are bypassed by the intermediate methanol cabonylation, as shown in **Figure 1.8**.[22]

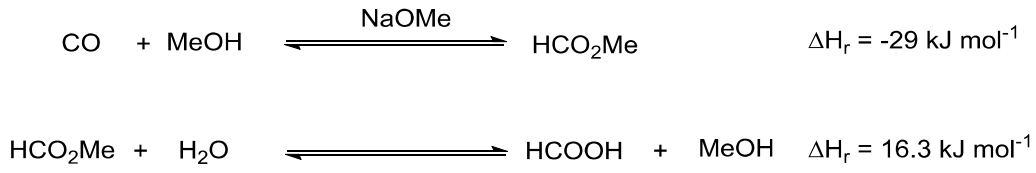


Figure 1.8 Methanol carbonylation catalysed by sodium methanolate followed by hydrolysis.

Consequently, the main production line for formic acid constitutes of two steps:

1) Carbonylation of methanol
2) Hydrolysis of methyl formate

The main producers of FA today are BASF SE, BP and Eastman (formerly Taminco/Kemira). Whilst the carbonylation of methanol is similar in most industrial processes, differences appear in the hydrolysis step.[22] In the following the carbonylation and hydrolysis steps are both discussed. Afterwards, two of the most commonly used process schemes, the Kemira-Leonard Process and BASF process are discussed.

Carbonylation of methanol

Typically, this step is conducted at 80°C, 4.5 MPa of CO and with 2.5 wt% of NaOMe as catalyst in methanol. Under these conditions, 30% methanol and 95% CO conversion is achieved. The rate of reaction can be increased with the pressure, temperature or with higher catalyst loadings. Additionally, mixing between the gas and liquid phases can be improved.[22]

Problematic side reactions involve the formation of sodium formate, which is not soluble in methyl formate leading to precipitation and the consequent encrustation and blockage of the operation unit, see **figure 1.9**.[22, 44]

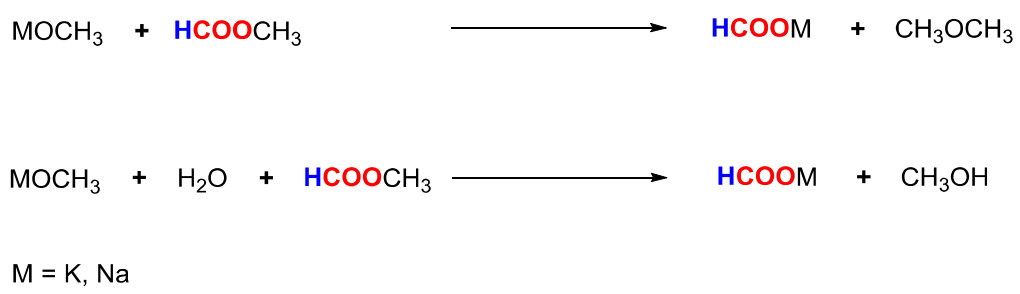


Figure 1.9 Catalyst deactivation during the carbonylation of methanol via product poisoning.

Furthermore, the catalyst must be separated from the reaction mixture to avoid the undesired decomposition of methyl formate into methanol and CO in the subsequent process steps. Also the CO utilised cannot contain CO_2, as the catalyst is deactivated by the formation of the unreactive carbonates (**figure 1.10**).[22]

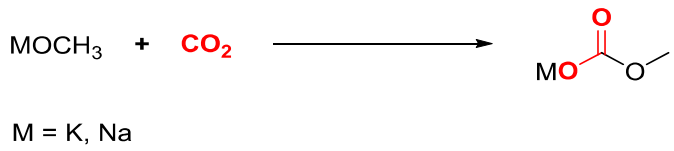


Figure 1.10 Catalyst deactivation during the carbonylation of methanol via Carbonate formation.

Hydrolysis of methyl formate

Even though the hydrolysis step is thermodynamically unfavourable, the reaction can be shifted to the product side by the addition of a stoichiometric excess of water. Unfortunately, this impedes the product separation processes, as formic acid forms azeotropes with water, as shown in **figure 1.3**. As an alternative, organic bases such as tertiary amines can be added to the reaction mixture to remove the formic acid from the equilibrium by forming formate-base adducts, see **figure 1.11**.[45]

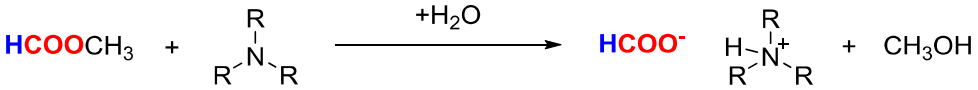


Figure 1.11 Formate amine adduct formation after hydrolysis to shift the thermodynamic equilibrium to the product side.

One plausible amine discussed in this perspective is the high boiling trihexylamine, which has also been investigated for the direct formation of formate synthesis from CO_2.[46]

Kemira-Leonard Process

This process plant was built by Kemira (now Eastman Chemical Company) according to the development undertaken by Leonard Process Co. in 1982 in Finland. Its production capacity is 20,000 t/a.[47]

In the Kemira-Leonard process, carbonylation takes place under 4 MPa CO pressure and 80°C in the presence of alkoxides as catalysts (**a**). The following hydrolysis is undertaken in two separate reactors under differing conditions. In the first reactor unit methyl formate is hydrolysed with equimolar amounts of water to yield formic acid (**c**), which is fed into the second reactor unit and an excess of methyl formate is added (**d**). Here the formic acid formed in the first step is used as catalyst for the following hydrolysis. The hydrolysis is operated at 120°C and 0.9 MPa.[47]

The following discharge cools the reaction adequately to avoid re-esterification of the formic acid and methanol (**e**). Separation of methanol is operated under vacuum, attenuating the reverse reaction (re-esterification) (**g**), although the condensation to methyl formate under vacuum presents a problem.

Consequently at any purification step methyl formate is fed back to the main hydrolysis reactor (**d**) to increase the overall yield.[47]

The wet formic acid in 80 wt% is dehydrated *via* distillation at 0.3 MPa (**h**). If higher concentrations are desired the product stream can be connected to a drying column downstream (**i**). Here distillation is undertaken at atmospheric pressure to give 98 wt% formic acid as the overhead product.[47]

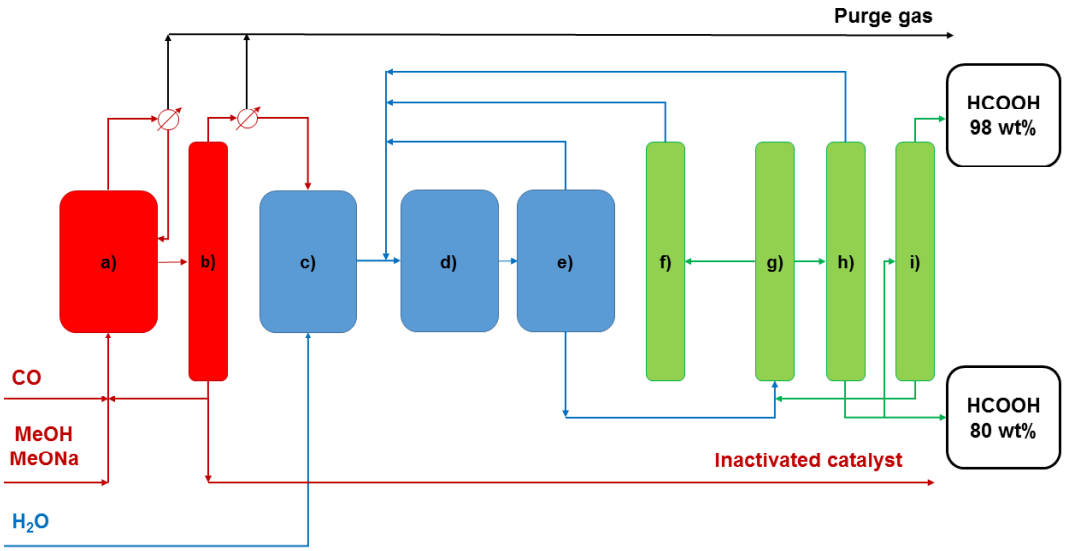


Figure 1.12 Kemira Leonard process for formic acid production. a) Methyl formate reactor; b) Methyl formate distillation column; c) Preliminary hydrolysis reactor; d) Main reactor; e) Flash tank; f) Recycle column; g) Acid stripping column; h) First product distillation column; i) Second product distillation column.[22, 47]

BASF Process

In 1981 BASF started the operation of a formic acid plant with a production capacity of 100,000 t/a in Ludwigshafen (Germany). The carbonylation step is virtually identical to the Kemira-Leonard process (**a** & **b**), but major differences occur during the hydrolysis step. The classical process utilizes, high excesses

of water (5 mol water per 1 mol methyl formate) during the hydrolysis step (**c**).[48]

In the classical process the high quantity of water is separated via liquid-liquid extraction with an amide to obtain dilute formic acid solution (**e**). The diluted formic acid solution is fed into a dehydration column (**f**) where further quantities are drawn off and formic acid is concentrated with the extraction agent to the amount that can be fed into the pure acid column (**g**). The pure acid column (**g**) is operated under vacuum and the extraction agent is drawn off at the bottom of the column, whilst pure formic acid is obtained as the overhead product.[48]

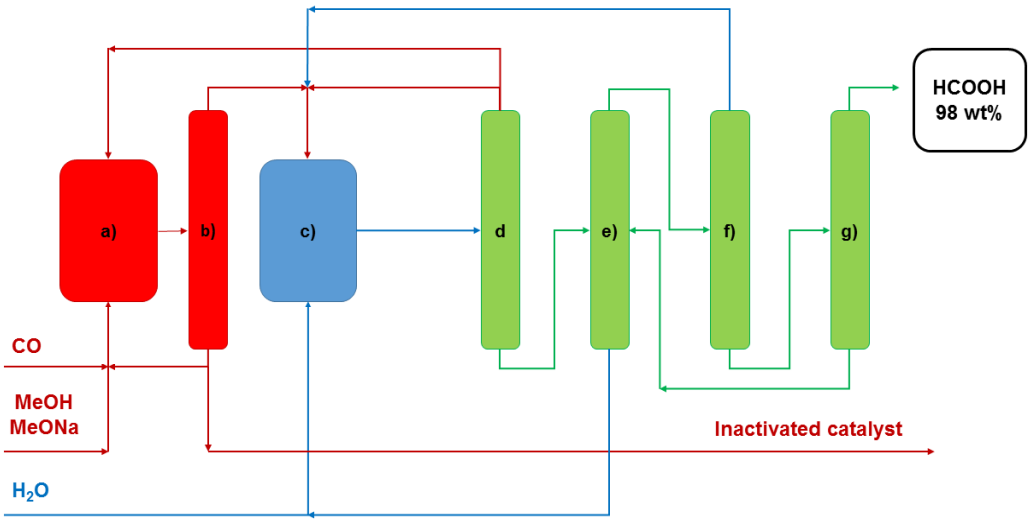


Figure 1.13 BASF process. a) Methyl formate reactor; b) Methyl formate distillation column; c) Hydrolysis reactor; d) Low-boiler column, e) Extraction unit; f) Dehydration column; g) Pure acid column.[22, 45, 48]

<u>Differences in between the Kemira-Leonard process and the BASF process</u>

Whilst the carbonylation in the Kemira-Leonard process and in the BASF process (see **Figure 1.12** and **Figure 1.13**) are operated under the same conditions, major differences do occur during the hydrolysis.[22, 45, 47-48] In the

Kemira-Leonard process no additives are used in the hydrolysis of methyl formate to formic acid. This leads to difficulties during the work up, i.e. the reverse esterification of formic acid and methanol to methyl formate takes place. In order to limit the reverse reaction, reagents have to be recycled and separated at each stage. For instance, MeOH is recycled back from reactor **b**) to **a**) and methyl formate is fed back from **e**), **f**) and **h**) back to **d**), see **Figure 1.12**.[22, 47]

In contrast, the BASF process uses organic bases to shift the equilibrium to the product side and to inhibit the reverse re-esterification reaction with organic bases. However, this leads to tedious purifications downstream. Consequently a reactive distillation operated under reduced pressure can be found downstream to separate the extraction agent from the product, see g) in **Figure 1.13**. [22, 45, 48]

Other methods

Other methods for the synthesis of formic acid involves the carbonylation of hydroxides, followed by the acidification of the formate salts; the hydrolysis of formamides and; the separation of formic acid as a side product during the synthesis of acetic acid via oxidation of hydrocabons.[22] Recently it was demonstrated that Keggin-type polyoxometallates or vanadium oxides can catalytically transform biomass to FA.[49-51] Furthermore, CO used for the carbonylation of methanol or hydroxides is currently produced by steam reforming of methane to CO and is thus directly linked to the employment of natural gases as a resource.[52-53]

1.2. Formic acid from CO_2

Note: Parts of this section are being published separately as a book chapter, see publication V.

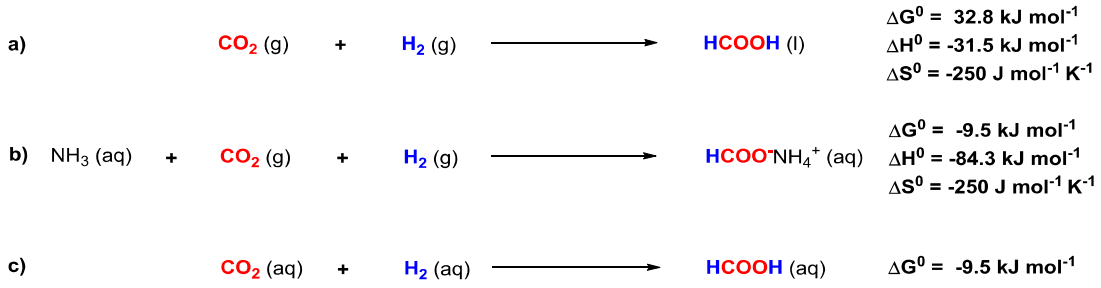
CO_2 represents a virtually unlimited carbon source, thus the synthesis of FA from CO_2 and hydrogen would be advantageous in terms of decarbonising the current chemical production chain and also would ensure future resource security. If CO_2 is efficiently transformed to FA, FA (and therefore CO_2) could be introduced easily into existing processing schemes. From a green chemistry perspective the direct hydrogenation of CO_2 to FA is interesting due to its high atom efficiency.[54-55] However, it is important to understand the main limitations which can lead to increased costs and higher CO_2 emissions than the amount transformed. As mentioned initially a notorious issue is hydrogen generation, which is both expensive and energy intensive and is currently based on the oxidation of fossil fuels.[28] In order to be viable, the H_2 used in the hydrogenation of CO_2 should be generated from renewable sources, i.e. *via* water splitting. Consequently, the hydrogenation of CO_2 is closely linked to emerging technologies.

1.2.1. Thermodynamic consideration

In the hydrogenation of CO_2 to FA, two gaseous molecules (CO_2 and H_2) are reacted to give a liquid (HCOOH). Therefore, the reaction is restrained by a high entropic (ΔS) factor, rendering the reaction endergonic in gas phase

(**Scheme 1.1a**). In order to shift the thermodynamics towards more favourable reaction conditions, the entropic barrier has to be lowered, or be overcompensated by the enthalpic (ΔH) contribution. In other words, the thermodynamic equilibrium has to be shifted by, for example, a consecutive reaction, consuming FA. This is typically achieved by the addition of bases, yielding formate adducts and salts.[14-15, 17] Here, the acid-base reaction in between FA and the base reduces ΔH and the reaction becomes more exothermic, compensating for the unfavourable entropy. This leads to a shift of the thermodynamic equilibrium (K_{eq}) towards the product side (**Scheme 1.1b**). Unfortunately, the formation of formate adducts and formate salts represents a major obstacles for the economic feasibility of such processes as the thermodynamic gain leads ultimately to tedious purification downstream in order to generate free FA.

Even though, lower yields of FA are obtained in the absence of base (compared to basic conditions), the reaction can be carried out in liquid phase due to the lowered entropic barrier (ΔS). Consequently, the equilibrium is slightly shifted towards the product side (**Scheme 1.1c**).[14-15, 46, 56-57]



Scheme 1. 1 Thermodynamic overview of CO_2 hydrogenation to FA[14]

As shown in **Scheme 1.1c**, the Gibbs free energy is only slightly negative in the liquid phase, resulting in relatively low K_{eq} and hence low concentrations of FA. Consequently reactions have to be carried out near the thermodynamic equilibrium, in order to achieve suitable concentrations.[14] The concentration of FA achieved during the hydrogenation can further be improved by increasing the concentration of reagents (CO_2 and H_2) in solution (Le Chatelier's principle). This can also be expressed by the thermodynamic equilibrium constant K_{eq} in relationship with the Gibbs free energy, see equation 1.1.

$$\Delta G = -\mathrm{RT} \ln K_{eq} \qquad (1.1)$$

Taking into account that, the equilibrium constant K_{eq} is directly linked to the concentration of reagents (here CO_2 and H_2) in solution, as described in equation 2.

$$K_{eq} = \frac{[HCOOH]}{[CO_2]_l [H_2]_l} \qquad (1.2)$$

It is evident that, if the equilibrium constant must be constant (ΔG is constant), increasing the gas pressure must increase the concentration of FA achievable at constant temperatures. This relationship is evidenced by Henry's law, see equation 1.3 (*C* is the solubility of a gas at a fixed temperature in a particular solvent, *k* is the Henry constant, P_x is the partial pressure of gas *x*).

$$C = k\mathrm{P}_x \qquad (1.3)$$

With equation 1.4 for the Gibbs free energy,

$$\Delta G = \Delta H - T\Delta S \qquad (1.4)$$

one can derive the van't Hoff equation combining equation 1.4 and 1.1. Equation 1.5 can be used to calculate the enthalpy and entropy of a reaction.

$$\ln K_{eq} = -\frac{\Delta H}{RT} + \frac{\Delta S}{R} \qquad (1.5)$$

Inserting equation 1.2 into equation 1.5 and resolving the natural logarithm gives equation 1.6.

$$\frac{[HCOOH]}{[CO_2]_l[H_2]_l} = \exp(-\frac{\Delta H}{RT} + \frac{\Delta S}{R}) \qquad (1.6)$$

Consequently it can easily be observed that reactions yielding FA must be carried out at relatively low temperatures (the reaction is exothermic) and high pressures (Le Chatelier's principle), see equation 1.6. It is important to note that, increasing the temperature will favour the formation of CO *via* the reverse water gas shift reaction (rWGS), see also **Figure 1.7**.[58] Both reactions are to a certain extent related, as in both cases the oxidation state of the carbon atom is reduced by 2. However the rWGS is highly endothermic and is therefore typically carried out at elevated temperatures.[58]

1.2.2. Kinetic considerations and catalyst design

General overview of kinetics

Carbon dioxide is an unreactive gas, with two slightly negatively polarized oxygens and a slightly electrophilic carbon.[59-60] In order facilitate the transfer a substituent onto the aforementioned carbon, the substituent needs to be a electron rich nucleophile. Consequently, in the bespoke hydrogenation of CO_2 to FA, an electron rich (nucleophilic) hydride is needed.[60] Theoretically, early transition metals form complexes with high hydride transfer capabilities (nucleophilic hydrides). This would facilitate the insertion of CO_2 into the metal

hydride bond (M-H). However, high hydride transfer capability in early transition metals is encountered by strong metal oxygen bonds. This would render the dissociation of formate from the metal centre challenging. As a consequence, most catalytic systems consist of metals from group 8 and 9 (group 8: Fe, Ru; group 9: Co, Rh, Ir). Here a balance in between hydride donation and M-O bond strength is achieved and is key for the development of efficient catalysts.[14-15, 17, 61-62]

Generally speaking the hydrogenation of CO_2 to FA can be separated into two main steps: 1) the insertion of CO_2 into a M-H bond and 2) hydride recovery.

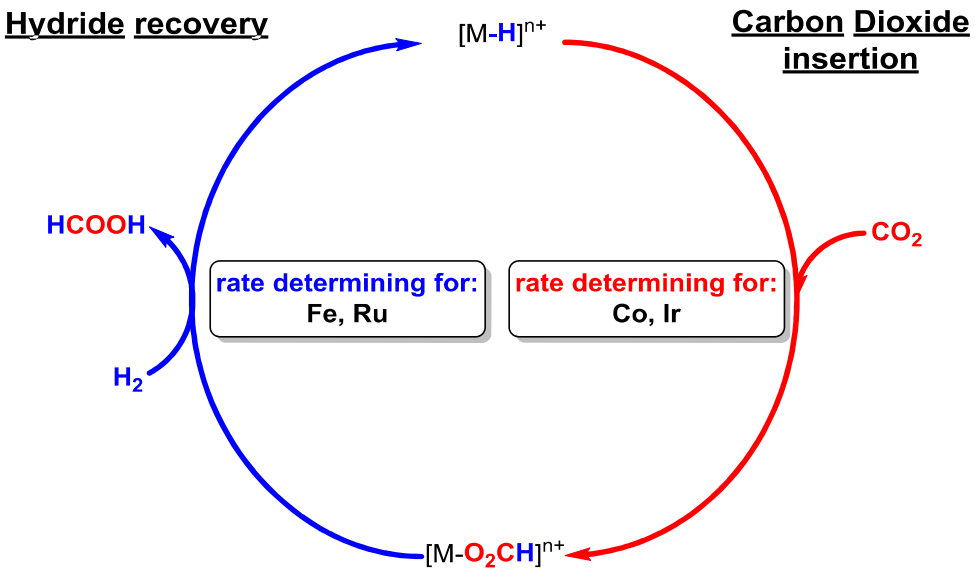


Figure 1.14 Main synthetic steps in the hydrogenation of CO_2 to FA/formate. Carbon dioxide insertion (red line) is typically rate determining for Co and Ir based catalysts. Hydride recovery (blue line) is typically rate determining for Fe and Ru based catalysts.

CO_2 insertion is mostly found to be the rate determining step for the group 9 metals (Co, Ir). This can be explained by the stronger M-H bond and weaker M-O bond, when compared to their counterparts from group 8 (Ru, Fe). In fact most catalytic systems containing Ru or Fe as the active species have the

hydride recovery as rate determining step.[14-15, 17, 61-66] In the following, electronic effects determining mechanistic aspects of both steps will be introduced.

1) CO_2 insertion

The insertion of CO_2 is rate determining for late transition metal catalysts, e.g. Co and Ir. This step consists of a hydride transfer from the active metal hydride onto CO_2, yielding the corresponding formate complex. This process can follow two distinct paths: the inner sphere - and outer sphere mechanism.[67] The mechanism for the CO_2 insertion (inner – vs. outer sphere) depends mainly on the sterical demand and the nucleophilicity of the transferred group.[67-68]

As most metal hydrides are relatively weak nucleophiles, CO_2 inserts commonly *via* an outer sphere mechanism into the bespoke metal hydride bond. The outer sphere mechanism constitutes of two transition states and an ionic intermediate and proceed generally slower as the inner sphere mechanism.[69] In contrast, the inner sphere mechanism is dominant with strong nucleophiles[67] (i.e. high capability of the metal to transfer a functional group onto an entering substrate molecule) and/or when a less sterically hindered system is generated around the active metal catalyst. In the inner sphere mechanism only one transition state has to be overcome.[67]

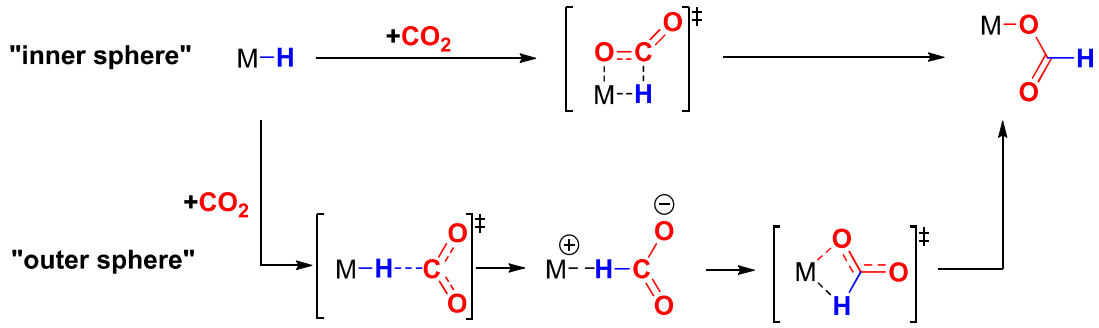


Figure 1. 15 CO_2 insertion via the inner respectively outer sphere mechanism into a metal hydride bond.[67]

The thermodynamic reaction profile of the CO_2 insertion can be determined by electrochemical measurements. Here the thermodynamic hydricity (represented as ΔG_H^0– in **Figure 1.16a**) can be determined by the reduction potential of the parent complex. A relationship in between the reduction potential of the parent complex and the hydricity of the active hydride complex has been established for a wide range of complexes.[70-71] Hereby, the hydricity represents the ability of a molecule to transfer a hydride to another molecule. In this way, a higher hydricity means - by definition - a lowered capability of a molecule to transfer a hydride. The thermodynamic properties of bespoke reaction can thus be assayed, by comparing the hydricity of the metal hydride with the hydricity of formate.[71] The hydricity of formate has been shown in

Figure *1.16* *a) Reaction scheme to determine thermochemical cycle and b) hydricity of various metal complexes against the reduction potential of the parent complex.*[71]

b as the straight line dividing the red and blue regions. The red region indicates a regime where the CO_2 insertion becomes endergonic (thermodynamically

disfavoured) and the blue shows the exergonic region (thermodynamically favoured).[71]

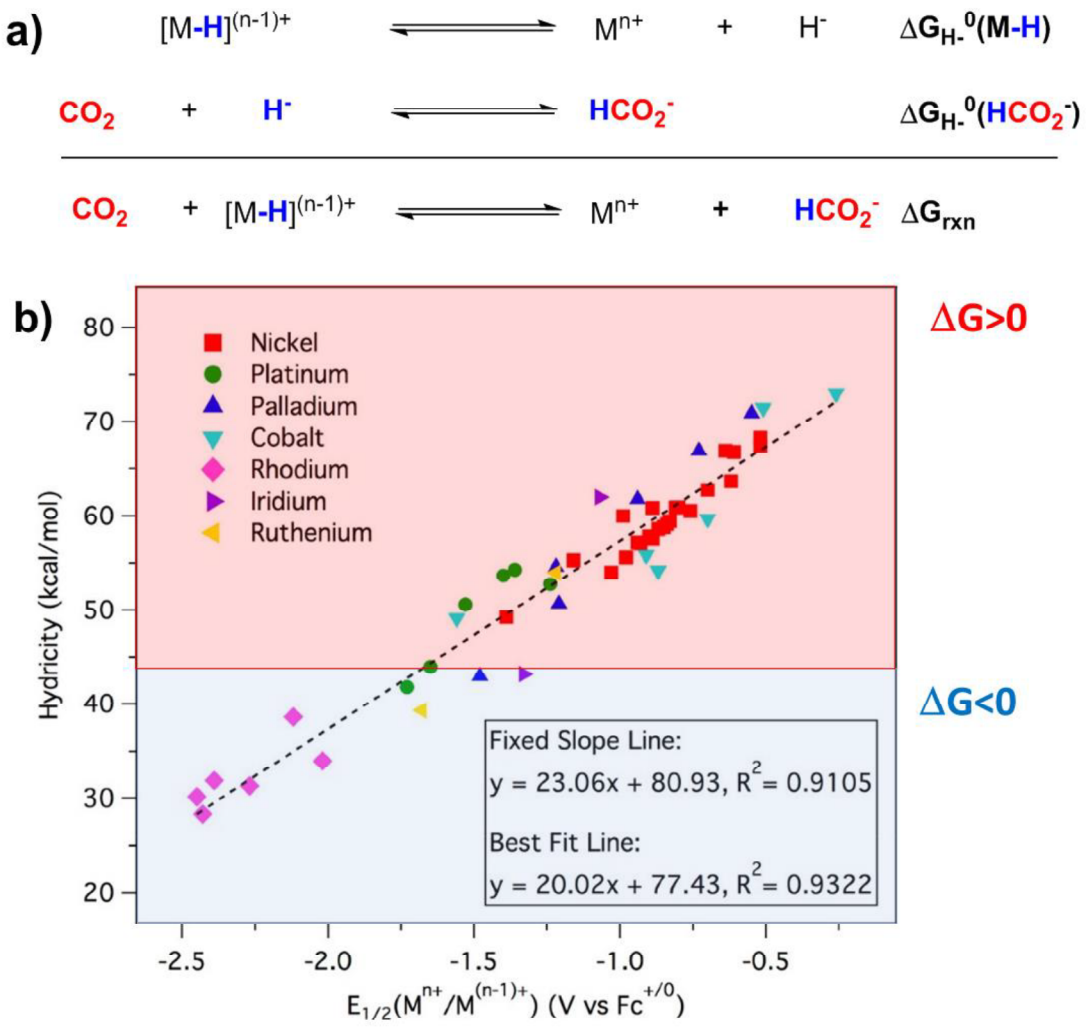


Figure 1.16 a) Reaction scheme to determine thermochemical cycle and b) hydricity of various metal complexes against the reduction potential of the parent complex.[71]

If the hydricity of the metal hydride is close to that of formate, the hydride recovery and CO_2 insertion are near thermoneutral, i.e. neither step in the catalytic transformation is strongly endergonic and thus each intermediate is easily interconverted.[72] As the difference in between the hydricities of ruthenium and iridium complexes fall close to those of formate, the most active catalysts can be found with bespoke noble metals.[14, 17, 61-62] Furthermore, all

Co complexes displayed in **Figure 1.16b** have a higher thermodynamic hydricity as formate and therefore most Co complexes do display an endergonic profile for the CO_2 insertion step.[71]

Therefore by lowering the hydricity of Co catalysts the rate of reaction in the CO_2 hydrogenation to FA can be enhanced. Linehan *et al.* demonstrated that a lowered hydricity led indeed to an increased catalytic activity culminating in a TOF of 6400 h^{-1} at 1.8 atm of CO_2/H_2 (1:1) at 21°C with [Co(1,2-bis(dimethylphosphino)ethane)$_2$H] (**1**) under basic conditions, i.e 2,8,9-triisopropyl-2,5,8,9-tetraaza-1-phosphabicyclo- [3,3,3] undecane (i.e. Verkade's base; Vkd's base) was used as the base. [72] The observed increase in rate was related to the CO_2 insertion being "more" themoneutral and thus the hydride transfer during CO_2 insertion being facilitated. [72] As a consequence the interconversion of the main intermediates was eased and an increased rate was observed. However, the thermodynamic model of hydricity fails with the analogous Rh catalyst.[72] This can be explained by the already very low hydricity of Rh catalysts, which makes this step exergonic. With the analogous Rh complexes the rate of CO_2 hydrogenation to FA can be increased by facilitating the addition of dihydrogen onto the metal centre. This step represents the rate determining step for most Rh catalysts and falls into the area of hydride recovery.[72]

2) Hydride recovery

Hydride recovery can be split into two different steps: the addition of dihydrogen onto the metal centre and the heterolytic splitting of H_2. In order to understand both steps, it is useful to investigate the metal dihydrogen complex

(σ-M-H_2). Historically, σ-M-H_2 complexes were assumed to be highly unstable and to exist only as transient species. Consequently, it was not until 1983 when the first dihydrogen complex was isolated by Kubas.[73-74] At the same time, Saillard and Hoffmann were able to calculate the first dihydrogen complex.[75] The intriguing bonding mode of dihydrogen with transition metals has since then led to the isolation of a plethora of dihydrogen complexes.[76] In all dihydrogen complexes, the H_2-ligand binds to the metal side on, as depicted in Error! Reference source not found.. The distance between both hydrogen atoms ranges hereby from 0.8 Å and 1.6 Å (Note: distance between H atoms in molecular H_2 is 0.74 Å). When the distance in between both hydrogen atoms exceeds 1.6 Å the H-H bond can be assumed to be broken.

σ-M-H_2 complex have been classified in 5 sub-classes depending on the H-H distance: true H_2-complexes (0.8 Å to 0.9 Å), elongated H_2-complexes (1.0 Å to 1.2 Å), compressed dihydrides (1.3 Å to 1.6 Å) and dihydrides (> 1.6 Å). Note that in dihydrides the H-H bond is effectively broken and cannot be assigned to σ-M-H_2 complex, and is instead best described as a M$(H)_2$ complex.[73, 76]

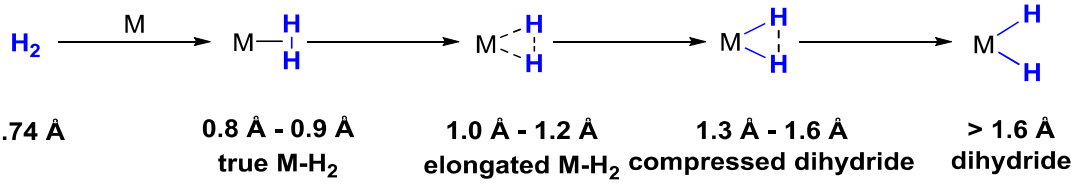


Figure 1.17 H-H distances in dihydrogen complexes ranging from 0.8Å to 1.6 Å.[76]

The breaking of the H-H bond can be regarded as a continuum process (Error! Reference source not found.). On the one hand, the H_2 ligand is stabilised by π-back-donation (BD) from the metal to H_2, whilst on the other hand, the σ-donation (SD) from the H_2 ligand to the metal further contributes to the stability

of the σ-M-H_2 complex.[76] Changing the electronic parameters of a parent complex will move the local minimum for the H_2 complex on this continuum, resulting in different H-H distances. The H-H distance depends on the strength of BD with stronger BD resulting in elongated H-H distances. Increasing the BD from a nucleophilic metal centre will ultimately result in the homolytic splitting (oxidative addition) of H_2, giving a dihydride.[77-78] In contrast decreased BD from electrophilic metal centres lead to the heterolytic cleavage of H_2 resulting in a M-H and a H^+. In this way, the pKa of M-H_2 complexes can be remarkably decreased (compared to molecular dihydrogen), i.e. cationic electrophilic complexes can have a pKa as low as -6 and therefore can even protonate organic solvents.[79] Stable σ-M-H_2 complexes are obtained when both electronic donations are in a good relative balance, i.e. neither the π-BD nor σ-donation are dominating the bonding mode. SD from the H_2 ligand and BD from the metal centre to the H_2 ligand, in addition to the continuous region for heterolytic cleavage, stable σ-M-H_2 complexes and homolytic cleavage are depicted in **Figure 1.18** below.[76]

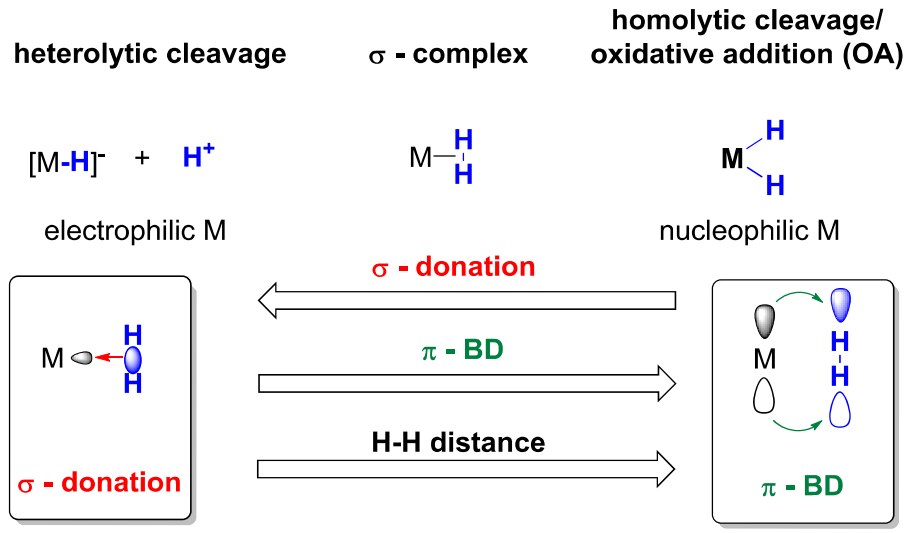


Figure 1.18 H_2 complex stability and reactivity in dependence of electronic properties of the metal centre.[76]

As shown in **Figure 1.18**, electrophilic metal complexes are beneficial for the heterolytic splitting of H_2. Unfortunately, electrophilic complexes generally create weak hydride donors (and the σ-M-H_2 complex is very unstable), hence are not regarded suitable for the hydrogenation of CO_2, see **Figure 1.16**.[70, 80] Instead, most catalytic systems utilize electron rich metals and thus require strong bases (such as Vkd's base, KOH, triethylamine, etc.) to recover the active hydride and to deprotonate the intermediate σ-M-H_2 complex.[81-82] As discussed above (**Scheme 1.1**) the utilisation of such strong bases also shifts the thermodynamic equilibrium to the product side.[14] The strength of the base needed to deprotonate the σ-M-H_2 complex is linked to the hydricity and can be determined electrochemically in a similar way as described in **Figure 1.16a**. As the free energy for the heterolytic splitting of molecular hydrogen and the pKa of the conjugated form of the base are generally known, the change in free energy can be calculated according to the equations presented in Error! Reference source not found. after the reduction potential of the parent complex has been determined.[71, 83]

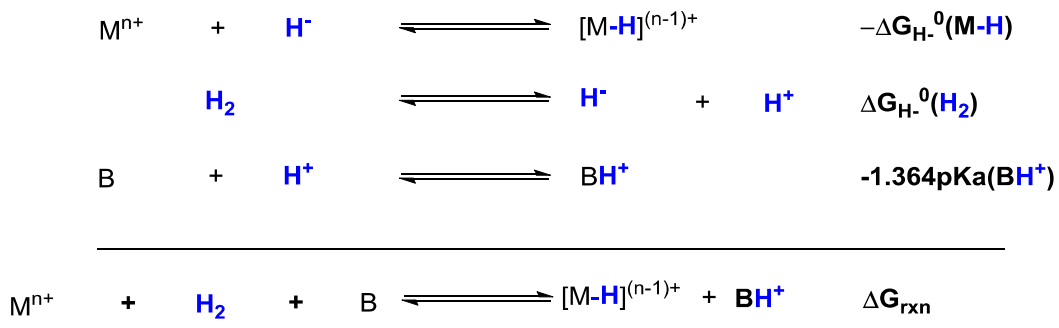


Figure 1. 19 Reaction scheme for the determination of base strength needed for deprotonation.[83]

Consequently, most catalytic systems utilise stoichiometric amounts of bases to shift the thermodynamic equilibrium to the product side and to deprotonate the intermediate σ-M-H_2, preventing the deactivation of the active hydride *via*

protonation. In the following section milestones in the development of homogeneous catalyst for the hydrogenation of CO_2 under basic conditions are discussed.

1.3. Catalysts under basic conditions

Note: Parts of this section are being published separately as a book chapter, see publication V.

In the presence of bases a plethora of catalysts have been shown to be active in the hydrogenation of CO_2 to formate salts and adducts. Those catalysts can be classified primarily by the type of ligand architecture, into: phosphine -, pincer based -, N-heterocyclic carbene and half sandwich catalysts.[84-97] Furthermore, catalysts can be classified by their active metal. For the most part however, the active catalysts utilize metals from group 8 and 9. Below, literature examples of catalysts active in the hydrogenation of CO_2 in the presence of base will be discussed based on their ligand architecture. The aim is to highlight catalyst development and cannot give a full picture of catalysts active in the hydrogenation of CO_2. A complete overview of the field can, however, be found in several recent reviews.[14, 17, 40]

1.3.1. Catalysts with phospine based ligand architectures

Although the first hydrogenation of CO_2 to FA dates back to 1935,[98] it was not until 1976 that the first pioneering work in the hydrogenation of CO_2 to formate

was conducted with homogenous catalysts by Inoue *et al.* using triphenylphosphine (PPh_3) complexes of Ru, Ir and Rh.[99] These catalysts displayed catalytic activity in the hydrogenation of CO_2 in benzene in the presence of triethylamine (NEt_3) as a base.[99] It was furthermore demonstrated that, small amounts of water can effectively accelerated the catalytic transformation of CO_2 to formate.[93, 100] Later, this concept was further elaborated and extended to more polar solvents such as DMSO.[101]

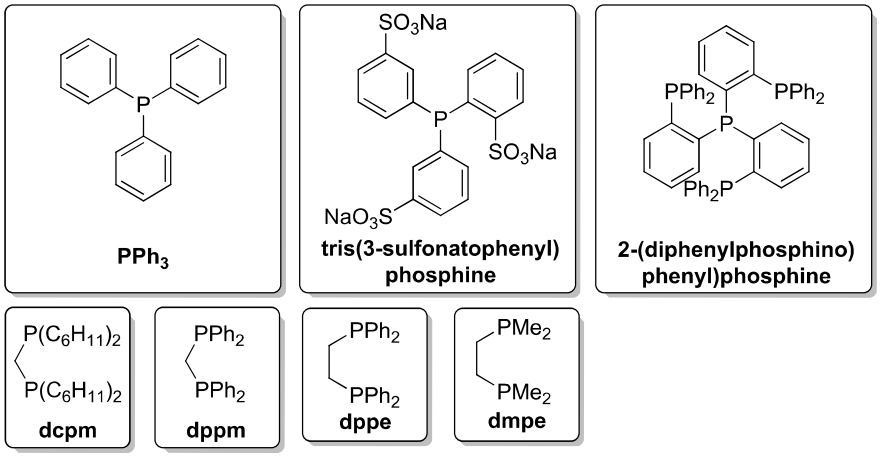


Figure 1.20 Phosphine compounds used as ligands for the synthesis of catalysts applied to the hydrogenation of CO_2 to FA.[17]

The accelerating effect of water was revisited in 1993 by Leitner *et al.,* when the group reported the first water soluble phosphine complex active for the hydrogenation of CO_2. They examined various catalysts and found that $[RhCl(tppts)_3]$ (**2**) (tppts: tris(3-sulfonatophenyl)phosphine) (see **Figure 1.20**) was the most active catalyst at 4 MPa H_2/CO_2 achieving a TON of 3440 at room temperature in a water:amine mixture.[94, 96, 102]

The precise role of water in the CO_2 hydrogenation to formic acid still remains under discussion. On the one hand it has been shown that some organic solvents and water form solvent-water cluster stabilising formic acid

thermodynamically.[1, 103] On the other hand CO_2 forms carbonates and carbonic acid in water, which on turn might be the true reagent source during the hydrogenation.[104-105]

Beller, Laurenczy *et al.* extended the system introduced by Leitner *et al*. [94, 96, 102] to various phosphine ligands in combination with $[RuCl_2(C_6H_6)]$ (**3**). They showed that the complexes, which are formed in situ, are active in the hydrogenation of CO_2 in the presence of aqueous $NaHCO_3$. The aforementioned phosphine ligands included PPh_3, 1,1-bis-(dicyclohexylphosphino)methane (dcpm), 1,2-bis-(diphenylphosphino)ethane (dppe), 1,1-bis-(diphenylphosphino)methane (dppm), and others. The highest catalytic activity was achieved when dppm was added, showing a TOF of 1200 h^{-1} after 2h at 70°C under 8.5 MPa of H_2/CO_2 (5/3.5), even though the catalyst deactivated after few hours.[106]

Non-precious metal phosphine based catalysts have also been reported to be active in the hydrogenation of CO_2 (or bicarbonate) to FA.[107-108] For instance [Iron(II)fluorotris[2-(diphenylphosphino)phenyl)phosphino]tetrafluoroborate] (**4**) achieved a TON of 7500 at 100°C under 6 MPa H_2.[108] As already mentioned in ***section 1.2.2.*** Linehan *et al.* investigated a series of phosphine based cobalt catalysts and achieved after optimising the thermodynamic hydricity TOF values ranging between 3400 h^{-1} and 74000 h^{-1} with **1**, depending on the pressure applied in the system (1 atm to 20 atm. However, a very strong base (verkade's base) is needed to deprotonate the Co-H_2 intermediate.[72] Examples of some of the phosphine ligands reported here are depicted in **Figure 1.20**.

Phosphine based complexes have also been integrated into carbon capture schemes. Here in a first step CO_2 is captured as carbamate using polyethylenimine (PEI). In the consecutive step the captured CO_2 is hydrogenated to FA in the presence of $RhCl_3 \bullet 3H_2O$ in combination with a monodentate phosphine ligand.[109] The sequential hydrogenation of CO_2 achieved a maximum TON of 852. Immobilised bidentate iminophosphine ligands in combination with Ir have also been found to be active under relatively mild conditions (60°C, 4 MPa, (p_{H2}:p_{CO2}) (1:1), 20 h). Here, a TON of 2800 after 20 h was reported.[110]

1.3.2. Catalysts with pincer-based ligand architectures

Pincer complexes have found a broad range of applications in catalysis, due to their high thermal and chemical robustness. Unsurprisingly, applications also include the hydrogenation of CO_2 to formic acid.

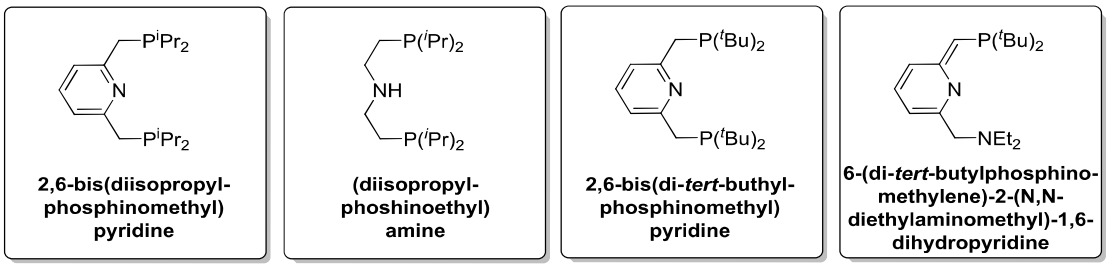


Figure 1.21 A selection of pincer ligands employed as ligands for Ir, Rh, Ru, Fe complexes applied for the CO_2 hydrogenation.[17]

Amongst the highest catalytic activity reported to date are reported with the pincer type ligand architecture, where a TOF value of 150,000 h^{-1} at 200°C and a TON value of 3,500,000 at 120°C was reported in water/THF (5/1) (v/v) in the presence of KOH under 8.5 MPa H_2/CO_2 (1/1) with [IrH_3(2,6-

bis(diisopropylphosphinomethyl)pyridine)] (**5**) (see **Figure 1.21** for the ligand structure).[89]

With the aliphatic complex [IrH_3((diisopropylphoshinoethyl)amine)] (**6**), TOF values of up to 18,780 h^{-1} and TON values of 348,000 were reported.[111] Interestingly, the secondary coordination sphere plays a crucial role in achieving high catalytic activities with IrH_3((diisopropylphoshinoethyl)amine)] (**7**) and [IrH_3(2,6-bis(diisopropylphosphinomethyl)pyridine)] (**8**). In the case of **7** a proton bridge is formed between the N-H and the formate ligand,[111] whilst in the case of the aromatic analogue **8**, a toggling in between de-aromatization 5 coordinative intermediate and the aromatized 6 coordinative hydride is observed.[89] For **8** the cooperative mechanism plays a crucial role for the addition of H_2 whilst with **7** the approaching CO_2 molecule interacts with the N-H group of the ligand, see **figure 1.22**.[89, 111]

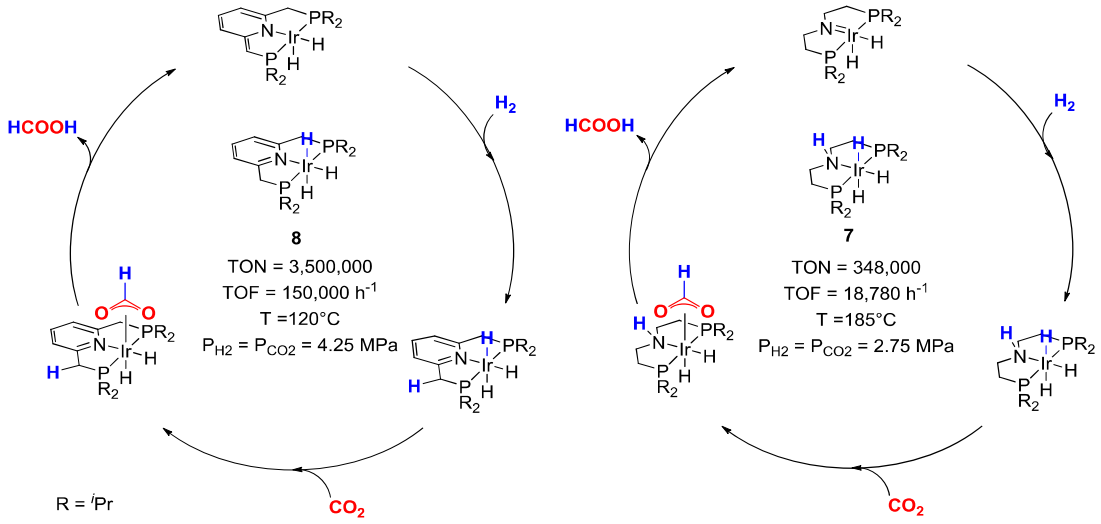
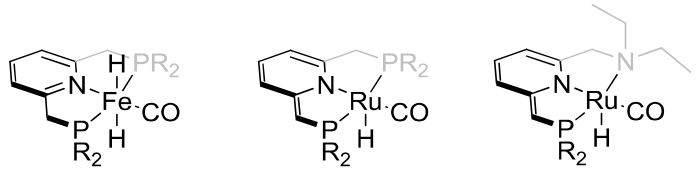


Figure 1.22 Comparison of aliphatic and aromatic Ir-pincer catalysts.[89, 111]

High activity was also reported by Milstein *et al.* for trans-[FeH_2(CO)(2,6-bis(di-tert-buthylphosphinomethyl)pyridine)] (**9**). **9** achieves a TOF of 160 h^{-1} and a TON of up to 780 at 60°C (representing a remarkable activity for a first row transition metal catalyst in the hydrogenation of CO_2) under 1 MPa in H_2O/THF

(10/1) (v/v) in the hydrogenation of CO_2 to FA.[112] The de-aromatised Ru derivative of trans-[FeH_2(CO)(2,6-bis(di-tert-butylphosphinomethyl)pyridine)] (**10**) possess higher activity than the Fe analogue.[113-114] Similarly, [RuH(CO)(6-(di-tertbutylphosphinomethylene)-2-(N,N-diethylaminomethyl)-1,6-dihydropyridine)] (**11**), is also active in the hydrogenation of CO_2 under basic conditions.[114]



9 **10** **11**

Figure 1.23 Fe amd Ru PNP pincer complexes investifated by Milstein and co-workers.[112-113]

Pidko *et al.* reported that [RuH(Cl)(CO)(2,6-bis(di-tert-butylphosphinomethyl)pyridine)] (**12**) achieved a TOF of 1,100,000 h^{-1} in DMF with DBU as a base under 4 MPa H_2/CO_2 at 120°C. This represents the highest catalytic activity reported for the hydrogenation of CO_2 to FA to date. In contrast to previous studies, it was demonstrated *via* DFT calculations that the de-aromatized intermediate (**12-Int1**) is less active as the dihydridic species **12-(H)$_2$1**.[90-91, 115]

In depth DFT studies demonstrated that the most active catalytic cycle does not involve a co-operative mechanism for the H_2 activation. In this case, the H_2 complex is directly deprotonated to free formic acid (**Figure 1.24**, cycle I).[115] However, pincer complexes normally participate in a co-operative mechanism during H_2 activation, leading to an intermediate 5 coordinate species (**12-Int1**) (cycle II). Unfortunately, these species are also active towards the insertion of CO_2 into the ligand architecture and provides an entry point into the third and

least active cycle (cycle III) (via **12-Int2**). A general overview of these catalyst cycles is represented in **figure 1.24**.[115]

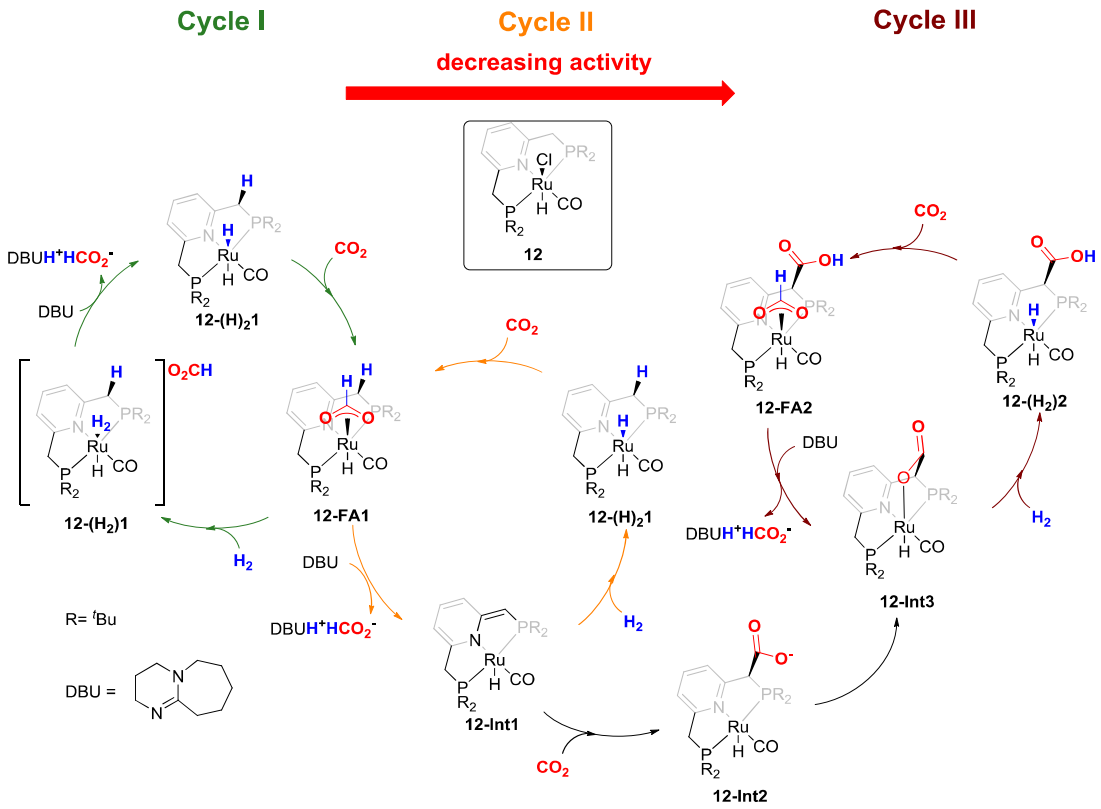
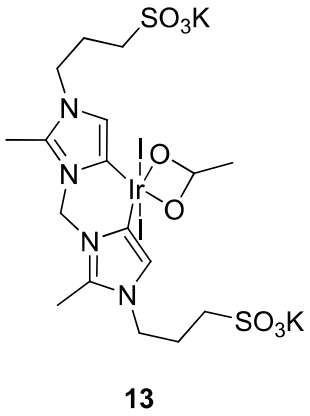


Figure 1.24 Three main catalytic cycles found by Pidko *et al.* Cycle I is the most active mechanism; no co-operative mechanism for H_2 activation is present; in Cycle II H_2 is activated in a co-operative fashion; at the same time CO_2 can be incorporated into the ligand architecture leading to the least active cycle III.[115]

A fundamental consequence of this mechanism is that excess amounts of hydrogen have to be employed in order to inhibit the catalyst to enter cycle III and thus ensuring the durability of pincer based catalysts in the hydrogenation of CO_2.[90-92, 116] A high conversion of H_2 is necessary for economic and environmental reasons connected with the sustainable generation of hydrogen.[28] Consequently, processes utilizing excess amounts of H_2 pose considerable hurdles to potential industrial implementation.[28]

1.3.3. Catalysts with NHC-carbene based ligand architectures

Peris and collaborators explored various thermally robust N-heterocyclic carbene (NHC) complexes for the hydrogenation of CO_2. Best results were obtained with the abnormally bond $[IrI_2(AcO)(bis\text{-}NHC)]$ (**13**) as the catalyst at 200°C under 6 MPa H_2/CO_2 (1/1).[86-87] A TON of 190,000 was achieved after 75 h. Generally NHC ligands display high electron donating character, thus a high catalytic activity was achieved for the investigated reaction. Furthermore, **13** is also active in in the transfer hydrogenation of CO_2 using isopropanol as the hydrogen source, resulting in a TON of 1000.[117] Employing isopropanol as a H_2 source is safer than employing pressurised H_2. The lowered activity compared to reactions carried out with pressurised H_2 was attributed to the difficult formation of the active metal hydride from isopropanol.[86-87, 117]



13

Figure 1.25 Complex **13**.

1.3.4. Half sandwich complexes as catalysts for the hydrogenation for CO_2

It has been shown that, the complex [Cp*Ir(4,4′-dihydroxy-2,2′-bipyridine)Cl]Cl (**14-a**) is catalytically active in the hydrogenation of CO_2 whilst the unmodified bipyridine complex (**15**) is inactive for the here discussed reaction. In this fashion **14-a** showed more than a 1000 fold increase in its initial TOF,

achieving a value of 5100 h^{-1}. This effect is attributed to electron donation from the oxyanion to the metal centre and the consequent "keto" resonance structure,[118] as shown in the **figure 1.26b**.

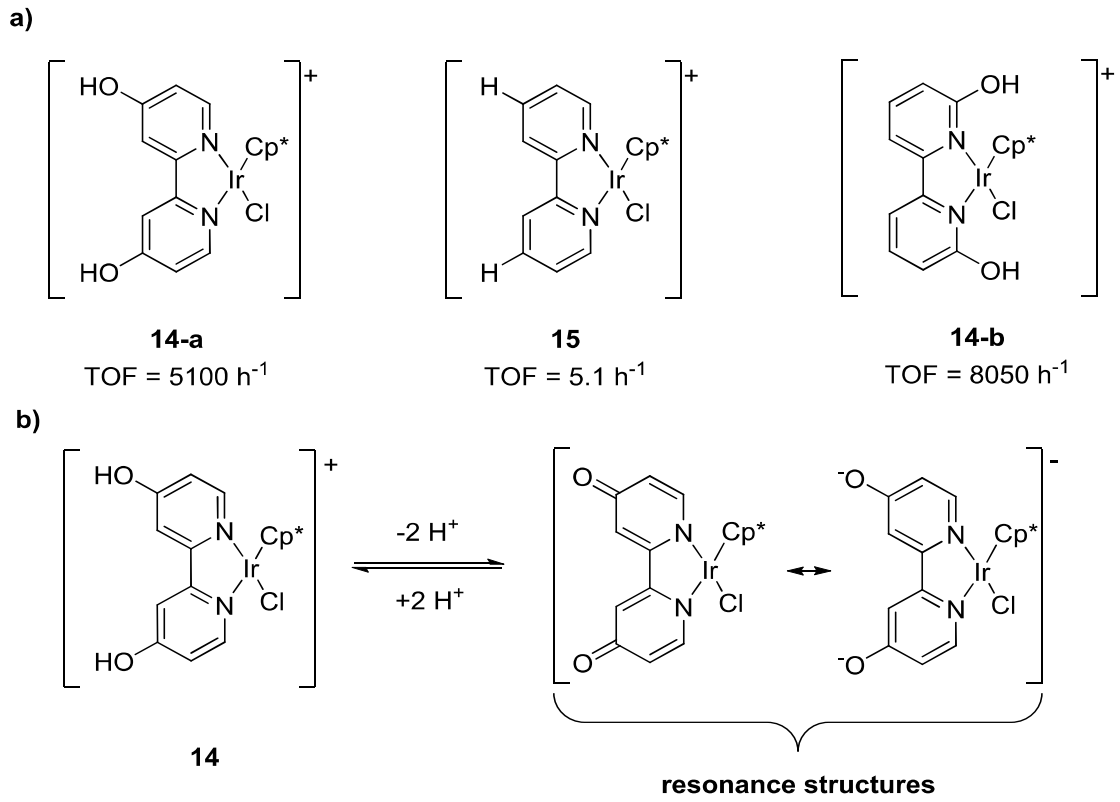


Figure 1.26 a) Complexes **14-a**, **14-b** and **15** with corresponding catalytic activity and b) Keto resonance structure of **14** after deprotonation.[118]

The catalytic activity can be correlated to the Hammett constant σ_P^+, i.e. higher electron donating properties lead to higher catalytic activities. This finding is in good correlation with the thermodynamic hydricity introduced in ***section 1.2.2***. However, it is noteworthy that upon switching the initial hydroxo group from the *para* position to the *ortho* position (in **14-b**), the catalytic activity was significantly increased reaching a TOF of 8050 h^{-1}. As the electron donation in para and *ortho* position is almost the same, the increased catalytic activity must be attributed to the facilitated formation of the active hydride from the M-

H_2 complex. Here the oxyanion in *ortho* position functions as a base, thus proton transfer from H_2 is facilitated.[84-85, 88, 119-121]

As all the systems introduced so far utilize bases, where the formation of formate salts and adducts is the key thermodynamic driving force for the reaction to proceed. Inevitably, this thermodynamic driving force would have to be reversed during the purification of formic acid from the reaction mixture, leading to energy intensive processes. As an alternative, research has shifted focus onto the direct hydrogenation of CO_2 to formic acid in the absence of bases.

1.4. Catalyst under acidic conditions

Although a considerable amount of research has been focused upon the catalyst development for the selective hydrogenation of CO_2 to FA, only a few examples have been reported in the absence of base. This is mainly due to the unfavourable thermodynamics (see **Scheme 1.1**) and the kinetic deactivation of metal hydride complexes in acidic media via protonation. Consequently, it was not until 2004 that the first catalyst was reported for the base free hydrogenation of CO_2 to FA.[63] In their breakthrough study, Ogo *et al.* used $[(\eta^6\text{-}C_6Me_6)Ru^{II}$(2,2′-bipyridine or 4,4′-dimethoxy-2,2′-bipyridine)$(OH_2)]SO_4$ (**16**) (see Figure 1.27) to hydrogenate CO_2 to FA under 2.5-5.5 MPa (H_2:CO_2; 1:1) in water.[63] A total concentration of 0.06 M of FA and a TON of 40 was achieved under optimised conditions and prolonged reaction times (72h).[63] After their first study, the same group investigated the reaction mechanism

for the base free hydrogenation, comparing their ruthenium complex with an iridium derivative. Whilst the key reaction intermediates remained the same, the group could show that Ir and Ru differ in their rate determining step, as shown in

Figure 1.27 Reaction mechanism for the hydrogenation of CO2 to FA under base free conditions using Ruthenium (left) and Iridium (right).[64]

Figure 1.27.[64]

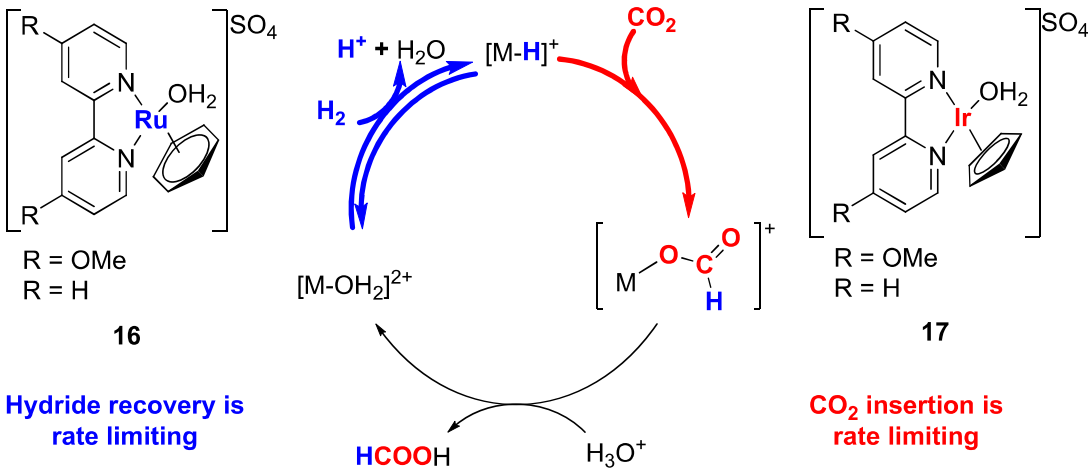


Figure 1.27 Reaction mechanism for the hydrogenation of CO_2 to FA under base free conditions using Ruthenium (left) and Iridium (right).[64]

As shown above, the metal hydride reacts with the CO_2 to form a formate complex. Afterwards, formate is cleaved as FA from the metal centre by water coordination. In the last step the hydride is recovered by heterolytic hydride splitting forming the active hydride complex and a proton. The hydride recovery step represents the rate limiting step for the Ru-catalyst, whilst the CO_2 insertion is rate limiting for the Ir-derivative.[64] The change in rate limiting steps are due to different strengths of hydride donation between Ru and Ir. For instance, Ru is a stronger hydride donor, hence the hydride transfer is fast (i.e. not rate limiting) in contrast to Ir. Conversely, Ru forms stronger M-O bonds

and, as a consequence of the stronger M-O binding, hydride recovery is rate limiting with most Ru-based catalysts.[63-66]

In 2016 the mechanism introduced by Ogo *et al.* was confirmed by Lu *et al*.[122] In their study, the group investigated Ir(III)-complexes with varying diimine ligands and assessed their reactivity in the hydrogenation of CO_2 to FA. After screening various ligands and reaction conditions, it was found that by replacing H_2O with D_2O as solvent, the TOF can be increased from 280 h^{-1} to 768 h^{-1}. This indicates a positive kinetic isotope effect (KIE) and indicates the turnover limiting step being the transformation of the aqua complex to an H_2 complex, i.e. the resting state of the catalyst is the aqua complex. In total, a TON of 10258 was achieved, giving a final concentration of 0.13M FA. Further evidence verifying the mechanism of the catalytic cycle was found using *in-situ* nuclear magnetic resonance (NMR) studies, where a hydride intermediate was detected upon addition of H_2 to the catalyst. However, after adding CO_2 the hydride immediately disappeared, indicating that the hydride is unstable under the acidic conditions and reacts rapidly. At all stages of the reaction, an Ir-aqua-complex could be detected thus confirming the mechanism proposed by Ogo *et al* (**Figure 1.26**).[2,122]

Although these early examples were encouraging, the TON, TOF and maximum final concentrations of FA achievable in water were far from satisfying. This might be due to the fast acidification of the reaction medium by formic acid over the course of the formation of FA, which in turn leads to the protonation of the active hydride species, inevitably leading to the depletion of the active catalyst. Consequently, the effect of sodium formate as a buffer was studied. It was suggested that the buffer might stabilize the pH at higher

values, and thereby prevent the deactivation of the catalyst by protonation.[123] Tri-3,3′,3″-Phosphanetriyltris(benzenesulfonic acid) trisodium salt Rhodium(I) chloride, $[RhCl(mtppms)_3]$ (**18**), was used as a catalyst precursor in 0.05 M sodium formate solution. The addition of NaO_2CH to the catalytic system increased the formation of FA by 200%, using 50 bar CO_2 and 50 bar H_2 for 20 h at 50 °C, giving a total concentration of free FA of 0.11 M with a TON of 55 with a TOF of 2.75 h^{-1}.[123]

In 2014 Laurenczy and co-workers showed that the buffering effect can also be achieved by using dimethyl sulfoxide (DMSO) as a co-solvent.[103] They found that in a solution of DMSO containing water (10 v/v%), a remarkable concentration 1.9 M of FA was achieved using Tetra(1,3,5-Triaza-7-phosphaadamantane)Ru(II)chloride, $[RuCl_2(PTA)_4]$ (**19**), as catalyst.[103] After 120h, the TON was determined to reach 500-1000, depending on the reaction conditions. It was assumed that DMSO and H_2O form solvent clusters, where DMSO acts as a proton acceptor and thus prevents fast acidification of the reaction medium. In agreement with the thermodynamic considerations outlined previously (equation 3 and 6 for the determination of the equilibrium constant) a linear relationship between the yield of FA and the total pressure was found. Furthermore, lower temperatures lead to an increase in yield of FA formed, which indicates that the reaction indeed reaches its thermodynamic equilibrium, as the reaction is exothermic in nature.[103]

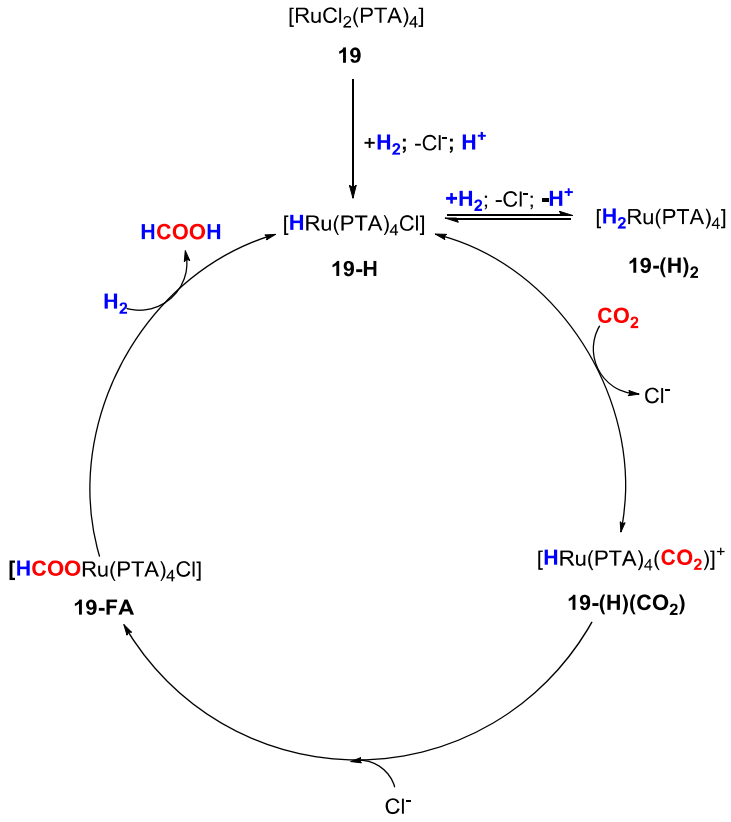
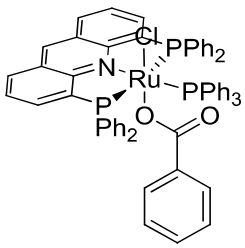


Figure 1.28 Catalytic mechanism for the hydrogenation of CO_2 to FA with $[RuCl_2(PTA)_4]$ described by Laurenzcy et al.[103]

In 2016 (4,5-bis(diphenylphosphino)acridine)Ru(II)(benzoate)(chloride, [Ru(acriphos)($PhCO_2$)Cl] (**20**), was tested as catalyst-precursor for the base free hydrogenation of CO_2 to FA.[1] Although a DMSO:H_2O mixture, similar to the solvent mixture described by Laurenczy *et al.*, was used only a 0.3 M solution was achieved. However, the catalytic activity was relatively high, yielding a TOF of 260 h^{-1} and a TON of 4200 in DMSO:H_2O mixture with 5 v/v% water at 60°C with 40 bar CO_2 and 80 bar H_2.[1] By adding NaOAc as a buffer the TOF was increased to 1019 h^{-1}, yielding a TON of 16310 and the



20

Figure 1.29 Depiction of Complex **20**.

concentration of FA reached 1.3 M under optimised conditions.[1] The decreased TOF and TON in the absence of NaOAc was attributed to deactivation caused by protonation of the catalyst to form an inactive cationic complex.[1]

Achard and co-workers reported Phosphine-pyridonate ligands containing octahedral ruthenium complexes to be active in the hydrogenation of CO_2 to FA. A TON of 355-370 was reported after 72 h at 50°C under 50 bar H_2 and 10 bar CO_2 yielding concentrations of 0.57-0.60 M in DMSO.[124] Interestingly, the ligand system has a hydroxyl group in *meta* position to the N of the pyridine ring. This suggests a similar reactivity as observed with proton responsive half sandwich complexes (see **figure 1.26**).[119, 124]

Since the concentrations of FA achieved (and catalytic TON) are far lower under acidic conditions than under corresponding basic conditions, process development has focused on systems using base as the thermodynamic driving force. The following section deals with major process schemes for the synthesis of formic acid from CO_2.

1.5. Existing processes for the transformation of CO_2 to formic acid

In the following, a collection of milestones in the development of plausible process schemes for the hydrogenation of CO_2 to FA will be presented. It is important to mention that all of these process schemes involve the formation of formate salts, thus the product must be separated from reactive mixture via reactive distillation,[46, 125-127] or by dissolution into super critical CO_2 ($scCO_2$).[128] Consequently, research has focused on the connection of the synthesis to upstream processes, or on the development of processes facilitating the separation of the FA from the base.

Interestingly, life cycle assessments show that the production of FA from CO_2 is beneficial compared to traditional synthetic processes, even if H_2 from traditional routes are used (e.g. steam methane reforming). This is mainly due to the tedious purification of FA in the traditional, fossil-fuel based synthesis of FA. Compared with other CO_2-based production lines for chemicals, such as MeOH and CH_4, the synthesis of FA from CO_2 achieves a positive environmental impact, because only one equivalent of H_2 is consumed, refer to ***section 1***, ***figure 1.2***.[28]

1.5.1. Connection to processes upstream

In 2016, a system for the hydrogenation of carbamates and ammonium carbonates coupled to the Haber Bosch system was proposed by Su *et al*.[129] Here, ammonia synthesised in the Haber Bosch Process and CO_2 are mixed to form carbamate or ammonium carbonate, depending on the water content in the system (i.e. ammonium carbonate is preferentially formed in the presence of water).[129] After adding 2.75 bar H_2 and catalytic amounts of Pd/C in an ethanol water mixture (70 wt% ethanol), the carbamate or carbonate is transformed into ammonium formate under very mild conditions, see **Figure 1.30**.[129] Furthermore, it was shown that the hydrogenation of ammonium carbonates proceeds faster and with higher efficiency than the corresponding reduction of ammonium carbamate.[129]

The low cost of the base and the utilisation of commercially available Pd/C catalyst was beneficial for the connection of the Haber Bosch process to catalytic hydrogenation. Furthermore, very mild conditions can be applied (20°C and 2.75 bar H_2), further improving the economic balance. The product, ammonium formate, is already used in silage aid, as a reagent in the Leuckart reaction for the preparation of primary amines and for transfer hydrogenations of functional groups.[34, 42]

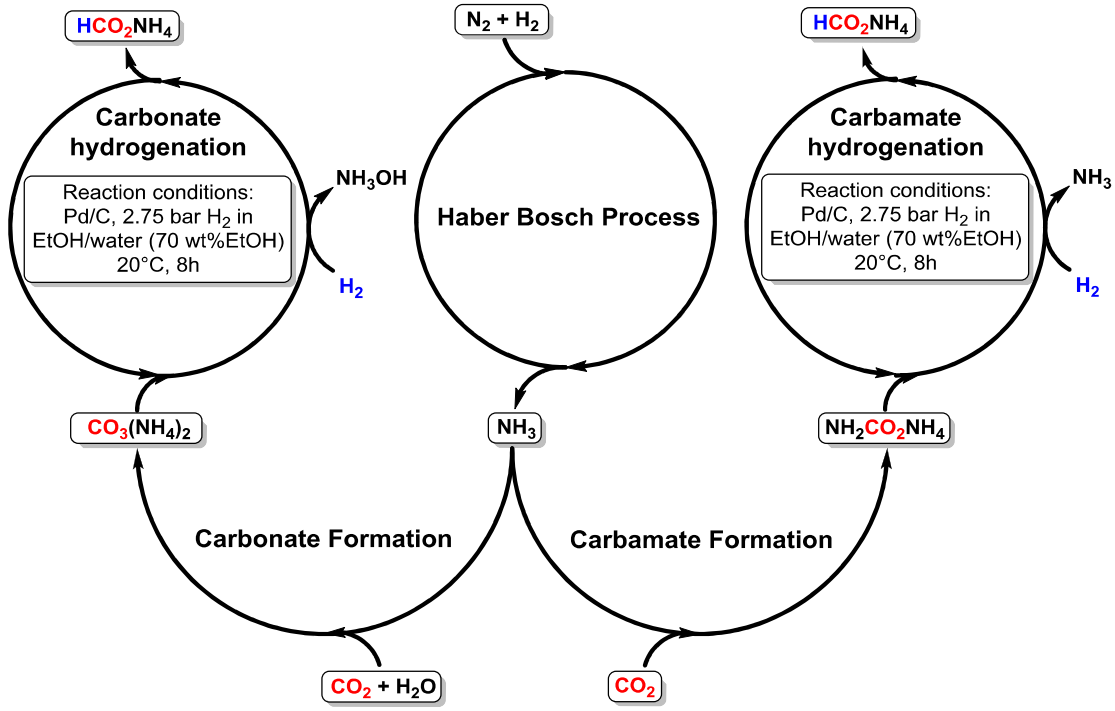


Figure 1. 30 Upstream connection of CO_2 hydrogenation to the Haber-Bosch process.[129]

Another possibility is the integration of the FA/formate synthesis with CO_2 scrubbing. In this regard, high catalytic turnovers (total TON 150,000) and turnover frequencies (TOF_{av} = 35,000 h^{-1}, TOF_{ini} = 180,000) can be achieved. Astonishingly, the best results were obtained with a biphasic system where the catalyst, [*cis*-Ru(dppm)$_2$Cl$_2$] (**21**) was dissolved in methyl-isobutylcarbinol (MIBC) and the formate adduct was quantitatively extracted into the aqueous phase. Commercially available CO_2 scrubbing agents methyldiethanolamine (Aminosol CST 115®) and monoethanolamine (MEA) were employed as bases. The catalyst phase could be recycled up to 11 times and only small amounts of catalyst leached into the product phase.[130] Interestingly, connecting CO_2 scrubbing with hydrogenation is proposed to "open the possibility for integrated approaches to carbon capture and utilization".[130]

1.5.2. Connection to downstream processing

A method to facilitate the downstream purification of FA is the formation of formate adducts with non-volatile bases. Under reactive distillation conditions the product can then be separated from the reaction mixture. As an additional challenge, the catalyst has to be separated from the formate adduct, because the harsh conditions applied during reactive distillation would favour the decomposition of the product to CO_2 and H_2. An interesting approach was demonstrated in 2011 by Schaub et al at BASF SE, where the reaction was carried out in the presence of the high boiling amine trihexylamine ($NHex_3$), $[Ru(H)_2(P\textit{n}Bu_3)_4]$ (**22**) as the catalyst and a high boiling diol as solvent. Various diols (2-methyl-1,3-propanediol, 1,3-propanediol, 1,2-propanediol and ethanediol) were tested and the best results were obtained with 2-methyl-1,3-propanediol.[46] Interestingly, without the diol no catalytic conversion can be obtained and this was attributed to additional proton bridging in between the OH groups of the diol and formic acid.[46] The process can be divided into 3 steps:

1) Formate synthesis
2) Extraction of the catalyst from the product
3) Reactive distillation to separate the product from the base and solvent

After extraction and reactive distillation, the solvent, base and catalyst are recycled back and can be reused in subsequent reaction cycles.[46] The process scheme is shown in **Figure 1.31**.

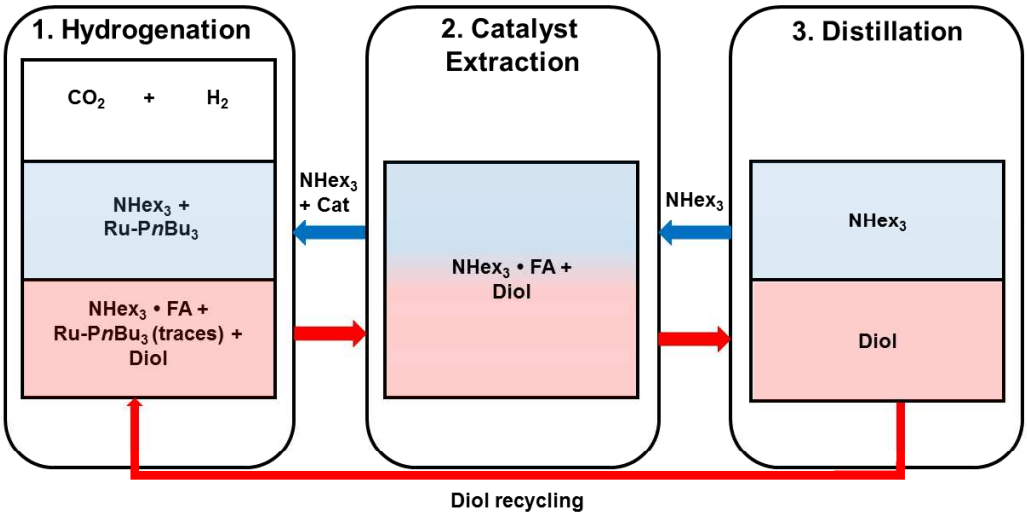


Figure 1.31 Process scheme for the hydrogenation of CO_2 to FA developed by BASF SE.[46]

Economic assessment found that the proposed process would be economically unsustainable.[131] This is mostly due to the high price of gas compression and the intensive consumption of chemicals employed as additives.[131]

As an alternative to the high boiling trihexylamine, ionic liquids (ILs) with functionalised side chains can be used as an immobilised base.[125-127] After either immobilising a homogeneous catalyst onto a silica surface,[125-126] or using heterogeneous Ru-NP on TiO_2,[127] the IL-formate adduct can be separated from the catalyst by hot filtration. Afterwards, a N_2 assisted reactive distillation liberates FA from the ionic liquid. The ionic liquid remains unmodified by the reactive distillation and can be reused for consecutive hydrogenations.[125-126]

Leitner and co-workers introduced the first continuous flow process for the hydrogenation of CO_2 to FA. In their system $scCO_2$ was used as the eluent phase, whilst functionalised ionic liquids, similar to those reported previously,[126-127] functioned as the immobilised basic phase. The catalyst was

also present in the IL phase. The best results were obtained with [Ru(cod)(methylallyl)$_2$] (**23**) and PBu$_4$TPPMS as catalyst, and amine functionalised imidazolium ILs or polystyrene functionalised with a basic functional group in combination with 1-ethyl-3-methylimidazolium bis(trifluoromethylsulfonyl)imide (EMIm.NTf$_2$).[128]

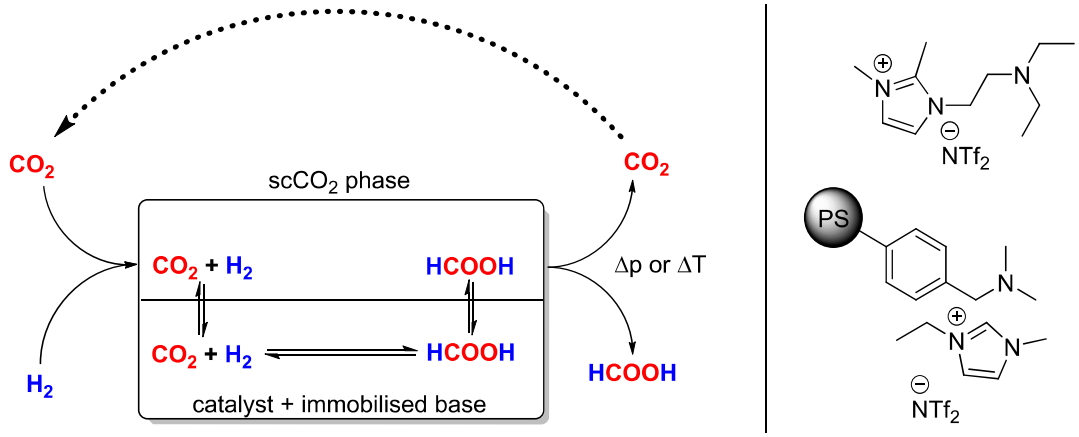


Figure 1.32 Process scheme using scCO$_2$ as FA stripping eluent with IL immobilised bases.[128]

The system depicted above can be kept working for >200h without any deactivation of the bases. Separation of FA was slow however, mainly due to the sluggish extraction of the product from the IL phase. The low TONs (on stream a TON of 485 was reported) achieved with this system was accounted for by the high catalyst concentration in the system.[128]

It is important to note at this stage that all of the approaches presented here do have inherent disadvantages. All presented processes are based on batch reaction designs in the presence of stoichiometric amounts of bases,[46, 130] leading to intense purifications steps and thus to a comparatively low throughput. Alternatively, scCO$_2$ is used as the eluent phase in a CSTR (CSTR = **c**ontinuous **s**tirred **t**ank **r**eactor) necessitating high compression demands limiting the economic viability (Note: compression of gas represents a major

cost factor).[128, 131] In order to improve the economic viability, higher throughputs would be desirable, which could be achieved with flow processes. Here the eluent phase should be organic solvents or water in the absence of base in order to decrease purification demands, thus reducing the amount of purification units in a plausible industrial process. However, the lack of additional stabilising thermodynamic forces will inevitably lead to lower yields of FA, see **section 1.2.1**.

Unfortunately, under base free conditions catalytic activity and stability is significantly reduced (see **section 1.4**). These effects are most likely due to the deactivation of the catalyst by protonation, thus necessitating a catalyst support phase which on the one hand stabilises the active hydride and prevents deactivation, but on the other hand facilitates the extraction of formic acid from the support phase into the eluent phase. For instance, a basic environment is likely to stabilise the catalyst in its active form, but would inherently lead to disadvantageous distribution functions in between the catalyst/ support – and the eluent phase. Alternatively, the catalyst phase could utilise buffers in order to stabilise the pH at an acceptable level preventing the discussed deactivation pathway, whilst enabling the extraction of formic acid from the support phase.

A key aim of this thesis was therefore to investigate the role of ionic liquids on the hydrogenation of CO_2 and to develop a viable catalytic system for the hydrogenation of CO_2 to formic acid in the absence of conventional bases. Ionic liquids display several beneficial properties for the investigated reaction, i.e. the ion pair can be tuned towards beneficial properties for the discussed transformation and by the variation of the counteranion (or functional groups

on the cation) the pKa of the ionic liquid can be tuned towards desired values. In the next part, a short overview of ionic liquids in general and their interaction with water and CO_2 is given.

1.6. General Overview over ILs

Ionic liquids (IL) are organic salts which are, as their name implies, liquid at (or near) room temperature.[132-135] They have attracted interest in various fields across both chemistry and physics, and are commonly applied as extracting agents, stabilising agents and in a broad variety of catalytic reactions.[132, 136] There is a huge range of possible ionic liquids, summarised in a range of recent reviews,[132-140] however this chapter will focus solely on dialkylimidazolium based ILs.

In order to understand modern ILs, it is useful to revisit the properties of classical molten salts. Near their melting point, such molten salts retain their near distance order, while long distance order is lost. So, the atom-atom and/or ion-ion distances and their ordering does not significantly change.[141-142] To a certain extent modern ILs can be described as a subgroup of molten salts but due to their asymmetry – either at the cation or the anion – the melting point is remarkably decreased. This asymmetry induces steric hindrance, which prevents ILs from forming ordered crystal structures at or near room temperature. Another difference is the formation of a cooperative network *via* hydrogen bonds between cations and anions.[138, 143-145] Due to the presence of these hydrogen bonds, a structural orientation is induced ("entropy effect"). ILs

therefore form pre-organised structures (**figure 1.33**), such as nanosized channels and pockets while in classical molten salts this is formed solely *via* ion-ion interaction.[146-147]

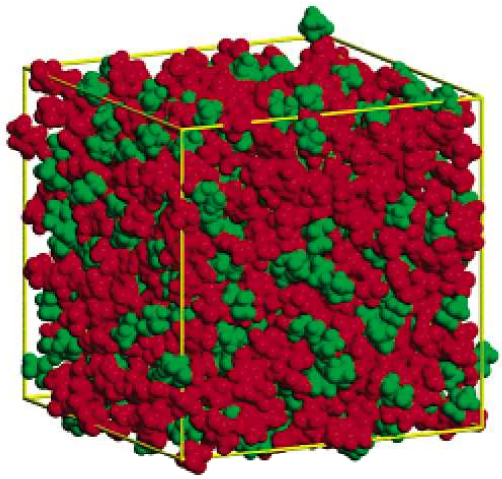


Figure 1.333D-structure formed by ionic liquids.[147]

The driving force for the formation of these nanostructures are either the π-stacking of the imidazolium ring or columbic ion-ion interactions. Consequently, two distinct structural formations can be observed. If columbic interactions are the driving force for the formation of the 3D-structures then columns with alternating anions and cations are formed, while when π-stacking dominates, columns of separated anions and cations are formed, as shown in **Figure 1.34**.[137]

Moreover weak interactions, such as van-der-Waals interactions start to play a crucial role by increasing chain length. Indeed it has been shown that imidazolium ILs with dodecyl side chains possess characteristics of liquids crystals.[148-149]

Considering the formation of H-bonds, it was found that the strength of these interactions can be tuned *via* the anions. Here, the strength of the expected

H-bonding interaction can be described the following sequence: $CF_3CO_2 > BF_4 > InCl_4 > BPh_4$.[150-151]

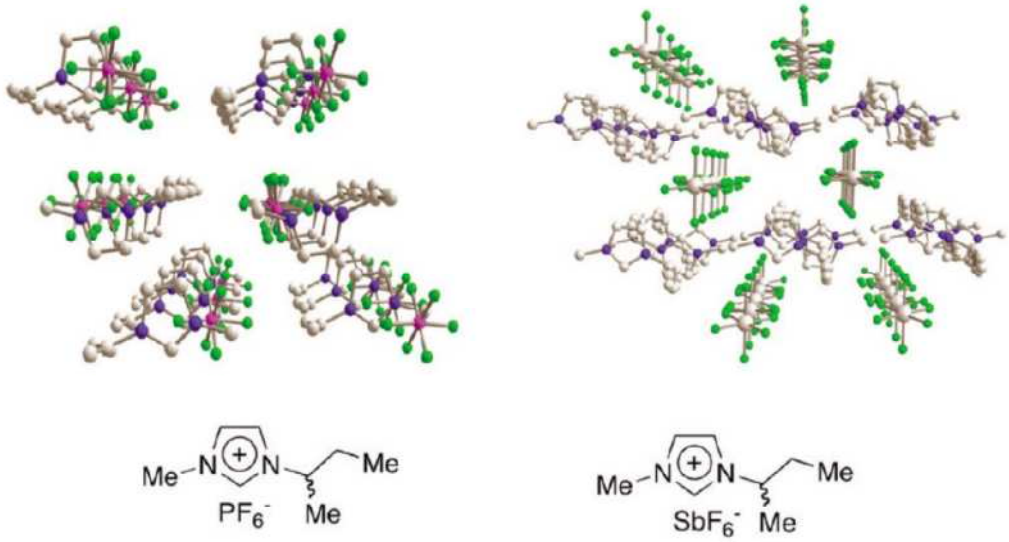


Figure 1.34 3D-ordering of ionic liquids, with dominating ionic interactions (left hand) and π-stacking as the dominating force.[137]

Furthermore, the anion influences the solubility of the ILs in water. So, it was found that the hydrophobicity of comparable ILs can be described by following anion row: $[BF_4]^- < [CH_3(C_2H_4O)_2SO_4]^- < [C(CN)_3]^- < [PF_6]^- < [N(SO_2CF_3)_2]^-$. The hydrophobicity can also be increased by adding longer alkyl side chains or by methylating position 2 in the imidazolium ring.[152]

The pre-organised structure of ILs and especially imidazolium ILs can be used to form well defined transition metal nanoparticles (MNP).[137] Indeed, ILs possess polar and unpolar regions, thus separating polar and unpolar compounds. The size of the nanoparticles formed in ILs depend highly on the size of those polar and non-polar compartments. This is because non-polar organometallic precursors can be separated from the polar nanoparticle, thus

leading to controllable concentrations of metal atoms during the formation of MNPs, allowing very small MNPs (<10 nm) to be easily synthesised.[153-154]

Furthermore, the formed nanoparticles are not stabilised by single cations or anions, but by aggregates of ion pairs. Consequently, the stabilisation cannot be described by the DLVO model, as pointed out in literature.[155] Dupont and co-workers showed by XPS studies that even weak coordinating ligands, such as the anions BF_4 and PF_6, do interact with the metal surface.[156] The same group demonstrated not only that the anion is responsible for stabilising the MNPs formed in the IL, but also that the imidazolium cation plays a role.[157-158]

Indeed, it can be assumed that the IL surrounding crystalline MNPs forms a semi ordered double layer. Consequently the model describing the stabilisation of MNP in ionic liquids must be a liquid film model (similar to micelles) which has impact in understanding the catalytic activities of MNP and in ionic liquids.[159-160]

Further evidence for micelle formation in ILs was found in 2016 by the Dupont group. The hydrogenation of benzene resulted in the formation of small amounts of cyclohexadiene. Remarkably, it should not be thermodynamically possible to form cyclohexadiene during the hydrogenation of benzene. It was also shown that the selectivity towards cyclohexadiene can be increased by utilizing bimetallic Ru@Pt nanoparticles. The authors concluded that due to synergistic effects, cyclohexadiene formation becomes favourable, however, upon removal of the IL cyclohexadiene was not detected anymore. This is a clear indicator for the non-innocence of the IL-phase. The authors suggest that the IL forms a micellar cell type structure which surrounds the MNP and,

because of the exothermicity of the full hydrogenation of benzene, the temperature inside this micelle is increased. As a consequence, the energetic level of the catalyst might be temporarily increased and therefore leads to formation of the thermodynamically "impossible" product. The system also used *n*-heptane as a co-solvent, which might help to facilitate removal of the product from the catalytically active micelle.[161]

These entropic effects could be significant in the hydrogenation of CO_2 to formic acid. Indeed, here the main hurdle to the transformation is the highly unfavourable contribution from the entropy change, see **scheme 1.1**. Utilizing ILs might capitalize on the entropic effect to lower the energetic hurdles inherent to the system.

1.6.1. Interaction of ILs with CO_2

The interaction of various ILs with CO_2 have been investigated in the literature. Early studies were done with the hydrophobic ILs 1-butyl-3-methylimidazolium hexafluorophosphate (BMI.PF_6) and 1-butyl-3-methylimidazolium tetrafluoroborate (BMI.BF_4). It was demonstrated that CO_2 is encapsulated into the voids formed by the IL 3D structure of the ion pairs. However, upon increasing the pressure of CO_2, the 3D structure is disturbed. This is facilitated by weaker interactions between the components of the IL, i.e. faster deformation is observed with BMI.BF_4 than with BMI.PF_6. The faster deformation of BMI.BF_4 is due to weaker stabilisation of the nanoaggregates due to a weaker H-Bond interactions.[162]

The absorption of CO_2 into the voids in the IL was further studied with branched and fluorinated dialkylimidazolium N-(bis)triflate (DAI.NTf_2) ILs. Here the supramolecular structures observed in ILs are of a more irregular shape. Consequently, the interactions observed in these ILs are of a weaker character and thus can be more easily broken down. This becomes evident when various pressures of CO_2 are applied. Under 10 bar CO_2, linear alkylimidazolium ILs outperform branched ones (in terms of CO_2 uptake), whilst under 80 bar CO_2 the reverse order is observed.[163]

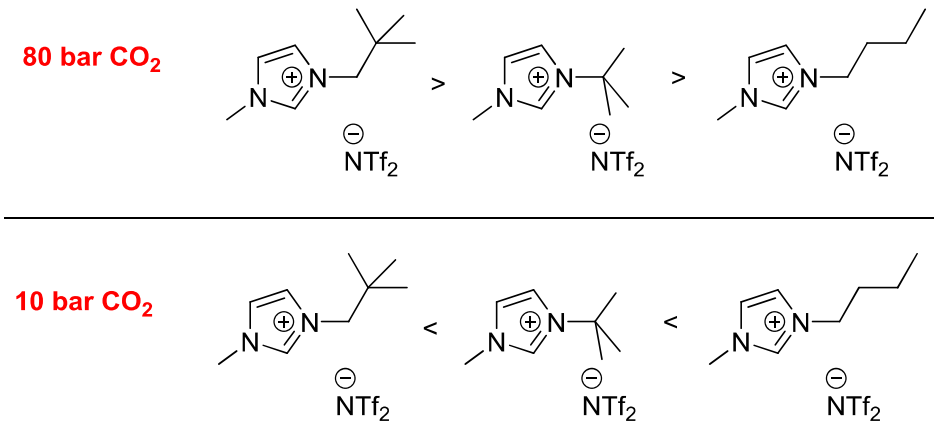


Figure 1.35 CO_2 uptake by differing ILs with NTf2 counteranions. Top row depicting the relative uptake of investigate ILs under 80 bar CO_2; bottom row at 10 bar CO_2.[163]

It was later shown that basic ILs (dialkylimidazolium acetate, dialkylimidazolium imidazolate, dialkylimidazolium triazolate) form supramolecular host-guest complexes with confined water trapped inside the IL networks. This host-guest complex is even maintained in solvents with high dielectric constants such as DMSO.[164-165]

The strong interaction between water and the basic ILs can be utilized to enhance the activity of ILs towards CO_2 capture. Here, the IL first activates water, which in turn acts as a nucleophile towards CO_2, forming carbonate

species.[166] It is important to note that the interaction between the counteranion and cation plays a crucial role in this mechanism, i.e. more basic counteranions can absorb higher quantities of CO_2.[166] The mechanism for water – and CO_2 activation with basic ILs is depicted in **Figure 1.36**.

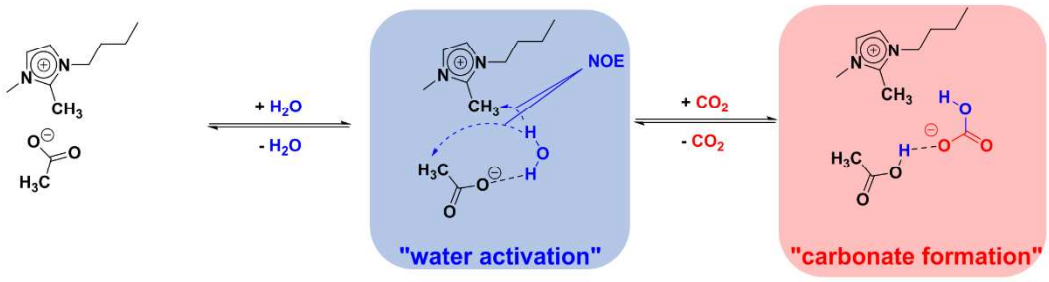


Figure 1.36 Activation of water in blue box and CO_2 (red box) by basic ILs. NOE stands for **N**uclear **O**verhauser **E**ffect, and describes a short distance in between protons.[166]

1.7 References

1. Rohmann, K.; Kothe, J.; Haenel, M. W.; Englert, U.; Hölscher, M.; Leitner, W., Hydrogenation of CO2 to Formic Acid with a Highly Active Ruthenium Acriphos Complex in DMSO and DMSO/Water. *Angewandte Chemie International Edition* **2016,** *55* (31), 8966-8969.
2. Griffin, P. W.; Hammond, G. P.; Norman, J. B., Industrial energy use and carbon emissions reduction in the chemicals sector: A UK perspective. *Applied Energy* **2018,** *227*, 587-602.
3. Mecking, S., Nature or Petrochemistry?—Biologically Degradable Materials. *Angewandte Chemie International Edition* **2004,** *43* (9), 1078-1085.
4. Vooradi, R.; Bertran, M.-O.; Frauzem, R.; Anne, S. B.; Gani, R., Sustainable chemical processing and energy-carbon dioxide management: Review of challenges and opportunities. *Chemical Engineering Research and Design* **2018,** *131*, 440-464.
5. Lancioni, R. A., The Importance of Price in International Business Development. *European Journal of Marketing* **1989,** *23* (11), 45-50.
6. Haibach, M. C.; Kundu, S.; Brookhart, M.; Goldman, A. S., Alkane Metathesis by Tandem Alkane-Dehydrogenation–Olefin-Metathesis Catalysis and Related Chemistry. *Accounts of Chemical Research* **2012,** *45* (6), 947-958.
7. Jarvis, S. M.; Samsatli, S., Technologies and infrastructures underpinning future CO2 value chains: A comprehensive review and comparative analysis. *Renewable and Sustainable Energy Reviews* **2018,** *85*, 46-68.
8. Willner, I.; Willner, B. In *Artificial photosynthetic model systems using light-induced electron transfer reactions in catalytic and biocatalytic assemblies*, Photoinduced Electron Transfer III, Berlin, Heidelberg, 1991//; Mattay, J., Ed. Springer Berlin Heidelberg: Berlin, Heidelberg, 1991; pp 153-218.
9. https://www.britannica.com/science/photosynthesis, 20.03.2019.
10. https://www.britannica.com/science/biodiversity, 20.03.2019.
11. Lund, H., Renewable energy strategies for sustainable development. *Energy* **2007,** *32* (6), 912-919.
12. Roy, S.; Cherevotan, A.; Peter, S. C., Thermochemical CO2 Hydrogenation to Single Carbon Products: Scientific and Technological Challenges. *ACS Energy Letters* **2018,** *3* (8), 1938-1966.
13. www.climate.gov/news-features/understanding-climate/climate-change-atmospheric-carbon-dioxide.
14. Klankermayer, J.; Wesselbaum, S.; Beydoun, K.; Leitner, W., Selective Catalytic Synthesis Using the Combination of Carbon Dioxide and Hydrogen: Catalytic Chess at the Interface of Energy and Chemistry. *Angewandte Chemie International Edition* **2016,** *55* (26), 7296-7343.
15. Leitner, W., Carbon Dioxide as a Raw Material: The Synthesis of Formic Acid and Its Derivatives from CO2. *Angewandte Chemie International Edition in English* **1995,** *34* (20), 2207-2221.

16. Leitner, W.; Dinjus, E.; Gaßner, F., Activation of carbon dioxide. *Journal of Organometallic Chemistry* **1994,** *475* (1), 257-266.
17. Wang, W.-H.; Himeda, Y.; Muckerman, J. T.; Manbeck, G. F.; Fujita, E., CO2 Hydrogenation to Formate and Methanol as an Alternative to Photo- and Electrochemical CO2 Reduction. *Chemical Reviews* **2015,** *115* (23), 12936-12973.
18. Han, Z.; Rong, L.; Wu, J.; Zhang, L.; Wang, Z.; Ding, K., Catalytic Hydrogenation of Cyclic Carbonates: A Practical Approach from CO2 and Epoxides to Methanol and Diols. *Angewandte Chemie International Edition* **2012,** *51* (52), 13041-13045.
19. Leu, M. K.; Vicente, I.; Fernandes, J. A.; de Pedro, I.; Dupont, J.; Sans, V.; Licence, P.; Gual, A.; Cano, I., On the real catalytically active species for CO2 fixation into cyclic carbonates under near ambient conditions: Dissociation equilibrium of [BMIm][Fe(NO)2Cl2] dependant on reaction temperature. *Applied Catalysis B: Environmental* **2019,** *245*, 240-250.
20. Li, Y.; Junge, K.; Beller, M., Improving the Efficiency of the Hydrogenation of Carbonates and Carbon Dioxide to Methanol. *ChemCatChem* **2013,** *5* (5), 1072-1074.
21. Klerk, A. d., Fischer–Tropsch Process. In *Kirk-Othmer Encyclopedia of Chemical Technology*, 2013.
22. Reutemann, W.; Kieczka, H., Formic Acid. In *Ullmann's Encyclopedia of Industrial Chemistry*, Wiley-VCH Verlag GmbH & Co. KGaA: 2000.
23. Ren, W.; Chang, W.; Dai, J.; Shi, Y.; Li, J.; Shi, Y., An Effective Pd-Catalyzed Regioselective Hydroformylation of Olefins with Formic Acid. *Journal of the American Chemical Society* **2016,** *138* (45), 14864-14867.
24. Fiedler, E.; Grossmann, G.; Kersebohm, D. B.; Weiss, G.; Witte, C., Methanol. In *Ullmann's Encyclopedia of Industrial Chemistry*, 2000.
25. Franz, A. W.; Kronemayer, H.; Pfeiffer, D.; Pilz, R. D.; Reuss, G.; Disteldorf, W.; Gamer, A. O.; Hilt, A., Formaldehyde. In *Ullmann's Encyclopedia of Industrial Chemistry*, 2016.
26. Häussinger, P.; Lohmüller, R.; Watson, A. M., Hydrogen. In *Ullmann's Encyclopedia of Industrial Chemistry*, 2000.
27. Schreck, M.; Niederberger, M., Photocatalytic Gas Phase Reactions. *Chemistry of Materials* **2019**.
28. Sternberg, A.; Jens, C. M.; Bardow, A., Life cycle assessment of CO2-based C1-chemicals. *Green Chemistry* **2017,** *19* (9), 2244-2259.
29. Müller, K.; Brooks, K.; Autrey, T., Hydrogen Storage in Formic Acid: A Comparison of Process Options. *Energy & Fuels* **2017,** *31* (11), 12603-12611.
30. Celaje, J. J. A.; Lu, Z.; Kedzie, E. A.; Terrile, N. J.; Lo, J. N.; Williams, T. J., A prolific catalyst for dehydrogenation of neat formic acid. *Nature Communications* **2016,** *7*, 11308.
31. Bierhals, J., Carbon Monoxide. In *Ullmann's Encyclopedia of Industrial Chemistry*, 2001.
32. Stumper, R., New researches on the poison of ants. *Compt. rend.* **1923,** *176*, 330-332.
33. Stumper, R., Poison of ants, particularly formic acid. *Compt. rend.* **1922,** *174*, 66-67.
34. Aresta, M.; Dibenedetto, A.; Angelini, A., Catalysis for the Valorization of Exhaust Carbon: from CO2 to Chemicals, Materials, and Fuels. Technological Use of CO2. *Chemical Reviews* **2014,** *114* (3), 1709-1742.

35. https://www.marketresearchfuture.com/reports/formic-acid-market-1132.
36. Huhtanen, P.; Rinne, M.; Nousiainen, J., Evaluation of the factors affecting silage intake of dairy cows: a revision of the relative silage dry-matter intake index. *Animal* **2007,** *1* (5), 758-770.
37. http://www.intermediates.basf.com/chemicals/formic-acid/leather-processing.
38. Loges, B.; Boddien, A.; Junge, H.; Beller, M., Controlled Generation of Hydrogen from Formic Acid Amine Adducts at Room Temperature and Application in H2/O2 Fuel Cells. *Angewandte Chemie International Edition* **2008,** *47* (21), 3962-3965.
39. Loges, B.; Boddien, A.; Gärtner, F.; Junge, H.; Beller, M., Catalytic Generation of Hydrogen from Formic acid and its Derivatives: Useful Hydrogen Storage Materials. *Topics in Catalysis* **2010,** *53* (13), 902-914.
40. Sordakis, K.; Tang, C.; Vogt, L. K.; Junge, H.; Dyson, P. J.; Beller, M.; Laurenczy, G., Homogeneous Catalysis for Sustainable Hydrogen Storage in Formic Acid and Alcohols. *Chemical Reviews* **2018,** *118* (2), 372-433.
41. Supronowicz, W.; Ignatyev, I. A.; Lolli, G.; Wolf, A.; Zhao, L.; Mleczko, L., Formic acid: a future bridge between the power and chemical industries. *Green Chemistry* **2015,** *17* (5), 2904-2911.
42. Zassinovich, G.; Mestroni, G.; Gladiali, S., Asymmetric hydrogen transfer reactions promoted by homogeneous transition metal catalysts. *Chemical Reviews* **1992,** *92* (5), 1051-1069.
43. Formamides. In *Ullmann's Encyclopedia of Industrial Chemistry*.
44. Hold only one ACS national meeting a year? *Chemical & Engineering News Archive* **1982,** *60* (37), 41-43.
45. FRIES, D. M. M., Klaus-Dieter; SCHÄFER, Martin; SCHNEIDER, Daniel; BASSLER, Peter; RITTINGER, Stefan;TELES, Joaquim Henrique; METHOD FOR PRODUCING FORMIC ACID. 05.06.2014, 2014.
46. Schaub, T.; Paciello, R. A., A Process for the Synthesis of Formic Acid by CO2 Hydrogenation: Thermodynamic Aspects and the Role of CO. *Angewandte Chemie International Edition* **2011,** *50* (32), 7278-7282.
47. Leonard, J. D. Preparation of formic acid by hydrolysis of methyl formate. 5 998, 1978.
48. Christoph Adami; Michael Slany; Karl, M.; Kaibel;, G.; Schäfer;, M.; Zehner;, P.; Röper, M. Method for producing methyl formate. US 7,053,239 B2 30.05.2006, 2003.
49. Jiang, L.; Dao-Jun, D.; Li, D.; Qing-Xiang, G.; Yao, F., Catalytic Air Oxidation of Biomass-Derived Carbohydrates to Formic Acid. *ChemSusChem* **2012,** *5* (7), 1313-1318.
50. Wolfel, R.; Taccardi, N.; Bosmann, A.; Wasserscheid, P., Selective catalytic conversion of biobased carbohydrates to formic acid using molecular oxygen. *Green Chemistry* **2011,** *13* (10), 2759-2763.
51. Albert, J.; Wolfel, R.; Bosmann, A.; Wasserscheid, P., Selective oxidation of complex, water-insoluble biomass to formic acid using additives as reaction accelerators. *Energy & Environmental Science* **2012,** *5* (7), 7956-7962.
52. Baufumé, S.; Grüger, F.; Grube, T.; Krieg, D.; Linssen, J.; Weber, M.; Hake, J.-F.; Stolten, D., GIS-based scenario calculations for a nationwide

German hydrogen pipeline infrastructure. *International Journal of Hydrogen Energy* **2013,** *38* (10), 3813-3829.
53. Chen, L.; Lu, Y.; Hong, Q.; Lin, J.; Dautzenberg, F. M., Catalytic partial oxidation of methane to syngas over Ca-decorated-Al2O3-supported Ni and NiB catalysts. *Applied Catalysis A: General* **2005,** *292*, 295-304.
54. Clark, J., Macquarrie, D. , Gronnow, M. and Budarin, V, Green Chemistry Principles. In *Process Intensification for Green Chemistry*, 2013
55. www.acs.org/content/acs/en/greenchemistry/principles/12-principles-of-green-chemistry.html. *last accessed*.
56. Jessop, P. G., *The Handbook of Homogeneous Hydrogenation* Wiley-VCH: Weinheim, 2007.
57. W. Leitner, E. D., F.Gaßner *AqueousPhase Organometallic Catalysis Concepts and Applications*. Wiley-VCH: Weinheim, 1998.
58. Prieto, G., Carbon Dioxide Hydrogenation into Higher Hydrocarbons and Oxygenates: Thermodynamic and Kinetic Bounds and Progress with Heterogeneous and Homogeneous Catalysis. *ChemSusChem* **2017,** *10* (6), 1056-1070.
59. Walther, D., Homogeneous-catalytic reactions of carbon dioxide with unsatureated substrates, reversible CO2-carriers and transcarboxylation reactions. *Coordination Chemistry Reviews* **1987,** *79* (1), 135-174.
60. Leitner, W., The coordination chemistry of carbon dioxide and its relevance for catalysis: a critical survey. *Coordination Chemistry Reviews* **1996,** *153*, 257-284.
61. Dong, K.; Razzaq, R.; Hu, Y.; Ding, K., Homogeneous Reduction of Carbon Dioxide with Hydrogen. *Topics in Current Chemistry* **2017,** *375* (2), 23.
62. Walter, L., Carbon Dioxide as a Raw Material: The Synthesis of Formic Acid and Its Derivatives from CO2. *Angewandte Chemie International Edition in English* **1995,** *34* (20), 2207-2221.
63. Hayashi, H.; Ogo, S.; Fukuzumi, S., Aqueous hydrogenation of carbon dioxide catalysed by water-soluble ruthenium aqua complexes under acidic conditions. *Chemical Communications* **2004,** (23), 2714-2715.
64. Ogo, S.; Kabe, R.; Hayashi, H.; Harada, R.; Fukuzumi, S., Mechanistic investigation of CO2 hydrogenation by Ru(ii) and Ir(iii) aqua complexes under acidic conditions: two catalytic systems differing in the nature of the rate determining step. *Dalton Transactions* **2006,** (39), 4657-4663.
65. Mondal, B.; Neese, F.; Ye, S., Toward Rational Design of 3d Transition Metal Catalysts for CO2 Hydrogenation Based on Insights into Hydricity-Controlled Rate-Determining Steps. *Inorganic Chemistry* **2016,** *55* (11), 5438-5444.
66. Mondal, B.; Neese, F.; Ye, S., Control in the Rate-Determining Step Provides a Promising Strategy To Develop New Catalysts for CO2 Hydrogenation: A Local Pair Natural Orbital Coupled Cluster Theory Study. *Inorganic Chemistry* **2015,** *54* (15), 7192-7198.
67. Hazari, N.; Heimann, J. E., Carbon Dioxide Insertion into Group 9 and 10 Metal–Element σ Bonds. *Inorganic Chemistry* **2017,** *56* (22), 13655-13678.
68. Heimann, J. E.; Bernskoetter, W. H.; Hazari, N.; Mayer, James M., Acceleration of CO2 insertion into metal hydrides: ligand, Lewis acid, and solvent effects on reaction kinetics. *Chemical Science* **2018,** *9* (32), 6629-6638.

69. Li-Xue, J.; Chongyang, Z.; Xiao-Na, L.; Hui, C.; Sheng-Gui, H., Formation of Gas-Phase Formate in Thermal Reactions of Carbon Dioxide with Diatomic Iron Hydride Anions. *Angewandte Chemie International Edition* **2017,** *56* (15), 4187-4191.
70. Wiedner, E. S.; Chambers, M. B.; Pitman, C. L.; Bullock, R. M.; Miller, A. J. M.; Appel, A. M., Thermodynamic Hydricity of Transition Metal Hydrides. *Chemical Reviews* **2016,** *116* (15), 8655-8692.
71. Waldie, K. M.; Ostericher, A. L.; Reineke, M. H.; Sasayama, A. F.; Kubiak, C. P., Hydricity of Transition-Metal Hydrides: Thermodynamic Considerations for CO2 Reduction. *ACS Catalysis* **2018,** *8* (2), 1313-1324.
72. Jeletic, M. S.; Hulley, E. B.; Helm, M. L.; Mock, M. T.; Appel, A. M.; Wiedner, E. S.; Linehan, J. C., Understanding the Relationship Between Kinetics and Thermodynamics in CO2 Hydrogenation Catalysis. *ACS Catalysis* **2017,** *7* (9), 6008-6017.
73. Kubas, G. J., Molecular hydrogen complexes: coordination of a .sigma. bond to transition metals. *Accounts of Chemical Research* **1988,** *21* (3), 120-128.
74. Kubas, G. J.; Ryan, R. R.; Swanson, B. I.; Vergamini, P. J.; Wasserman, H. J., Characterization of the first examples of isolable molecular hydrogen complexes, M(CO)3(PR3)2(H2) (M = molybdenum or tungsten; R = Cy or isopropyl). Evidence for a side-on bonded dihydrogen ligand. *Journal of the American Chemical Society* **1984,** *106* (2), 451-452.
75. Saillard, J. Y.; Hoffmann, R., Carbon-hydrogen and hydrogen-hydrogen activation in transition metal complexes and on surfaces. *Journal of the American Chemical Society* **1984,** *106* (7), 2006-2026.
76. Kubas, G., *Metal-dihydrogen and σ-bond coordination: The consummate extension of the Dewar-Chatt-Duncanson model for metal-olefin π bonding*. 2001; Vol. 635, p 37-68.
77. Triguero, L.; Föhlisch, A.; Väterlein, P.; Hasselström, J.; Weinelt, M.; Pettersson, L. G. M.; Luo, Y.; Ågren, H.; Nilsson, A., Direct Experimental Measurement of Donation/Back-Donation in Unsaturated Hydrocarbon Bonding to Metals. *Journal of the American Chemical Society* **2000,** *122* (49), 12310-12316.
78. Hasegawa, T.; Li, Z.; Parkin, S.; Hope, H.; McMullan, R. K.; Koetzle, T. F.; Taube, H., Determination of the Structure of [Os(.eta.2-H2)en2CH3CO2]PF6 by X-ray and Neutron Diffraction. *Journal of the American Chemical Society* **1994,** *116* (10), 4352-4356.
79. Morris, R. H., Brønsted–Lowry Acid Strength of Metal Hydride and Dihydrogen Complexes. *Chemical Reviews* **2016,** *116* (15), 8588-8654.
80. Pitman, C. L.; Brereton, K. R.; Miller, A. J. M., Aqueous Hydricity of Late Metal Catalysts as a Continuum Tuned by Ligands and the Medium. *Journal of the American Chemical Society* **2016,** *138* (7), 2252-2260.
81. Osadchuk, I.; Tamm, T.; Ahlquist, M. S. G., Theoretical Investigation of a Parallel Catalytic Cycle in CO2 Hydrogenation by (PNP)IrH3. *Organometallics* **2015,** *34* (20), 4932-4940.
82. Lilio, A. M.; Reineke, M. H.; Moore, C. E.; Rheingold, A. L.; Takase, M. K.; Kubiak, C. P., Incorporation of Pendant Bases into Rh(diphosphine)2 Complexes: Synthesis, Thermodynamic Studies, And Catalytic CO2 Hydrogenation Activity of [Rh(P2N2)2]+ Complexes. *Journal of the American Chemical Society* **2015,** *137* (25), 8251-8260.

83. Waldie, K. M.; Brunner, F. M.; Kubiak, C. P., Transition Metal Hydride Catalysts for Sustainable Interconversion of CO2 and Formate: Thermodynamic and Mechanistic Considerations. *ACS Sustainable Chemistry & Engineering* **2018,** *6* (5), 6841-6848.
84. Hull, J. F.; Himeda, Y.; Wang, W.-H.; Hashiguchi, B.; Periana, R.; Szalda, D. J.; Muckerman, J. T.; Fujita, E., Reversible hydrogen storage using CO2 and a proton-switchable iridium catalyst in aqueous media under mild temperatures and pressures. *Nat Chem* **2012,** *4* (5), 383-388.
85. Himeda, Y.; Miyazawa, S.; Hirose, T., Interconversion between Formic Acid and H2/CO2 using Rhodium and Ruthenium Catalysts for CO2 Fixation and H2 Storage. *ChemSusChem* **2011,** *4* (4), 487-493.
86. Sanz, S.; Azua, A.; Peris, E., '([small eta]6-arene)Ru(bis-NHC)' complexes for the reduction of CO2 to formate with hydrogen and by transfer hydrogenation with iPrOH. *Dalton Transactions* **2010,** *39* (27), 6339-6343.
87. Azua, A.; Sanz, S.; Peris, E., Water-Soluble IrIII N-Heterocyclic Carbene Based Catalysts for the Reduction of CO2 to Formate by Transfer Hydrogenation and the Deuteration of Aryl Amines in Water. *Chemistry – A European Journal* **2011,** *17* (14), 3963-3967.
88. Himeda, Y.; Onozawa-Komatsuzaki, N.; Sugihara, H.; Kasuga, K., Simultaneous Tuning of Activity and Water Solubility of Complex Catalysts by Acid−Base Equilibrium of Ligands for Conversion of Carbon Dioxide. *Organometallics* **2007,** *26* (3), 702-712.
89. Tanaka, R.; Yamashita, M.; Nozaki, K., Catalytic Hydrogenation of Carbon Dioxide Using Ir(III)−Pincer Complexes. *Journal of the American Chemical Society* **2009,** *131* (40), 14168-14169.
90. Filonenko, G. A.; Conley, M. P.; Copéret, C.; Lutz, M.; Hensen, E. J. M.; Pidko, E. A., The impact of Metal–Ligand Cooperation in Hydrogenation of Carbon Dioxide Catalyzed by Ruthenium PNP Pincer. *ACS Catalysis* **2013,** *3* (11), 2522-2526.
91. Filonenko, G. A.; van Putten, R.; Schulpen, E. N.; Hensen, E. J. M.; Pidko, E. A., Highly Efficient Reversible Hydrogenation of Carbon Dioxide to Formates Using a Ruthenium PNP-Pincer Catalyst. *ChemCatChem* **2014,** *6* (6), 1526-1530.
92. Filonenko, G. A.; Smykowski, D.; Szyja, B. M.; Li, G.; Szczygieł, J.; Hensen, E. J. M.; Pidko, E. A., Catalytic Hydrogenation of CO2 to Formates by a Lutidine-Derived Ru–CNC Pincer Complex: Theoretical Insight into the Unrealized Potential. *ACS Catalysis* **2015,** *5* (2), 1145-1154.
93. Tsai, J. C.; Nicholas, K. M., Rhodium-catalyzed hydrogenation of carbon dioxide to formic acid. *Journal of the American Chemical Society* **1992,** *114* (13), 5117-5124.
94. Fornika, R.; Gorls, H.; Seemann, B.; Leitner, W., Complexes [(P2)Rh(hfacac)](P2= bidentate chelating phosphane, hfacac = hexafluoroacetylacetonate) as catalysts for CO2 hydrogenation: correlations between solid state structures, 103Rh NMR shifts and catalytic activities. *Journal of the Chemical Society, Chemical Communications* **1995,** (14), 1479-1481.
95. Hutschka, F.; Dedieu, A.; Eichberger, M.; Fornika, R.; Leitner, W., Mechanistic Aspects of the Rhodium-Catalyzed Hydrogenation of CO2 to Formic AcidA Theoretical and Kinetic Study. *Journal of the American Chemical Society* **1997,** *119* (19), 4432-4443.

96. Graf, E.; Leitner, W., Direct formation of formic acid from carbon dioxide and dihydrogen using the [{Rh(cod)Cl}2]-Ph2P(CH2)4PPh2 catalyst system. *Journal of the Chemical Society, Chemical Communications* **1992,** (8), 623-624.
97. Elek, J.; Nádasdi, L.; Papp, G.; Laurenczy, G.; Joó, F., Homogeneous hydrogenation of carbon dioxide and bicarbonate in aqueous solution catalyzed by water-soluble ruthenium(II) phosphine complexes. *Applied Catalysis A: General* **2003,** *255* (1), 59-67.
98. Farlow, M. W.; Adkins, H., The Hydrogenation of Carbon Dioxide and a Correction of the Reported Synthesis of Urethans. *Journal of the American Chemical Society* **1935,** *57* (11), 2222-2223.
99. Inoue, Y.; Izumida, H.; Sasaki, Y.; Hashimoto, H., CATALYTIC FIXATION OF CARBON DIOXIDE TO FORMIC ACID BY TRANSITION-METAL COMPLEXES UNDER MILD CONDITIONS. *Chemistry Letters* **1976,** *5* (8), 863-864.
100. Munshi, P.; Main, A. D.; Linehan, J. C.; Tai, C.-C.; Jessop, P. G., Hydrogenation of Carbon Dioxide Catalyzed by Ruthenium Trimethylphosphine Complexes: The Accelerating Effect of Certain Alcohols and Amines. *Journal of the American Chemical Society* **2002,** *124* (27), 7963-7971.
101. Ezhova, N. N.; Kolesnichenko, N. V.; Bulygin, A. V.; Slivinskii, E. V.; Han, S., Hydrogenation of CO2 to formic acid in the presence of the Wilkinson complex. *Russian Chemical Bulletin* **2002,** *51* (12), 2165-2169.
102. Gassner, F.; Leitner, W., Hydrogenation of carbon dioxide to formic acid using water-soluble rhodium catalyststs. *Journal of the Chemical Society, Chemical Communications* **1993,** (19), 1465-1466.
103. Moret, S.; Dyson, P. J.; Laurenczy, G., Direct synthesis of formic acid from carbon dioxide by hydrogenation in acidic media. **2014,** *5*, 4017.
104. González, E.; Marchant, C.; Sepúlveda, C.; García, R.; Ghampson, I. T.; Escalona, N.; García-Fierro, J. L., Hydrogenation of sodium hydrogen carbonate in aqueous phase using metal/activated carbon catalysts. *Applied Catalysis B: Environmental* **2018,** *224*, 368-375.
105. Ohlin, C. A.; Laurenczy, G., CARBON DIOXIDE REDUCTION IN BIPHASIC AQUEOUS-IONIC LIQUID SYSTEMS BY PRESSURIZED HYDROGEN. *High Pressure Research* **2003,** *23* (3), 239-242.
106. Christopher, F.; Ralf, J.; Albert, B.; Gabor, L.; Matthias, B., Ruthenium-Catalyzed Hydrogenation of Bicarbonate in Water. *ChemSusChem* **2010,** *3* (9), 1048-1050.
107. Christopher, F.; Carolin, Z.; Ralf, J.; Wolfgang, B.; Matthias, B., Catalytic Hydrogenation of Carbon Dioxide and Bicarbonates with a Well-Defined Cobalt Dihydrogen Complex. *Chemistry – A European Journal* **2012,** *18* (1), 72-75.
108. Ziebart, C.; Federsel, C.; Anbarasan, P.; Jackstell, R.; Baumann, W.; Spannenberg, A.; Beller, M., Well-Defined Iron Catalyst for Improved Hydrogenation of Carbon Dioxide and Bicarbonate. *Journal of the American Chemical Society* **2012,** *134* (51), 20701-20704.
109. Li, Y.-N.; He, L.-N.; Liu, A.-H.; Lang, X.-D.; Yang, Z.-Z.; Yu, B.; Luan, C.-R., In situ hydrogenation of captured CO2 to formate with polyethyleneimine and Rh/monophosphine system. *Green Chemistry* **2013,** *15* (10), 2825-2829.

110. Xu, Z.; McNamara, N. D.; Neumann, G. T.; Schneider, W. F.; Hicks, J. C., Catalytic Hydrogenation of CO2 to Formic Acid with Silica-Tethered Iridium Catalysts. *ChemCatChem* **2013,** *5* (7), 1769-1771.
111. Schmeier, T. J.; Dobereiner, G. E.; Crabtree, R. H.; Hazari, N., Secondary Coordination Sphere Interactions Facilitate the Insertion Step in an Iridium(III) CO2 Reduction Catalyst. *Journal of the American Chemical Society* **2011,** *133* (24), 9274-9277.
112. Robert, L.; Yael, D. P.; Gregory, L.; W., S. L. J.; Yehoshoa, B. D.; David, M., Low-Pressure Hydrogenation of Carbon Dioxide Catalyzed by an Iron Pincer Complex Exhibiting Noble Metal Activity. *Angewandte Chemie International Edition* **2011,** *50* (42), 9948-9952.
113. Matthias, V.; Moti, G.; A., I. M.; Yael, D.-P.; Yehoshoa, B.-D.; David, M., A New Mode of Activation of CO2 by Metal–Ligand Cooperation with Reversible C□C and M□O Bond Formation at Ambient Temperature. *Chemistry – A European Journal* **2012,** *18* (30), 9194-9197.
114. Huff, C. A.; Kampf, J. W.; Sanford, M. S., Role of a Noninnocent Pincer Ligand in the Activation of CO2 at (PNN)Ru(H)(CO). *Organometallics* **2012,** *31* (13), 4643-4645.
115. Filonenko, G. A.; Hensen, E. J. M.; Pidko, E. A., Mechanism of CO2 hydrogenation to formates by homogeneous Ru-PNP pincer catalyst: from a theoretical description to performance optimization. *Catalysis Science & Technology* **2014,** *4* (10), 3474-3485.
116. Filonenko, G. A.; Cosimi, E.; Lefort, L.; Conley, M. P.; Copéret, C.; Lutz, M.; Hensen, E. J. M.; Pidko, E. A., Lutidine-Derived Ru-CNC Hydrogenation Pincer Catalysts with Versatile Coordination Properties. *ACS Catalysis* **2014,** *4* (8), 2667-2671.
117. Sanz, S.; Benítez, M.; Peris, E., A New Approach to the Reduction of Carbon Dioxide: CO2 Reduction to Formate by Transfer Hydrogenation in iPrOH. *Organometallics* **2010,** *29* (1), 275-277.
118. Hansch, C.; Leo, A.; Taft, R. W., A survey of Hammett substituent constants and resonance and field parameters. *Chemical Reviews* **1991,** *91* (2), 165-195.
119. Wang, W.-H.; Muckerman, J. T.; Fujita, E.; Himeda, Y., Mechanistic Insight through Factors Controlling Effective Hydrogenation of CO2 Catalyzed by Bioinspired Proton-Responsive Iridium(III) Complexes. *ACS Catalysis* **2013,** *3* (5), 856-860.
120. Ertem, M. Z.; Himeda, Y.; Fujita, E.; Muckerman, J. T., Interconversion of Formic Acid and Carbon Dioxide by Proton-Responsive, Half-Sandwich Cp*IrIII Complexes: A Computational Mechanistic Investigation. *ACS Catalysis* **2016,** *6* (2), 600-609.
121. Onishi, N.; Xu, S.; Manaka, Y.; Suna, Y.; Wang, W.-H.; Muckerman, J. T.; Fujita, E.; Himeda, Y., CO2 Hydrogenation Catalyzed by Iridium Complexes with a Proton-Responsive Ligand. *Inorganic Chemistry* **2015,** *54* (11), 5114-5123.
122. Lu, S.-M.; Wang, Z.; Li, J.; Xiao, J.; Li, C., Base-free hydrogenation of CO2 to formic acid in water with an iridium complex bearing a N,N[prime or minute]-diimine ligand. *Green Chemistry* **2016,** *18* (16), 4553-4558.
123. Zhao, G.; Joó, F., Free formic acid by hydrogenation of carbon dioxide in sodium formate solutions. *Catalysis Communications* **2011,** *14* (1), 74-76.

124. Sahoo, A. R.; Jiang, F.; Bruneau, C.; Sharma, G. V. M.; Suresh, S.; Roisnel, T.; Dorcet, V.; Achard, M., Phosphine-pyridonate ligands containing octahedral ruthenium complexes: access to esters and formic acid. *Catalysis Science & Technology* **2017,** *7* (16), 3492-3498.
125. Zhang, Z.; Hu, S.; Song, J.; Li, W.; Yang, G.; Han, B., Hydrogenation of CO2 to Formic Acid Promoted by a Diamine-Functionalized Ionic Liquid. *ChemSusChem* **2009,** *2* (3), 234-238.
126. Zhang, Z.; Xie, Y.; Li, W.; Hu, S.; Song, J.; Jiang, T.; Han, B., Hydrogenation of Carbon Dioxide is Promoted by a Task-Specific Ionic Liquid. *Angewandte Chemie International Edition* **2008,** *47* (6), 1127-1129.
127. Upadhyay, P. R.; Srivastava, V., Selective hydrogenation of CO2 gas to formic acid over nanostructured Ru-TiO2 catalysts. *RSC Advances* **2016,** *6* (48), 42297-42306.
128. Wesselbaum, S.; Hintermair, U.; Leitner, W., Continuous-Flow Hydrogenation of Carbon Dioxide to Pure Formic Acid using an Integrated scCO2 Process with Immobilized Catalyst and Base. *Angewandte Chemie* **2012,** *124* (34), 8713-8716.
129. Su, J.; Lu, M.; Lin, H., High yield production of formate by hydrogenating CO2 derived ammonium carbamate/carbonate at room temperature. *Green Chemistry* **2015,** *17* (5), 2769-2773.
130. Scott, M.; Blas Molinos, B.; Westhues, C.; Franciò, G.; Leitner, W., Aqueous Biphasic Systems for the Synthesis of Formates by Catalytic CO2 Hydrogenation: Integrated Reaction and Catalyst Separation for CO2-Scrubbing Solutions. *ChemSusChem* **2017,** *10* (6), 1085-1093.
131. Pérez-Fortes, M.; Schöneberger, J. C.; Boulamanti, A.; Harrison, G.; Tzimas, E., Formic acid synthesis using CO2 as raw material: Techno-economic and environmental evaluation and market potential. *International Journal of Hydrogen Energy* **2016,** *41* (37), 16444-16462.
132. Dupont, J.; Scholten, J. D., On the structural and surface properties of transition-metal nanoparticles in ionic liquids. *Chemical Society Reviews* **2010,** *39* (5), 1780-1804.
133. Dupont, J.; Spencer, J., On the Noninnocent Nature of 1,3-Dialkylimidazolium Ionic Liquids. *Angewandte Chemie International Edition* **2004,** *43* (40), 5296-5297.
134. Dupont, J.; Suarez, P. A. Z., Physico-chemical processes in imidazolium ionic liquids. *Physical Chemistry Chemical Physics* **2006,** *8* (21), 2441-2452.
135. Stassen, H. K.; Ludwig, R.; Wulf, A.; Dupont, J., Imidazolium Salt Ion Pairs in Solution. *Chemistry – A European Journal* **2015,** *21* (23), 8324-8335.
136. Scholten, J. D.; Leal, B. C.; Dupont, J., Transition Metal Nanoparticle Catalysis in Ionic Liquids. *ACS Catalysis* **2012,** *2* (1), 184-200.
137. Dupont, J., From Molten Salts to Ionic Liquids: A "Nano" Journey. *Accounts of Chemical Research* **2011,** *44* (11), 1223-1231.
138. Dupont, J., On the solid, liquid and solution structural organization of imidazolium ionic liquids. *Journal of the Brazilian Chemical Society* **2004,** *15*, 341-350.
139. Migowski, P.; Dupont, J., Catalytic Applications of Metal Nanoparticles in Imidazolium Ionic Liquids. *Chemistry – A European Journal* **2007,** *13* (1), 32-39.

140. Wender, H.; Migowski, P.; Feil, A. F.; Teixeira, S. R.; Dupont, J., Sputtering deposition of nanoparticles onto liquid substrates: Recent advances and future trends. *Coordination Chemistry Reviews* **2013,** *257* (17–18), 2468-2483.
141. Biggin, S.; Enderby, J. E., Comments on the structure of molten salts. *Journal of Physics C: Solid State Physics* **1982,** *15* (11), L305.
142. Corradini, D.; Madden, P. A.; Salanne, M., Coordination numbers and physical properties in molten salts and their mixtures. *Faraday Discussions* **2016,** *190* (0), 471-486.
143. Dieter, K. M.; Dymek, C. J.; Heimer, N. E.; Rovang, J. W.; Wilkes, J. S., Ionic structure and interactions in 1-methyl-3-ethylimidazolium chloride-aluminum chloride molten salts. *Journal of the American Chemical Society* **1988,** *110* (9), 2722-2726.
144. Dupont, J.; Suarez, P. A. Z.; De Souza, R. F.; Burrow, R. A.; Kintzinger, J.-P., C□H-π Interactions in 1-n-Butyl-3-methylimidazolium Tetraphenylborate Molten Salt: Solid and Solution Structures. *Chemistry – A European Journal* **2000,** *6* (13), 2377-2381.
145. Consorti, C. S.; Suarez, P. A. Z.; de Souza, R. F.; Burrow, R. A.; Farrar, D. H.; Lough, A. J.; Loh, W.; da Silva, L. H. M.; Dupont, J., Identification of 1,3-Dialkylimidazolium Salt Supramolecular Aggregates in Solution. *The Journal of Physical Chemistry B* **2005,** *109* (10), 4341-4349.
146. Antonietti, M.; Kuang, D.; Smarsly, B.; Zhou, Y., Ionic Liquids for the Convenient Synthesis of Functional Nanoparticles and Other Inorganic Nanostructures. *Angewandte Chemie International Edition* **2004,** *43* (38), 4988-4992.
147. Canongia Lopes, J. N. A.; Pádua, A. A. H., Nanostructural Organization in Ionic Liquids. *The Journal of Physical Chemistry B* **2006,** *110* (7), 3330-3335.
148. Binnemans, K., Ionic Liquid Crystals. *Chemical Reviews* **2005,** *105* (11), 4148-4204.
149. Machado, G.; Scholten, J. D.; Vargas, T. d.; Teixeira, S. R.; Ronchi, L.; Dupont, J., Structural aspects of transition-metal nanoparticles in imidazolium ionic liquids. *International Journal of Nanotechnology* **2007,** *4* (5), 541-563.
150. Gozzo, F. C.; Santos, L. S.; Augusti, R.; Consorti, C. S.; Dupont, J.; Eberlin, M. N., Gaseous Supramolecules of Imidazolium Ionic Liquids: "Magic" Numbers and Intrinsic Strengths of Hydrogen Bonds. *Chemistry – A European Journal* **2004,** *10* (23), 6187-6193.
151. da Silveira Neto, B. A.; Ebeling, G.; Gonçalves, R. S.; Gozzo, F. C.; Eberlin, M. N.; Dupont, J., Organoindate Room Temperature Ionic Liquid: Synthesis, Physicochemical Properties and Application. *Synthesis* **2004,** *2004* (08), 1155-1158.
152. Freire, M. G.; Santos, L. M. N. B. F.; Fernandes, A. M.; Coutinho, J. A. P.; Marrucho, I. M., An overview of the mutual solubilities of water–imidazolium-based ionic liquids systems. *Fluid Phase Equilibria* **2007,** *261* (1–2), 449-454.
153. Schroder, U.; Wadhawan, J. D.; Compton, R. G.; Marken, F.; Suarez, P. A. Z.; Consorti, C. S.; de Souza, R. F.; Dupont, J., Water-induced accelerated ion diffusion: voltammetric studies in 1-methyl-3-[2,6-(S)-dimethylocten-2-yl]imidazolium tetrafluoroborate, 1-butyl-3-methylimidazolium

tetrafluoroborate and hexafluorophosphate ionic liquids. *New Journal of Chemistry* **2000,** *24* (12), 1009-1015.
154. Anderson, J. L.; Armstrong, D. W.; Wei, G.-T., Ionic Liquids in Analytical Chemistry. *Analytical Chemistry* **2006,** *78* (9), 2892-2902.
155. Ott, L. S.; Finke, R. G., Transition-metal nanocluster stabilization for catalysis: A critical review of ranking methods and putative stabilizers. *Coordination Chemistry Reviews* **2007,** *251* (9–10), 1075-1100.
156. Fonseca, G. S.; Machado, G.; Teixeira, S. R.; Fecher, G. H.; Morais, J.; Alves, M. C. M.; Dupont, J., Synthesis and characterization of catalytic iridium nanoparticles in imidazolium ionic liquids. *Journal of Colloid and Interface Science* **2006,** *301* (1), 193-204.
157. Scholten, J. D.; Ebeling, G.; Dupont, J., On the involvement of NHC carbenes in catalytic reactions by iridium complexes, nanoparticle and bulk metal dispersed in imidazolium ionic liquids. *Dalton Transactions* **2007,** (47), 5554-5560.
158. Ott, L. S.; Cline, M. L.; Deetlefs, M.; Seddon, K. R.; Finke, R. G., Nanoclusters in Ionic Liquids: Evidence for N-Heterocyclic Carbene Formation from Imidazolium-Based Ionic Liquids Detected by 2H NMR. *Journal of the American Chemical Society* **2005,** *127* (16), 5758-5759.
159. Stowell, C. A.; Korgel, B. A., Iridium Nanocrystal Synthesis and Surface Coating-Dependent Catalytic Activity. *Nano Letters* **2005,** *5* (7), 1203-1207.
160. Korgel, B. A.; Fitzmaurice, D., Small-angle x-ray-scattering study of silver-nanocrystal disorder-order phase transitions. *Physical Review B* **1999,** *59* (22), 14191-14201.
161. Dupont, J.; Weilhard, A.; Abarca, G. A.; Viscardi, J.; Prechtl, M. H. G.; Scolten, J. D.; Bernardi, F.; Baptista, D. L., Challenging Thermodynamics: Hydrogenation of Benzene to 1,3-Cyclohexadiene by Ru@Pt Nanoparticles. *ChemCatChem* **2016**, n/a-n/a.
162. Corvo, M. C.; Sardinha, J.; Menezes, S. C.; Einloft, S.; Seferin, M.; Dupont, J.; Casimiro, T.; Cabrita, E. J., Solvation of Carbon Dioxide in [C4mim][BF4] and [C4mim][PF6] Ionic Liquids Revealed by High-Pressure NMR Spectroscopy. *Angewandte Chemie International Edition* **2013,** *52* (49), 13024-13027.
163. Corvo, M. C.; Sardinha, J.; Casimiro, T.; Marin, G.; Seferin, M.; Einloft, S.; Menezes, S. C.; Dupont, J.; Cabrita, E. J., A Rational Approach to CO2 Capture by Imidazolium Ionic Liquids: Tuning CO2 Solubility by Cation Alkyl Branching. *ChemSusChem* **2015,** *8* (11), 1935-1946.
164. Zanatta, M.; Girard, A.-L.; Marin, G.; Ebeling, G.; dos Santos, F. P.; Valsecchi, C.; Stassen, H.; Livotto, P. R.; Lewis, W.; Dupont, J., Confined water in imidazolium based ionic liquids: a supramolecular guest@host complex case. *Physical Chemistry Chemical Physics* **2016,** *18* (27), 18297-18304.
165. Zanatta, M.; Dupont, J.; Wentz, G. N.; dos Santos, F. P., Intermolecular hydrogen bonds in water@IL supramolecular complexes. *Physical Chemistry Chemical Physics* **2018,** *20* (17), 11608-11614.
166. Simon, N. M.; Zanatta, M.; dos Santos, F. P.; Corvo, M. C.; Cabrita, E. J.; Dupont, J., Carbon Dioxide Capture by Aqueous Ionic Liquid Solutions. *ChemSusChem* **2017,** *10* (24), 4927-4933.

Chapter 2: Motivation and Objectives

Increasing the throughput for the synthesis of formic acid from CO_2 (i.e. implementing flow processes) is desirable not only from an economic-, but also from an environmental point of view. However, such hypothetical process faces several challenges. In terms of recyclability, the catalyst - and the support phase have to be immobilised. In order to facilitate a fast extraction of FA, the support phase should only generate relatively weak interaction with formic acid in comparison to the eluent phase. This will inherently lead to a low pH in the reaction, because protons are not consumed in a consecutive acid-base reaction of formic acid with the support, thus demanding high product tolerance from the utilized catalysts.

The aim of this thesis is to develop a reaction media, where weak additional stabilising forces in comparison to additive free conditions would facilitate the CO_2 hydrogenation under relatively acidic conditions. In general, the conducted research focuses onto the intermediate regime where formic acid is not stabilised by strong thermodynamic forces, as depicted in ***section 1.3***, whilst avoiding rapid catalyst deactivation as laid out in ***section 1.4***. These studies will enable future researchers to develop multifunctional catalyst phases combining high catalyst stability with high extraction efficiencies for formic acid.

The first objective is to use ILs such as 1-butyl-(2,)3-methylimidazolium acetate (BMMI.OAc) as an additive for the hydrogenation of CO_2 to formic acid. Hereby, the IL should only mildly disturb the thermodynamic profile of the

reaction, i.e. no formate salt or formate adduct formation should be measurable. In order to test this hypothesis, the thermodynamic properties of the system will be investigated using a commercially available complex as pre-catalyst.

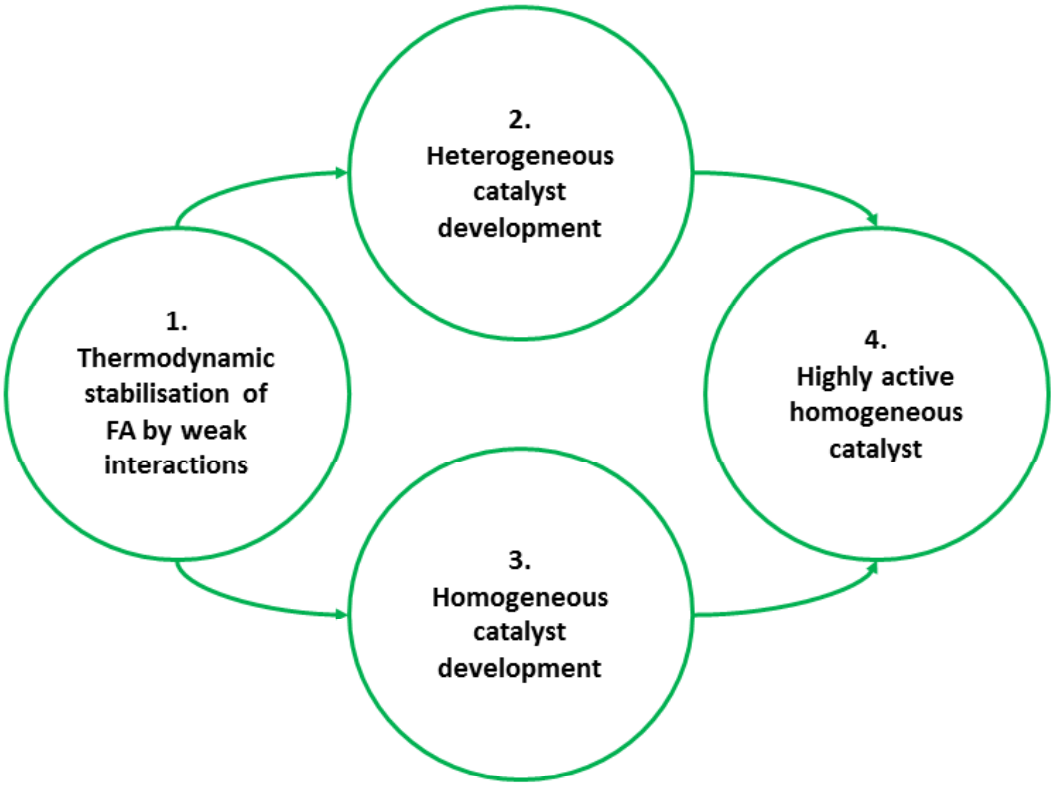


Figure 2.1 Flow chart for the development of this thesis.

The following objectives are focused on the development of a robust and highly active catalyst for the hydrogenation of CO_2 to formic acid. In a first step, heterogeneous bimetallic RuFe nanoparticles will be tested and compared to their monometallic counterparts. The aim here is to find positive synergistic/metal dilution effects.

As an alternative to heterogeneous catalysts a series of Ru-pyridylideneamide complexes prepared by collaborators will be introduced and then catalytic tests will be performed. Ligating groups surrounding the active metal centre will be

consequently varied in order to develop a relationship in between electron donation and catalytic activity and then investigated towards the tolerance of an increasingly acidic reaction condition.

Utilizing the knowledge gathered with the Ru-pyridylideneamide complexes, a highly active and stable Ru-CNC pincer complex will be introduced in the final part. This complex should display a high thermal stability, whilst at the same time the entry to deactivation cycles as discussed in **section 1.3.2**, is prevented. The complex developed here should be regarded as an entry point to further studies involving catalyst resistance towards an acidifying reaction media and the development of immobilisation strategies by modifying functional groups at the ligand scaffold.

Chapter 3: Methodology

This section briefly describes methodological procedures undertaken in this thesis. For more detailed descriptions the reader is referred to the corresponding publications.

3.1. Chemical Syntheses

Ionic liquids (ILs) were synthesized under standard conditions in air without further purification of reagents and following reported literature methods.[1] In contrast, all syntheses of catalytic species were undertaken with dried and degassed solvents under a dry argon atmosphere. A detailed description of purification procedures is given below.

3.1.1. Ionic liquid synthesis

In general, the ionic liquids used in this project are synthesized in two-steps. The first step consists of the quaternisation of the imidazole precursor with the corresponding alkyl halide, whilst in the second step – the anion exchange – the halide is exchanged for the desired counter-anion. In the first step, 1-methylimidazole or 1,2-dimethylimidazole were quaternized with an alkyl chloride in acetonitrile under reflux for 5d. The corresponding dialkylimidazolium halides are obtained in high yields (70%-90%) after

precipitation from ethyl acetate (or diethylether, where chlorodecane was used as the quarterisation agent).

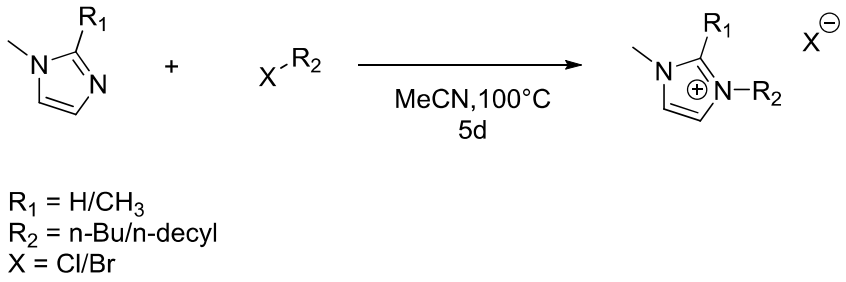


Figure 3.1 Overview of the quarterisation of 1-methylimidazole, respectively 1,2-dimethylimidazole to the corresponding alkylimidazolium halides in the presence of butylhalide or decylhalide.

In the second step, an anion exchange is performed on the intermediate halide salts formed in step 1. Here, two distinct protocols were used. In the case of PF_6^- (hexafluorophosphate), BF_4^- (tetrafluoroborate) and NTf_2^- (bis((trifluoromethyl)sulfonyl)amide) anions, the ion exchange was undertaken *via* a salt metathesis route utilizing the insolubility of the resulting ionic liquids in water as the thermodynamic driving force (**Figure 3.2a**). In the case of formate, acetate or imidazolate anions, the ion exchange is undertaken using an acid-base reaction of the hydroxide form of the IL and the appropriate acidic counter anion species. The hydroxide IL is prepared from the halide salt by ion exchange on a basic amberlite resin (amberlite IRA402(OH)), as shown in **Figure 3.2b**. After exchanging the halide to a hydroxide the hydroxide IL is neutralised with the desired counter anion, i.e. acetic acid in the case of acetate ILs, to form the desired product and water.

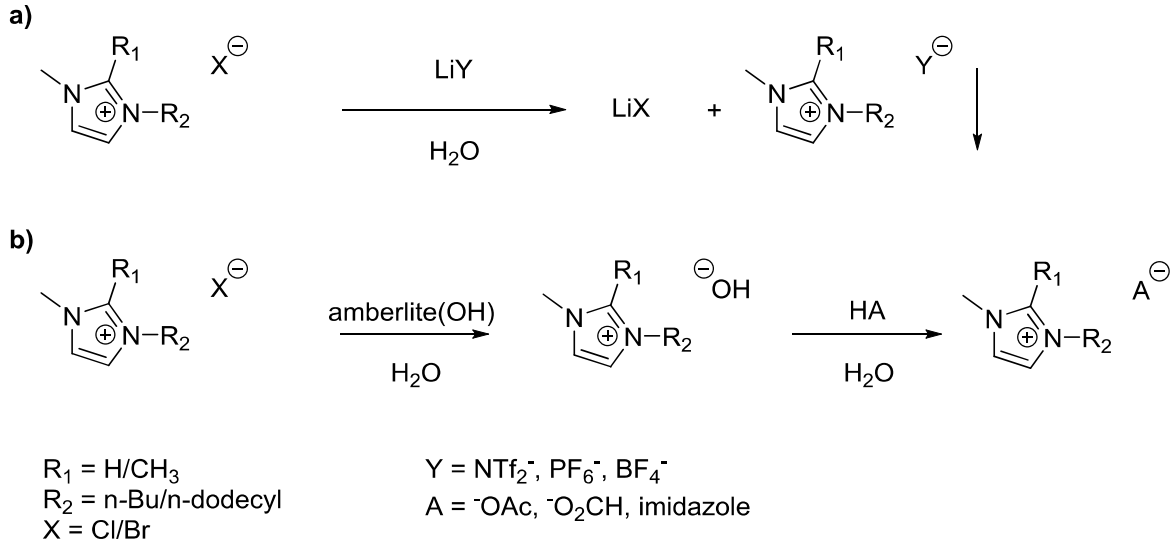


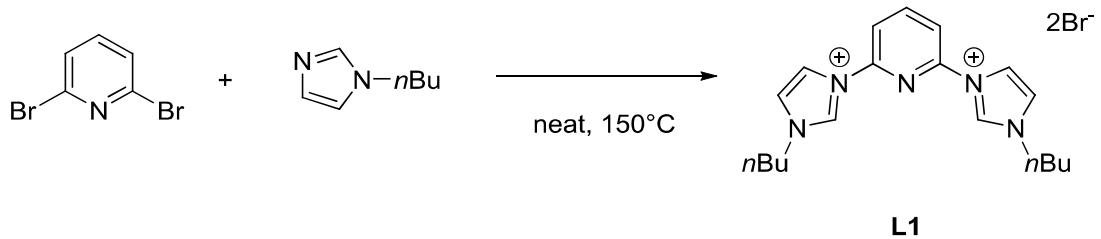
Figure 3.2 Overview over IL preparation utilized in this project; a) depicts the direct salt metathesis with lithium salts and alkylimidazolium halides; b) depicts ion exchange via the hydroxide IL.

Both synthetic routes give the desired ionic liquids in high yield (>90%). More information can be found in the corresponding publications.

3.1.2. Pincer ligand synthesis

Synthesis of 2,6-bis(1-butylimidazolium)pyridine dibromide

The synthesis of 2,6-bis(1-butylimidazolium)pyridine dibromide is a straight forward one-pot synthesis and follows a previously reported method.[2] 1-butylimidazole and 2,6-dibromopyridine yield the desired product *via* nucleophilic substitution at the 2 and 6 position on the bromopyridine. After repeated precipitation the product is obtained in good yield (60%-70%).



L1

Figure 3.3 General overview of the synthesis of 2,6-bis(1-butylimidazolium)pyridine.

3.1.3. Pincer complex synthesis

Note that the synthesis of the pincer complexes was performed under the strict exclusion of water, air and light, using standard Schlenck techniques in order to prevent undesired decomposition of the complexes. In the following, purification of the solvents used in each reaction is described.

Purification of reagents

All solvents were dried and degassed prior to synthesis of the pincer complexes. The pre-dried solvents were distilled under a dry argon counter-flux to remove oxygen contaminations. Argon was dried by passing it over a drying column containing anhydrous $Cu(SO_4)$ and molecular sieves. All inert manipulation were undertaken using standard Schlenk techniques with flame dried glassware.

Methanol:

Wet methanol was dried over KOH powder for 7d. Then the solvent was distilled under a dry argon counter-flux at 90°C and stored over activated molecular sieves.

Benzene:

Wet benzene was dried over NaK for 7d. Then the solvent was distilled under a dry argon counter-flux at 90°C and stored over activated molecular sieves.

Tetrahydrofuran:

Pre-dried Tetrahydrofuran from a *PureSolv* solvent tower was further dried over Na and benzophenone. Upon reflux the reaction mixture turned blue and was then distilled and stored over molecular sieves.

Diethylether:

Pre-dried Diethlylether from a *PureSolv* solvent tower was further dried over Na and benzophenone. Upon reflux the reaction mixture turned blue and was then distilled and stored over molecular sieves.

Acetonitrile:

Pre-dried Diethlylether from a *PureSolv* solvent tower was further dried over CaH for 7d and then distilled under argon counter-flux and stored over molecular sieves.

Dichloromethane:

Pre-dried Dichloromethane from a *PureSolv* solvent tower was further dried over CaH for 7d and then distilled under argon counter-flux and stored over molecular sieves.

Dimethylsulfoxide:

Wet DMSO was dried over CaH for 7d. Then the solvent was distilled under vacuum at 90°C and stored over activated molecular sieves and argon.

Synthesis of Ru-CNC complex

The synthesis of the Ru-CNC pincer was undertaken by a two-step procedure. In a first step the corresponding silver complex is formed (**Figure 3.4a**),

followed by transmetalation with Ru (**Figure 3.4b**). In this fashion the desired complex is synthesized in in good yield (36%).

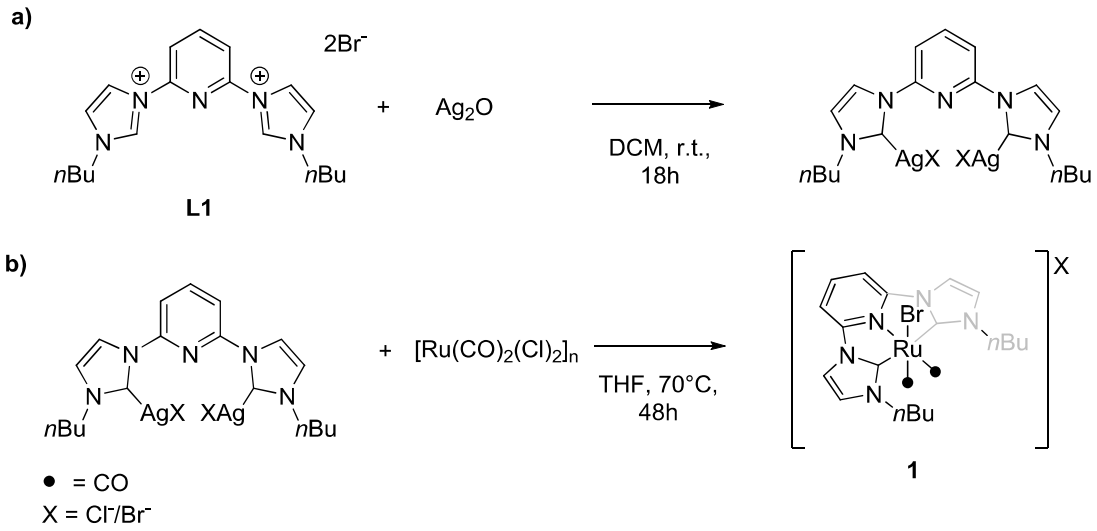


Figure 3.4 Synthesis of Ru-CNC complex a) Insertion of Ag forming silver carbene complex and b) formation of complex 24.

It is important to note that the silver complex was not analysed, but used immediately after its formation and separation from the reaction media, due to its high reactivity with light.

3.2. Equipment

3.2.1. 5512 50.0 cm^3 stirred Parr batch reactor

Hydrogenation of CO_2 to formic acid was performed in a 50.0 cm^3 stainless steel Parr reactor equipped with an overhead stirrer. The reactor description and standard procedure is given below

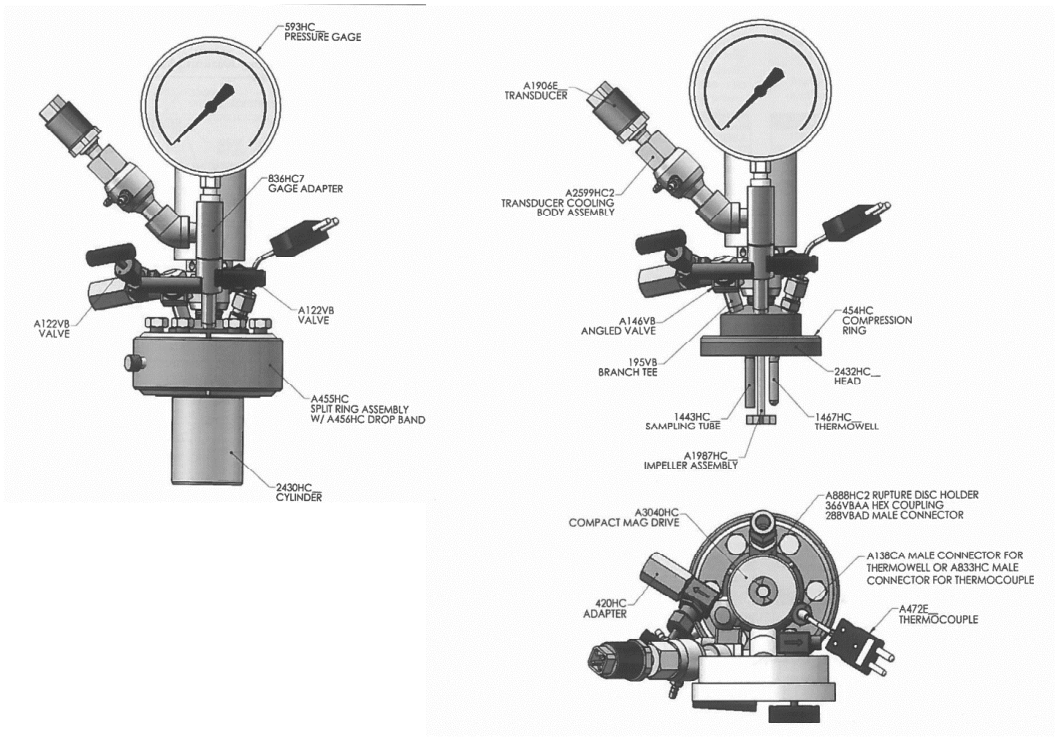


Figure 3.5 Side-view of 50 mL small stirred Parr reactor (top) and top-view of 50 mL small stirred Parr reactor.[8]

Great care and precaution should be used to prevent explosion and injuries when operating the reactor under high pressures. In a standard operating procedure, reactants and the desired volume of solvent is loaded into the vessel and it is ensured that threads are clean and then the outer retaining ring brought up around the split ring closure.. Each cap screw was tightened with a wrench delivered with the reactor in a criss-cross manner. The reactor was let to stand for five minutes and then the screws were checked again and if necessary tightened again.

The internal thermocouple was securely connected to the 4848 reactor controller. The stirring head was lowered to the compact magnetic drive. The temperature controller was set to the required temperature. The desired

pressure was achieved when the temperature reached the equilibrium. For further details the reader is referred to the corresponding publications.

3.2.2. High pressure NMR-tube

Mechanistic studies were conducted in a high pressure NMR-tube. The tube description and standard procedure is given below. The high pressure NMR-tube consists mainly of two parts. The upper part consists of a needle valve out of non-magnetic aluminium which is screwed onto the base, which connects the tube to the valve. The valve can be connected to the pressure source via 1/8" tubing. The tube consists out of non-magnetic ZrO_2 and is connected to the valve by a Viton O-Ring. The internal volume of the tube is ca. 1 mL and can be pressurised up to 1000 bar. A schematic description of the high pressure NMR tube is given below.

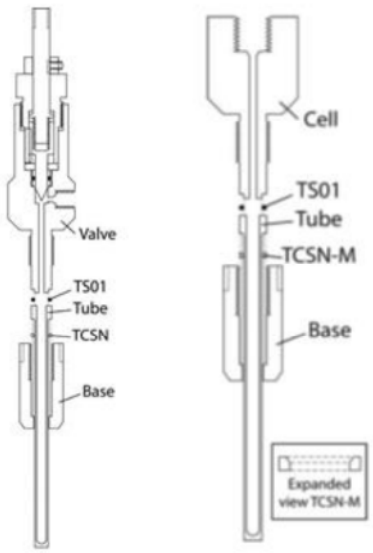


Figure 3.6 Schematic description of high pressure NMR-tube.[ref]

Standard procedure for High Pressure NMR-tube

Reactants and desired volume of solvent were loaded into the cell. Alternatively this could be done by the transfer line delivered with the system. Then the valve is threaded into the base. Only proper, non-magnetic tools were used for tightening the tube. After the set-up is finished the gas sample was transferred into the system with the transfer line. Once the sample was prepared the valve was closed. The handle is attached to the stem, the set screw is tightened with the 3/16" hex driver. Pressurizing was performed with a syringe pump by the Daedalus innovations LLC**.** This prevented the potential of over pressurization.

Finally the NMR cell is lowered into the magnet using the chain attached to the tube, as shown in the figure below



Figure 3.7 Chain attached to the assembled high pressure NMR-tube.

3.3 References

1. Zanatta, M.; dos Santos, F. P.; Biehl, C.; Marin, G.; Ebeling, G.; Netz, P. A.; Dupont, J., Organocatalytic Imidazolium Ionic Liquids H/D Exchange Catalysts. *The Journal of Organic Chemistry* **2017,** *82* (5), 2622-2629.
2. Loch, J. A.; Albrecht, M.; Peris, E.; Mata, J.; Faller, J. W.; Crabtree, R. H., Palladium Complexes with Tridentate Pincer Bis-Carbene Ligands as Efficient Catalysts for C−C Coupling. *Organometallics* **2002,** *21* (4), 700-706.
3. Cosier, J.; Glazer, A. M., *J. Appl. Crystallogr.* **1986,** *19*, 105−107.
4. CrysAlisPro. . **2014,** *Agilent Technologies: Yarnton, UK*

5. Sheldrick, G. M., *SADABS Program for Area Detector Absorption Correction;* **1996,** *University of Göttingen, Germany*.
6. Sheldrick, G. M., *Acta Crystallogr., Sect. A: Found. Crystallogr.* **2008,** *64*, 112-122.
7. Dolomanov, O. V., Bourhis, L. J., Gildea, R. J, Howard, J. A. K. & Puschmann, H. , *J. Appl. Crystallogr. 2009, 42, 339−341.*

2009, *42*, 339-341.
8. Company, P. I., 5500 Compact Micr Reactors In *Operation Instruction Manual*, Parr Instrument Company: 2016; p 14.

Chapter 4: ILs as additives for CO_2 hydrogenation

4.1. Publication I: Selective CO_2 hydrogenation to formic acid with Multifunctional Ionic Liquids.

Contribution of the author: The author drew the research plan and synthesized all the ionic liquids and planned and conducted all the experimental work in this publications. The author furthermore contributed in to the preparation of the manuscript.

Reprinted with permission from *ACS Catal.* **2018**, 8, 3, 1628-1634 Copyright 2018 American Chemical Society.

ACS Catalysis

Research Article

Cite This: ACS Catal. 2018, 8, 1628−1634

pubs.acs.org/acscatalysis

Selective CO_2 Hydrogenation to Formic Acid with Multifunctional Ionic Liquids

Andreas Weilhard,[†,‡] Muhammad I. Qadir,[§] Victor Sans,*[,†,‡] and Jairton Dupont*[,†,§]

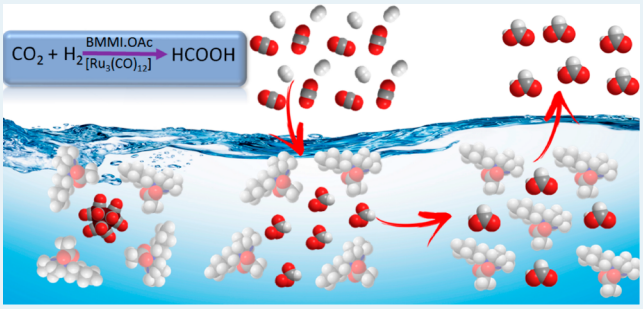
[†]GSK Carbon Neutral Laboratories for Sustainable Chemistry, University of Nottingham, NG7 2GA Nottingham, U.K.

[‡]Faculty of Engineering, University of Nottingham, NG7 2RD, Nottingham, U.K.

[§]Institute of Chemistry, UFRGS, Av. Bento Gonçalves, 9500, Porto Alegre 91501-970, Rio Grande do Sul Brazil

Supporting Information

ABSTRACT: The development of simple, cost-effective, and sustainable methods to transform CO_2 into feedstock chemicals is essential to reduce the dependence of the chemical industry on fossil fuels. Here, we report the selective and efficient catalytic hydrogenation of CO_2 to formic acid (FA) using a synergistic combination of an ionic liquid (IL) with basic anions and relatively simple catalysts derived from the precursor $[Ru_3(CO)_{12}]$. Very high TON (17000) and TOF values have been observed, and FA solutions with concentrations of up to 1.2 M have been produced. In this system, the imidazolium-based IL associated with the acetate anion acts as a precursor for the formation of the catalytically active Ru−H species, as a catalyst stabilizer, and as an acid buffer, shifting the equilibrium toward free formic acid. Moreover, the IL acts as an entropic driver (via augmentation of the number of microstates), lowering the entropic contribution imposed by the IL surrounding the catalytically active sites. The favorable thermodynamic conditions enable the reaction to proceed efficiently at low pressures, and furthermore the immobilization of the IL onto a solid support facilitates the separation of FA at the end of the reaction.



KEYWORDS: *carbon dioxide, hydrogenation, ionic liquids, formic acid, selective, mild, sustainable*

INTRODUCTION

Formic acid (FA) is a primary product of the chemical industry with a production capacity of 600000 tons per year and a projected annual increase of 22%.[1] Most commonly, formic acid is synthesized by MeOH carbonylation, yielding a formate ester which is then hydrolyzed with an excess of water.[2] The transformation of CO_2 to FA in one step using H_2 from renewable sources represents a more sustainable alternative to the current synthesis, being less resource intensive, using an abundant resource (CO_2), and avoiding the generation of intermediates and the need for tedious purifications. Furthermore, the direct synthesis of formic acid from CO_2 potentially represents a vector for hydrogen storage.[3−5] Unfortunately, this transformation is hugely challenging due to the inherent kinetic and thermodynamic stability of CO_2.[6,7] One strategy which has been used frequently to overcome thermodynamic limitations is the use of suitable bases.[8] Under these conditions, a plethora of catalysts based on N-heterocyclic carbenes,[9,10] half-sandwich compounds,[3,11,12] pincer ligands,[13−16] and phosphines[8,17−20] combined with noble metals such as Ir, Ru, and Rh have been described and reported, in some cases, to display very high TON and TOF values.[13] A key consideration in these systems is the synthesis of stable formate adducts or salts, requiring tedious purifications to separate the formic acid.[6,21−23]

An ideal scenario would involve the direct formation of formic acid in base-free systems or systems with weak bases, where the FA could be readily recovered. Due to the aforementioned limitations, such systems are rather scarce (see Table S1 in the Supporting Information for a summary of results and TON and TOF values).[24,26] Formate buffers have been introduced to stabilize the catalyst in the acidic aqueous media, thus increasing the achievable concentration of formic acid with moderate success (up to a final concentration of 0.11 M).[27] Alternatively, the employment DMSO or DMSO/water mixtures yielded high formic acid concentrations, although the catalytic activity was relatively low.[28] In 2016, Leitner and co-workers reported a Ru(triphos) catalyst which achieved high TON and TOF in the presence of sodium acetate (NaOAc).[29]

Ionic liquids (ILs) are very interesting media for the transformation of carbon dioxide, due to its high solubility in solutions of IL and aqueous or organic solvents with significant aqueous content.[30a] This is particularly important in those ILs based on imidazolium cations which are associated with basic anions such as acetate, due to the formation of bicarbonate and the acid-buffering properties of these solutions.[30b]

Received: November 16, 2017
Revised: January 9, 2018
Published: January 11, 2018

Downloaded via UNIV NOTTINGHAM on March 26, 2019 at 21:13:51 (UTC).
See https://pubs.acs.org/sharingguidelines for options on how to legitimately share published articles.

© 2018 American Chemical Society

DOI: 10.1021/acscatal.7b03931
ACS Catal. 2018, 8, 1628−1634

ILs with basic anions, such as 1,3-propyl-2-methylimidazolium formate (PPMI·O_2CH), enhance the yield of the reaction by thermodynamically favoring product formation.[31] Indeed, in this system, a change in enthalpy of −20 kJ mol^{-1} was observed, being higher than that in conventional organic solvents and water but lower than that when formate adducts are formed. Consequently, a scaled-up process would have to overcome a lower energy barrier: e.g., reactive distillation is not necessary to form formic acid from formate adducts during product isolation.[31] Furthermore, high activity (TOF = 300 h^{-1}) in the presence of 3-propyl-1,2-dimidazolium formate (PMMI·O_2CH) has been reported, although the extraction efficiency of FA from the IL into the apolar $scCO_2$ phase reached only 10% after >60 h.[32]

Here, we present a remarkably active and selective catalytic system, where ILs with basic anions perform multiple roles in the direct hydrogenation of CO_2 to formic acid using a Ru catalyst (Figure 1). The ILs play a key role in the stabilization

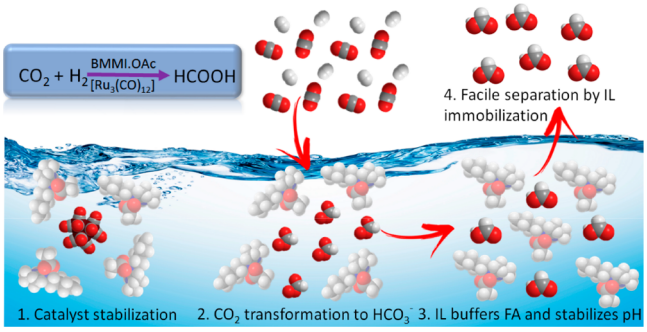


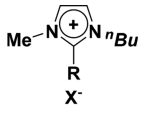
Figure 1. Multiple roles performed by ILs in the selective and efficient hydrogenation of CO_2 to formic acid (FA). ILs with basic anions are shown to (1) stabilize the catalyst, (2) facilitate formation of bicarbonate in the presence of water, (3) buffer the reaction media, and (4) facilitate the isolation of FA from the reaction mixture upon immobilization of the IL followed by simple filtration.

of the catalyst, assist the transformation of CO_2 into bicarbonate, and buffer the system, shifting the equilibrium toward production of formic acid.

RESULTS AND DISCUSSION

Hydrogenation of CO_2 to Formic Acid. First, the roles of a series of ILs were explored under reaction conditions usually employed for the hydrogenation of CO_2 to formic acid using ruthenium-based catalyst precursors (Table 1). Remarkably, when 1,2-dimethyl-3-butylimidazolium acetate (BMMI·OAc) was employed, very high turnover numbers (TON) were observed (up to 17000) with an average turnover frequency (TOF) of 102 h^{-1}. Under these conditions, a 1.1 M solution of FA was obtained (entry 6, Table 1). An increased TOF of 300 h^{-1} was obtained at 80 °C, though at the expense of a lower TON of 6875 (Table 1, entry 8). When the reaction time was increased to 40 h, a TON of 8355 was reached at the cost of a lower TOF (200 h^{-1}) (Table 1, entry 9). It is important to note that these very high TON and TOF values were achieved using a simple, cheap, and commercially available $[Ru_3(CO)_{12}]$ species as the precatalyst under substantially milder conditions in comparison to the state of the art for FA synthesis from CO_2 without the use of bases for formate stabilization.[28,29,32] Table S1 shows a comparison with the best reported values in the literature.

Table 1. Catalytic Hydrogenation of CO_2 to FA by $[Ru_3(CO)_{12}]$ Catalyst at 60 °C



R = Me, X = OAc, **BMMI.OAc**
R = Me, X = Cl, **BMMI.Cl**
R = Me, X = HCO_2, **BMMI.O_2CH**
R = Me, X = Imidazolate, **BMMI.Im**
R = H, X = OAc, **BMI.OAc**

entry[a]	IL	t/h	[FA]/M	TON[d]	TOF[e]/h^{-1}
1		4			
2	BMMI·Cl	4			
3	BMMI·Im	4			
4	BMMI·OAc	4	0.42	267.2	67
5	BMMI·OAc	72	1.10	700	9.7
6[b]	BMMI·OAc	168	1.10	17000	102.4
8[c]	BMMI·OAc	20	0.43	6875	300
9[c]	BMMI·OAc	40	0.52	8355	200
10	BMI.OAc	4	0.12	80	20
11	BMMI·O_2CH	4	0.09	55	13.8
12	BMMI·O_2CH	72	0.46	296	4.1
13	$N(Bu)_4$·OAc	4	0.24	157	39
14	$N(Bu)_4$·OAc	72	0.96	617	8.6
15	NaOAc	4	0.06	35.6	9

[a]Reaction conditions for entries 1−5 and 10−15: cat. (7.8 μmol), BMMI·OAc (0.66 M, 0.7 g), DMSO/H_2O (5 v/v%; DMSO (5.24 mL, 67 mmol), H_2O (0.24 mL, 13.2 mmol)), and CO_2/H_2 (1:1, 40 bar). [b]Reaction conditions: cat. (0.3 μmol), CO_2/H_2 (30 bar CO_2/40 bar H_2), and 70 °C. [c]Reaction conditions: cat. (0.3 μmol), CO_2/H_2 (30 bar CO_2/30 bar H_2), and 80 °C. [d]Calculated as mol of FA/mol of $[Ru_3(CO)_{12}]$ using ^{1}H NMR. [e]Calculated as TON/$t_{reaction}$.

The specific interaction of BMMI·OAc with the reaction media was demonstrated by exploring the same reaction using a series of ILs with different properties. In the first instance, no FA (or any other product) formation was observed without an IL (Table 1, entry 1). This reveals that the IL has a vital role in the hydrogenation of CO_2 to FA on the basis of its buffering properties and stabilization of weak carbonic acid species. The formation of FA is favorable under basic reaction conditions, and therefore different ILs with basic anions (BMMI·Cl and BMMI·Im) were also investigated (Table 1, entries 2 and 3). Surprisingly, no FA was observed when BMMI·Cl was employed, which may be related to the IL poisoning the catalysts during CO_2 hydrogenation reactions.[26] Despite the theoretical buffering and basic properties of BMMI·Im, no catalytic activity was observed (Table 1, entry 3), possibly due to the ability of the imidazolate anion to bind to the catalytically active species to form carbenes, thus competing with the CO_2 hydrogenation reaction. This would also be the case for other basic counteranions such as triazolate, and therefore more detailed studies with other highly basic and possibly strongly coordinating ILs were dismissed. When BMMI·O_2CH was employed, relatively low activity for FA formation (TON = 55) was observed, in comparison to BMMI·OAc (Table 1, entries 4, 11, and 12). This effect may be due to the lower pK_a of the formate counteranion in comparison to the acetate anion. The higher pH resulting from this buffering process prevents the protonation of Ru−H active species, thus keeping it in an active state.[27,29,33] Furthermore, the IL $(N)Bu_4$·OAc and NaOAc showed lower activities than BMMI·OAc, with TONs of 157 and 35.6, respectively (Table 1, entries 13−15), after 4 h.

An important feature of the IL's ability to stabilize the formation of formic acid is a broad solvent compatibility. Indeed, various organic solvents in combination with BMMI·

DOI: 10.1021/acscatal.7b03931
ACS Catal. 2018, 8, 1628−1634

OAc were employed for the hydrogenation of CO_2 to formic acid. The hydrogenation was found to occur in a variety of solvents (see Table 2) where a range of different product concentrations were observed, indicating that the solvent still plays a role in the reaction outcome. The highest concentration was obtained with DMSO in combination with 5 v/v% H_2O, in agreement with previous reports.[28,29] Higher concentrations of water led to decreased catalytic activity, probably due to the dissociation of the DMSO/H_2O clusters (see Table S2 in the Supporting Information).[29] In methyl *tert*-butyl ether, 2-methyltetrahydrofuran, and 1,4-dioxane, a phase separation could be observed after the reaction was complete, where the IL, catalyst, and FA were all dissolved in the same phase and the solvent had separated (Table 2, entryies 4–6). This might be explained by the poor solubility of water and IL in these solvents.

Table 2. Solvent Effect on FA Concentration and Catalytic Activity Observed[a]

entry	solvent[b]	t[c]/h	[FA]/M	TON	TOF/h^{-1}
1	DMSO/H_2O	32	1.2	3609	106
2	THF/H_2O	18	0.7	2165	120
3	MeCN/H_2O	21	0.50	1567	78
4[d]	MtBE/H_2O	20	0.83	2578	128
5[d]	MeTHF/H_2O	18	0.66	2062	114
6[d]	dioxane/H_2O	20	0.52	1629	81

[a]Reaction conditions: cat. [$Ru_3(CO)_{12}$] = 3.2 × 10^{-4} M; $V_{reaction}$= 5 mL; IL BMMI·OAc; [IL] = 0.66 M; P_{H2} = P_{CO2} = 30 bar; T = 60 °C. [b]5% v/v water. [c]Reaction time was adjusted until constant pressure was observed. [d]Biphasic mixture observed after the reaction.

Role of IL in the Reaction Mechanism and in Stabilizing the Active Catalytic Species. The good results observed in terms of catalytic activity and selectivity under remarkably mild conditions encouraged us to investigate the reaction mechanism to understand the roles played by the ionic liquid. It has been previously shown that organic carbonates are readily hydrogenated to yield the corresponding formate esters.[34] On the basis of prior work[30] we hypothesized a bicyclic catalytic mechanism. In the first cycle, the IL catalyzes the formation of HCO_3^- via "activated water" which is coordinated to BMMI·OAc in a way similar to that previously reported.[30] Indeed a signal of HCO_3^- at 158 ppm was observed in the ^{13}C NMR, measured under relevant reaction conditions, of a mixture of IL, DMSO/H_2O, and [$Ru_3(CO)_{12}$] (see Figure 2d). The carbonate formed in situ then enters the second cycle, where it is hydrogenated by the Ru hydride species to yield a formate complex, along with an associated elimination of water (Figure 2a). The signal assignable to catalyst-bound formic acid can be found at 166 ppm. Furthermore, a peak at 122 ppm assignable to CO_2 was observed (Figure 2d), confirming the proposed mechanism. A signal at 220 ppm corresponding to Ru−CO (see Figure S2) and ESI-MS data (Figure 2e) indicate that the Ru cluster core is not transformed into monometallic species or Ru nanoparticles.

The amount of H_2O in the solvent was found to play a significant role (Table S2). An increasing amount of water seems to have a positive effect on the activity up to 5% in volume. Afterward, presumably the stabilization of the formic acid formed worsens due to the ineffective clustering of the buffer. The dissociation of H_2O was not involved in the rate-determining step, as opposed to previously reported mechanisms.[25,26] This was determined by replacing H_2O with D_2O,

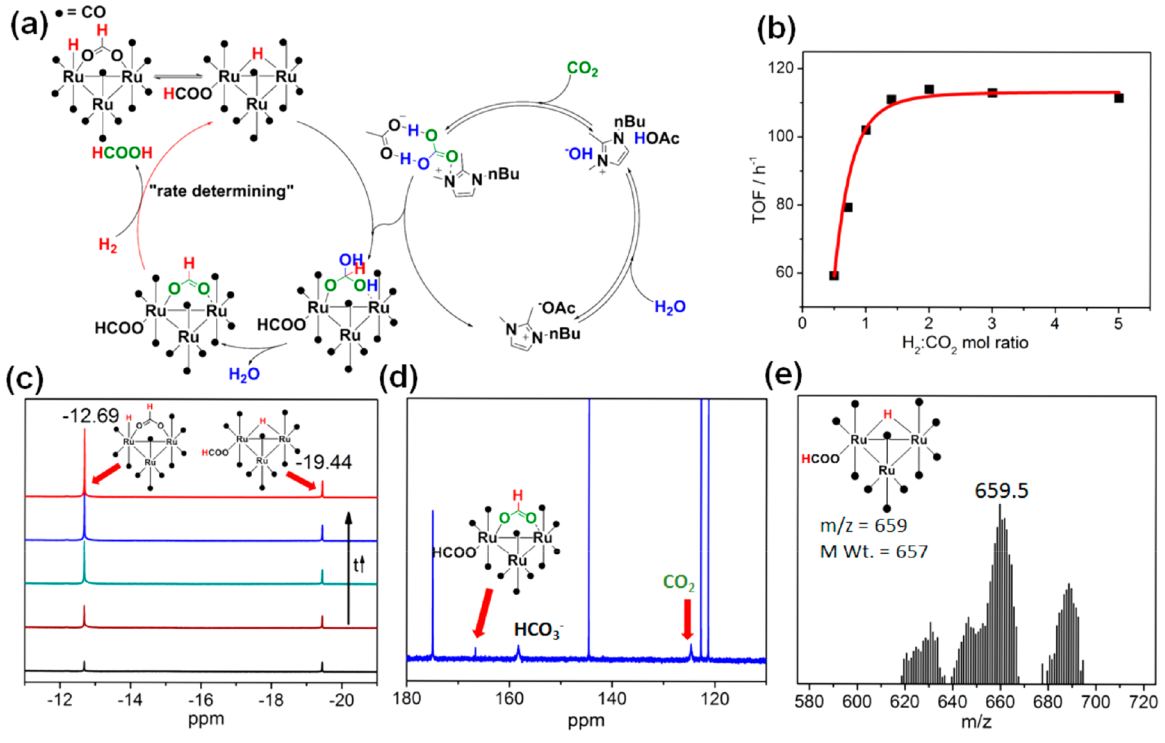


Figure 2. (a) Proposed mechanism for CO_2 hydrogenation to FA. (b) TOF vs gas phase composition. Reaction conditions: total pressure 60 bar, t = 4 h, T = 60 °C, BMMI·OAc IL (0.66 M), [$Ru_3(CO)_{12}$] = 7.8 μmol, and DMSO/H_2O (5 v/v%; DMSO (5.24 mL, 67 mmol), H_2O (0.24 mL, 13.2 mmol)). (c) High-pressure ^1H NMR and (d) high-pressure ^{13}C NMR spectra, both at P_{CO2} = P_{H2} = 20 bar, T = 25 °C, with 23 μmol [$Ru_3(CO)_{12}$] in DMSO/water with BMMI·OAc. (e) ESI-MS spectra of the [$Ru_3(CO)_{11}(H)(HCOO)$] complex.

DOI: 10.1021/acscatal.7b03931
ACS Catal. 2018, 8, 1628−1634

leading to a secondary kinetic effect and a reduction in activity: i.e., the TOF decreased to 87 h^{-1} in the presence of D_2O versus 118 h^{-1} in the presence of H_2O (see Table S3 in the Supporting Information for more detail). One explanation for the secondary kinetic isotopic effect might be described by the formation of the carbonate prior to the rate-determining step, thus giving further insight into the catalytic mechanism.

In this case, the rate-determining step was found to be the regeneration of the active hydride species via abstraction of FA from the catalytic cycle with hydrogen. A TOF of 120 h^{-1} can be observed at a ratio of 2/1 (H_2/CO_2), which decreases almost in a linear fashion to 60 h^{-1} when the ratio of H_2 to CO_2 was lowered (Figure 2b). The hydrogenation step has been described previously as being rate determining with other Ru catalysts.[25] An increase in the partial pressure of H_2 above a ratio of 2/1 in comparison to that of CO_2 showed no further increase in the reaction rate. This might be explained by the saturation of the liquid phase with H_2 in this regime, thus the limiting the effective concentration of H_2 available for the reaction.[35]

Formic acid can split from the metal center by forming either a bridged or terminal hydride. If a terminal hydride is formed, this hydride would undergo isomerization to a bridged hydride, regenerating the active species. In this regard, it is worth mentioning that bridged hydrides have been described as thermodynamically more stable.[36] Furthermore, trinuclear Ru carbonyl complexes with bridging acid ligands, similar to the complex proposed here, have been described previously, and thus this is a more plausible mechanism.[37]

The IL is not only involved in the transformation of CO_2 to HCOOH but also assists the formation of the active species. Indeed, the active species are only observed in the presence of IL and H_2, indicating a cooperative mechanism involving the IL, water, and hydrogen. The formation of the same hydride species was observed in the reaction mixture and in the in situ high-pressure ^1H NMR. The hydrides at −12.48 and −19.48 ppm correspond to a terminal and to a bridging hydride, respectively[38] (see Figure 2c and Figure S1 in the Supporting Information), akin to those already observed for dialkylimidazolium ILs with other anions.[39,40] Interestingly, a singlet at 8.48 ppm, corresponding to FA, can be detected even in the absence of CO_2, suggesting hydration of one CO ligand; we suggest that the transformation of CO to HCOO takes place due to the interplay of $[Ru_3(CO)_{12}]$ with BMMI·OAc and H_2. In the ^{13}C NMR, the HCOO ligand from $[Ru_3(CO)_{11}(H)(HCOO)]$ was confirmed by observation of a peak at 164 ppm (see Figure S2 in the Supporting Information), analogous to that observed in Figure 2d. In addition, ESI-MS analysis revealed a peak at m/z 659, corroborating the presence of $[Ru_3(CO)_{11}(H)(HCOO)]$ (see Figure 2e). No interaction between the BMMI·OAc IL and $[Ru_3(CO)_{12}]$ catalyst was observed by ^{13}C NMR spectroscopy. Moreover, when the catalyst was exposed to hydrogen in the absence of IL, the formate peak was not observed and the hydride peak previously observed at −19.48 ppm shifted to −17.16 ppm, indicating that a different hydride complex is formed in the absence of IL. Surprisingly, in the presence of solely IL (i.e., without hydrogen and carbon dioxide), a hydride peak with low intensity at −19.48 ppm was observed, which suggests that the Ru cluster may be protonated by residual H_2O. Furthermore, no carbene signal[39] was observed by ^{13}C NMR in any experiment conducted in BMMI·OAc, indicating that there is no interaction between the IL and the Ru cluster, via direct bond formation.

The activation barrier for the rate-determining step was determined to be 58 ± 4 kJ mol^{-1}, which is relatively small, given that no electron-donating and/or multidentate ligands have been employed.[14−16,28b] The range of temperature (50−70 °C) was chosen to avoid catalyst decomposition[41] and side reactions such as the reverse water-gas shift reaction at increased temperatures (see Table S4 in the Supporting Information and Figure 3).[39,42]

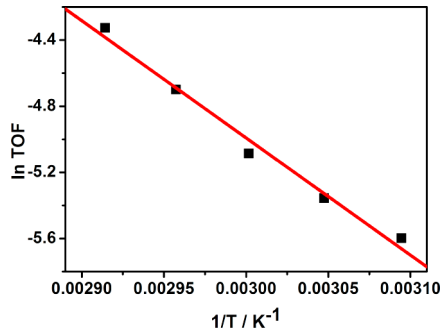


Figure 3. Arrhenius plot for the direct hydrogenation of CO_2 to FA.

Effect of Buffering on FA Stabilization. The IL plays an active role in the formation and stabilization of the catalytically active species and also in the stabilization of the FA via a buffering effect. A linear relationship was found on the double-logarithmic scale between the amount of IL present and that of formic acid (Figure 4). This behavior can be explained by the Henderson−Hasselbalch equation typically employed to describe buffering systems. It can be assumed that the IL prevents the deactivation of the catalyst via protonation by

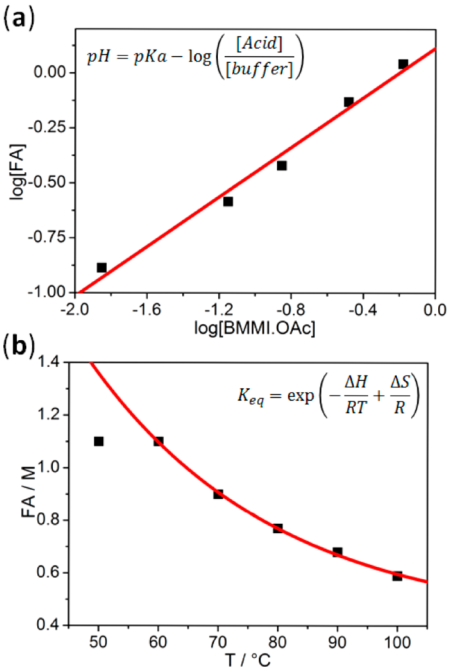


Figure 4. (a) FA concentration vs IL concentration on a double-logarithmic scale. Reaction conditions: $P_{H2} = P_{CO2} = 20$ bar, $T = 60$ °C, 5 mL of DMSO/water (5 v/v% water). (b) FA concentration as a function of the temperature of the reaction. Reaction conditions: $P_{H2} = P_{CO2} = 20$ bar, 3.3 mmol of BMMI·OAc in 5 mL of DMSO/water (5 v/v% water).

DOI: 10.1021/acscatal.7b03931
ACS Catal. 2018, 8, 1628−1634

stabilizing the pH at a level that preserves the catalyst in an active state. Another insight that suggests a buffering effect is that a higher acid to buffer ratio can be achieved at low concentrations of buffer (see Figures S3 and S4 in the Supporting Information). A FA/IL ratio of 9/1 was observed at [IL] = 14 mM, which decreased to 3/1 for [IL] = 140 mM, reaching a final value of 1.5/1 for [IL] = 0.66 M (see Figure S3 in the Supporting Information).

Further evidence for the buffering effect is found in the van't Hoff plot, representing the equilibrium constant at different temperatures (see Table S5 and Figure S5 in the Supporting Information). Values of $\Delta H = -13.26 \pm 0.65$ kJ mol^{-1} and $\Delta S = -17.4 \pm 1.8$ J K^{-1} mol^{-1} were observed. The relatively low value of ΔH suggests that no significant proton abstraction, i.e. formate synthesis, is occurring because in the presence of bases the change in enthalpy can be expected to be in the range of −30 to −84 kJ mol^{-1}.[7] Furthermore, the observed enthalpy change falls between that of pure DMSO/water and pure IL, indicating a weak interaction between the IL and the FA, presumably through hydrogen bonding.[29,31] In addition, the relatively low entropic contribution to the reaction (−17.4 ± 1.8 J K^{-1} mol^{-1}) makes FA the favorable product. The low entropic contribution might be explained by the organization of IL clusters formed in DMSO, which may form IL−FA adducts due to the augmentation of microstates (entropic driver) imposed by the IL surrounding the catalytically active sites.[43]

The linear behavior of the van't Hoff plot manifests itself in the exponential decay of the FA concentration observed upon increasing the reaction temperature (Figure 4b). For instance, a final concentration of FA of 0.6 M can be achieved at 100 °C. The concentration increases exponentially when the temperature is successively decreased, reaching 1.1 M at 60 °C. However, when the temperature is further reduced to 50 °C,the concentration does not increase, indicating an overacidification leading to a kinetic deactivation of the catalyst prior to reaching the thermodynamic equilibrium as observed at high pressures (Figure 4b).

The reaction rate was found to be dependent on the total pressure. An increased reaction rate can be observed at increased pressure, which can be explained by the increased concentration of the reagents in the liquid phase (according to Henry's law) and the decreased viscosity of the liquid phase at higher concentrations of dissolved gas (see Figure S6 in the Supporting Information).[44] Furthermore, the increased concentration of CO_2 in the liquid phase might enhance the solubility of H_2, as H_2 is highly soluble in CO_2, which in turn is soluble in the ILs.[45−47] The final concentration obtained at low pressures was found to have a linear relationship with the pressure, in agreement with Henry's law.

The favorable thermodynamic parameters in the presence of the IL make the reaction viable at low pressures, where high concentrations of FA (0.47 M) could be observed at low total pressures (6 bar, $P_{H2} = P_{CO2} = 3$ bar). At low pressures, a linear correlation between pressure and concentration of FA was observed, in agreement with Henry's law (Figure 5). This was not the case at higher pressures (>40 bar), potentially due to the catalyst deactivation due to overacidification of the reaction media or to the saturation of the liquid phase. This is a remarkable result from a processing perspective, since gas compression is the second highest cost after the generation of hydrogen.[48] This suggests that the IL system developed here has extraordinary potential for developing new cost-effective routes toward CO_2 valorization.

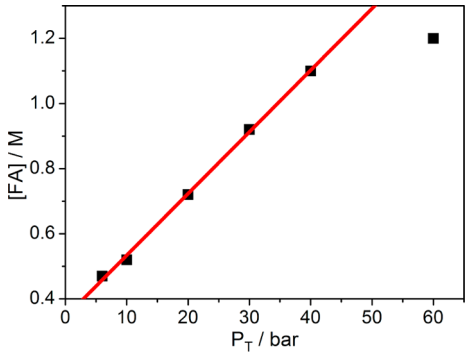


Figure 5. Concentration of FA obtained as a function of the total gas pressure. High concentrations of FA were synthesized at low pressures. Reaction conditions: T = 60 °C, 3.3 mmol of BMMI·OAc in 5 mL of DMSO/water (5 v/v% water).

A critical aspect for the development of viable industrial or commercial processes is the separation of the FA from the IL at the end of the reaction. Our results indicate that the buffering nature of the interaction between FA and the IL, where no formate salts have been formed, should facilitate separation at the end of the synthesis. Nevertheless, it is challenging to separate the liquid FA in a non-energy-intensive fashion. Distillation might lead to unwanted dehydration or dehydrogenation reactions,[5] and stripping with a carrier solvent, like $scCO_2$, has been shown to have limited efficiency.[31] On the other hand, grafting imidazolium derivatives to commercially available Merrifield resins is a simple strategy to immobilize this type of IL,[49] leading to solid-supported catalysts with properties analogous to those of homogeneous ILs.[50−52] A similar strategy was employed here, by supporting 1,2-dimethylimidazole onto a microporous Merrifield resin (2 mmol of Cl/g, 1% cross-linking) followed by anion exchange to the acetate salt according to literature procedures (see the Supporting Information for more details).[53] The supported IL was then employed in place of BMMI·OAc under conditions similar to those previously described. At the end of the reaction the suspension was filtered and characterized by ^{1}H NMR. The polymer was reutilized in subsequent reaction cycles.

Under optimized conditions ($P_{H2} = P_{CO2} = 30$ bar, T = 60 °C, 0.5 g of polymer, 2 mmol of IL equivalent, 10 mL of solvent) a 0.3 M solution of FA (in DMSO/water) was collected by simple filtration, resulting in a FA solution (as shown in Figure 6a) as opposed to the control experiment (Figure 6b), where the employment of a homogeneous ionic liquid led to a FA−IL mixture. Notably, only traces of FA could be isolated when the reaction was carried out in THF, possibly due to the lower polarity of the solvent leading to a competitive adsorption of the FA on the immobilized IL. This clearly indicates that the reaction is forming formic acid instead of formate adducts with the IL, because in the case of formate adduct formation, separation of the formic acid from the IL would be highly unfavorable. Even though the catalyst was only physically adsorbed onto the polymer, the system maintained its activity for five consecutive cycles (see Table S6 in the Supporting Information). Following this, a reduction in activity was observed, which was attributed to catalyst leaching. The extent of this was confirmed by ICP-OES analysis of the filtrate, which showed significant amounts of ruthenium (Table S6).

In addition, the filtrate (FA in the absence of IL) was stable against decomposition. At 60 °C no FA decomposition was

DOI: 10.1021/acscatal.7b03931
ACS Catal. 2018, 8, 1628−1634

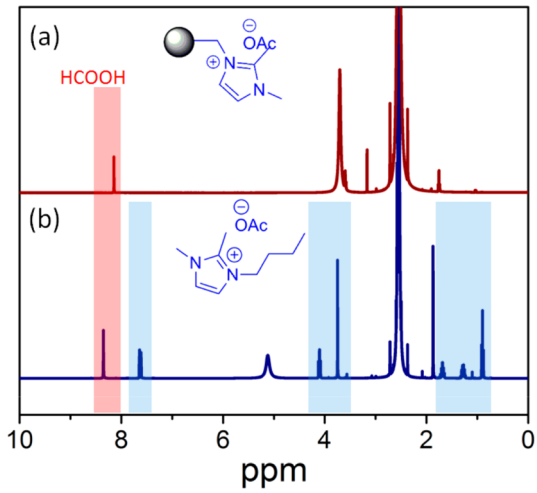


Figure 6. Comparison of the ^{1}H NMR spectra after FA synthesis for (a) the reaction employing immobilized IL and (b) the reaction employing homogeneous IL.

observed, even after addition of fresh catalyst (0.016 mmol). Conversely, the FA decomposition proceeds in the presence of IL at 60 °C, thus indicating that the IL plays a role not only in the formation of formic acid but also in its decomposition (Table S7).

CONCLUSIONS

ILs with basic anions are advantageous for the effective hydrogenation of CO_2 under base-free conditions. In this context, the IL plays multiple roles. First, it enhances the catalytic activity of the cheap, simple, and readily available $[Ru_3(CO)_{12}]$ catalyst by forming an intermediate carbonate species which is readily reduced to formic acid. High-pressure NMR studies confirmed this and the reaction of CO_2 with water containing ILs to form bicarbonate. Furthermore, the IL shifts the equilibrium by acting as a buffer for the acid, thus preventing catalyst deactivation via protonation. A profound thermodynamic influence has been observed, where the ionic liquid acts as an enthalpic and entropic driver, by structuring the surroundings of the catalyst, thus lowering its contribution and thermodynamically favoring the process.

The finely tuned interaction between the formic acid and the ionic liquid enables the transformation at low pressure and with a broad range of solvents. In addition, it facilitates the separation at the end of the synthesis. A covalently immobilized ionic liquid was found to be as effective as homogeneous ILs, and separation was achieved by simple filtration. Indeed, this represents a major advantage over systems utilizing bases, because reactive distillations could be avoided in future process schemes, thereby enhancing the economic viability of sustainable CO_2 valorization.

ASSOCIATED CONTENT

Supporting Information

The Supporting Information is available free of charge on the ACS Publications website at DOI: 10.1021/acscatal.7b03931.

Experimental details about CO_2 hydrogenation experiments, elucidation of catalytic intermediates, ESI-MS analysis, and thermodynamic parameter calculations (PDF)

AUTHOR INFORMATION

Corresponding Authors

*E-mail for V.S.: Victor.sanssangorrin@nottingham.ac.uk.
*E-mail for J.D.: Jairton.dupont@ufrgs.br.

ORCID

Victor Sans: 0000-0001-7045-5244
Jairton Dupont: 0000-0003-3237-0770

Notes

The authors declare no competing financial interest.

ACKNOWLEDGMENTS

The authors are grateful to CAPES, INCT-Catal., FAPERGS, CNPq, Petrobras, and the Faculty of Engineering from the University of Nottingham for funding.

REFERENCES

(1) Mac Dowell, N.; Fennell, P. S.; Shah, N.; Maitland, G. C. *Nat. Clim. Change* **2017**, *7* (4), 243−249.
(2) Reutemann, W.; Kieczka, H. In *Ullmann's Encyclopedia of Industrial Chemistry*; Wiley-VCH: Weinheim, Germany, 2000.
(3) Hull, J. F.; Himeda, Y.; Wang, W.-H.; Hashiguchi, B.; Periana, R.; Szalda, D. J.; Muckerman, J. T.; Fujita, E. *Nat. Chem.* **2012**, *4*, 383−388.
(4) Loges, B.; Boddien, A.; Gärtner, F.; Junge, H.; Beller, M. *Top. Catal.* **2010**, *53*, 902−914.
(5) Grasemann, M.; Laurenczy, G. *Energy Environ. Sci.* **2012**, *5*, 8171−8181.
(6) Leitner, W. *Angew. Chem., Int. Ed. Engl.* **1995**, *34*, 2207−2221.
(7) Schaub, T.; Paciello, R. A. *Angew. Chem., Int. Ed.* **2011**, *50*, 7278−7282.
(8) Inoue, Y.; Izumida, H.; Sasaki, Y.; Hashimoto, H. *Chem. Lett.* **1976**, *5*, 863−864.
(9) Azua, A.; Sanz, S.; Peris, E. *Chem. - Eur. J.* **2011**, *17*, 3963−3967.
(10) Sanz, S.; Azua, A.; Peris, E. *Dalton Trans.* **2010**, *39*, 6339−6343.
(11) Himeda, Y.; Onozawa-Komatsuzaki, N.; Sugihara, H.; Kasuga, K. *Organometallics* **2007**, *26*, 702−712.
(12) Himeda, Y.; Miyazawa, S.; Hirose, T. *ChemSusChem* **2011**, *4*, 487−493.
(13) Tanaka, R.; Yamashita, M.; Nozaki, K. *J. Am. Chem. Soc.* **2009**, *131*, 14168−14169.
(14) Filonenko, G. A.; Smykowski, D.; Szyja, B. M.; Li, G.; Szczygieł, J.; Hensen, E. J. M.; Pidko, E. A. *ACS Catal.* **2015**, *5*, 1145−1154.
(15) Filonenko, G. A.; van Putten, R.; Schulpen, E. N.; Hensen, E. J. M.; Pidko, E. A. *ChemCatChem* **2014**, *6*, 1526−1530.
(16) Filonenko, G. A.; Hensen, E. J. M.; Pidko, E. A. *Catal. Sci. Technol.* **2014**, *4*, 3474−3485.
(17) Graf, E.; Leitner, W. *J. Chem. Soc., Chem. Commun.* **1992**, 623−624.
(18) Fornika, R.; Gorls, H.; Seemann, B.; Leitner, W. *J. Chem. Soc., Chem. Commun.* **1995**, 1479−1481.
(19) Elek, J.; Nádasdi, L.; Papp, G.; Laurenczy, G.; Joó, F. *Appl. Catal., A* **2003**, *255*, 59−67.
(20) Tsai, J. C.; Nicholas, K. M. *J. Am. Chem. Soc.* **1992**, *114*, 5117−5124.
(21) Klankermayer, J.; Wesselbaum, S.; Beydoun, K.; Leitner, W. *Angew. Chem., Int. Ed.* **2016**, *55*, 7296−7343.
(22) Wang, W.-H.; Himeda, Y.; Muckerman, J. T.; Manbeck, G. F.; Fujita, E. *Chem. Rev.* **2015**, *115*, 12936−12973.
(23) Dong, K.; Razzaq, R.; Hu, Y.; Ding, K. *Top. Curr. Chem.* **2017**, *375*, 23.
(24) Hayashi, H.; Ogo, S.; Fukuzumi, S. *Chem. Commun.* **2004**, *0*, 2714−2715.
(25) Ogo, S.; Kabe, R.; Hayashi, H.; Harada, R.; Fukuzumi, S. *Dalton Trans.* **2006**, *0*, 4657−4663.
(26) Lu, S.-M.; Wang, Z.; Li, J.; Xiao, J.; Li, C. *Green Chem.* **2016**, *18*, 4553−4558.

DOI: 10.1021/acscatal.7b03931
ACS Catal. 2018, 8, 1628−1634

(27) Zhao, G.; Joó, F. *Catal. Commun.* **2011**, *14*, 74−76.
(28) (a) Qadir, M. I.; Weilhard, A.; Fernandes, J. A.; de Pedro, I.; Vieira, B.; Waerenborgh, J. C.; Dupont, J. *ACS Catal.* **2018**, DOI: 10.1021/acscatal.7b03804. (b) Moret, S.; Dyson, P. J.; Laurenczy, G. *Nat. Commun.* **2014**, *5*, 4017. (c) Sahoo, A. R.; Jiang, F.; Bruneau, C.; Sharma, G. V. M.; Suresh, S.; Roisnel, T.; Dorcet, V.; Achard, M. *Catal. Sci. Technol.* **2017**, *7*, 3492−3498.
(29) Rohmann, K.; Kothe, J.; Haenel, M. W.; Englert, U.; Hölscher, M.; Leitner, W. *Angew. Chem., Int. Ed.* **2016**, *55*, 8966−8969.
(30) (a) Cui, G.; Wang, J.; Zhang, S. *Chem. Soc. Rev.* **2016**, *45*, 4307−4339. (b) Simon, N. M.; Zanatta, M.; Dos Santos, F. P.; Corvo, M. C.; Cabrita, E. J.; Dupont, J. *ChemSusChem* **2017**, *10*, 4927−4933.
(31) Yasaka, Y.; Wakai, C.; Matubayasi, N.; Nakahara, M. *J. Phys. Chem. A* **2010**, *114*, 3510−3515.
(32) Wesselbaum, S.; Hintermair, U.; Leitner, W. *Angew. Chem.* **2012**, *124*, 8713−8716.
(33) vom Stein, T.; Meuresch, M.; Limper, D.; Schmitz, M.; Hölscher, M.; Coetzee, J.; Cole-Hamilton, D. J.; Klankermayer, J.; Leitner, W. *J. Am. Chem. Soc.* **2014**, *136*, 13217−13225.
(34) Balaraman, E.; Gunanathan, C.; Zhang, J.; Shimon, L. J. W.; Milstein, D. *Nat. Chem.* **2011**, *3*, 609−614.
(35) Burgess, S. A.; Kendall, A. J.; Tyler, D. R.; Linehan, J. C.; Appel, A. M. *ACS Catal.* **2017**, *7*, 3089−3096.
(36) Nevinger, L. R.; Keister, J. B.; Maher, J. *Organometallics* **1990**, *9*, 1900−1905.
(37) Aime, S.; Dastrù, W.; Gobetto, R.; Viale, A. *Organometallics* **1998**, *17*, 3182−3185.
(38) Brewer, S. A.; Holloway, J. H.; Hope, E. G. *J. Fluorine Chem.* **1995**, *70*, 167−169.
(39) Ali, M.; Gual, A.; Ebeling, G.; Dupont, J. *ChemCatChem* **2014**, *6*, 2224−2228.
(40) Ali, M.; Gual, A.; Ebeling, G.; Dupont, J. *ChemSusChem* **2016**, *9*, 2129−2134.
(41) Krämer, J.; Redel, E.; Thomann, R.; Janiak, C. *Organometallics* **2008**, *27*, 1976−1978.
(42) Tominaga, K.-i.; Sasaki, Y.; Hagihara, K.; Watanabe, T.; Saito, M. *Chem. Lett.* **1994**, *23*, 1391−1394.
(43) Luza, L.; Rambor, C. P.; Gual, A.; Bernardi, F.; Domingos, J. B.; Grehl, T.; Brüner, P.; Dupont, J. *ACS Catal.* **2016**, *6*, 6478−6486.
(44) Baker, S. N.; Baker, G. A.; Kane, M. A.; Bright, F. V. *J. Phys. Chem. B* **2001**, *105*, 9663−9668.
(45) Solinas, M.; Pfaltz, A.; Cozzi, P. G.; Leitner, W. *J. Am. Chem. Soc.* **2004**, *126*, 16142−16147.
(46) Blanchard, L. A.; Hancu, D.; Beckman, E. J.; Brennecke, J. F. *Nature* **1999**, *399*, 28−29.
(47) Anthony, J. L.; Maginn, E. J.; Brennecke, J. F. *J. Phys. Chem. B* **2002**, *106*, 7315−7320.
(48) Pérez-Fortes, M.; Schöneberger, J. C.; Boulamanti, A.; Harrison, G.; Tzimas, E. *Int. J. Hydrogen Energy* **2016**, *41*, 16444−16462.
(49) Sans, V.; Karbass, N.; Burguete, M. I.; Compan, V.; Garcia-Verdugo, E.; Luis, S. V.; Pawlak, M. *Chem. - Eur. J.* **2011**, *17*, 1894−1906.
(50) Sans, V.; Gelat, F.; Karbass, N.; Burguete, M. I.; Garcia-Verdugo, E.; Luis, S. V. *Adv. Synth. Catal.* **2010**, *352*, 3013−3021.
(51) Burguete, M. I.; Garcia-Verdugo, E.; Garcia-Villar, I.; Gelat, F.; Licence, P.; Luis, S. V.; Sans, V. *J. Catal.* **2010**, *269*, 150−160.
(52) Sans, V.; Gelat, F.; Burguete, M. I.; Garcia-Verdugo, E.; Luis, S. V. *Catal. Today* **2012**, *196*, 137−147.
(53) Burguete, M. I.; Erythropel, H.; Garcia-Verdugo, E.; Luis, S. V.; Sans, V. *Green Chem.* **2008**, *10*, 401−407.

DOI: 10.1021/acscatal.7b03931
ACS Catal. 2018, 8, 1628−1634

4.2. Results and Discussion

An initial screening of various ionic liquids (ILs), under variation of both - the anion and cation - in DMSO:H_2O (5 v/v H_2O) as the solvent system and [$Ru_3(CO)_{12}$] as the pre-catalyst, revealed that 1-butyl-2,3-dimethylimidazolium acetate (BMMI.OAc) offer the best performance in terms of turnovernumber (TON) and turnovernumber frequency (TOF). Under optimised conditions, a TON of up to 17,000 and TOF of up to 300 h^{-1} was obtained. Thereafter, the thermodynamic effects of BMMI.OAc as an additive were investigated, see **publication I**, **table 1**.

4.2.1. Thermodynamic effect of ionic liquids onto the hydrogenation of CO_2 to formic acid

In a first step the effect of temperature onto the reaction outcome was tested. Here an exponential decay for the achieved concentration of formic acid in the temperature range in between 60°C and 100°C was observed, see **publication I**, **Figure 4b**, whilst below 60°C a plateauing of the achieved concentration was observed. This indicates that [Ru_3CO_{12}] reaches the thermodynamic equilibrium at temperatures higher than 60°C, whilst at lower temperatures the catalyst deactivates prior reaching the thermodynamic equilibrium. However, in order fully validate these experiments and to disregard catalyst deactivation at temperatures higher than 60°C, the decomposition of formic acid should also be evaluated under elsewise

identical reaction conditions (i.e. under $P(H_2) = P(CO_2) = 20$ bar in the presence of BMMI.OAc). Assuming that the thermodynamic equilibrium was reached, in **publication I** a van't Hoff plot for the determination of thermodynamic parameters was produced. This was achieved by straight forward mathematical transformations to obtain the equilibrium constant, (see publication I, SI for more details) (**figure 4.1a**).

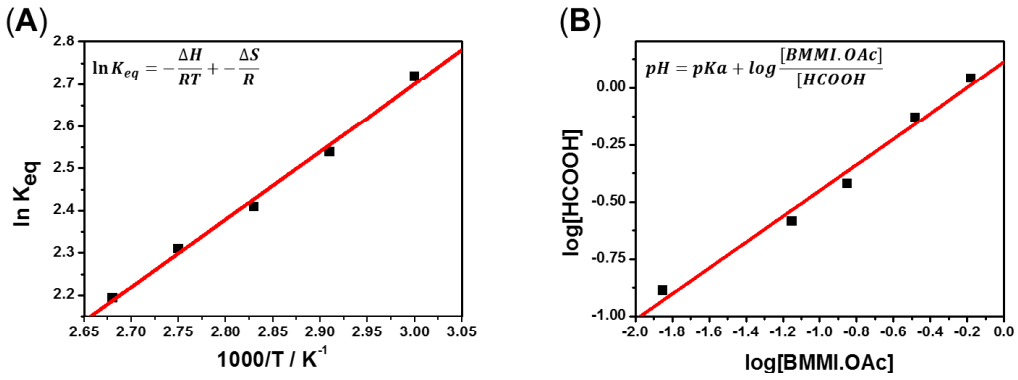


Figure 4.1 a) Van't Hoff plot obtained from the linear relationship between ln K_{eq} and T^{-1}. Reaction conditions: $[Ru_3(CO)_{12}]$ (7.8 μmol) BMMI.OAc IL (3.3 mmol), CO_2/H_2 (1:1, 40 bar), T= 60 °C, t= 72 h, DMSO/H_2O (5 v/v%). (ΔH= -13.26±0.65 kJ mol^{-1}; ΔS= -17.4±1.8 kJ mol^{-1}); **b**) Double logarithmic dependence of the concentration of FA as a function of the concentration of IL employed. Reaction conditions: 60°C, 5 mL DMSO/water (5 v/v% water) at $P_{H2} = P_{CO2}$ = 20 bar and 7.8 μmol $[Ru_3CO_{12}]$ t = 72 h.

From the van't Hoff plot an enthalpy of -13 kJ mol^{-1} can be obtained (**figure 4.1a**). This indicates that formic acid is only stabilised by one additional H-bond compared to the pure solvent system (in DMSO:H_2O with 5 v/v% H_2O a enthalpy of -10 kJ mol^{-1} has been reported).[1] Furthermore, formate salt formation can be excluded as under basic conditions the enthalpy of this reaction has been described to fall to values in between -28 kJ mol^{-1} and -84 kJ mol^{-1}.[2]

The nature of the stabilisation observed with BMMI.OAc for the formation of formic acid can further demonstrated by varying the amount of IL used for the reaction. This variation produced a double logarithmic relationship in between the concentration of IL in the system and the achieved concentration of formic acid (**figure 4.1b** and **publication I**, **figure 4a**). Mathematically, buffering systems are described by the Henderson-Hasselbach equation which would produce a linear relationship in between the employed buffer and the formed acid on log-log scale. The observed double logarithmic relationship might be related to the stabilisation of the pH of the reaction media at higher values as in the absence of IL and thereby protecting the active hydride from deactivation *via* protonation. It is important to note that this effect is solely a kinetic effect and not a thermodynamic one, however it demonstrates the beneficial role of the IL in comparison to unmodified conditions.

Furthermore, the favourable thermodynamic properties have beneficial effects onto the reaction parameters, such as pressure, solvent and separation of the product.

Utilization of favourable thermodynamic properties of ionic liquids in the hydrogenation of CO_2 to formic acid

In **figure 4.2a** a plausible interaction in between the FA and BMMI.OAc is depicted. The main stabilising force can be contributed to the acetate counterion, building H-bonds with FA and stabilising the pH at tolerable values. The cation, 1-butyl-2,3-dimethylimidazolium was chosen, because of its unreactive nature, thus preventing coordination to the catalyst, see also **publication I**, **table 1, entry 10 & 13-15**.

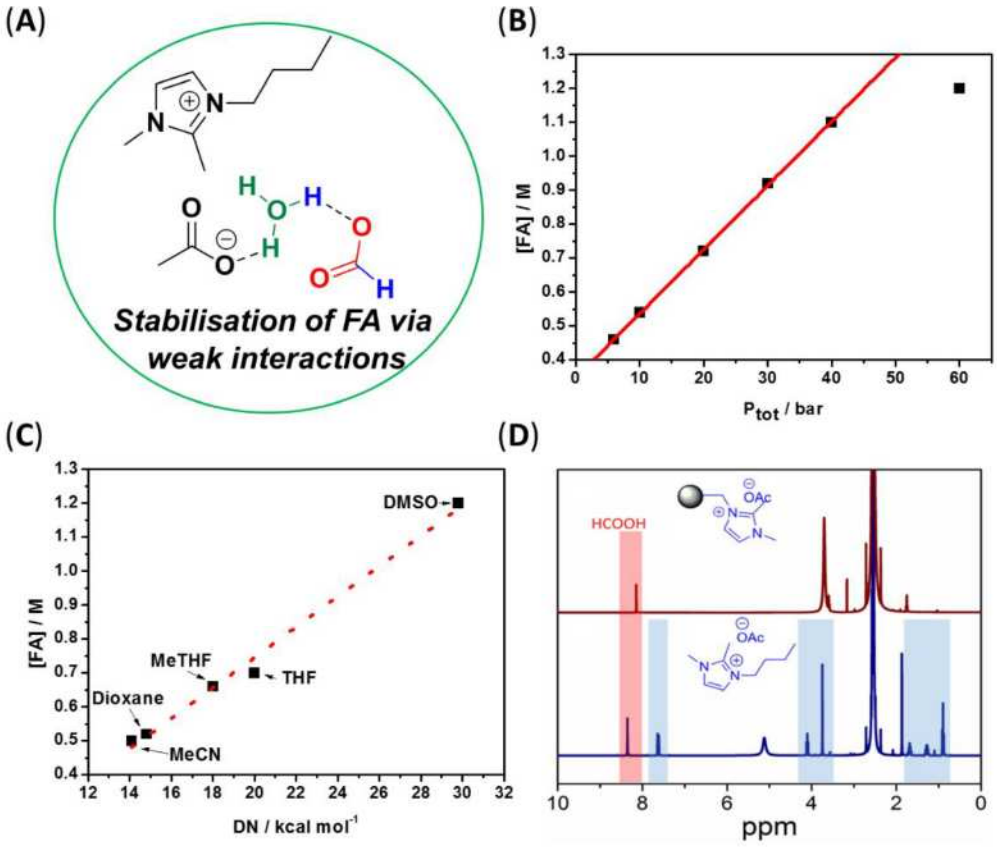


Figure 4.2 (**A**) Plausible interaction of formic acid with water and BMMI.OAc; (**B**) concentration of FA achieved vs. total pressure at 60°C in 5 mL DMSO/water (5 v/v% water) with 3.3 mmol BMMI.OAc and 7.8 µmol [Ru_3CO_{12}] after t = 72 h, **see also figure 5 publication I**; (**C**) concentration of FA achieved as a function of the solvent at T = 60°C with 1.6 µmol [Ru_3CO_{12}] in 5 mL solvent (always 5 v/v% H_2O) with 3.3 BMMI.OAc under P_{H2}=P_{CO2}= 30 bar, see also **see also table 2 publication I** ; (**D**) Comparison of the ^1H NMR spectra after FA synthesis for the reaction employing immobilized IL (top) and the reaction employing homogeneous IL bottom **see also figure 6 publication I**.

The favourable thermodynamic properties of BMMI.OAc in the hydrogenation of CO_2 to formic acid can be exploited to operate the reaction under a broad range of conditions, including at low pressure (**figure 4.2b**). Even at a pressure as low as 6 bar ($P(H_2)$ =$P(CO_2)$ = 3 bar) a high concentration of formic acid (0.46 M) was obtained, which is considerably higher than most reported values in the literature.[1, 3-5] Upon increasing the pressure the yield of formic acid increases (as predicted by Henry's law) linearly, see also **publication I**, **figure**

5. This finding is especially important if it is taken into account that the compression of gas represents one major obstacles for the system to operate economically.[6]

Beneath this beneficial operational window, various organic solvents can be used in the reaction. Interestingly, the concentration of formic acid which can be achieved with varying solvents, seems to be linearly dependent on the donor number (DN) of the solvent (**figure 4.2c**). It is important to note that, the donor number is a descriptor for the lewis acidity/basicity of the solvent (i.e. the ability to coordinate to positively charged lewis acids). Hereby, a higher donor number indicates a higher lewis basicity, thus the linear dependence of the concentration of FA achieved and the donor number might be explainable by the ability of the solvent to form H-bonds, thus stabilising the formic acid by these interactions. Similar effects have already been described to be beneficial for the solvent system DMSO:H_2O (5 v/v% H_2O).[1]

Crucially, the weak thermodynamic stabilisation between the FA and the IL facilitates the separation of the product from an immobilised ionic liquid matrix by simple filtration at the end of the reaction (**figure 4.2d** and **figure 6** in **publication I**). As shown in **table 4.1** a 0.3 M FA concentration in DMSO:H_2O (5 v/v% H_2O) is obtained.

In order to estimate the efficiency of the system the theoretical yield was estimated with the linear relationship in between the concentration of formic acid and the concentration of IL, depicted in **figure 4.1b** (and **figure 4a** in **publication I**). Hereby, it was assumed that the catalyst is deactivated prior reaching the thermodynamic equilibrium. Under the assayed conditions the

theoretical yield (IL concentration = 0.2M) is 0.5 M, thus an extraction efficiency of ca. 60% can be estimated (Note that the resin was not washed with any further solvent to separate FA from the polymer matrix). This finding indicates that ca. 40% of the formed FA remain absorbed into the polymer matrix after the reaction. In order to fully recover the formed FA additional energy must be applied, which could be done by additional amounts of solvent.

Table 4.1 Recylcing experiments with IL immobilised onto a Merrifield resin, see also **publication I Supporting Information section 6**.

Entry	cycle	Metal leaching [a]/ %	FA conc.[b]/ M	TON[c]	Theoretical yield/ %
1	1	27	0.3	112	60
2	2	27	0.3	142	60
3	3	19	0.3	169	60
4	4	14	0.3	193	60
5	5	0.8	0.1	208	20

Reaction conditions: 7.8 µmol [Ru_3CO_{12}], 10 mL DMSO:H_2O (5 v/v% H_2O), T = 60°C P(H2) = P(CO2) = 30 bar, t = 18h 500 mg Merrifield immobised IL, 2 mmol IL; Calculated by measuring the Ru content in the filtrate by ICP-OES and comparing the obtained metal content to the amount of Ru initially in the reaction mixture; b) determined by ^{1}H-NMR with THF as an external standard; c) calculated by dividing the achieved concentration of FA by the concentration (remaining) in the reaction mixture.

No leaching of the IL was observed, thus the utilisation of ILs in the hydrogenation of CO_2 to formic acid might present an attractive path for plausible industrial process schemes. Indeed, the system was re-utilised 4 times without loss of activity. However, the catalyst used in this hypothetical process should be co-immobilised in order to prevent leaching (as observed with [Ru_3CO_{12}]) and subsequent decomposition of formic acid during

purification steps. In the case with [Ru_3CO_{12}] as the catalyst, the activity dropped at the 5th cycle, thus confirming the loss of catalyst during each reaction cycle. **Table 4.1** summarises the aforementioned recycling experiments.

4.2.2. Kinetic and mechanistic implications of BMMI.OAc as an additive in the hydrogenation of CO_2 to formic acid

As displayed in **publication I figure 2d**, the formation of carbonate was observed during the hydrogenation of CO_2 to formic acid. Consequently, a bicyclic mechanism was proposed for the studied reaction, see **publication I figure 2a** and figure below for the mechanistic cycle.

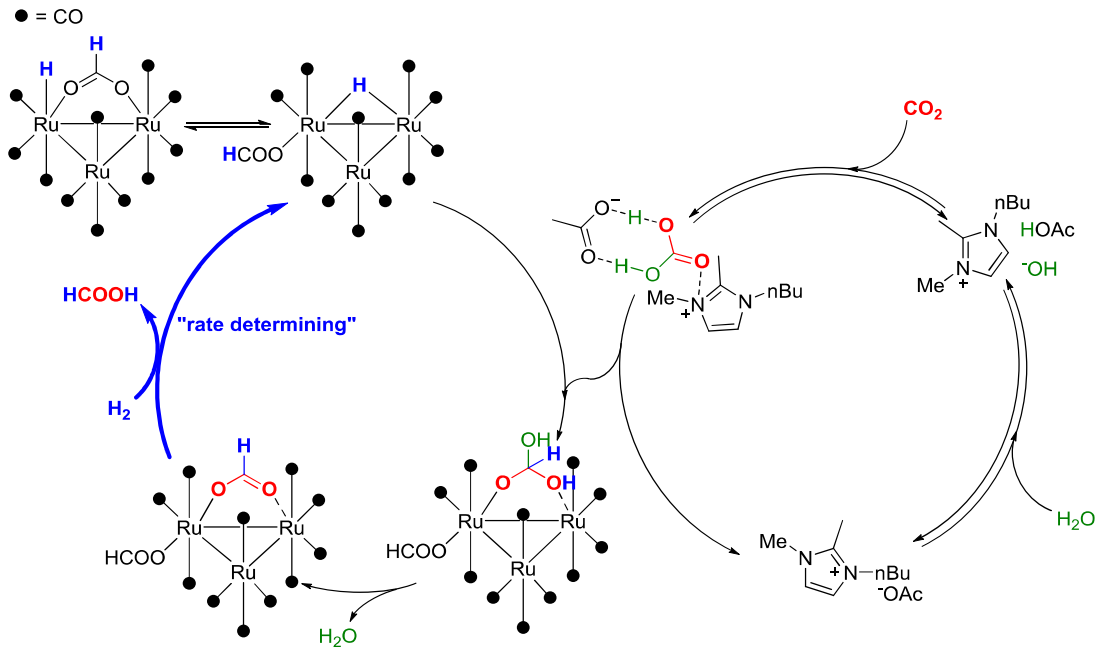


Figure 4.3 Proposed mechanism: In a first step CO_2 is activated by the interplay in between CO_2, BMMI.OAc and H_2O to form carbonate. The carbonate acts as the "true" carbon source for the formation of formic acid.

However, compared to formic acid, CO_2 and hydrogen, carbonates are thermodynamically very stable products (see **Figure 4.4**), hence the hydrogenation of carbonate is an unlikely event. Consequently, carbonate is unlikely to play the role as portrait in **figure 2**, **publication I**.

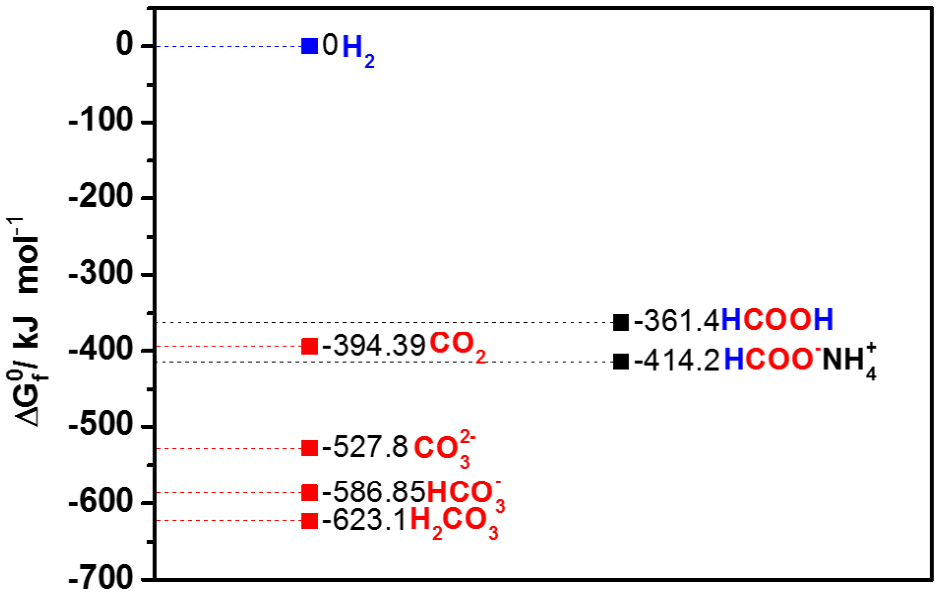


Figure 4.4 Standard molar Gibbs free energy change of formation at 298 K of H_2, CO_2, CO_3^{2-}, HCO_3^-, H_2CO_3, formic acid and ammonium formate.[7]

Furthermore, the hydrogenation of carbonate would involve the intermediate formation of a reactive orthoformate anion ($HC(OH)O_2^{2-}$), see **figure 4.3** and **figure 4.5** In order to assess this reaction path, the hydricity determination of intermediates could be used (see also ***section 1.2.2***). Unfortunately, the hydricity of orthoformate $\Delta G_{H^-}(HC(OH)O_2)$ is not known. Instead, $\Delta G_{H^-,eff}$ has been estimated by the determination for a C-O bond cleavage ($\Delta G^0(OH)$) and C-H bond formation $\Delta G_{H^-}(HCO_2)$, see **figure 4.5**.[8]

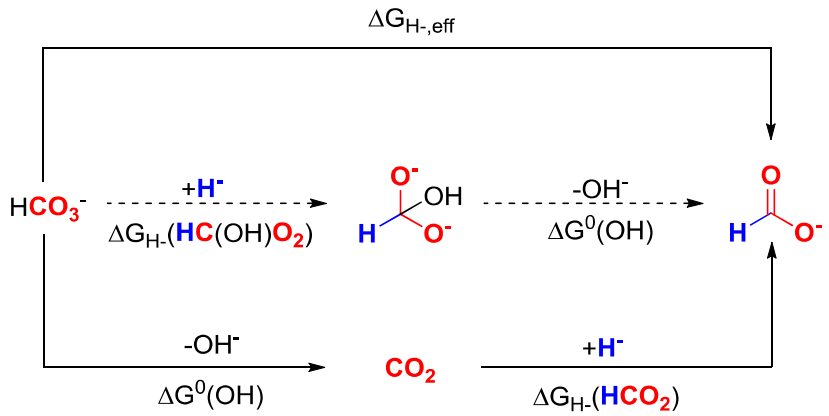


Figure 4.5 Plausible pathway for the hydrogenation HCO_3, with corresponding thermodynamic parameters describing each transformation.[8]

As $\Delta G^0(OH)$ is a pH dependent function, $\Delta G_{H-,eff}$ for the hydride transfer to carbonate is also pH dependent and Wiedner et al have described $\Delta G_{H-,eff}$ as $\Delta G_{H-,eff}$ = -34.8 kcal mol^{-1} + (1.364·pH) kcal mol^{-1}.[8] Accordingly, HCO_3^- is a better hydride acceptor at pH<7.8, whilst CO_2 is the better hydride acceptor at pH>7.8 (Note: $\Delta G_{H-}(HCO_2)$ = -24 kcal mol^{-1}).[8] However, as the hydricity of the intermediate orthoformate anion $\Delta G_{H-}(HC(OH)O_2)$ is not known, the assessment of the kinetic barrier for the transformation of HCO_3^- to $HC(OH)O_3^{2-}$ and finally to HCO_2^- is challenging. Furthermore, all values introduced here are determined in aqueous solutions, and the effect of DMSO and BMMI.OAc on these values are not known. However, both, DMSO and BMMI.OAc, represent relatively basic compounds, thus the effective pH of the system can be estimated to be relatively high.

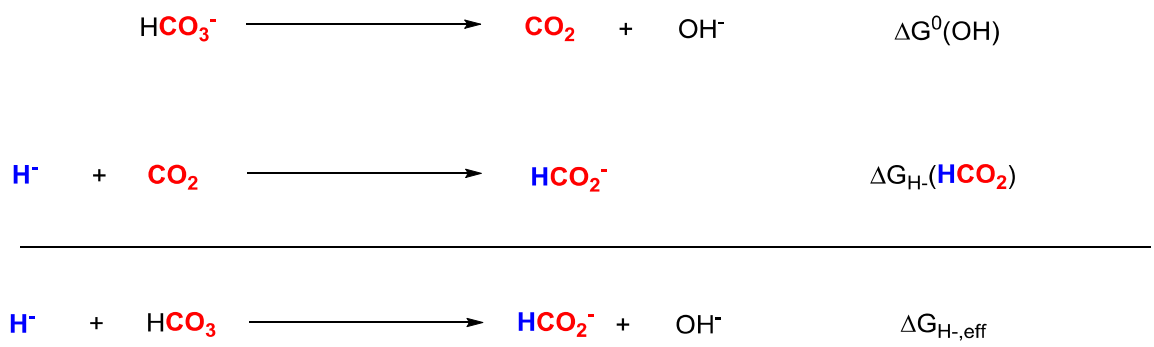


Figure 4.6 Depiction of the thermochemical cycle to determine $\Delta G_{H^-,eff}$ for the transformation of carbonate to formate.[8]

As a result, four scenarios could be imagined as the role for carbonate; a) it could act as a weak base, deprotonating an intermediate H_2 complex and act as CO_2 reservoir; b) it could induce H-bonds stabilising formic acid; c) it could not be participating in the transformation in any means and just constitute of an side reaction of the studied transformation or; d) being the hydride accepting species, although the last case is the least likely one due to high thermodynamic demands, see **figure 4.4**.[7]

It is important to note that, the catalytically active species are only formed in the presence of IL and H_2, as evidenced by separate experiments. The interplay between hydrogen, the ionic liquid and $[Ru_3CO_{12}]$ resulted in the simultaneous formation of a bridged hydride and the hydration of a CO ligand to a formate ligand. In the absence of IL, a dihydridic species is formed, whilst no hydrolysis of a CO ligand was observed. For further information the reader is referred to **publication I**.

4.3. Concluding remarks on the utilization of ionic liquids as additives for the hydrogenation of CO_2 to formic acid

This part demonstrated that ionic liquids can be used to buffer the reaction mixture and thus shift the thermodynamic equilibrium to the product side. However, future studies should test the system in the dehydrogenation of formic acid under elsewise identical conditions to test whether the catalyst reaches the thermodynamic equilibrium. Nevertheless, it can be concluded that the utilisation of ionic liquids represents an attractive alternative to basic conditions, where formate salts and adducts are formed. At the same time the buffering properties allow catalyst to operate this reaction with high efficiency, because the depletion of the active species is prevented. Furthermore, the weak interactions in between the ionic liquid and formic acid, (i.e. no formate salt of formate adduct formation), the product can be separated by simple filtration of the reaction media, if the IL is immobilised onto a polymer matrix.

However, the leaching of the catalyst from the polymer matrix was observed. In order to operate this reaction in an economically feasible fashion, it would be desirable to immobilise the catalyst to prevent decomposition of formic acid during the product purification. Consequently, in the first step heterogeneous RuFe-nanoparticles were investigated. The next chapter summarizes the results obtained with these bimetallic nanocatalysts.

4.4. Experimental

4.4.1. Synthesis of IL immobilized onto a Merrifield resin

A precise synthetic protocol can be found in **publication I**, **SI section 5**. Here a general overview for the synthesis of IL immobilised onto a Merrifield resin is given (information on the Merrifield resin can be found in **publication I**, **SI General information**).

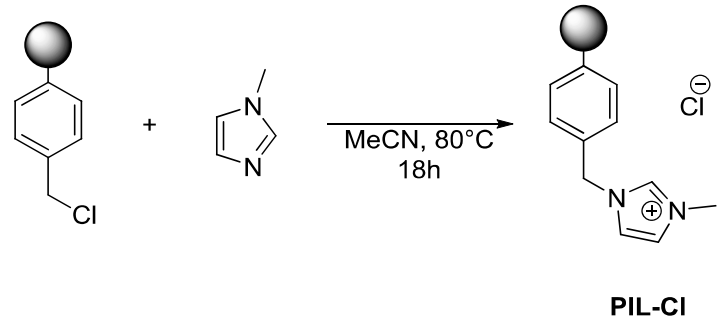
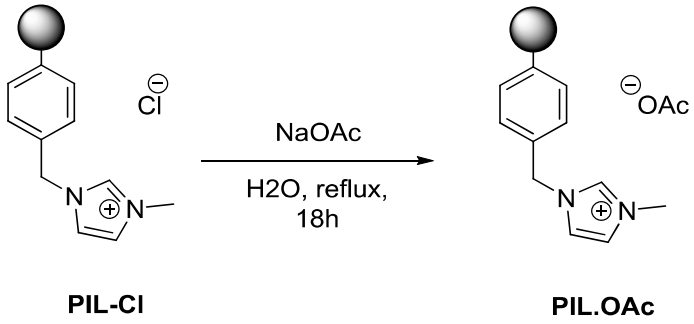


Figure 4.7 Reaction scheme for the synthesis of PIL-Cl.

In a first step a commercially available Merrifield resin was transformed to the corresponding **PIL-Cl** at 80°C in MeCN with excess amounts of 1-methylimidazole. The crude product was separated by simple filtration and washed extensively with MeCN, H_2O and THF to remove excess amounts of 1-methylimidazole. It is important to note that the product is hygroscopic and tends to swell in polar solvents. Solvent residues were removed in vacuum to give the product as a white powder; IR analysis can be found in **publication I**, **SI section 5**.



PIL-Cl **PIL.OAc**

Figure 4.8 Reaction scheme for the synthesis of PIL.OAc.

In the second step the counteranion was exchanged to AcO^- with excess amounts of NaOAc in H_2O under reflux. The obtained solid was washed extensively with MeCN, H_2O and THF to give a white product, which was dried in vacuum, see **publication I**, **SI section 5.2** for further information. The in this way obtained **PIL.OAc** was impregnated with $[Ru_3CO_{12}]$, by stirring both compounds in THF, followed by removal of the solvent in vacuum, see **publication I**, **SI section 5.3** for further information.

The impregnated **PIL.OAc** was loaded into a Parr reactor, DMSO:H_2O (5 v/v% H_2O) was added, the system pressurized with CO_2 and H_2 (30 bar each), giving a total pressure of 60 bar, the reactor heated to 60°C and the reaction mixture was agitated under hard stirring. After 18h the reactor was cooled to room temperature, carefully vented and the obtained reaction mixture filtered, using conventional filter paper and a funnel. The obtained liquid phase was analysed via ^{1}H-NMR and ICP-OES, whilst the filtrate was dried in vacuum and then directly used for consecutive cycles, see **publication I**, **SI section 6** for further information.

4.5. Publication I Supporting Information: Selective CO_2 hydrogenation to formic acid with Multifunctional Ionic Liquids.

Contribution of the author: The author drew the research plan and synthesized all the ionic liquids and planned and conducted all the experimental work in this publications. The author furthermore contributed in to the preparation of the manuscript.

Reprinted with permission from *ACS Catal.* **2018**, 8, 3, 1628-1634 Copyright 2018 American Chemical Society.

Supporting information

Selective CO_2 hydrogenation to formic acid with multifunctional ionic liquids

Andreas Weilhard,[†¥] Muhammad I. Qadir,[‡] Victor Sans *[†¥] and Jairton Dupont*[†‡]

[†]GSK Carbon Neutral Laboratories for Sustainable Chemistry, University of Nottingham, NG7 2GA, Nottingham, UK

[‡]Institute of Chemistry–UFRGS–Av. Bento Gonçalves, 9500, Porto Alegre, 91501-970, RS, Brazil

[¥]Faculty of Engineering, University of Nottingham, NG7 2RD, Nottingham, UK

E-mail: jairton.dupont@ufrgs.br; victor.sanssangorrin@nottingham.ac.uk

Table of Contents

1 LITERATURE S2

2 GENERAL EXPERIMENTAL INFORMATION S2

2.1 KINETIC ISOTOPIC EXPERIMENTS AND EFFECT OF WATER CONTENT S3

2.2 ELUCIDATING CATALYTIC INTERMEDIATES S4

2.3 DETERMINATION OF THE ACTIVATION BARRIER E_A S5

2.4 CO_2 HYDROGENATION VS IONIC LIQUID AMOUNT EFFECT S6

3 EQUILIBRIUM CONSTANT (K_{EQ}) S7

4 REACTION RATE DEPENDENCE FROM PRESSURE S12

5 IMMOBILISED IONIC LIQUID S13

5.1 IMMOBILISATION OF 1,2-DIMETHYLIMIDAZOLE ONTO MERRIFIELD RESIN S13

5.2 ION EXCHANGE OF PIL-CL WITH NAOAC S13

5.3 IMPREGNATION OF FUNCTIONALISED MERRIFIELD RESIN WITH $[Ru_3(CO)_{12}]$ S14

6 HYDROGENATION OF CO_2 IN THE PRESENCE OF IMMOBILISED IL S14

7 DECOMPOSITION OF FORMIC ACID S15

8 CATALYTIC HYDROGENATION OF CO_2 ..... S15

9 REFERENCES S16

1 Literature

Table S1: Summary of homogeneous CO_2-hydrogenation systems to prepare free formic acid (HCO_2H) by different catalysts from literature

Entry	Cat.	H_2/CO_2	Solvent	$[HCO_2H]$ / M	TON	TOF / h^{-1}	Ref
1	$[Ru_2Cl_2(PTA)_4]$	1:1 (100 bar)	DMSO	1.9	749	7.34	1
2	$[Ru(Acriphos)(PPh_3)(Cl)(PhCO_2)]$	2:1 (120 bar)	$DMSO/H_2O$	0.33	4200	260	2
3	$[(\eta^6C_6Me_6)Ru^{II}(L)(OH_2)SO_4]$	2.5:1 (80 bar)	Acidic conditions	-	55	-	3
4	$[(CpIr^{III}(L)(OH_2)]$	1:0.73 (95 bar)	Citrate Buffer	-	18	-	4
5	$[RhCl(mtppms)_3]$	1:1 (100 bar)	H_2O/HCO_2Na	0.13	-	-	5
6	$[Ru(cod)(methally)_2]$	1:1 (50 bar)	Basic IL	0.54	599	314	6
7	**$[Ru_3(CO)_{12}]$**	**1.33:1 (70 bar)**	**$DMSO/H_2O$ IL BMMI.OAc**	**1.2**	**17000**	**102**	**This work**
8	**$[Ru_3(CO)_{12}]$**	**1:1 (60 bar)**	**$DMSO/H_2O$ IL BMMI.OAc**	**1.1**	**6875**	**300**	**This work**

2 General experimental information

All the ionic liquids (1,2-dimethyl-3-butylimidazolium acetate, 1,2-dimethyl-3-butylimidazolium chloride, 1,2-dimethyl-3-butylimidazolium formate, 1,2-dimethyl-3-butylimidazolium imidazolate, 1-Butyl-3-methylimidazolium acetate, *n*-tetrabutylammonium acetate) were prepared from literature methods.[7] $[Ru(Cl)_2(CO)_2]_n$ complex was synthesized according to a reported method.[8] 1,2-dimethylimidazole, Imidazole and 2-methylimidazole were purchased from IOLITEC while *n*-chlorbutane, sodium acetate, tetrabutylammonium chloride, dimethylsulfoxide, deuterated dimethylsulfoxide and Merrfield's peptide resin (mesh 100-200; 3.5-4.5 mmol g^{-1} Cl^- functionalised; 1% cross-linked) were obtained from Sigma Aldrich. $RuCl_3 \cdot xH_2O$ was provided by Precious Metals Online; $[Ru_3(CO)_{12}]$ was from Acros Organics. All the ILs were placed under vacuum at 50 °C for 2-3 h prior to use. NMR measurements were performed on a 400 MHz Bruker with d1 = 50s and ESI-MS analysis was performed on a Bruker microTOFII.

2.1 Kinetic isotopic experiments and effect of water content

A Parr reactor (50 mL) was loaded with the 5 mg [$Ru_3(CO)_{12}$] and 700 mg BMMI.OAc (3.3 mmol). Then DMSO and water with varying ratios (giving a total volume of 5 mL) was introduced into the reactor. The reactor was flushed with CO_2 gas in order to remove the air. Afterwards, the reactor was filled with 20 bar CO_2 and 20 bar H_2 gas, till the desired total pressure of 40 bar was reached at room temperature. The reaction was conducted at 50°C using a heating mantle under vigorous stirring. After the 4h, the reactor was cooled down to room temperature and carefully vented. The reaction mixture was analysed directly by ^{1}H NMR spectroscopy in DMSO-d_6 to determine the amount of formic acid formed.

Table S2. Hydrogenation of CO_2 to FA with varying water contents. The experiments were performed at 50°C with reaction duration of 4h, with 7.8 μmol of [$Ru_3(CO_{12})$] catalyst and 3.3 mmol BMMI.OAc (0.66M) with $P_{CO2} = P_{H2} = 20$ bar.

Entry	DMSO:H_2O (v/v% H_2O)	TON	TOF / h^{-1}
1	2.5	136	34
2	5	160	40
4	10	136	34
5	12.5	116	29
6	20	40	10

The kinetic isotopic effects were studied with an analogous protocol to the abovementioned, with varying experimental conditions. The solvent mixtures were prepared by combining 5.24 mL of DMSO (67 mmol) and 0.24 mL of water (13.2 mmol) or 0.24 mL D_2O (11.9 mmol). The gas mixture employed consisted of 20 bar CO_2 and 40 bar H_2 gas, to yield a total pressure of 60 bar reached at room temperature. The reaction was conducted at 60°C. After the 4h, the reactor was cooled down to room temperature and carefully vented. The reaction mixture was analysed directly by ^{1}H NMR spectroscopy in DMSO-d_6 to determine the amount of formic acid formed.

Table S3. D_2O experiments; each entry represents the average of 2 separate runs. The deviation was less than 5% for each run. The experiments were performed at 60°C with reaction duration of 4h.

Entry	Cat.	Cat. / μmol	Solvent system	IL / [M]	P_{H2} / bar	P_{CO2} / bar	TON	TOF / h^{-1}
1	[$Ru_3(CO_{12})$]	7.8	DMSO:H_2O (5 v/v% H_2O)	BMMIm.OAc (0.66)	40	20	472	118
2	[$Ru_3(CO_{12})$]	7.8	DMSO:D_2O (5 v/v% D_2O)	BMMIm.OAc (0.66)	40	20	349	87

2.2 Elucidating catalytic intermediates

A Parr reactor (50 mL) was loaded with 200 mg of BMMI.OAc (0.94 mmol, 6 eq) and 100 mg of [$Ru_3(CO)_{12}$] (0.15 mmol, 1 eq) and DMSO:water mixture (5 v/v% water; DMSO= 5.27 mL (67 mmol) , H_2O= 0.24 mL (13.2 mmol)) was added. Then the reactor was charged with 30 bar H_2 and heated to 60°C and stirred for 24 h. The obtained reaction mixture was analysed via ^{1}H-NMR, ^{13}C-NMR and ESI-MS. Two new singlets can be observed at 8.36 ppm and -19.48ppm in ^{1}H-NMR. Furthermore, a hydride signal can be seen at -12.72 ppm which can be assigned to a terminal hydride complex. The ^{13}C-NMR gives a new signal at 165ppm and ESI-MS reveals a mass of 659 m/z proposed complex structures are depicted in the figures below.

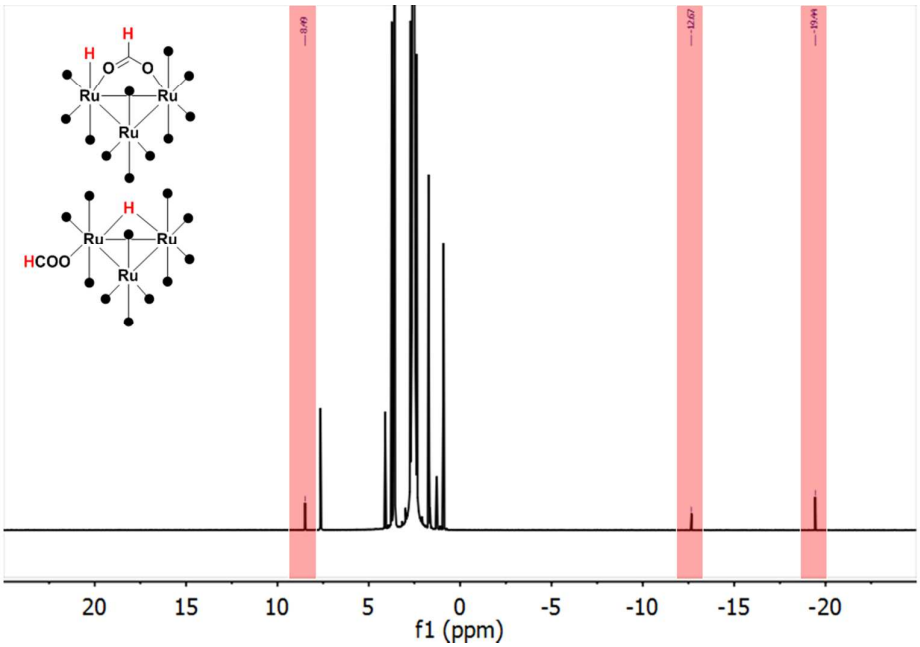


Figure S1. ^{1}H NMR of reaction mixture represents hydrides species at –19.48 ppm and –12.72 ppm.

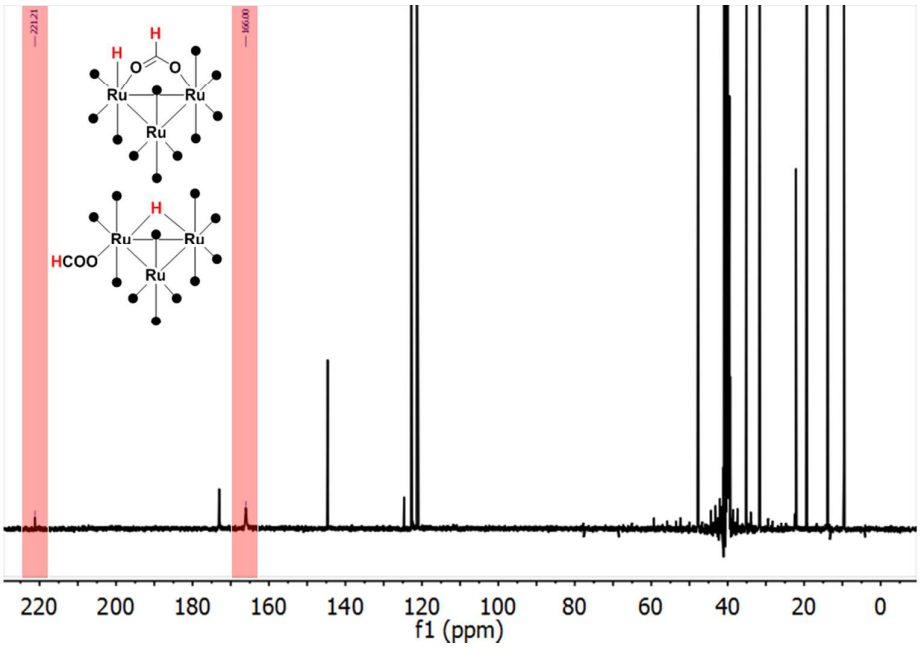


Figure S2.[13]C NMR of reaction mixture represents carbonyl species at 165.56 ppm.

2.3 Determination of the activation barrier E_a

For the Arrhenius plot, the initial TOF was measured at various temperatures. The Parr reactor (50 mL) was loaded with 5 mg (0.0078 mmol, 1 *eq*) of $[Ru_3(CO)_{12}]$ and 700 mg (3.3 mmol, 420 *eq*) of BMMI.OAc. Then DMSO:water (5 v/v% water, DMSO= 5.27 mL (67 mmol) , H_2O= 0.24 mL (13.2 mmol)) mixture was added, flushed with CO_2 to remove air, charged with 20 bar CO_2 and filled with H_2 till 40 bar total pressure. The reaction mixture is heated till the desired reaction temperature and stirred for 4h. The reaction mixture was analysed via ^{1}H-NMR. The TOF is given as the ratio between the amount of formic acid formed and the catalyst amount divided by 4h (14400 s). Plotting the logarithmic TOF in s^{-1} against the inverse temperature in K^{-1} gives a linear system as shown in equation below.

$$\ln TOF = \ln A - \frac{E_a}{RT}$$

As shown in the equation above, by multiplying the slope with the negative gas constant $-R$ one easily derives the activation energy E_a. The intercept describes the logarithmic pre-exponential factor $\ln A$. The table below depicts the results obtained with the Arrhenius plot.

Table S4. Results from the Arrhenius plot.

Slope/K	Intercept	E_a/kJ mol^{-1}	ln A
-7088 ± 495	16.3 ± 1.5	58 ± 4	16.3 ± 1.5

2.4 CO_2 hydrogenation vs ionic liquid amount effect

The effect of the IL during CO_2 hydrogenation was investigated. The maximum amount of formic acid formed during the CO_2-hydrogenation was determined at varying IL-concentrations. A non-linear relation in between FA/ IL ratio and the IL concentration can be observed. For instance, a ratio of 9:1 can be achieved at an IL concentration of 14 mM. Then the ratio decreases in an exponential fashion reaching 3:1 at 140 mM and finally 1.5:1 at 0.66M BMMI.OAc IL. It can be concluded that the IL acts in contrast to systems containing bases, such as amines or hydroxides, rather as a buffer than as a classical base. Indeed systems containing bases form classically formate adducts and the amount of formate is in linear relation to the utilised base.[9] Indeed, it is very likely that the buffering properties of the acetate IL functions as a buffer protects the catalyst from deactivation via protonation. Furthermore the concentration of formic acid achieved during the reaction is almost the same as previously described in literature[2], though much milder conditions were applied. Therefore, it can be assumed that the ionic liquid is not only playing a crucial role as a buffer, but is also be involved into shifting the equilibrium to formic acid.

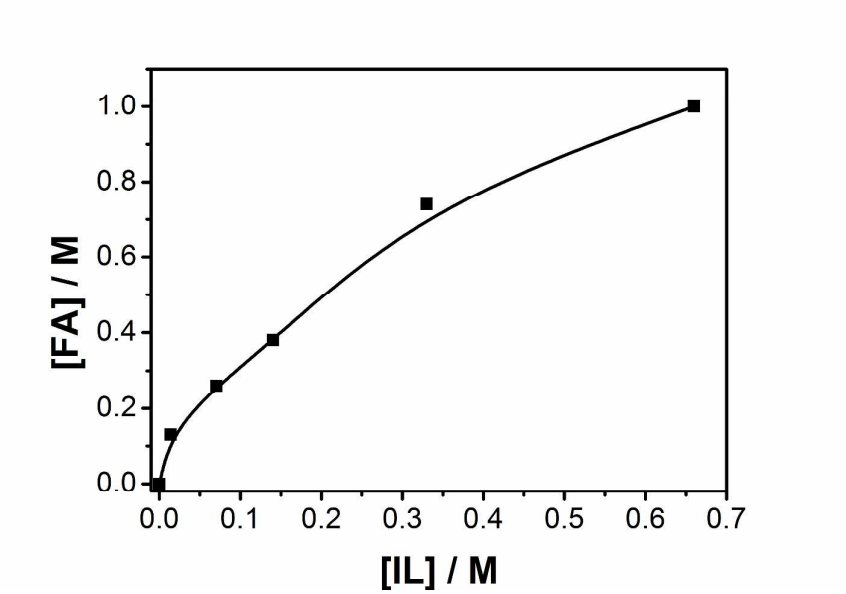


Figure S3. Dependence of formic acid concentration to BMMI.OAc IL concentration. Reaction conditions: $[Ru_3(CO)_{12}]$= 7.8 mmol, CO_2/H_2 (1:1, 40 bar), DMSO/water (5 v/v% water); DMSO= 5.27 mL (67 mmol) , H_2O= 0.24 mL (13.2 mmol), Time= 4h, and 60°C.

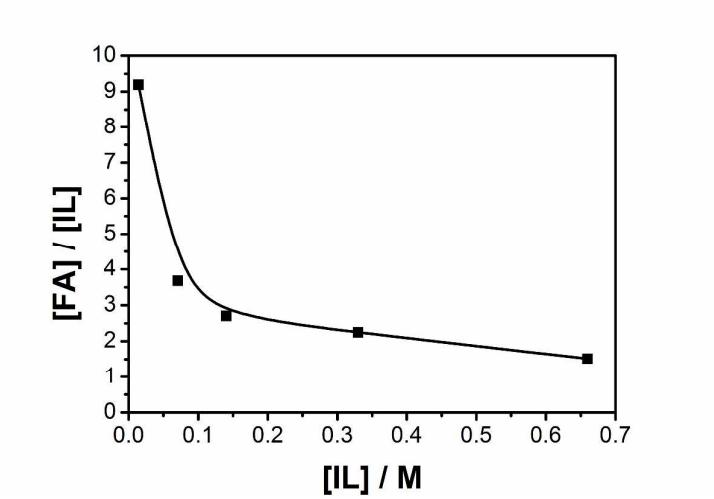
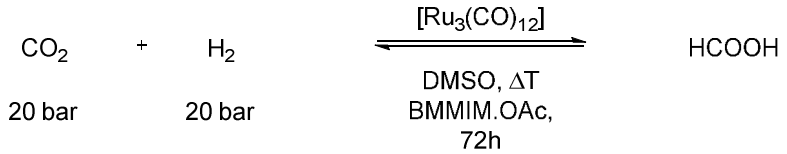


Figure S4. Dependence of the molar ration of formic acid to BMMI.OAc IL concentration. Reaction conditions: $[Ru_3(CO)_{12}]$= 7.8 mmol, CO_2/H_2 (1:1, 40 bar), DMSO/water (5 v/v% water); DMSO= 5.27 mL (67 mmol) , H_2O= 0.24 mL (13.2 mmol), Time= 4h, and 60°C.

3 Equilibrium constant (K_{eq})

In order to identify the equilibrium constant K_{HCOOH}, the reaction was performed as described above. The reaction was conducted for 72 h at various temperatures, as indicated in the scheme below.



Scheme S1. Hydrogenation of CO_2 to formic acid

Calculations according to literature procedure.[10]

The system of interest is defined by a liquid phase and gas phase. Whilst the catalytic reaction takes place in solution so does the gas phase function as a reservoir for the reagents CO_2 and H_2.

The equilibrium constant K_{eq} for the hydrogenation of CO_2 to HCOOH is in liquid phase is defined by equation 1. In equation 1, brackets symbolise the concentration and subscripts define the phase in which the compound is situated,

$$K_{eq} = \frac{[HCOOH]}{[CO_2]_{aq} \cdot [H_2]_{aq}} \quad (1)$$

But in order to calculate the equilibrium constant in a closed system, where partial amounts of gas is consumed the reaction quotient Q_{HCOOH} has to be considered, which is defined as:

$$Q_{HCOOH} = \frac{x_{HCOOH}}{x_{CO2} x_{H2}} \quad (2)$$

In equation 2, x_{HCOOH}, x_{CO2} and x_{H2} are the yield fractions of the formic acid, CO_2 and H_2.

The equilibrium constant and the reaction quotient in equilibrium are interrelated by equation 3,

$$K_{eq} = \frac{\beta_{HCOOH}}{\beta_{CO2} \cdot \beta_{H2}} \, Q_{HCOOH} (3)$$

The factors β_{HCOOH}, β_{CO2} and β_{H2} are the activities of formic acid, CO_2 and H_2 and are defined by equation 4.

$$\beta = \frac{moles\ of\ HCOOHC, CO_2, H_2 in\ the\ liquid\ phase}{total\ moles\ of\ HCOOH, CO_2,\ H_2} (4)$$

If we assume that formic acid is solely present in the liquid phase equation 3 simplifies to equation 5, where V_l is the volume of the liquid phase and n_{tot} is the amount of compounds in the system.

$$K_{eq} = \frac{V_l}{n_{tot}} \frac{1}{\beta_{CO2} \cdot \beta_{H2}} \, Q_{HCOOH} (5)$$

$$K_{eq} = \frac{1}{\beta_{H_2} \beta_{CO_2}} Q_{HCOOH} = \frac{V_l}{n_{tot}} \frac{1}{\beta_{H_2} \beta_{CO_2}} \frac{x_{HCOOH}}{x_{CO_2} x_{H_2}} \quad (1)$$

In equation 1, $x_{HCOOH,}$ x_{CO2} and x_{H2} are the corresponding molar fractions in the liquid phase; β_{CO2} and β_{H2} are the ratios of gases in solution and the total amount of gas in the reactor; n_{tot}

is the total number of moles of reagents in the reactor and V_l is the volume of the liquid phase.

Hence, 1 mol of H_2 and 1 mol of CO_2 react to form 1 mol of HCOOH and the partial pressure of CO_2 and H_2 were equal, x_{HCOOH} can be calculated according to equation 6:

$$x_{HcooH} = \frac{[HCOOH]}{\left([CO2]_l + [CO2]_g \cdot \frac{1-p_t}{p_t}\right) + ([H2]_l + [H2]_g \cdot \frac{1-p_t}{p_t})} (6)$$

But because,

$$n_{CO_2,tot} = n_{H_2,tot} (7)$$

Where $n_{CO_2,tot}$ and $n_{H_2,tot}$ are the total amounts of CO_2 and H_2, it can be written:

$$\left([CO2]_l + [CO2]_g \cdot \frac{1-p_t}{p_t}\right) = ([H2]_l + [H2]_g \cdot \frac{1-p_t}{p_t}) (8)$$

And thus equation 6 simplifies to equation 9:

$$x_{HcooH} = \frac{[HCOOH]}{2\left([CO2]_l + [CO2]_g \cdot \frac{1-p_t}{p_t}\right)} (9)$$

Where the quotient p_t describes the filling factor:

$$p_t = \frac{volume\ of\ the\ lqiuid\ phase\ at\ reaction\ temperature}{total\ volume\ of\ the\ reactor} = \frac{l_T^{liq}}{L} (10)$$

The sum of yield fractions is defined to be 1, as shown in equation 11:

$$x_{H2} + x_{Co2} + x_{HCOOH} = 1 (11)$$

But because the reaction consumes 1 equivalent of CO_2 and 1 mol H_2 to form 1 mol HCOOH and because the initial amounts of gases is equal we can get

$$x_{Co2} = x_{H2} (12)$$

So, we get

$$x_{CO2} + x_{Co2} + x_{HCOOH} = 1$$

$$2x_{CO2} + x_{HCOOH} = 1$$

$$x_{CO2} = \frac{1 - x_{HCOOH}}{2} (13)$$

And

$$x_{H2} = \frac{1 - x_{HCOOH}}{2} (14)$$

As shown in equation, the equilibrium constant can now be denoted as:

$$K_{HCOOH} = \frac{V_l}{n_{tot}} \frac{1}{\beta_{H2}\beta_{CO2}} \cdot Q_{HCOOH} (5)$$

Where n_{tot} is the total amount of reagents in the system and V_l is the volume of the liquid phase. n_{tot} can be calculated by:

$$n_{tot} = ((\left([CO2]_l + [CO2]_g \cdot \frac{1 - p_t}{p_t}\right) + ([H2]_l + [H2]_g \cdot \frac{1 - p_t}{p_t}))V_{tot}$$
$$= 2\left([CO2]_l + [CO2]_g \cdot \frac{1 - p_t}{p_t}\right) V_{tot} = \frac{[HCOOH]}{x_{HCOOH}} \cdot V_{tot} (15)$$

With equation 15 in equation 5 we get equation 16:

$$K_{HCOOH} = \frac{x_{HCOOH} V_l}{[HCOOH] V_{tot} \beta_{H2} \beta_{CO2}} \cdot Q_{HCOOH} (16)$$

Here $\beta_{H2}, \beta_{HCOOH}$ and β_{CO2} are

$$\beta = \frac{moles\ of\ HCOOHC, CO_2, H_2 in\ the\ liquid\ phase}{total\ moles\ of\ HCOOH, CO_2,\ H_2} (4)$$

If the partial pressure is given then the molar concentration of the gases in the liquid phase is given by:

$$[CO_2]_l = \frac{p_{CO2} d_T}{k_{H,CO2}} (16)$$

And

$$[H_2]_l = \frac{p_{H2} d_T}{k_{H,H2}} (17)$$

Where p_{CO2} and p_{H2} are the partial pressure, $k_{H,H2}$ and $k_{H,CO2}$ are the Henry's constants at the reaction temperatures and d_T is the molar concentration of liquid DMSO at given reaction temperature.

The concentration of the gases in the gas phase can be calculated according to the ideal gas law:

$$[CO_2]_g = \frac{p_{CO2}}{RT} (18)$$

And

$$[H_2]_g = \frac{p_{H2}}{RT} (19)$$

With equations 16, 17,18 and 19 in equation 4 the β values can be calculated according to equation 20 and 21:

$$\beta_{CO2} = \frac{[CO_2]_l p_T}{[CO_2]_l p_T + [CO_2]_g (1 - p_T)} = \frac{p_T}{K_D(CO_2)((1 - p_T) + p_T} (20)$$

And:

$$\beta_{H2} = \frac{[H_2]_l p_T}{[H_2]_l p_T + [H_2]_g (1 - p_T)} = \frac{p_T}{K_D(H_2)(1 - p_T) + p_T} (21)$$

Here, $K_D(CO_2)$ and $K_D(H_2)$ are introduced as the liquid-gas distribution given by

$$K_D(CO_2) = \frac{k_{H,CO2}}{RTd_T} = \frac{[CO2]_g}{[CO2]_l} (22)$$

And:

$$K_D(H_2) = \frac{k_{H,H2}}{RTd_T} = \frac{[H2]_g}{[H2]_l} (23)$$

With equation 20 and 21 in equation 16 the equilibrium constant for formic acid K_{HCOOH} can be calculated with equation 24:

$$K_{HCOOH} = \frac{x_{HCOOH} V_l}{[HCOOH] V_{tot}} \cdot \frac{K_D(H_2)(1 - p_T) + p_T}{p_T} \cdot \frac{K_D(CO_2)(1 - p_T) + p_T}{p_T} \cdot Q_{HCOOH} (24)$$

The Henry constant $k_{H,H2}$ and $k_{H,CO2}$ are obtained from literature[11-12]. The molar concentration of DMSO at the reaction temperatures is depicted from reference.[13]

Table S5. Results from the van't Hoff plot.

Slope	**Intercept**	**ΔH [kJ mol^{-1}]**	**ΔS [J K^{-1}mol^{-1}]**
1595±78	-2.09±0.22	-13.26±0.65	-17.4±1.8

It is very important to note that the calculations were performed assuming the ideal gas law for the reagents in gas phase. The Henry constants and molar (volume) concentration assumed to be the same as for pure DMSO.

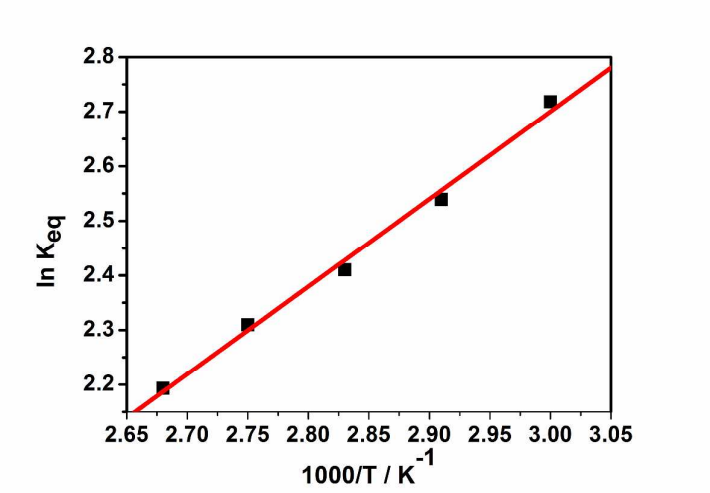


Figure S5. Van't Hoff plot. Reaction conditions: $[Ru_3(CO)_{12}]$ (7.8 μmol) BMMI.OAc IL (3.3 mmol), CO_2/H_2 (1:1, 40 bar), T= 60 °C, t= 72h, DMSO/H_2O (5 v/v%). (ΔH=-13.26±0.65 kJ mol^{-1}; ΔS=-17.4±1.8 kJ mol^{-1}).

4 Reaction rate dependence on pressure

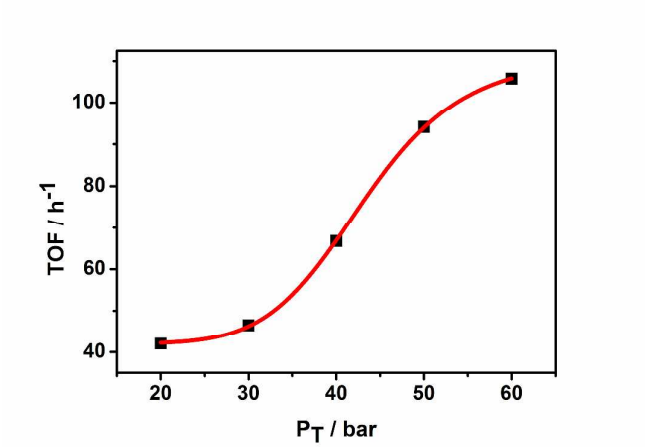


Figure S6. TOF vs total gas pressure of reaction). All the reactions were conducted for 4h at 60 °C, BMMI.OAc IL (0.66 M), $[Ru_3(CO)_{12}]$ (7.8 μmol) and DMSO/H_2O (5 v/v%; DMSO (5.24 mL, 67 mmol), H_2O (0.24 mL, 13.2 mmol).

5 Immobilised ionic liquid

5.1 Immobilisation of 1,2-dimethylimidazole onto Merrifield resin

In a round bottom flask with condenser and stirrer bar, 384 mg 1,2-dimethylimdazole (4 mmol, 2 eq) and 500 mg of Merrifield's peptide resin (2 mmol Cl functionalized, 1 eq) are mixed in MeCN and stirred at 80°C for 18h. The mixture is filtered and the remaining solid is consecutively washed with 500 mL MeCN and 500 mL water and 500 mL THF. The solid residue is dried in vacuum for 24h at 40°C, giving a white solid (PIL-Cl). The changes observed in the ATR-IR spectra (Figure S7) are in agreement with literature reports.[14] ATR-IR(cm^{-1}): 3360, 3025, 2921, 1585, 1325, 1025, 750, 699, 550.

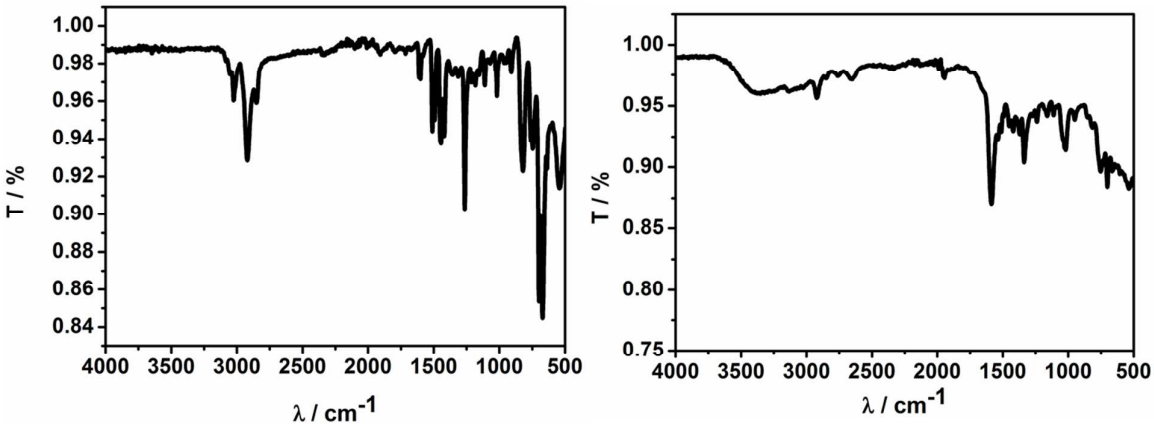


Figure S7. IR-Spectra of unfunctionalized Merrifield resin as obtained from sigma Aldrich (left) and Merrifield resin functionalized with 1,2-dimethylimidazolium chloride (right).

5.2 Ion exchange of PIL-Cl with NaOAc

In a round bottom flask with condenser and stirrer bar the functionalised Merrifield resin (PIL-Cl) and 20 g NaOAc (0.3 mmol, 10 eq) are mixed in 70 mL distilled water and heated under refluxed for 18h. The white solid is filtered and consecutively washed with 1L water, 500 mL THF and 500 MeCN and dried in vacuum for 24 h at 40°C to give the hygroscopic product (PIL.OAc). The IR spectra (Figure S8) is in agreement with literature reports.[14] ATR-IR(cm^{-1}): 3300, 3025, 2921, 1560, 1395, 1335, 1235, 1025, 700, 650, 550.

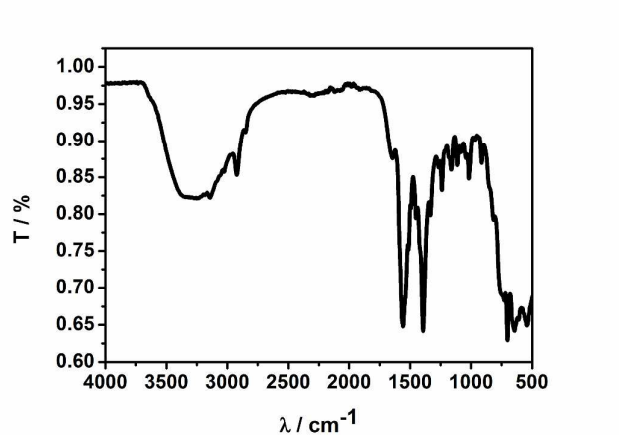


Figure S8. IR-Spectra of Merrifield resin functionalized with 1,2-dimethylimidazolium acetate.

5.3 Impregnation of functionalised Merrifield resin with $[Ru_3(CO)_{12}]$

5 mg $[Ru_3(CO)_{12}]$ (0.0078 mmol, 1 eq) is dissolved in 5 mL THF and 500 mg PIL.OAc (2 mmol functionalised with IL, 256 eq) is added. The solvent is slowly evaporated to give an orange solid.

6 Hydrogenation of CO_2 in the presence of immobilised IL

505 mg of the impregnated PIL.OAc is added to a Parr reactor, 10.48 mL DMSO and 0.48 mL water is added, the reactor sealed and charge with 30 bar CO_2 and filled with H_2 to 60 bar. The reaction mixture is heated to 60 °C and stirred for 18h.

The system is carefully vented and the solution filtered and the filtrate is analysed via ^{1}H-NMR with THF as an external standard. The remaining solid is washed with water and dried in vacuum at 40°C for 5h. The as obtained dry solid is used for consecutive circles, till a drop in FA concentration in the filtrate is observed.

Table S6. Merrifield resin functionalised with 1,2-methylimidazolium acetate and $[Ru_3(CO)_{12}]$. Metal is physisorbed. (Cat amount 5 mg). (500 mg merrifield).

Entry	Cycle	Metal leaching (%)	Solvent	T [°C]	pH2 [bar]	pCO2 [bar]	t [h]	FA conc [M]	TON	TOF [h^{-1}]

1	1	27	DMSO:water (5 v/v% water)	60	30	30	18	0.3	112	6.2
2	2	27	DMSO:water (5 v/v% water)	60	30	30	18	0.3	142	7.9
3	3	19	DMSO:water (5 v/v% water)	60	30	30	18	0.3	169	9.4
4	4	14	DMSO:water (5 v/v% water)	60	30	30	18	0.3	193	10.7
5	5	0.8	DMSO:water (5 v/v% water)	60	30	30	18	0.1	208	11.5

7 Decomposition of formic acid

In a round bottom flask with stirrer bar and condenser a 1.1 M formic acid (5.5 mmol, 0.2 mL, 343 eq) solution in 5 mL DMSO/water (5 v/v% water) is mixed with 10 mg [$Ru_3(CO)_{12}$] (0.016 mmol, 1 eq) in the presence/absence of 700 mg BMMI.OAc (3.3 mmol, 206 eq) and heated to 60°C, respectively 100°C. In regular periods samples are taken and analysed via ^{1}H-NMR. In the absence of BMMI.OAc THF is used as an external standard.

Table S7. Decomposition of formic acid in the presence/absence of 3.3 mmol BMMI.OAc (700 mg, 206 eq) and 10 mg [$Ru_3(CO)_{12}$] (0.016 mmol, 1 eq) in 5 mL DMSO/water (5 v/v%water).

Entry	IL /M	Consumed formic acid/ mmol	t /h	T /°C	TON	TOF /h^{-1}
1	0.66	1.73	48	60°C	108	2.2
2	0.66	3.32	48	100°C	207	4.3
3	-	0	48	60°C	0	0
4	-	3.92	72	100°C	245	3.4

8 Catalytic hydrogenation of CO_2

In a typical catalytic experiment, a Parr reactor (50 mL) was loaded with the desired amount of catalyst and ionic liquid. Then 5.24 mL of DMSO (67 mmol) and 0.24 mL of water (13.2 mmol) was introduced into the reactor. The reactor was flushed with CO_2 gas in order to remove the air. Afterwards, the reactor was filled with CO_2 and H_2 gas, till the desired total pressure was reached at room temperature. The reaction was conducted at desired temperature using a heating mantle under vigorous stirring. After the desired reaction time, the reactor was cooled down to room temperature and carefully vented. The reaction mixture

was analysed directly by ^{1}H NMR spectroscopy in DMSO-d_6 to determine the amount of formic acid formed with the ionic liquid as internal standard.

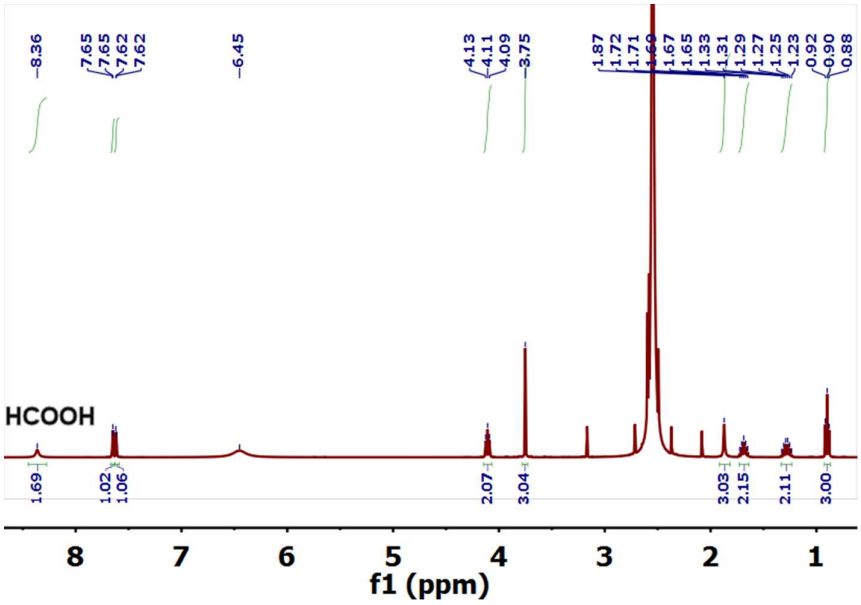


Figure S9: Representative ^{1}H NMR-spectrum of a CO_2 hydrogenation to free formic acid by $[Ru_3(CO)_{12}]$ catalyst in DMSO/H_2O/BMMI.OAc.

9 References

1. Moret, S.; Dyson, P. J.; Laurenczy, G., *Nat. Commun.* **2014,** *5*, 4017.
2. Rohmann, K.; Kothe, J.; Haenel, M. W.; Englert, U.; Hölscher, M.; Leitner, W., *Angew. Chem. Int. Ed.* **2016,** *55* (31), 8966-8969.
3. Hayashi, H.; Ogo, S.; Fukuzumi, S., *Chem. Commun.* **2004,** (23), 2714-2715.
4. Ogo, S.; Kabe, R.; Hayashi, H.; Harada, R.; Fukuzumi, S., *Dalton Trans.* **2006,** (39), 4657-4663.
5. Zhao, G.; Joó, F., *Catal. Commun.* **2011,** *14* (1), 74-76.
6. Wesselbaum, S.; Hintermair, U.; Leitner, W., *Angew. Chem.* **2012,** *124* (34), 8713-8716.
7. Zanatta, M.; dos Santos, F. P.; Biehl, C.; Marin, G.; Ebeling, G.; Netz, P. A.; Dupont, J., *J. Org. Chem.* **2017,** *82* (5), 2622-2629.
8. Brewer, S. A.; Holloway, J. H.; Hope, E. G., *J. Fluorine Chem.* **1995,** *70* (2), 167-169.
9. Leitner, W., *Angew. Chem. Int. Ed. Engl.* **1995,** *34* (20), 2207-2221.
10. Yasaka, Y.; Yoshida, K.; Wakai, C.; Matubayasi, N.; Nakahara, M., *J. Phys. Chem. A* **2006,** *110* (38), 11082-11090.
11. Shokouhi, M.; Farahani, H.; Hosseini-Jenab, M., *Fluid Ph. Equilibria* **2014,** *367*, 29-37.
12. Symons, E. A., *Can. J. Chem.* **1971,** *49* (24), 3940-3947.
13. Cowie, J. M. G.; Toporowski, P. M., *Can. J. Chem.* **1961,** *39* (11), 2240-2243.
14. Sans, V.; Karbass, N.; Burguete, M. I.; Compañ, V.; García-Verdugo, E.; Luis, S. V.; Pawlak, M., *Chem. Eur. J.* **2011,** *17* (6), 1894-1906.

4.4. References

1. Rohmann, K.; Kothe, J.; Haenel, M. W.; Englert, U.; Hölscher, M.; Leitner, W., Hydrogenation of CO2 to Formic Acid with a Highly Active Ruthenium Acriphos Complex in DMSO and DMSO/Water. *Angewandte Chemie International Edition* **2016,** *55* (31), 8966-8969.
2. Schaub, T.; Paciello, R. A., A Process for the Synthesis of Formic Acid by CO2 Hydrogenation: Thermodynamic Aspects and the Role of CO. *Angewandte Chemie International Edition* **2011,** *50* (32), 7278-7282.
3. Hayashi, H.; Ogo, S.; Fukuzumi, S., Aqueous hydrogenation of carbon dioxide catalysed by water-soluble ruthenium aqua complexes under acidic conditions. *Chemical Communications* **2004,** (23), 2714-2715.
4. Ogo, S.; Kabe, R.; Hayashi, H.; Harada, R.; Fukuzumi, S., Mechanistic investigation of CO2 hydrogenation by Ru(ii) and Ir(iii) aqua complexes under acidic conditions: two catalytic systems differing in the nature of the rate determining step. *Dalton Transactions* **2006,** (39), 4657-4663.
5. Moret, S.; Dyson, P. J.; Laurenczy, G., Direct synthesis of formic acid from carbon dioxide by hydrogenation in acidic media. **2014,** *5*, 4017.
6. Pérez-Fortes, M.; Schöneberger, J. C.; Boulamanti, A.; Harrison, G.; Tzimas, E., Formic acid synthesis using CO2 as raw material: Techno-economic and environmental evaluation and market potential. *International Journal of Hydrogen Energy* **2016,** *41* (37), 16444-16462.
7. Chase, M. W., *NIST-JANAF Thermochemical Tables*. 4 ed.; American Institute of Physics: 1998.
8. Wiedner, E. S.; Linehan, J. C., Making a Splash in Homogeneous CO2 Hydrogenation: Elucidating the Impact of Solvent on Catalytic Mechanisms. *Chemistry – A European Journal* **2018,** *24* (64), 16964-16971.

Chapter 5: RuFe nanoparticles for CO_2 hydrogenation

5.1. Introduction

In the hydrogenation of CO_2 to formic acid, it is crucial to separate the catalyst from the reaction media before purification steps are undertaken as elsewise the reaction can be reversed to yield CO_2 and H_2.[1-5] In this regard homogeneous catalysts display a fundamental disadvantage as these are notoriously difficult to separate from the reaction media. For instance Schaub et al. reported that CO addition after the reaction (CO poisons the homogeneous catalysts) increases the yield of formic acid obtained during the hydrogenation of CO_2 in the presence of trihexylamine, see ***section 1.5.2***.[6] In this regard heterogeneous catalyst offer an attractive alternative, as the active metal can easily be immobilised onto solid supports, ultimately facilitating the separation of products. In the following heterogeneous catalyst for the hydrogenation of CO_2 to formic acid will be briefly discussed. For a more detailed discussion the reader is referred to recent reviews.[2, 7-8]

The first report on the hydrogenation of CO_2 to formic acid dates back to 1935.[9] Farlow and Adkins reported Raney Nickel to be active in the hydrogenation of CO_2 to formic acid at 80°C in the presence of NEt_3.[9] Since then Pd on graphite nitride supports and Pd on carbon nanotubes have been reported to be active in the hydrogenation of CO_2 to formic acid.[10-13] Furthermore, Au nanoparticles on TiO_2 have been used in the hydrogenation of CO_2 to formic acid. It is important to note that the reaction have shown to take place at the interface of the Au particles the support.[14-15]

Another active catalyst species is Ru immobilised on TiO_2. Interestingly, here an ionic liquid with a basic site was used to shift the equilibrium to the product side. After the reaction the catalyst can be separated from the reaction media by simple filtration. After the filtration formic acid can be separated from the ionic liquid by reactive distillation and the ionic liquid can be recycled for 10 consecutive cycles.[16]

From a catalyst design point of view, it is important to mention, that metal dilution have been reported to have a beneficial effect onto the rate of CO_2 hydrogenation to formic acid. For instance PdNi on carbon nanotubes showed superior activity over their corresponding monometallic counterparts.[13] This publication indeed utilizes the metal dilution effect by diluting the active metal Ru in Fe. Furthermore, it is important to note that all the here presented systems utilize base to shift the thermodynamic equilibrium, which would lead to tedious purifications as discussed earlier. Therefore the aim of this work was to use acetate ILs to shift the equilibrium by weak interactions to the product side whilst avoiding the formation of formate salts and adducts, possible facilitating product separation downstream. If a highly active catalyst would have been achieved, the plan would have been to develop a flow process with the here developed catalysts.

5.2. Publication II: Selective Carbon Dioxide Hydrogenation Driven by Ferromagnetic RuFe Nanoparticles in Ionic Liquids.

Contribution of the author: The author contributed to this publication by drawing the research plan for the hydrogenation of CO_2 to formic acid with RuFe nanoparticles. Catalyst synthesis, catalytic experiments and the synthesis of ionic liquids were performed by Dr. Irfan Quadir, in Porto Alegre, Brazil at the Universidade Federal do Rio Grande do Sul (UFRGS). The author furthermore contributed in to the preparation of the manuscript.

Reprinted with permission from *ACS Catal.* **2018**, 8, 2, 1621-1627 Copyright 2018 American Chemical Society.

ACS Catalysis

Research Article

Cite This: ACS Catal. 2018, 8, 1621−1627

pubs.acs.org/acscatalysis

Selective Carbon Dioxide Hydrogenation Driven by Ferromagnetic RuFe Nanoparticles in Ionic Liquids

Muhammad I. Qadir,[†] Andreas Weilhard,[‡] Jesum A. Fernandes,[‡] Imanol de Pedro,[§] Bruno J. C. Vieira,[∥] João C. Waerenborgh,[∥] and Jairton Dupont*[,†,‡]

[†]Institute of Chemistry, UFRGS, Av. Bento Gonçalves, 9500, Porto Alegre 91501-970, Rio Grande do Sul, Brazil

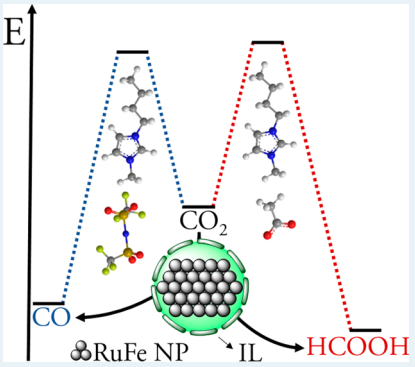
[‡]GSK Carbon Neutral Laboratories for Sustainable Chemistry, University of Nottingham, NG8 2GT Nottingham, UK

[§]Departmento CITIMAC, Facultad de Ciencias, Universidad de Cantabria, 390005 Santander, Spain

[∥]Centro de Ciências e Tecnologias Nucleares, Instituto Superior Técnico, Universidade de Lisboa, 2695-066 Bobadela LRS, Portugal

Supporting Information

ABSTRACT: CO_2 is selectively hydrogenated to HCO_2H or hydrocarbons (HCs) by RuFe nanoparticles (NPs) in ionic liquids (ILs) under mild reaction conditions. The generation of HCO_2H occurs in ILs containing basic anions, whereas heavy HCs (up to C_{21} at 150 °C) are formed in the presence of ILs containing nonbasic anions. Remarkably, high values of TONs (400) and a TOF value of 23.52 h^{-1} for formic acid with a molar ratio of 2.03 per BMI·OAc IL were obtained. Moreover, these NPs exhibited outstanding abilities in the formation of long-chain HCs with efficient catalytic activity (12% conversion) in a BMI·NTf_2 hydrophobic IL. The IL forms a cage around the NPs that controls the diffusion/residence time of the substrates, intermediates, and products. The distinct CO_2 hydrogenation pathways (HCO_2H or FT via RWGS) catalyzed by the RuFe alloy are directly related to the basicity and hydrophobicity of the IL ion pair (mainly imposed by the anion) and the composition of the metal alloy. The presence of Fe in the RuFe alloy provides enhanced catalytic performance via a metal dilution effect for the formation of HCO_2H and via a synergistic effect for the generation of heavy HCs.

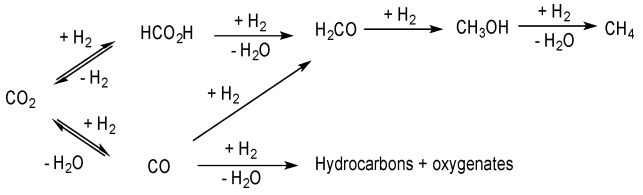


KEYWORDS: *RuFe nanoparticles, carbon dioxide, selective hydrogenation, ferromagnetic, ionic liquids*

1. INTRODUCTION

The conversion of CO_2 into chemicals and fuels is becoming a key component of processes that will comprise a resource and energy-efficient future for the chemical industry.[1] CO_2 can be hydrogenated in sequence to HCO_2H, formaldehyde, methanol, and then methane, or it can be first converted to CO via the reverse water-gas shift reaction (RWGS)[2,3] and further reduced, yielding formaldehyde, methanol, and methane (Scheme 1).[4] Eventually heavier HCs/oxygenates are formed through the Fischer−Tropsch process.[5] Therefore, depending on delicate thermodynamic/kinetic balances and in particular on the fine-tuning of the properties of electronic and geometric catalysts, a series of chemical commodities and fuels can be produced from CO_2 hydrogenation via either the CO or the HCO_2H pathways.

Scheme 1. Reaction Pathways for CO_2 Hydrogenation



Currently, the catalysis of the reduction of CO_2 to HCO_2H is predominantly focused on homogeneous precious platinum-group metals (e.g., Rh, Ru, and Ir) associated with relatively sophisticated ligands.[6,7] These catalyst precursors are highly active, allowing turnover frequencies (TOFs) of several hundred thousand catalytic cycles. However, these systems typically involve *stoichiometric amounts* of an amine or another strong base as a coreagent or buffer solution.[8,9] Conversely, examples of heterogeneous-based catalysts are relatively rare and give only very low CO_2 conversions.[10] There is also a profusion of reports on the use of FT catalytic systems using CO_2 that are based on Fe, Co, and Ni catalysts, but they usually operate at high temperatures (>250 °C).[11,12] In fact, Fe-based catalysts are considered to be ideally suited for CO_2 hydrogenation due to their intrinsic WGS and RWGS activity.[13] Hence, the generation of HCs from CO_2 hydrogenation involves a delicate balance between the RWGS (CO_2 partial hydrogenation) and FT (CO hydrogenation) pathways.[14] This can in principle be better accomplished by the use of a bimetallic catalyst that can induce both the RWGS and the FT reactions. However, classical bimetallic heterogeneous catalysts

Received: November 7, 2017
Revised: December 23, 2017
Published: January 4, 2018

Downloaded via UNIV NOTTINGHAM on March 28, 2019 at 18:31:30 (UTC).
See https://pubs.acs.org/sharingguidelines for options on how to legitimately share published articles.

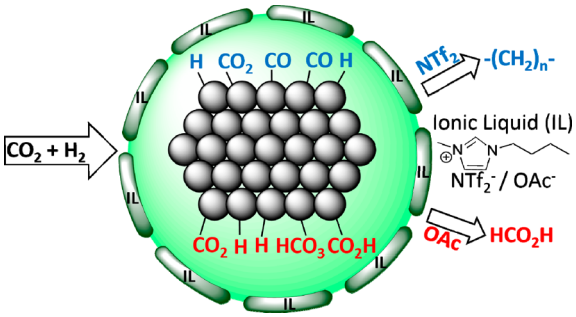
© 2018 American Chemical Society

DOI: 10.1021/acscatal.7b03804
ACS Catal. 2018, 8, 1621−1627

such as CoFe[15] and CoPt[16] usually mainly produce light HCs (C_1–C_4).

We now address the challenge of the use of hydrophilic/hydrophobic ILs as catalytic supports for bimetallic RuFe NPs. This system can drive CO_2 hydrogenation in IL/buffered media to the formation of HCO_2H or, by employing a hydrophobic IL to shift the equilibrium, toward FT products via the RWGS (Scheme 2). Indeed, ILs form a cage around NPs, providing an ionic nanocontainer environment that allows control of the diffusion of reactants, intermediates, and products (mainly via hydrophobicity and contact ion pairs) to the catalytically active sites. Hence, the geometric and electronic properties of NPs supported in ILs can be tuned by the proper choice of IL cations and anions, along with NPs that strongly influence the residence time/diffusion of the reactants, intermediates, and products in the nanoenvironment.[17,18] Moreover, the CO_2 solubility in ILs can be modulated by the use of ILs associated with basic anions via the formation of bicarbonates.[19]

Scheme 2. Supported IL RuFe NP Catalysts for the Chemoselective Hydrogenation of CO_2



We now report that CO_2 hydrogenation can be performed under mild reaction conditions, employing RuFe alloy NPs in ILs where the chemoselectivity (leading to HCO_2H or HC) can be modulated by the proper choice of the IL anion.

2. RESULTS AND DISCUSSION

2.1. Preparation and Characterization of RuFe NPs in ILs. The hydrophobic BMI·NTf_2 IL was chosen in view of its stability and its ability to stabilize small mono- and bimetallic NPs of Fe[20] and Ru.[21] The hydrophilic BMI·OAc IL was selected due to its buffering properties and its stabilization of weak carbonic acids, which make it ideal for the reduction of CO_2 to HCO_2H. The bimetallic RuFe alloy NPs were prepared by reduction/decomposition of equimolar amounts of [Fe$(CO)_5$] and [Ru(Me-allyl)$_2$(COD)] under hydrogen (18 bar) at 150 °C for 23 h. A relatively stable black "solution" was formed, from which highly air sensitive RuFe NPs were isolated by the addition of dichloromethane and centrifugation. In situ TEM (Figure 1a,b) of RuFe NPs in the BMI·NTf_2 IL showed the presence of irregularly shaped NPs with a mean diameter of 1.7 ± 0.3 nm together with agglomerates of between 10 and 25 nm.

EDX elemental mapping of Fe and Ru (Figure 1c) with their overlay provided a direct view of the metal atom distribution, confirming the alloyed state of the NPs. XRD analysis (Figure S1) of the isolated material showed the typical diffraction patterns of a RuFe alloy (JCPDS No. 65-6545), in particular a hexagonal-close-packed crystalline structure.[22]

XPS analysis (Figure 1d,e and Table S1) showed the C 1s, Ru 3d, and Fe 2p peaks. The Ru $3d_{5/2}$ peak was deconvoluted into three components corresponding to Ru^0, Ru^{4+}, and a satellite peak of Ru^{4+}, which have been demonstrated to be catalytically active sites.[23,24] The broad Fe $2p_{3/2}$ peak indicates the presence of Fe in different valence states. The deconvolution of this peak shows the presence of a small amount of Fe^0 (shoulder at ~706.7 eV),[25] with the main component being a mixture of Fe^{2+} and Fe^{3+} in octahedral sites

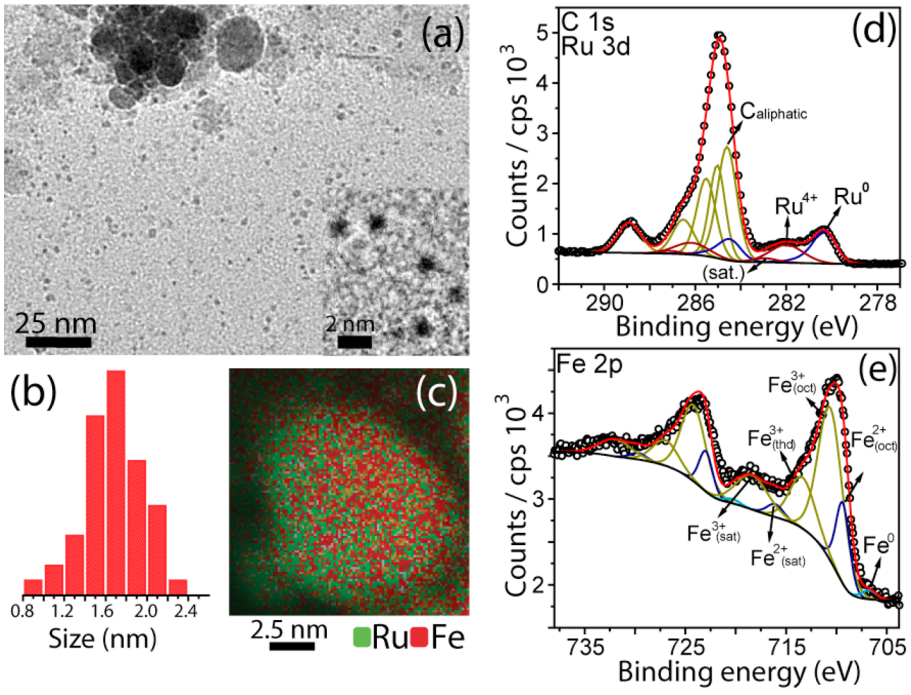


Figure 1. (a, b) TEM image of RuFe NPs and size distribution, (c) EDS map, overlay of Ru-L and Fe-K of RuFe NPs in BMI-NTf_2, and (d, e) XPS analysis of the Ru 3d and Fe 2p signals.

DOI: 10.1021/acscatal.7b03804
ACS Catal. 2018, 8, 1621–1627

and Fe^{3+} in tetrahedral sites.[26] The F 1s signal showed a peak associated with uncoordinated NTf_2 (688.6 eV), and a new component appeared at 684.8 eV, which may be attributed to the IL interaction with RuFe NPs (Figure S2) as already reported for other NPs.[18]

Mössbauer spectra at 4 and 295 K (Figure 2a,b and Table S2) of the as-prepared RuFe NPs reflected the presence of a

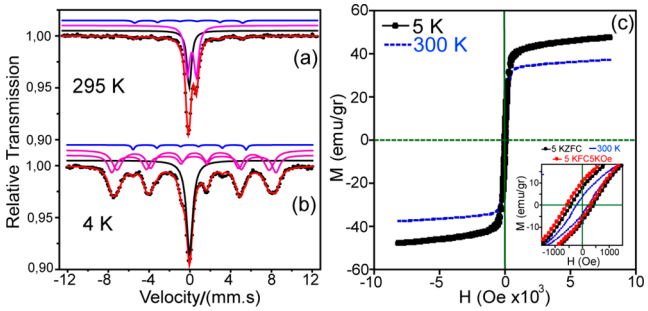


Figure 2. (a, b) Mössbauer spectra of isolated RuFe NPs. (c) Magnetic hysteresis loops, $M(H)$, collected at 300 and 5 K after cooling in zero field (ZFC). The inset shows the loops around $H = 0$ for 300 and 5 K after cooling in ZFC and 50 kOe (FC).

RuFe alloy, nanosized Fe^{3+} oxides, and a minor amount of α-Fe.[27] The magnetization measurements presented an exchange bias field (HEB) value of ~110 Oe at 5 K (Figure 2c), which is characterized by the structurally disordered surface of the nanosized Fe^{3+} and Ru^{4+} oxides.[27] Moreover, the magnetization response to the applied magnetic field at 300 K displays nonsaturating values of magnetization (related to the presence of a paramagnetic contribution from the RuFe alloy)[28] with a small hysteresis loop (HC = 208 Oe, M_r = 3.7 emu/g) associated with a small proportion of metallic Fe (Figure 2).[27,28]

A deeper magnetic analysis (Figure S4) suggests that metallic Ru and Fe are mainly in the core and nanosized Fe and Ru oxides are probably formed by surface oxidation of the NPs, which is in agreement with the XPS and Mössbauer analyses.

2.2. FTS Catalytic Properties of NPs in ILs. The RuFe NPs are active catalysts for the hydrogenation of CO_2 to heavy HCs in hydrophobic BMI·NTf_2 IL at 150 °C using a gas mixture (H_2/CO_2 = 4/1) under 8.5 bar (Table 1). No significant HC production was detected over Fe NPs of 4–5 nm[20] (conversion 4%, Table 1, entry 1), which might be due to surface poisoning of the catalyst by carbon deposition, causing rapid deactivation.[29] This phenomenon has been observed extensively when iron oxide is used without stabilizers or promoters for CO_2 hydrogenation.[30] When monometallic Ru NPs of 2–3 nm are used,[21] the formation of HC was detected with 10% conversion of CO_2 (Table 1, entry 2). These results are in opposition to earlier reports, in which only CH_4[31] or HCO_2H[32,33] was observed with Ru as a catalyst, indicating the crucial role of the hydrophobic IL (BMI·NTf_2).

Table 1. CO_2 Hydrogenation to HC in BMI·NTf_2 by RuFe NPs[a]

			product selectivity (% C_{at})			
entry	NP	conversion (%)	CH_4	C_2–C_4	C_5–C_6	C_7–C_{21}
1	Fe	4	28	18	54	
2	Ru	10	21	52	27	
3	RuFe	12	2	57	31	10
4	RuFe[b]	5	35	10	16	
5	RuFe[c]	10	37	34	29	
6	RuFe[d]	10		11	39	
7	RuFe[e]	12	8	4	78	10
8	RuFe[f]	3	100			

[a]Reaction conditions: 20 mg of NPs, 0.5 g of IL, CO_2/H_2 (1/4, 8.5 bar), 64 h, and 150 °C. [b]With BMI·BF_4 IL (CO = 39%). [c]With BMI·FAP IL. [d]With BMI·OAc IL (CO = 50%). [e]Reaction at 175 °C. [f]Without IL.

By incorporation of Ru into Fe, the RuFe catalyst inherits the advantages of both components, in which Ru increases the total activity of Fe by stabilizing it, and Fe tunes the selectivity toward higher HC through FT (Table 1, entry 3) by promoting the dominance of the RWGS. It is notable that the hydrophobic IL (BMI·NTf_2) has a remarkable influence on the conversion of CO_2 to heavy HCs, not only stabilizing the catalytic system but also repelling the formed water from the active catalytic phase of the RuFe NPs, hence decreasing the water-gas shift reaction (WGS) and increasing the RWGS and the FT reaction. Meanwhile, in the water-soluble BMI·BF_4 IL, RuFe NPs displayed a lower activity (5%) and selectivity, with the production of a larger amount of CO (39%, entry 4, Table 1). This effect may arise due to its hydrophilic nature that not only reduces the rate of CO_2 hydrogenation but may also reduce the FT catalytically active surface species with the dominant CO path formation. The catalytic performance observed, 12% CO_2 conversion and selectivity 10% for heavy HCs (C_7–C_{21}), by RuFe NPs in BMI·NTf_2 at 150 °C for 64 h (Table 1, entry 3), is higher than that obtained using classical Fe oxides,[11,34] FeCo,[15,35] or CoPt[16,36] which operates at >240 °C with 10–30% CO_2 conversion and mainly produces gaseous HCs (C_1–C_5).

In addition, we also examined the CO_2 hydrogenation in BMI·FAP (FAP = trifluorotris(pentafluoroethyl)phosphate) hydrophobic IL under our standard conditions. Unfortunately, RuFe revealed less catalytic activity (10% conversion) and selectvity to higher chain HC in comparison to CO_2 hydrogenation in BMI·NTf_2 IL (Table 1, entry 5). This effect may be correlated to the greater diffusion coefficients of CO_2 in BMI·NTf_2 IL in comparison to BMI·FAP IL at higher temperature and pressure.[37] However, the use of BMI·PF_6 hydrophobic IL is limited because of the generation of HF due to partial decomposition of the PF_6^- anion during catalytic reactions in the presence of NPs and formed water. Moreover, in hydrophilic BMI·OAc IL RuFe NPs showed very high selectivity toward CO (50%) with lower selectivity to FTS products (Table 1, entry 6). It is worth noting that no hydrocarbons were detected at 100 °C, whereas an increase in reaction temperature (175 °C) using BMI·NTf_2 IL under standard conditions did not affect the conversion (12%) but did affect selectivities toward heavier hydrocarbons (78% C_5–C_6, 10% C_7–C_{21}, 4% C_2–C_4 and 8% CH_4 (Table 1, entry 7).

The catalytic activity of RuFe NPs was also monitored at different H_2/CO_2 gas pressures using BMI·NTf_2 IL at 150 °C for 64 h (Figure 3). At 3 bar of the H_2/CO_2 gas mixture, we did not observe the hydrogenated products and CO. A very low conversion (2%) was observed at 5 bar of gas pressure with a selectivity of $<C_7^+$ HCs. Increasing the reaction pressure increased conversion, shifting the equilibrium of the reaction toward higher hydrocarbons. A conversion of 14% was reached with the selectivities of HCs 4% of CH_4, 47% of C_2–C_4, 34% C_5–C_6, and 12% C_7–C_{21}. The recyclability of RuFe NPs was

DOI: 10.1021/acscatal.7b03804
ACS Catal. 2018, 8, 1621–1627

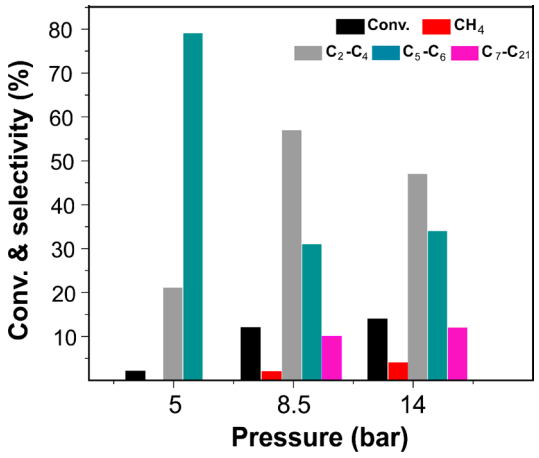


Figure 3. Catalytic hydrogenation of CO_2 vs gas pressure to HC by RuFe NPs in BMI·NTf_2. Reaction conditions: 20 mg of NPs, 0.5 g of IL, CO_2/H_2 (1/4), 64 h, and 150 °C.

also studied (Figure S5). We observed no signficant changes in conversion until three runs but a decrease in the formation of $>C_{6+}$ HCs after the second run, which may be correlated to the deposition of coke on the surface of the catalyst.

2.3. CO_2 Hydrogenation to Formic Acid. Remarkably, CO_2 hydrogenation by RuFe NPs in DMSO/D_2O solution containing a hydrophilic IL associated with basic acetate anion produces exclusively HCO_2H at 60 °C (Table 2). No HCO_2H was formed using Fe NPs (entry 1, Table 2), whereas when Ru NPs were applied, HCO_2H was observed with a molar ratio of 1.18 HCO_2H/IL (Table 2, entry 2). By incorporating Fe into Ru NPs, the HCO_2H/IL molar ratio reached 1.66 with a TON of 56 (Table 2, entry 3), which shows a positive metal dilution effect.[38] The addition of small amounts of water has a significant effect under the same reaction conditions because of its dual roles. It not only may accelerate the reaction because of the combination of CO_2 with water and IL to form bicarbonate but may also provide a solvent system with DMSO, which plays an important role in stabilizing the formed HCO_2H through H bonding.[8] Moreover, water has a strong influence on the structural organization and electronic properties of imidazolium-based ILs.[39,40] Additional increases in water content decreased the HCO_2H production, resulting in a HCO_2H/IL ratio of 1.01 and a consequently lower TON of 34. High TON values (400) and TOF of 23.52 h^{-1} with an HCO_2H/IL molar ratio of 2.03 were observed using a small amount of catalyst (1.0 mg, Table 2, entry 5).

Table 2. CO_2 Hydrogenation to HCO_2H by RuFe NPs[a]

entry	NP	IL	D_2O/DMSO (%)[b]	HCO_2H/IL (M)[c]	TON[d]/TOF (h^{-1})
1	Fe	BMI·OAc	5		
2	Ru	BMI·OAc	5	1.18	19/0.79
3	RuFe	BMI·OAc	5	1.66	56/2.33
4	RuFe	BMI·OAc	10	1.01	34/1.42
5	RuFe[e]	BMI·OAc	5	2.03	400/23.52
6	RuFe[f]		5		
7	RuFe	BMI·BF_4	5		

[a]Reaction conditions unless specified otherwise: 5.0 mg of NPs, 36 mg of IL (0.18 mmol), 33 mg of D_2O (1.8 mmol), 2.84 g of DMSO (36.4 mmol), CO_2/H_2 (1/2, 30 bar), 60 °C, and 24 h. [b]Molar ratio of D_2O in DMSO. [c]Molar ratio of the HCO_2H produced to the IL added. [d]Moles of HCO_2H per moles of Ru surface atoms. [e]1.0 mg of NPs, 54 mg of IL (0.27 mmol), 33 mg of D_2O (1.8 mmol), 2.84 g of DMSO (36.4 mmol), CO_2/H_2 (1/2, 30 bar), 60 °C, and 17 h. [f]Without BMI·OAc.

It is important to note that no HCO_2H was observed in the absence of the BMI·OAc, which reflects its vital role in the hydrogenation of CO_2 to HCO_2H on the basis of its buffering properties and stabilization of weak carbonic acid species.[19] Although the TONs obtained are much lower than those employing homogeneous catalytic systems that yield formates (not free formic acid),[6] they are higher than those obtained using heterogeneous catalysts[32,41] and in our case free formic acid is obtained. Moreover, the addition of a small amount of a weak base such as NaOAc (5 mg) did not affect the catalytic activity.

To investigate the effect of the CO_2/H_2 gas mixture on the rate of the hydrogenation reaction, several different mixtures of the gases were studied, as shown in Figure 4. The reaction rate is significantly dependent on the concentration of H_2 in the gas phase (Figure 4a). The turnover frequency was 7.32 h^{-1} at a CO_2/H_2 concentration ratio of 1/1 and increased to 23.52 h^{-1} at a ratio of 1/4 (CO_2/H_2) representing the rate-limiting step, influenced by the concentration of hydrogen, indicating a zero-order reaction. Moreover, the influence of the reaction temperature ranging from 25 to 75 °C is depicted in Figure 4b. The rate of the reaction increases with temperature at a fixed pressure up to 60 °C. The turnover frequency was only 8.8 h^{-1} at 25 °C and reached a value of 23.52 h^{-1} at 60 °C. It is important to note that, on an increase in the reaction temperature (75 °C), the rate of the reaction decreased significantly; this may be due to the decomposition of HCO_2H into CO and H_2O. Hence, in addition to formic acid, formation of CO with a minor quantity of CH_4 was detected in the gas phase of the reaction at 75 °C. A similar trend was also reported when PdNi/CNT-GR catalyst[41] was used for the hydrogenation of CO_2 to FA in water at different temperatures.

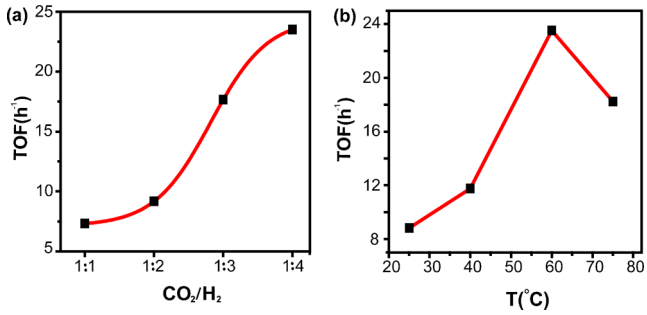


Figure 4. Formic acid production vs concentration of the gas mixture (a) and temperature (b). Reaction conditions: 1.0 mg of RuFe NPs, 54 mg of IL (0.27 mmol), 33 mg of D_2O (1.8 mmol), 2.84 g of DMSO (36.4 mmol), CO_2/H_2 (30 bar), 60 °C, and 17 h.

Interestingly, IL (BMI·OAc) plays an important role not only in the formation of active species but also in the stabilization of the FA. For instance, we observed a linear relationship between the amount of IL and the amount of formic acid on a double-logarithmic scale (Figure 5), which provides evidence that IL acts as a buffer during the hydrogenation of CO_2 to FA. This

DOI: 10.1021/acscatal.7b03804
ACS Catal. 2018, 8, 1621−1627

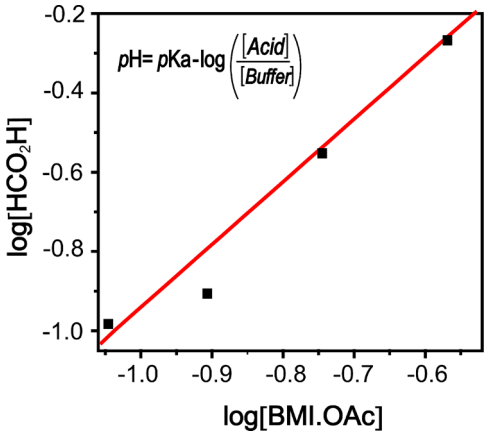
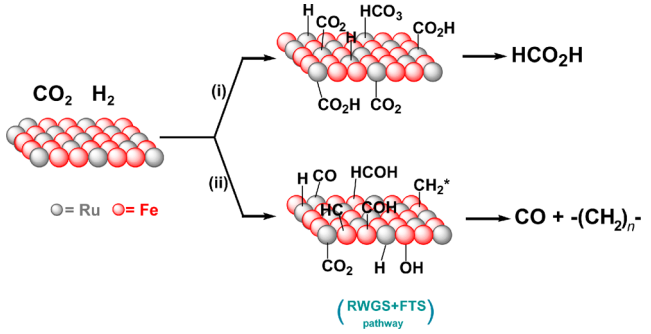


Figure 5. Relationship between the amount of BMI·OAc IL and HCO_2H. Reaction conditions: 1.0 mg of RuFe NPs, 33 mg of D_2O (1.8 mmol), 2.84 g of DMSO (36.4 mmol), CO_2/H_2 (1/4, 30 bar), 60 °C, and 17 h.

behavior is explained by the Henderrson−Hasselbach equation for buffering systems[42,43] and is consistent with the formation of free formic acid (not formates) and conistent with the FA/IL ratio of 2/1 (entry 5, Table 2).

2.4. Proposed Reaction Pathways for CO_2 Hydrogenation by NPs in ILs. A proposed reaction mechanism for the hydrogenation of CO_2 to FA and HCs is represented in Scheme 3. The production of FA can be followed by the

Scheme 3. Schematic Representation of Mechanistic Routes for the Formation of FA (i) and Hydrocarbons by RuFe NPs in IL (ii)



hydrogenation of formed bicarbonate (HCO_3^-) by Ru, which can be generated by the absorption of CO_2 in aqueous acetate-based imidazolium IL systems[19] or/and the carbonate species through the insertion of CO_2 into Ru−H bond. An in situ (high-pressure) HP-NMR experiment (Figure S6) was performed at 25 °C using 40 bar of an H_2/CO_2 (1/1) gas mixture and Ru NPs revealed the presence of HCO_3^- (158 ppm) and dissolved CO_2 (124 ppm). On the other hand, hydrocarbon production has been considered to proceed by a two-step process with the initial conversion of CO_2 into CO by the RWGS followed by chain propagation via FTS. The formed CO follows the FTS pathway on the surface of Ru and Fe.[44] It is presumed that CO is activated as surface Fe carbides followed by sequential hydrogenation to CH, CH_2, CH_3, and eventually CH_4 or to C_{2+} HC.[45] It is also proposed that the formed potential surface species (HCO*, HCOH*, CH*, and CH_2*) correspond to the suggested monomers in the CO insertion mechanism to the growing chain.[46] Since Fe-based catalysts are active FTS catalysts to produce long-chain HCs during the hydrogenation of CO_2,[47,48] it can be assumed that the Fe phase in RuFe NPs is dominant over the Ru phase for FTS in the production of heavier HCs.

3. CONCLUSION

We have shown that the simple codecomposition of Fe and Ru complexes in ILs yields ferromagnetic alloy colloidal solutions constituted mainly of 1.7 nm NPs. The presence of metallic Ru and Fe in the core of NPs, surrounded by a RuFe alloy that has surface Fe and Ru oxides, was confirmed by magnetic and XPS analysis. The IL forms a cage around the NPs that controls the diffusion/residence time of the substrates, intermediates, and products. The distinct CO_2 hydrogenation pathways (HCO_2H or FT via RWGS) catalyzed by the RuFe alloy are directly related to the nature of the IL anion support and of the metal alloy. Therefore, the combination of an RWGS with an FT active metal associated with IL anion basicity and hydrophobicity is a highly promising approach to access a new family of catalytic systems for selective CO_2 reduction to heavy HC or formic acid.

4. EXPERIMENTAL SECTION

All of the catalytic reactions and preparation of the NPs were conducted in a 25 mL stainless steel high-pressure glass-lined Fischer−Porter reactor having a high-precision pressure gauge to monitor the reaction and to calculate the catalytic activity under an argon atmosphere in the glovebox. Bis(2-methylallyl)-(1,5-cyclooctadiene)ruthenium and iron(0) pentacarbonyl complexes and DMSO were purchased from Sigma-Aldrich. Solvents were purified before use. BMI·OAc (1-butyl-3-methyl-1*H*-imidazol-3-ium acetate) and BMI·NTf_2 (1-butyl-3-methyl-1*H*-imidazol-3-ium bis((trifluoromethyl)sulfonyl)amide), BMI·BF_4 (1-butyl-3-methyl-1*H*-imidazol-3-ium tetrafloroborate), anc BMI·FAP (FAP = trifluorotris(pentafluoroethyl)-phosphate) ILs were prepared by well-known methods.[49,50] The purified ILs were dried and degassed under high vacuum at 50 °C for 2 days prior to use for the preparation of NPs and catalysis. H_2 (>99.999%) and CO_2 (>99.999%) were purchased from White-Martins Ltd. (Brazil). X-ray diffraction (XRD) experiments were conducted in a D/max-3B diffractometer with Cu Kα radiation. The scans were made in the 2θ range 20−70° with a scan rate of 10°/min (wide-angle diffraction). Mössbauer spectra were collected in transmission mode using a conventional constant-acceleration spectrometer and a 25 mCi ^{57}Co source in a Rh matrix. The velocity scale was calibrated using α-Fe foil. Isomer shifts (IS) are given relative to this standard at room temperature. The low-temperature spectrum was collected in a bath cryostat with the sample immersed in liquid He. The absorber was obtained by packing the powdered samples into a Perspex holder. The spectra were fitted to Lorentzian lines using a nonlinear least-squares method. Variable-temperature magnetic susceptibility measurements were performed using a standard PPMS magnetometer while heating from 2 to 300 K at 50 Oe after cooling in either the presence (field cooling, FC) or the absence (zero field cooling, ZFC) of the applied field. Low-amplitude (HAC = 1 Oe) ac susceptibility curves were measured from 5 to 100 K as a function of the frequency, between 100 and 10^4 Hz, in the absence of a direct current (dc) applied field. Magnetization as a function of field (H) was measured using the same magnetometer in the $-80 \leq H/\text{kOe} \leq 80$ ranges at 300 and

DOI: 10.1021/acscatal.7b03804
ACS Catal. 2018, 8, 1621−1627

5 K after cooling the sample in zero field. In order to investigate the EB effect in these NPs, the sample was cooled from 300 to 5 K under a constant applied magnetic field of 50 kOe (H_{cool}). After that, a hysteresis loop was recorded between −80 and 80 kOe at T = 5 K. NMR spectra were recorded on a Varian-400 NMR spectrometer at 22 °C with a relaxation delay of 2 s and 90° pulse angle with 600 scans. GC-TCD analyses were run with an Agilent MicroGC System 3000A apparatus. GC analyses were run with an Agilent GC System 6820 containing a DB-17 column. GC-MS analyses were run with a Shimadzu QP50 (EI, 70 eV). A CO_2 hydrogenation test without IL was performed in a DRIFT cell at respective temperature.

4.1. Preparation of RuFe NPs. RuFe NPs were prepared by the single-step reduction/hydrogenation of bis(2-methylallyl)(1,5-cyclooctadiene)ruthenium and iron(0) pentacarbonyl complexes in BMI·NTf_2 IL. Typically, a Fischer−Porter reactor containing 3 mL of IL was placed under reduced pressure at room temperature for 30 min and filled with argon. Then, [Ru(Me-allyl)$_2$(COD)] (0.5 mmol, 159.7 mg) and [Fe(CO)$_5$] (0.5 mmol, 98 mg) were poured into the IL under an argon atmosphere and magnetically stirred for 2 min. The reactor was flushed with hydrogen gas (3 × 5 bar) to remove argon. Then hydrogen (18 bar) was charged in the reactor and the reaction mixture was stirred vigorously at room temperature for 5 min and heated at 120 °C for 30 min. Afterward, the reaction temperature was increased to 150 °C and kept for 23 h. Then, the reactor was cooled and kept under reduced pressure in order to remove the volatiles. The resulting RuFe NPs were retained in IL under argon prior to use for characterization and catalysis.

4.2. CO_2 Hydrogenation to HC by RuFe NPs in ILs. Typically, 20 mg of isolated RuFe NPs was dispersed into 0.5 mL of IL in a glass-lined Fischer−Porter reactor (25 mL) and kept under high vacuum for 30 min at room temperature and the reactor was filled with argon. Then the reactor was purged three times with an H_2/CO_2 (4/1) gas mixture to replace argon, filled with 8.5 bar of an H_2/CO_2 (4/1) gas mixture, and dipped into a silicon oil bath that was maintained at 150 °C, and the reaction was allowed to proceed for 64 h. The conversion was monitored by a total pressure drop. The reactor was cooled in an ice/water bath and then connected to a Micro GC to analyze the gaseous products (C_1−C_6). The liquid products (>C_6) were extracted by dried diethyl ether and analyzed with GC by comparing with authentic products. Product selectivity has been calculated as the equivalent amount of the desired HC with respect to the total amount of HC produced. The selectivity to oxygenates was below 1% C_{at} and was therefore excluded.

4.3. CO_2 Hydrogenation to Formic Acid by RuFe NPs. Catalytic hydrogenation of CO_2 to formic acid was also evaluated in a glass-lined stainless steel Fischer−Porter high-pressure reactor (25 mL). Typically, in a Fischer−Porter reactor, 5.0 mg of isolated RuFe NPs was dispersed in a solution containing BMI·OAc (36 mg, 0.18 mmol), DMSO (2.84 g, 36.4 mmol), and D_2O (33 mg, 1.8 mmol) under an argon atmosphere. The argon in the reactor was replaced by hydrogen gas, the reactor was filled with 5 bar of hydrogen, and the reaction mass was stirred at room temperature for 10 min. Then the reaction reactor was flushed with CO_2 to remove hydrogen and subsequently charged with CO_2 (10 bar) and H_2 (20 bar). The reaction was conducted at 60 °C for 24 h in a silicon oil bath. Afterward, the reactor was cooled to room temperature in ice-cooled water and carefully vented. The reaction mixture was centrifuged to remove NPs and analyzed directly by ^{1}H NMR using DMSO-d_6 to determine the amount of formic acid produced. TONs were calculated by moles of formic acid formed per mole of Ru surface atoms.[51] The results shown in Table 2 were obtained by performing each reaction at least twice to confirm reproducibility.

■ ASSOCIATED CONTENT

Supporting Information

The Supporting Information is available free of charge on the ACS Publications website at DOI: 10.1021/acscatal.7b03804.

Experimental details and data for XRD, XPS, Mossbauer, and magnetic analysis of RuFe NPs and NMR spectra (PDF)

■ AUTHOR INFORMATION

Corresponding Author

*E-mail for J.D.: Jairton.dupont@ufrgs.br.

ORCID

Jairton Dupont: 0000-0003-3237-0770

Notes

The authors declare no competing financial interest.

■ ACKNOWLEDGMENTS

The authors are grateful to CAPES-PNPD, INCT-Catal., FAPERGS and CNPq for partial financial support. B.J.C.V. and J.C.W. thank the Portuguese foundation for Science and Technology (FCT, contract UID/multi/04349/2013). The authors are grateful for the support of The Nanoscale and Microscale Research Centre (nmRC) for the TEM and XPS measurements.

■ REFERENCES

(1) Porosoff, M. D.; Yan, B.; Chen, J. G. *Energy Environ. Sci.* **2016**, *9*, 62.

(2) Posada-Perez, S.; Ramirez, P. J.; Evans, J.; Vines, F.; Liu, P.; Illas, F.; Rodriguez, J. A. *J. Am. Chem. Soc.* **2016**, *138*, 8269.

(3) Roiaz, M.; Monachino, E.; Dri, C.; Greiner, M.; Knop-Gericke, A.; Schlogl, R.; Comelli, G.; Vesselli, E. *J. Am. Chem. Soc.* **2016**, *138*, 4146.

(4) Kattel, S.; Yan, B.; Yang, Y.; Chen, J. G.; Liu, P. *J. Am. Chem. Soc.* **2016**, *138*, 12440.

(5) Prieto, G. *ChemSusChem* **2017**, *10*, 1056.

(6) Klankermayer, J.; Wesselbaum, S.; Beydoun, K.; Leitner, W. *Angew. Chem., Int. Ed.* **2016**, *55*, 7296.

(7) Alvarez, A.; Bansode, A.; Urakawa, A.; Bavykina, A. V.; Wezendonk, T. A.; Makkee, M.; Gascon, J.; Kapteijn, F. *Chem. Rev.* **2017**, *117*, 9804.

(8) Rohmann, K.; Kothe, J.; Haenel, M. W.; Englert, U.; Hölscher, M.; Leitner, W. *Angew. Chem., Int. Ed.* **2016**, *55*, 8966.

(9) Moret, S.; Dyson, P. J.; Laurenczy, G. *Nat. Commun.* **2014**, *5*, 4017.

(10) Wang, M.; Zhang, J.; Yan, N. *Front. Chem.* **2013**, *1*, 17.

(11) Albrecht, M.; Rodemerck, U.; Schneider, M.; Bröring, M.; Baabe, D.; Kondratenko, E. V. *Appl. Catal., B* **2017**, *204*, 119.

(12) Geng, S.; Jiang, F.; Xu, Y.; Liu, X. *ChemCatChem* **2016**, *8*, 1303.

(13) Newsome, D. S. *Catal. Rev.: Sci. Eng.* **1980**, *21*, 275.

(14) Spencer, M. S. *Catal. Lett.* **1995**, *32*, 9.

(15) Gnanamani, M. K.; Jacobs, G.; Hamdeh, H. H.; Shafer, W. D.; Liu, F.; Hopps, S. D.; Thomas, G. A.; Davis, B. H. *ACS Catal.* **2016**, *6*, 913.

(16) Xie, C.; Chen, C.; Yu, Y.; Su, J.; Li, Y.; Somorjai, G. A.; Yang, P. *Nano Lett.* **2017**, *17*, 3798.

DOI: 10.1021/acscatal.7b03804
ACS Catal. 2018, 8, 1621−1627

(17) Luza, L.; Rambor, C. P.; Gual, A.; Bernardi, F.; Domingos, J. B.; Grehl, T.; Brüner, P.; Dupont, J. *ACS Catal.* **2016**, *6*, 6478.
(18) Luza, L.; Rambor, C. P.; Gual, A.; Alves Fernandes, J.; Eberhardt, D.; Dupont, J. *ACS Catal.* **2017**, *7*, 2791.
(19) Simon, N. M.; Zanatta, M.; Dos Santos, F. P.; Corvo, M. C.; Cabrita, E. J.; Dupont, J. *ChemSusChem* **2017**, *10*, 4927.
(20) Krämer, J.; Redel, E.; Thomann, R.; Janiak, C. *Organometallics* **2008**, *27*, 1976.
(21) Prechtl, M. H. G.; Scariot, M.; Scholten, J. D.; Machado, G.; Teixeira, S. R.; Dupont, J. *Inorg. Chem.* **2008**, *47*, 8995.
(22) Ye, T.-N.; Li, J.; Kitano, M.; Sasase, M.; Hosono, H. *Chem. Sci.* **2016**, *7*, 5969.
(23) Liu, X. L.; Zeng, J. L.; Wang, J.; Shi, W. B.; Zhu, T. Y. *Catal. Sci. Technol.* **2016**, *6*, 4337.
(24) Over, H.; Seitsonen, A. P.; Lundgren, E.; Wiklund, M.; Andersen, J. N. *Chem. Phys. Lett.* **2001**, *342*, 467.
(25) Gonzalez-Arellano, C.; Yoshida, K.; Luque, R.; Gai, P. L. *Green Chem.* **2010**, *12*, 1281.
(26) Beji, Z.; Sun, M.; Smiri, L. S.; Herbst, F.; Mangeney, C.; Ammar, S. *RSC Adv.* **2015**, *5*, 65010.
(27) Nemati, Z.; Khurshid, H.; Alonso, J.; Phan, M. H.; Mukherjee, P.; Srikanth, H. *Nanotechnology* **2015**, *26*, 405705.
(28) Qadri, S. B.; Keller, T. M.; Laskoski, M.; Little, C. A.; Lubitz, P.; Osofsky, M. S.; Khan, H. R. *Appl. Phys. A: Mater. Sci. Process.* **2007**, *86*, 391.
(29) Wang, W.; Wang, S.; Ma, X.; Gong, J. *Chem. Soc. Rev.* **2011**, *40*, 3703.
(30) Sai Prasad, P. S.; Bae, J. W.; Jun, K.-W.; Lee, K.-W. *Catal. Surv. Asia* **2008**, *12*, 170.
(31) Melo, C. I.; Szczepanska, A.; Bogel-Lukasik, E.; Nunes da Ponte, M.; Branco, L. C. *ChemSusChem* **2016**, *9*, 1081.
(32) Upadhyay, P. R.; Srivastava, V. *Catal. Lett.* **2017**, *147*, 1051.
(33) Srivastava, V. *Catal. Lett.* **2014**, *144*, 1745.
(34) Pérez-Alonso, F. J.; Ojeda, M.; Herranz, T.; Rojas, S.; González-Carballo, J. M.; Terreros, P.; Fierro, J. L. G. *Catal. Commun.* **2008**, *9*, 1945.
(35) Gnanamani, M. K.; Hamdeh, H. H.; Jacobs, G.; Shafer, W. D.; Hopps, S. D.; Thomas, G. A.; Davis, B. H. *ChemCatChem* **2017**, *9*, 1303.
(36) Dorner, R. W.; Hardy, D. R.; Williams, F. W.; Davis, B. H.; Willauer, H. D. *Energy Fuels* **2009**, *23*, 4190.
(37) Gonzalez-Miquel, M.; Bedia, J.; Abrusci, C.; Palomar, J.; Rodriguez, F. *J. Phys. Chem. B* **2013**, *117*, 3398.
(38) Luska, K. L.; Bordet, A.; Tricard, S.; Sinev, I.; Grünert, W.; Chaudret, B.; Leitner, W. *ACS Catal.* **2016**, *6*, 3719.
(39) Zanatta, M.; Girard, A. L.; Marin, G.; Ebeling, G.; Dos Santos, F. P.; Valsecchi, C.; Stassen, H.; Livotto, P. R.; Lewis, W.; Dupont, J. *Phys. Chem. Chem. Phys.* **2016**, *18*, 18297.
(40) Zanatta, M.; Dos Santos, F. P.; Biehl, C.; Marin, G.; Ebeling, G.; Netz, P. A.; Dupont, J. *J. Org. Chem.* **2017**, *82*, 2622.
(41) Nguyen, L. T. M.; Park, H.; Banu, M.; Kim, J. Y.; Youn, D. H.; Magesh, G.; Kim, W. Y.; Lee, J. S. *RSC Adv.* **2015**, *5*, 105560.
(42) Po, H. N.; Senozan, N. M. *J. Chem. Educ.* **2001**, *78*, 1499.
(43) de Levie, R. *Chem. Educ.* **2002**, *7*, 132.
(44) Wang, W.; Wang, S.; Ma, X.; Gong, J. *Chem. Soc. Rev.* **2011**, *40*, 3703.
(45) James, O. O.; Chowdhury, B.; Mesubi, M. A.; Maity, S. *RSC Adv.* **2012**, *2*, 7347.
(46) Ojeda, M.; Nabar, R.; Nilekar, A. U.; Ishikawa, A.; Mavrikakis, M.; Iglesia, E. *J. Catal.* **2010**, *272*, 287.
(47) Porosoff, M. D.; Yan, B.; Chen, J. G. *Energy Environ. Sci.* **2016**, *9*, 62.
(48) Yang, H.; Zhang, C.; Gao, P.; Wang, H.; Li, X.; Zhong, L.; Wei, W.; Sun, Y. *Catal. Sci. Technol.* **2017**, *7*, 4580.
(49) Cassol, C. C.; Ebeling, G.; Ferrera, B.; Dupont, J. *Adv. Synth. Catal.* **2006**, *348*, 243.
(50) Qiu, J.; Zhao, Y.; Li, Z.; Wang, H.; Fan, M.; Wang, J. *ChemSusChem* **2017**, *10*, 1120.
(51) Umpierre, A. P.; de Jesús, E.; Dupont, J. *ChemCatChem* **2011**, *3*, 1413.

DOI: 10.1021/acscatal.7b03804
ACS Catal. 2018, 8, 1621−1627

5.3. Results and Discussion

5.3.1. Catalytic activity of RuFe nanoparticles in the hydrogenation of CO_2 to formic acid

The bimetallic RuFe-nanoalloys were prepared by simple co-reduction/decomposition of $Fe(CO)_5$ and [Ru(methylallyl)$_2$(COD)] in 1-butyl-3-methylimiazolium bis(trifluoromethysulfono)imide (BMI.NTf$_2$) at 150°C under 18 bar of H_2. Employing this method, highly air sensitive black solution is obtained, containing RuFe-nanoalloys with a mean diameter of 1.7 ± 0.3 nm, characterized by HRTEM. The nanoalloys can be separated from the IL by the addition of dichloromethane followed by centrifugation and thoroughly washed with DCM to remove residual BMI.NTf$_2$. For further information see **publication II**.

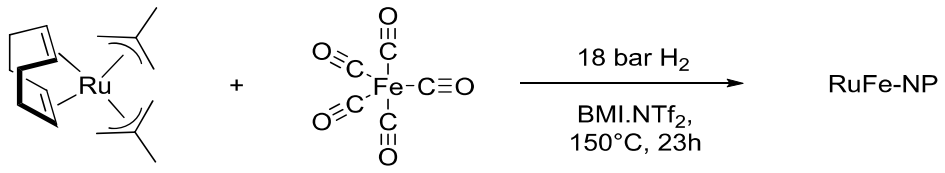


Figure 5.1 Synthetic scheme for the formation of RuFe-NP.

After the isolation of the as-formed RuFe-NP, these heterogeneous catalysts were re-dispersed in 1-butyl-3-methylimidazolium acetate (BMI.OAc) and after the addition of DMSO/D_2O the reactivity of the aforementioned catalysts toward the formation of FA at 60 °C (**table 5.1**) was tested. The RuFe-nanoparticles are active in the hydrogenation of CO_2 to FA. Here a TON value of up to 400 and a TOF of 23.52 h^{-1} with a concentration of a FA 0.14M (**table 5.1**, **entry 5**) can be achieved. No FA was formed using Fe NPs (4 nm-5 nm)[17] (**entry 2**, **table 5.1**), whereas when Ru NPs (2 nm - 3 nm)[18] were applied, FA

was observed, although the catalytic activity was significantly lower as with the bimetallic counterparts (**table 5.1**, **entry 3**). These results demonstrate a positive metal dilution effect.[19]

Table 5.1 CO_2 hydrogenation to HCO_2H by RuFe NPs, see also **table 2 publication II**[a)]

Entry	NPs	IL	D_2O/ DMSO[b)]	[FA]/ M	TON[d)]/TOF h^{-1}
1	RuFe	BMI.OAc	5%	0.11	56/2.33
2	Fe	BMI.OAc	5%	-	-
3	Ru	BMI.OAc	5%	0.08	19/0.79
4	RuFe	BMI.OAc	10%	0.07	34/1.42
5	RuFe[e]	BMI.OAc	5%	0.14	400/23.52
6	RuFe[f]	-	5%	-	-

Reaction conditions: 5.0 mg NPs, 36 mg IL (0.18 mmol), 33 mg D_2O (1.8 mmol), 2.84 g DMSO (36.4 mmol), CO_2/H_2 (1:2, 30 bar) 60 °C and 24h. [b)]Molar ratio of D_2O in DMSO. [c)]concentration of FA calculated with IL as internal standard. [d)]Moles of FA per moles of Ru surface atoms. [e)]1.0 mg NPs, 54 mg IL (0.27 mmol), 33 mg D_2O (1.8 mmol), 2.84 g DMSO (36.4 mmol), CO_2/H_2 (1:2, 30 bar) 60 °C and 17h. [f)]Without BMI.OAc.

Water might accelerate the reaction because of additional H-bonding in between H_2O, DMSO and IL and thus facilitate the active intermediate formation (M-H or M-O_2CH). Furthermore, it has been demonstrated that FA forms clusters with water and DMSO, stabilising the product thermodynamically.[20] Moreover, water has a strong influence on the structural organization and electronic properties of imidazolium based ILs.[21-22] Additional increases in water content decreased the FA production (**table 5.1**, **entry 4**).

It is important to note that no formic acid was observed in the absence of the BMI.OAc, which reflects its vital role in the hydrogenation of CO_2 to formic acid based on its buffering properties and stabilization of weak carbonic acid species, as already depicted in ***chapter 4***.[23]

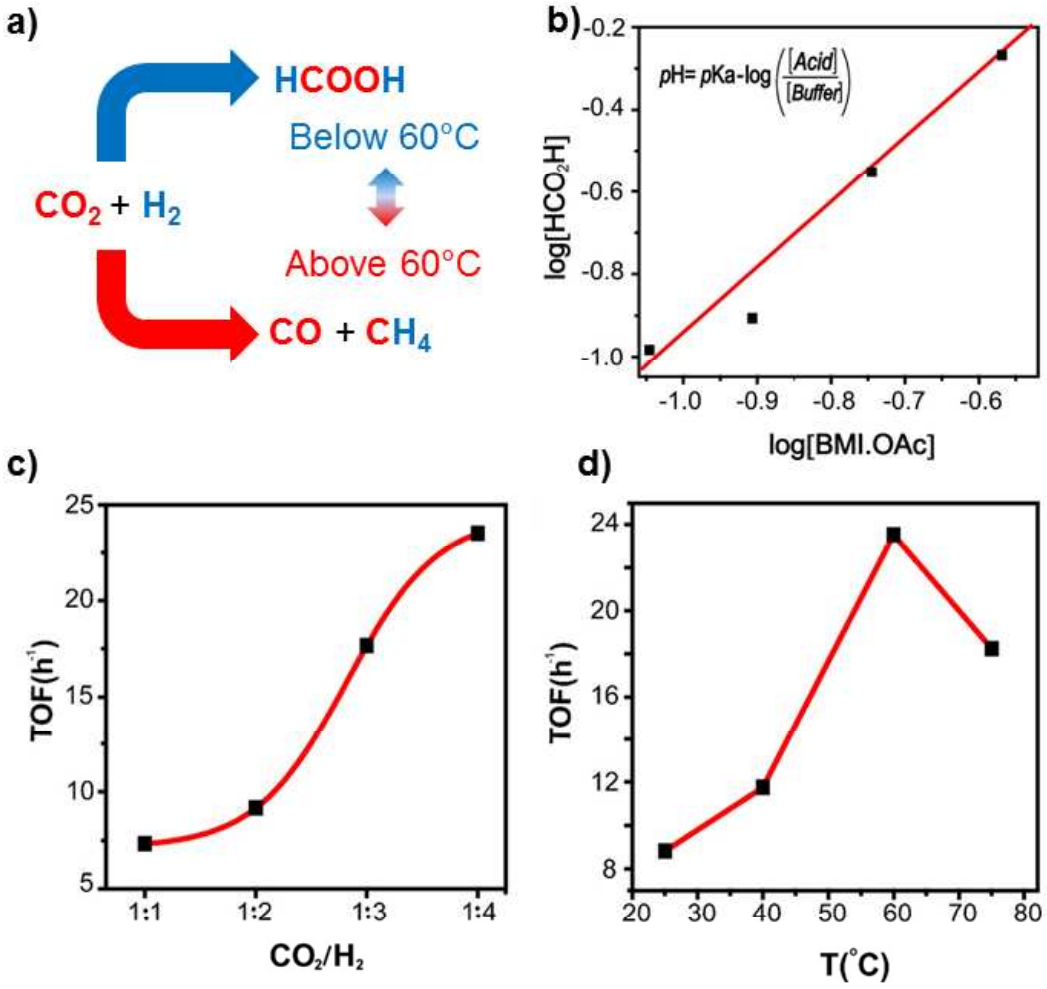


Figure 5.2 a) depiction of the competiting rWGS reaction and the desired hyfrogenation to FA b) relationship between the amount of BMI.OAc IL and HCO_2H on log log scale, see also **publication II figure 5** c) the TOF and the gas composition, see also **publication II figure 4a**; d) the temperature and the TOF towards FA, see also **publication II figure 4b**. Reaction condition: 1.0 mg NPs, 33 mg D_2O (1.8 mmol), 2.84 g DMSO (36.4 mmol), CO_2/H_2 (1:4, 30 bar) 60 °C and 17h.

Furthermore, as observed with $[Ru_3(CO)_{12}]$ catalyst in ***chapter 4*** the ionic liquid (BMI.OAc) played an important role not only in the formation of active species but also in the stabilization of the FA. Indeed, a linear relationship

between the concentration of IL and the concentration of FA in double logarithm scale (**Figure 5.2b** and **figure 5 in publication II**) was observed.

In order to improve the catalytic activity of RuFe-nanoparticles the effect of the CO_2 and H_2 gas mixture was studied. The TOF of the catalyst is significantly dependent on the concentration of H_2 in the gas phase (**Figure 5.2c** and **publication II figure 4a**). So the TOF can be increased to 23.5 h^{-1} at a ratio of 1:4 (CO_2/H_2). This indicates, the hydrogen activation to be the turnover limiting step for RuFe-nanoparticles.

Upon increasing the temperature the TOF of the catalyst can be increased until reaching a maximum value at 60°C, reaching here a TOF of 23.5 h^{-1}, see **Figure 5.2d** and **publication II figure 4b**. Upon further increasing the temperature the observed TOF towards FA decreased due to the preferred formation CO and CH_4 as indicated by headspace analysis (for further information refer to publication II). This side reaction represented the main hurdle for the catalyst optimization (depicted in **Figure 5.2a**)

5.4. Concluding remarks on the utilization of heterogeneous catalyst for the hydrogenation of CO_2 to formic acid

The here studied RuFe nanoparticles did show catalytic activity towards the hydrogenation of CO2 to formic acid. Under optimised conditions a TON of up to 400 and a TOF up to 24 h^{-1} can be achieved. Upon increasing the temperature the dehydration of formic acid took place, limiting the operational window for the studied reaction.

Even though the presented RuFe-NP show catalytic activity towards the hydrogenation of CO_2 to formic acid, the measured rates are far lower than those obtained with the simple complex $[Ru_3(CO)_{12}]$. For comparison, the highest measured TON with RuFe-Np is 400 and the highest TOF is 23.5 h^{-1}. In comparison, a TON of 17,000 and a TOF of 300 h^{-1} was observed with $[Ru_3(CO)_{12}]$ as the pre-catalyst under similar conditions. Furthermore the homogeneous catalyst shows a higher selectivity towards FA then their heterogeneous counterparts, as under increased reaction temperature with RuFe-nanoparticles the formation CO instead of FA was observed. In contrast to this observation the homogenous counterpart can easily be operated up to a reaction temperature of 100°C without a loss of selectivity.

The activity of the heterogeneous RuFe-nanoparticles in the rWGS (CO + H_2O) is observed in the gas phase already at a temperature of 75°C) can be utilized in the hydrophobic IL BMI.NTf_2 to yield hydrocarbons. The mechanism for the formation of hydrocarbons is believed to follow the reverse Water-Gas-Shift reaction followed by the Fischer-Tropsch synthesis, which is thermodynamically favoured by the hydrophobic nature of the utilized IL BMI.NTf_2 shifting the thermodynamic equilibrium to the side of CO, by expelling water from the catalyst surface. The formed CO is in subsequent a reaction hydrogenated to the aforementioned hydrocarbons. For further information see publication **II**.

As the aim of this thesis was the synthesis of FA from CO_2 and H_2, and the very simple catalyst precursor $[Ru_3(CO)_{12}]$ (**25**) outperformed the heterogeneous counterparts, the attention was shifted towards homogeneous catalysts with designed ligand - and complex properties. Hereby the attention

was laid upon the electronic and mechanistic aspects concerning the hydrogenation of CO_2 to FA.

5.5 Publication II Supporting Information: Selective Carbon Dioxide Hydrogenation Driven by Ferromagnetic RuFe Nanoparticles in Ionic Liquid

Contribution of the author: The author contributed to this publication by drawing the research plan for the hydrogenation of CO_2 to formic acid with RuFe nanoparticles. Catalyst synthesis, catalytic experiments and the synthesis of ionic liquids were performed by Dr. Irfan Quadir, in Porto Alegre, Brazil at the Universidade Federal do Rio Grande do Sul (UFRGS). The author furthermore contributed in to the preparation of the manuscript.

Reprinted with permission from *ACS Catal.* **2018**, 8, 2, 1621-1627 Copyright 2018 American Chemical Society.

Supporting information

Selective Carbon Dioxide Hydrogenation Driven by Ferromagnetic RuFe Nanoparticles in Ionic Liquids

Muhammad I. Qadir, [‡] Andreas Weilhard, [†] Jesum A. Fernandes, [†] Imanol de Pedro,[⊥] Bruno J. C. Vieira, [▽] João C. Waerenborgh[▽] and Jairton Dupont[*‡†]

[‡]Institute of Chemistry–UFRGS–Av. Bento Gonçalves, 9500, Porto Alegre, 91501-970, RS, Brazil

[†]GSK Carbon Neutral Laboratories for Sustainable Chemistry–NG8 2GT, University of Nottingham, UK

[⊥]Departmento CITIMAC, Facultad de Ciencias, Universidad de Cantabria, 390005 Santander, Spain

[▽]Centro de Ciências e Tecnologias Nucleares, Instituto Superior Técnico, Universidade de Lisboa, 2695-066 Bobadela LRS, Portugal

* jairton.dupont@ufrgs.br

Table of contents

Content	Pages
1. XRD analysis	**S2**
2. XPS analysis of RuFe NPs	**S3**
3. Mössbauer analysis of RuFe NPs	**S5**
4. Magnetic measurements of RuFe NPs	**S7**
5. Recyclability of RuFe NPs	**S11**
6. High pressure ^{13}C NMR using Ru NPs	**S12**
7. Representative ^{1}H NMR spectrum for the hydrogenation of CO_2 to free formic acid (HCO_2H)	**S13**
8. CO_2 hydrogenation to hydrocarbons by different catalysts from literature	**S14**
9. Heterogeneous CO_2 hydrogenation to free formic acid by different heterogeneous catalysts from literature	**S15**
10. Heterogeneous CO_2 hydrogenation to formate (HCO_2^-) by different heterogeneous catalysts from literature	**S16**
11. References	**S17**

1. XRD analysis

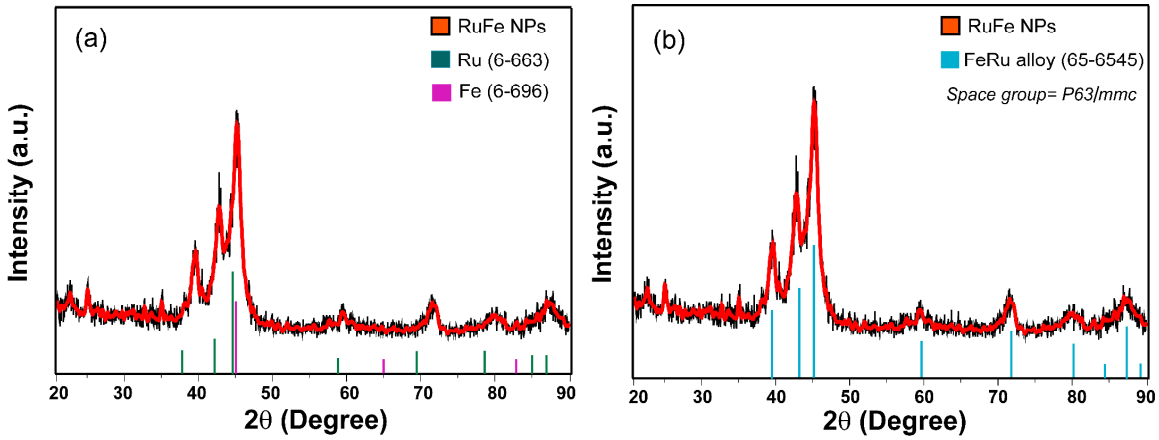


Figure S1. XRD measurement of isolated RuFe NPs, the peaks positions were shifted to higher angles, relative to Ru, indicating that Fe was incorporated into the Ru hcp structure to form an alloy phase. Similar trend has been reported else where.[1]

2. XPS analysis of RuFe NPs

X-ray photoelectron spectroscopy (XPS) measurements were performed using a Kratos AXIS Ultra DLD instrument. The chamber pressure during the measurements was 5×10^{-9} Torr. Wide energy range survey scans were collected at pass energy of 80 eV in hybrid slot lens mode and a step size of 0.5 eV. High-resolution data on the Fe 2p, Ru 3d, C 1s, Cl 2p, F 1s, O 1s, N 1s and S 2p photoelectron peaks was collected at pass energy 20 eV over energy ranges suitable for each peak, and collection times of 5 min, step sizes of 0.1 eV. The charge neutraliser filament was used to prevent the sample charging over the irradiated area. The X-ray source was a monochromated Al Kα emission, run at 10 mA and 12 kV (120 W). The energy range for each 'pass energy' (resolution) was calibrated using the Kratos Cu $2p_{3/2}$, Ag $3d_{5/2}$ and Au $4f_{7/2}$ three-point calibration method. The transmission function was calibrated using a clean gold sample method for all lens modes and the Kratos transmission generator software within Vision II. The data were processed with CASAXPS (Version 2.3.17). The high resolution data was charge corrected to the reference $C_{aliphatic}$ 1s signal at 284.8 eV.[2]

Table S1. XPS fittings of Ru3d5/2 and Fe2p3/2.

Compound	Binding energy (eV)	FWHM (eV)	Atomic (%)
$Ru3d_{5/2}$			
Ru^{0}	280.2	1.11	32.4
Ru^{4+}	281.9	1.60	23.9
Ru^{4+} (sat)	282.8	1.30	3.87
$Fe2p_{3/2}$			
Fe^{0}	706.7	1.67	0.76
Fe^{2+} (oct)	709.4	1.55	8.10
Fe^{3+} (oct)	710.5	3.08	35.3
Fe^{3+} (thd)	713.1	2.87	8.56
Fe^{2+} (sat)	715.7	3.77	6.14
Fe^{3+} (sat)	718.7	3.70	7.92

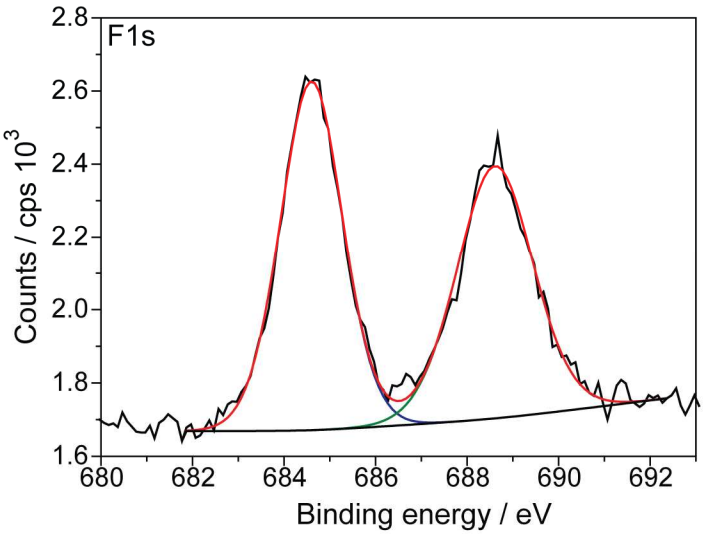


Figure S2. XPS measurement of F 1s region in RuFe NPs. The F1s signal showed a peak at 684.8 eV, which may be attributed to the interaction of fluorine of anion of IL with RuFe NPs.

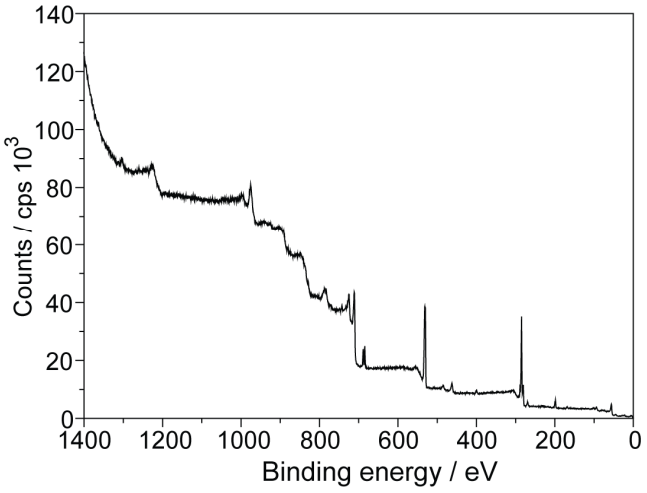


Figure S3. XPS wide scan of RuFe NPs.

3. Mössbauer analysis of RuFe NPs

Room temperature Mössbauer spectrum of as prepared RuFe NPs (Figure 2a, 2b and Table S2), showed two absorption peaks in the velocity range between -0.5mm/s and 1.5 mm/s, which may be fitted by a singlet and a doublet. The estimated isomer shifts (Table S2) relative to metallic αFe at 295 K, IS, and quadrupole splitting, QS, are similar to those reported for FeRu catalysts supported on MgO[3] and SiO_2.[4-5] The singlet is attributed to FeRu alloy. The IS of the doublet is consistent with high-spin Fe^{3+}, S=5/2, and may be assigned to a nano-sized Fe^{3+} oxide which is superparamagnetic at room temperature.[6] In addition to these subspectra a sextet with very low intensity peaks is also observed at 295 K. The estimated parameters for this sextet are typical of metallic αFe. In order to confirm the analysis of the 295 K data, a spectrum was also obtained at 4 K. Instead of the doublet, a six-line pattern with broad peaks is now observed.

This pattern may be approximated by two magnetic sextets with IS and magnetic hyperfine fields, B_{hf} , typical of Fe^{3+} (S=5/2) oxides. The sum of the relative areas of these sextets suggests the incorporation of approximately 68% of the Fe in Fe^{3+} oxides. These are nano-sized since at 295 K they give rise to a doublet. In fact at room temperature the relaxation time τ_R for the reversal of magnetization in nano-sized oxide particles is smaller than the Larmor precession time τ_L of the nuclear magnetic moment and only a quadrupole doublet is observed in the Mössbauer spectrum. As the temperature decreases τ_R increases and at 4K it is already higher than τ_L allowing the observation of the magnetic sextets.[7] At 4 K the singlet due to FeRu alloy is still present evidencing no magnetic transition. This is not surprising considering that the iron-ruthenium alloys above 23%Ru content are paramagnets. The increase in IS relative to 295 K is explained by the second order Doppler shift. Finally a very low intensity sextet with parameters typical of αFe is also present. The sum of the relative areas of the sextets due to the nano-sized Fe^{3+} oxides at 4 K is slightly higher than the relative area of the doublet at 295 K. The relative areas of the FeRu alloy and α Fe sub-spectra are correspondingly lower at 295 K. As explained by Niemantsverdriet[4] and Nagorny[3] this results from a lower Debye temperature of the nano-sized Fe^{3+} oxides, which suggests they are a surface phase probably formed at the surface of the FeRu alloy particles. The Mössbauer data therefore shows the presence of FeRu alloy, nano-sized Fe^{3+} oxides and a

minor amount of αFe (Table S2). The nano-sized Fe^{3+} oxides are probably due to surface oxidation of the FeRu NPs.

Table S2. Estimated parameters from the Mössbauer spectra of RuFe NPs taken at room temperature (295 K) and 4 K.

Sample	Temperature	Contribution of Fe phase	IS (mm/s)	QS (mm/s)	B_{hf} (T)	I (%)
RuFe NPs	295 K	FeRu alloy	0.05	0.05	-	34
		Fe^{3+}	0.31	0.89	-	60
		αFe	0.00	0.00	32.8	6
RuFe NPs	4 K	FeRu alloy	0.08	0.06	-	29
		Fe^{3+}	0.51	-0.03	50.1	25
		Fe^{3+}	0.50	-0.13	46.4	43
		αFe	0.12	0.00	34.5	3

*IS (mm/s) isomer shift relative to metallic α-Fe at 295 K; QS (mm/s) quadrupole splitting; B_{hf} (tesla) magnetic hyperfine field; I relative areas. Estimated errors are ± 0.02 mm s^{-1} for IS and QS, Γ, < 0.2 T for B_{hf} and ± 2% for *I*.

4. Magnetic measurements of RuFe NPs

Figure S4a displays the variation of magnetization curve with temperature, measured under an applied field of 50 Oe in the zero-field-cooled (ZFC) and field-cooled-warming (FCW) protocols. As can be seen, upon an increase in the temperature from 2 K, the ZFC magnetization increases and reaches a maximum with a value near of 60 K. This temperature could be considerate the blocking temperature (T_B), defined as the temperature at which the NPs moments do not relax during the time scale of the dc magnetization measurement. The value of T_B obtained is relatively consistent with the nanoscale dimensions detected by TEM analysis, using the well-known expression $K_{eff}V \approx 25k_\beta T_B$ with K_{eff} being the effective magnetic anisotropy constant.[8] To derive rough volume estimation, it is possible to assume the order of magnitude of a bulk common iron oxide ($\approx 1 \times 10_{-5}$ erg/cm^3). With this, we get a mean size for the diameter D ≈ 3 nm. In contrast with the typical behavior of superparamagnetic (SPM) ensembles, in which the ZFC and FC curves converge just above T_B, an irreversibility between the ZFC and FCW curves persists even at 300 K, far above the blocking temperature; this behavior may be attributed to enlarged anisotropy in the system or strong interparticle interactions denoting similar characteristic than reported in others superspin glass (SSG) systems that are ferromagnetic in the ground state.[9] Moreover, instead of the expected monotonic rise with decreasing temperature of superparamagnetic coupling, the FCW magnetization reaches a maximum at ≈ 47 K and then decreases below this temperature (see inset of Figure S4a). A drop in the FCW magnetization below a critical temperature is usually associated with the collective freezing of the system and can indicate the presence of a spin-glass like phase.[10]

The magnetic behavior detected of Figure S4a indicates that a deeper analysis of magnetization dynamics in the NP ensemble is necessary to classify the magnetic coupling of these NPs. To this end, low-amplitude (H_{AC}= 1 Oe) ac susceptibility curves were measured from 5 to 100 K as a function of the frequency, between 100 and 10^4 Hz, in the absence of a direct current (dc) applied field (Figure S4b and S4c), which allows us to probe the relaxation of particles in different time windows. As can be seen, the peak

position of the temperature of freezing, T_f, shifts toward higher values with increasing frequency in the real part of the susceptibility M′(T).

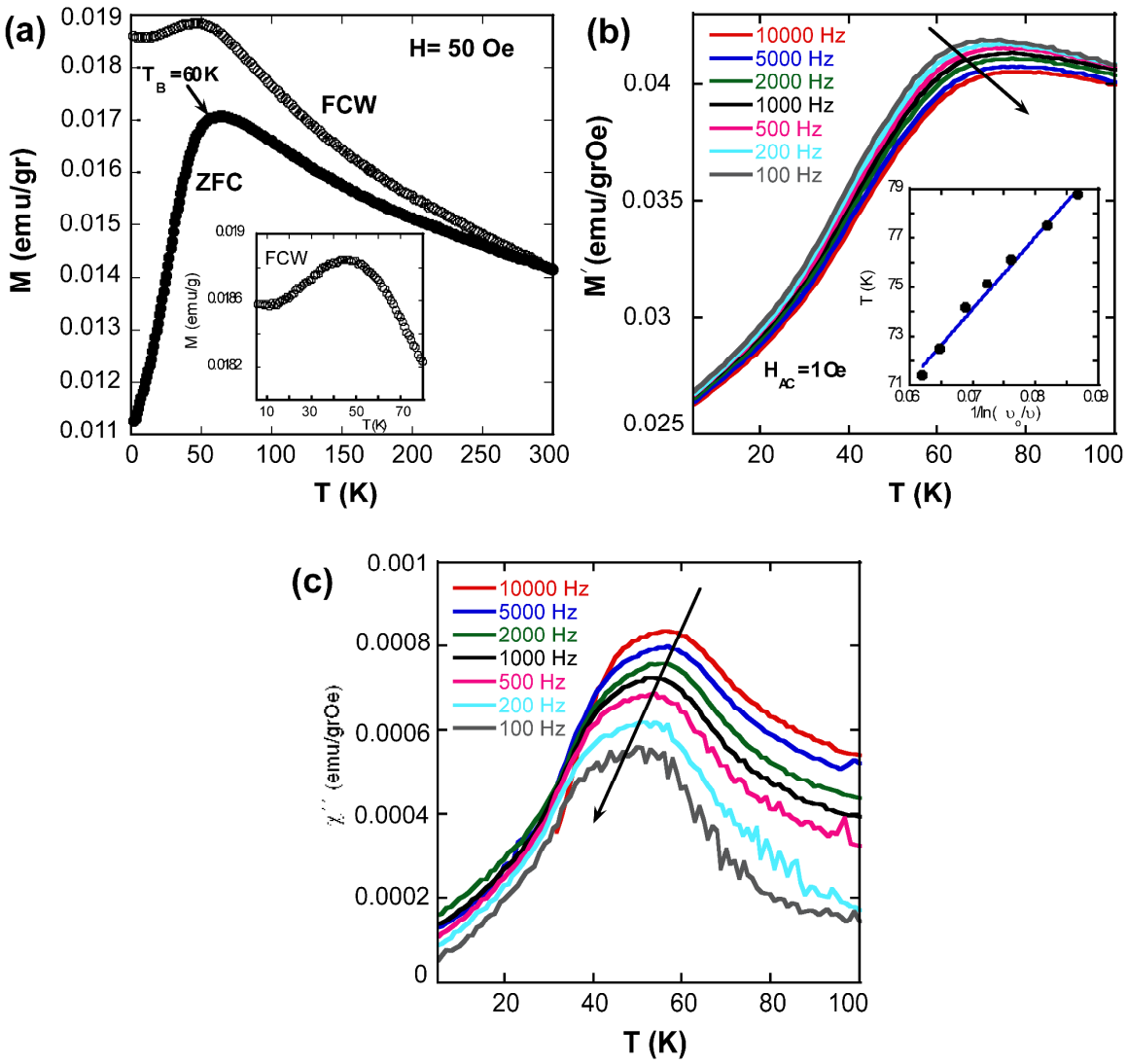


Figure S4. (a) Temperature dependence of magnetization under zero-field cooled (ZFC) and field cooled-warming (FCW) protocols at 50 Oe. The inset displays an expanded view of MFCW below 75 K, (b) real part (M') of the ac magnetization measured under different excitation frequencies from 10000 to 100 Hz. The blue solid line of the inset of figure shows the fit to the Vogel-Fulcher model, and (c) imaginary part (M'') of the ac magnetization measured under different excitation frequencies from 10000 to 100 Hz.

The peak shift per frequency decade is quantified in the phenomenological parameter $\phi = \Delta T_f/T_f \Delta(\log f)$. Depending on the interactions between the magnetic moments, T_f can be weakly (strong interactions) or strongly (weak interactions) dependent on the frequency.

In the presented NPs, $\phi = 0.025$. This calculated value is outside the expected range for superparamagnetic compounds ($\phi = 0.100–0.130$) but is in the range of many canonical spin glass systems ($\phi = 0.005–0.06$).[10] This scenario is usually considered as fingerprint of the spin-glass-like behavior in NPs. The characterization of the collective freezing process through which the system crosses into the low-temperature glassy regime was initially performed by fitting T_f to the Neel-Arrhenius (NA) law. The fitting yielded unphysical results. This issue clearly shows that the dynamics of these NPs cannot be explained with a non-interacting particle model. Thus, we extended our analysis to the Vogel-Fulcher (VF) model of relaxation for interacting particles or spin clusters with uniaxial anisotropy that takes into account weak interparticle interactions.

$$\tau = \tau_0 exp\left[\frac{E_a}{K_B(T_B - T_0)}\right]$$

Ea is the anisotropy energy barrier and τ_0 is the relaxation time of individual NP. The term T_o is the characteristic temperature which gives a qualitative measure of the interparticle interaction energy. The obtained fitted (inset of Figure S4b) parameters have reasonable values of Ea = 292 K, $\tau_0 = 1.9 \times 10^{-13}$s, and $T_o = 54$ K. The proximity of the fitted value T_0 to the cusp in the FCW curve indicates collective freezing below 50 K. In the absence of an external magnetic field, the E_a can be assumed to be proportional to the particle volume V, $E_a = K_{eff} V \sin^2\theta$, where K_{eff} is an effective magnetic anisotropy constant and θ is the angle between the magnetic moment of the particle and its easy magnetization axis. Using the average particle radii from TEM data and assuming that are spherical particles, we obtained the values of $K_{eff} = 1.534 \times 10^{-3}$ erg/cm^3. The resulting effective anisotropy is quite larger than the magnetocrystalline anisotropy constant of most common iron oxides $\approx 1 \times 10^{-5}$ erg/cm^3, and therefore some contribution can be detected from the surface spins.[11]

In order to study the response of magnetization to the applied magnetic field, we have measured the M(H) curves within ± 80 kOe range at two selected temperatures: 300 and 5 K (Figure 2c). M(H) loops for both temperatures display nonsaturating values of magnetization, this feature being more remarkable in the case of 5 K. This issue could be relate with the presence of paramagnetic contribution of the FeRu alloy[12] in the NPs as

detected in Mossbauer spectroscopy. In addition, a small hysteresis loop is found (H_C = 208 and 410 Oe, Mr = 3.7 and 8.7 emu/g for 300 and 5 K, respectively, see the inset in Figure 2c), as expected from the splitting of the $M_{ZFC}(T)$ and $M_{FCW}(T)$ curves up to T = 300 K (Figure S4a). A striking consequence of the different orientation of the surface and core spins, as well as the large number of uncompensated spins at the shell of the NPs is the observation of exchange bias (EB) (i.e. a horizontal shift in the M–H loop and an increase in coercivity after cooling in a magnetic field). Recent experiments have demonstrated that core/shell particles Fe/γ-Fe_2O_3 core/shell, core/void/shell NPs display this phenomenon with a collective freezing of spins into a super spin glass-like state, mediated by dipolar interparticle interactions.[13] In order to investigate the EB effect in these NPs, the sample was cooled from 300 down to 5 K under a constant applied magnetic field of 50 KOe (H_{cool}). After that, a hysteresis loop was recorded between -50 and 50 kOe at T = 5 K (see inset of Figure 2c). The EB field[14] is denoted as the horizontal shift of the central point of the loop measured under a given H_{cool}, relative to that measured under H_{cool} = 0 loop, i.e., H_{EB} = _(H_{C1} + H_{C2})/2, where H_{C1} and H_{C2} are the left and right coercive fields, respectively. In these NPs, H_{EB} reaches a value of ~ 110 Oe at 5 K. Therefore; we suggest here the following explanation for the existence of a low-temperature EB effect. In the presence of an applied magnetic field, the small fraction of FM Fe core spins align parallel to the field direction during the cooling process from $T>T_B$ down to $T_f<T>T_B$, while the magnetically disordered iron oxide spins thermally fluctuate. Therefore, these (core)@(shell) nanoparticulated system is characterized by a structurally disordered shell that, rather than being AFM, behave as a SG-like system due to its reduced dimensionality of NPs.

5. Recyclability of RuFe NPs

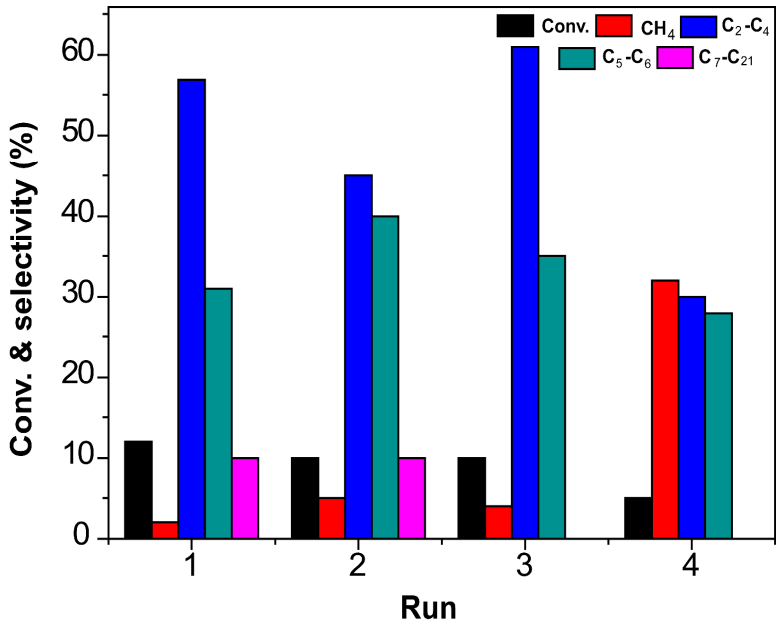


Figure S5. Recyclability of RuFe NPs in BMI.NTf_2 IL; Cat. 20 mg, IL= 0.5 g, 8.5 bar (CO_2/H_2, 1:4), 150 °C and 64 h. CO (10%) was detected in forth run.

6. High-pressure ^{13}C-NMR spectrum using Ru NPs

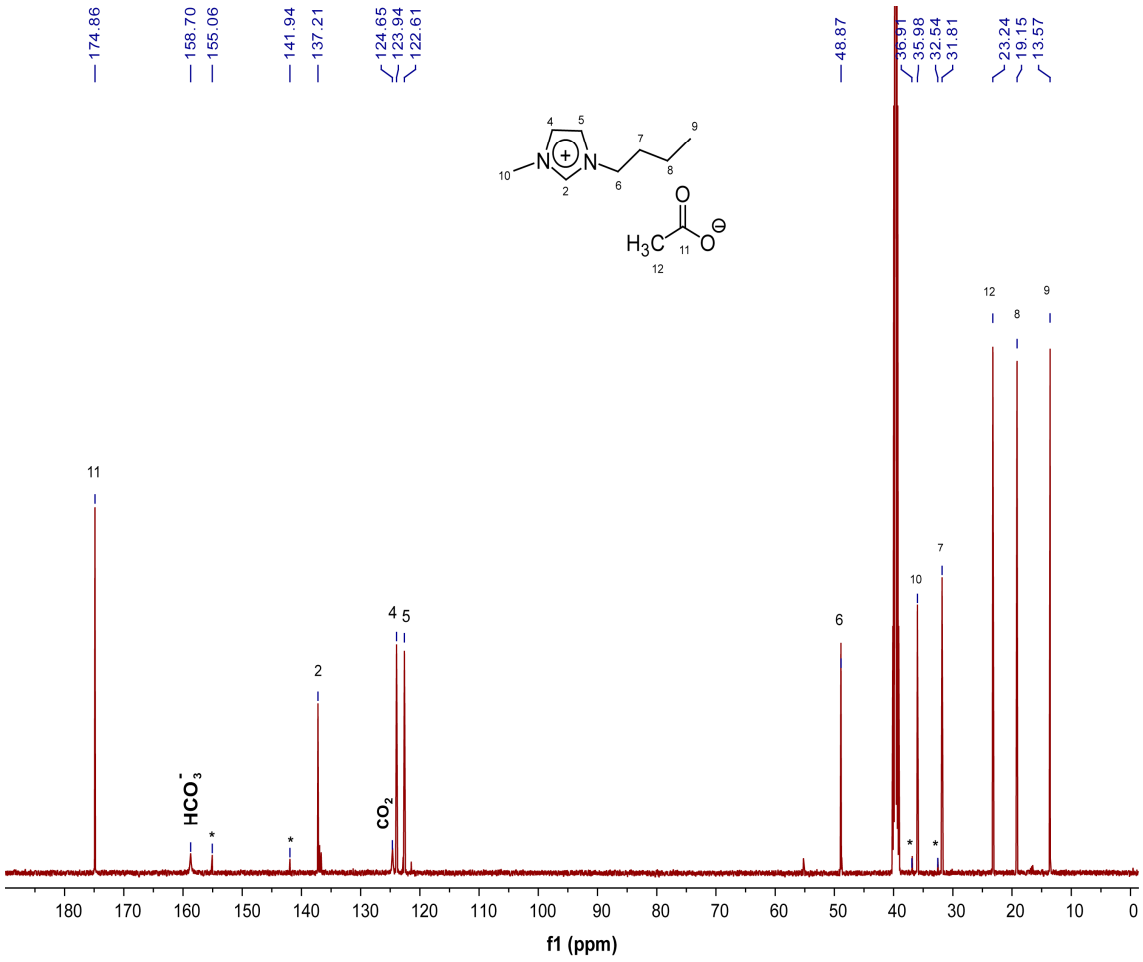


Figure S6. High-pressure ^{13}C{H}-NMR at 25 °C of BMI.OAc/D_2O/DMSO-d_6 using Ru NPs (2 mg) at 40 bar of CO_2/H_2 (1:1). (*-Signals of CO_2-imidazolium adduct)

7. Representative ^{1}H NMR spectrum for the hydrogenation of CO_2 to formic acid (HCO_2H)

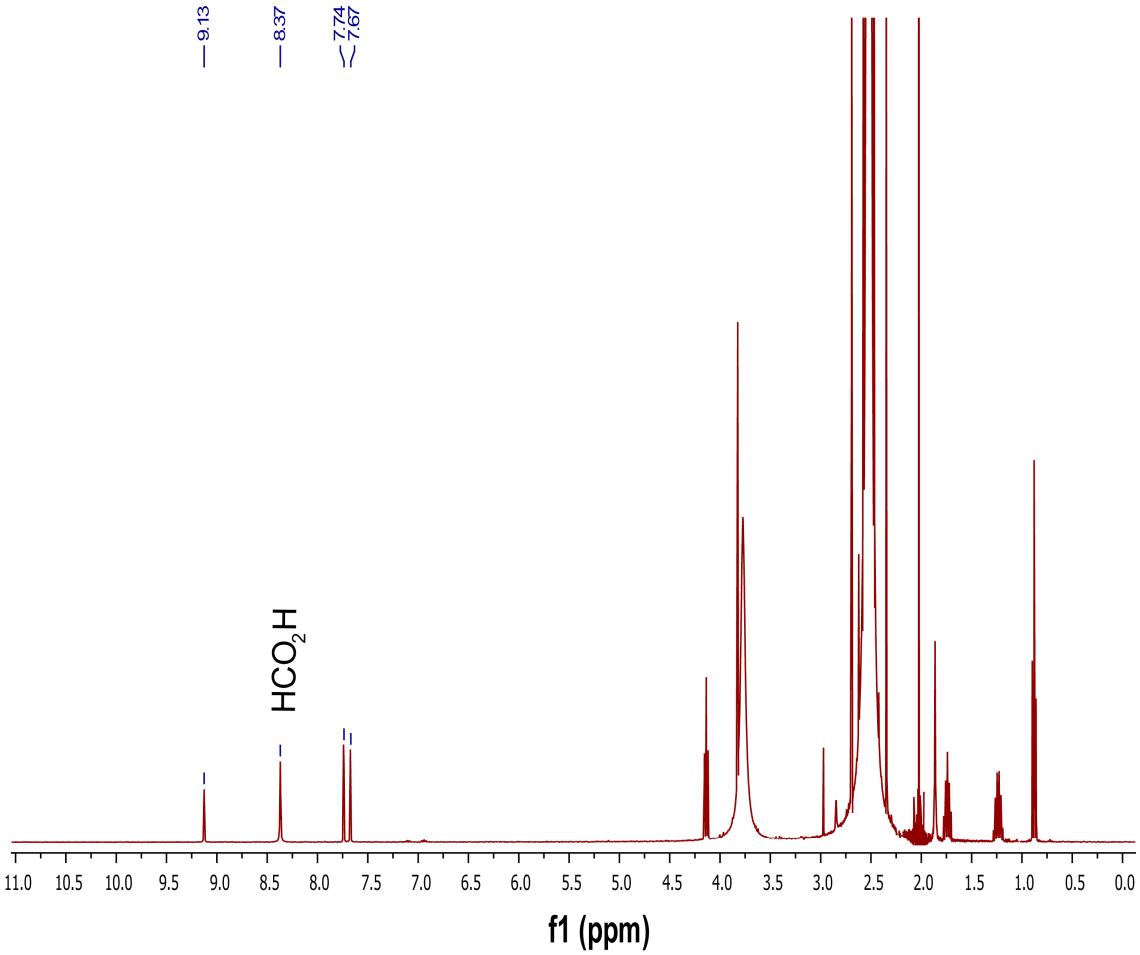


Figure S7. Typical ^{1}H NMR spectrum of a CO_2 hydrogenation to formic acid (HCO_2H) in DMSO/D_2O/BMI.OAc.

8. CO_2 hydrogenation to hydrocarbons by different heterogeneous catalysts from literature

Table S3. Summary of catalytic hydrogenation of CO_2 by Fischer-Tropsch by different catalysts from literature [a]

Ref.	Type of Cat.	Cat.	Conv. (%)	T/t	*P* (bar)	Selectivity (%)			
						CO	CH_4	C_2-C_4	$>C_{5+}$
[15]	Fixed-bed	Co-Pt/Al_2O_3	6.8	220 °C	19	-	93.1	6.8	-
[16]	Fixed-bed	Co-Fe-K	27.2	270 °C	9.2	13.9	70.8	13.2	0.4
[17]	Fixed-bed	Co-Fe-K	14.5	240 °C	12	15.1	54.3	26.7	-
[18]	Fixed-bed	CeO_2-Pt@mSiO_2-Co	10	250 °C		-	60	40	-
[19]	Fixed-bed	Fe_2O_3	40	350 °C	15	15	12	37	36
[20]	Fixed-bed	Fe-Zn-Zr/HY	22	340 °C/2 h	50	13	9	63	15
[21]	Fixed-bed	Fe_2O_3	26.9	300 °C	10	19	38	37	4
[22]	Fixed-bed	Fe_2O_3/ZIF	30	300 °C	30	18	20	52	10
[23]	Fixed-bed	FeK/Al_2O_3	54.4	400 °C	30	15	20	33.9	31.1
This study	-	Fe NPs	4.0	150 °C/64 h	8.5	-	28	72	-
This study	-	Ru NPs	10.0	150 °C/64 h	8.5	-	21	79	-
This study	-	RuFe NPs	12.0	150 °C/64 h	8.5	-	2	88	10

[a] Conditions: All the catalysts were pretreated under H_2 or CO at 300 °C for >12 h (except our).

9. Heterogeneous CO_2 hydrogenation to free formic acid by different heterogeneous catalysts from literature

Table S4. Summary of heterogeneous CO_2-hydrogenation to prepare free formic acid (HCO_2H) by different catalysts from literature

Ref.	Cat.	T (°C)	*P* (MPa)	Solvent	Time	TON/HCO_2H Conc. (M)	TOF [h^{-1}]
[24]	PdNi/CNT-GR	40	5	H_2O	15	6.4/0.02	0.43
[25]	Ru NPs	50	50	Ionic liquid (DAMI-TfO)	2	19,862/-	9,931
This study	Ru NPs	60	3	DMSO/H_2O/Ionic liquid (BMI.OAc)	24	19/1.18	0.79
This study	RuFe NPs	60	3	DMSO/H_2O/Ionic liquid (BMI.OAc)	24	56/1.66	2.33
This study	FeRu NPs	60	3	DMSO/H_2O/Ionic liquid (BMI.OAc)	17	400/2.03	23.52

10. Heterogeneous CO_2 hydrogenation to formate (HCO_2^-) by different heterogeneous catalysts from literature

Table S5. Summary of heterogeneous CO_2-hydrogenation systems to prepare formate (HCO_2^-) by different catalysts from literature

Ref.	Cat.	T (°C)	*P* (MPa)	Solvent	Base/Additive	Time	TON/formate conc. (M)	TOF/h
[26]	Ru/Ac	80	13.5	EtOH	NEt_3	1	10/0.05	10
[26]	Ru/Al_2O_3	80	13..5	EtOH	NEt_3	1	91/0.455	91
[27]	Au/Al_2O_3	70	40	EtOH	NEt_3	20	215/0.20	11
[27]	Au/TiO_2	70	40	EtOH	NEt_3	20	111/0.09	5.5
[28]	Au/TiO_2	40	18	NEt_3	NEt_3	52	855	16.4
[29]	MCM-Si-$(CH_2)_3$-NH_2-$RuCl_3$	80	14.2	EtOH	PPh_3/ NEt_3	1	1022/0.40	1022
[30]	Ir-PN-SBA-15	90	4	H_2O	NEt_3	1	1100/0.1	1100
[31]	PEI_{1800}-PN/Ir	120	4	H_2O	NEt_3	1	248/0.04	248
[32]	{Si-$(CH_2)_3$-$NH(CSCH_3)Ru$-CL_3-(PPH_3)}	80	18	H_2O	Amine-based ionic liquid	2	920/1.16	2
[33]	{Si-$(CH_2)_3$-$NH(CSCH_3)Ru$-CL_3-(PPH_3)}	80	18	H_2O	Amine-based ionic liquid	2	206/0.49	103

11. References

(1). Ye, T.-N.; Li, J.; Kitano, M.; Sasase, M.; Hosono, H., *Chem. Sci.* **2016,** 7, 5969-5975.
(2). Eltouny, N.; Ariya, P. A., *Phys. Chem. Chem. Phys.* **2014,** 16, 23056-23066.
(3). Nagorny, K.; Bubert, S., *J. Catal.* **1987,** 108, 112-134.
(4). Niemantsverdriet, J. W.; Aschenbeck, D. P.; Fortunato, F. A.; Delgass, W. N., *J. Mol. Catal.* **1984,** 25, 285-293.
(5). Martens, J. H. A.; Prins, R.; Niemantsverdriet, J. W., *J. Catal.* **1987,** 108, 259-262.
(6). Zboril, R.; Mashlan, M.; Petridis, D., *Chem. Mater.* **2002,** 14, 969-982.
(7). Herber, R. H., *The Mössbauer Effect and Its Application in Chemistry*. ACS: 1967; Vol. 68, p 196.
(8). Leal, B. C.; Scholten, J. D.; Alves, M. C. M.; Morais, J.; de Pedro, I.; Fernandez Barquin, L.; Dupont, J., *Inorg. Chem.* **2016,** 55, 865-870.
(9). Lin, C.-R.; Chiang, R.-K.; Wang, J.-S.; Sung, T.-W., *J. Appl. Phys.* **2006,** 99, 08N710.
(10). Khurshid, H.; Lampen-Kelley, P.; Iglesias, Ò.; Alonso, J.; Phan, M.-H.; Sun, C.-J.; Saboungi, M.-L.; Srikanth, H., *Sci. Rep.* **2015,** 5, 15054.
(11). Goya, G. F.; Berquó, T. S.; Fonseca, F. C.; Morales, M. P., *J. Appl. Phys.* **2003,** 94, 3520-3528.
(12). Qadri, S. B.; Keller, T. M.; Laskoski, M.; Little, C. A.; Lubitz, P.; Osofsky, M. S.; Khan, H. R., *Appl. Phys. A* **2007,** 86, 391-394.
(13). Nemati, Z.; Khurshid, H.; Alonso, J.; Phan, M. H.; Mukherjee, P.; Srikanth, H., *Nanotechnology* **2015,** 26, 405705.
(14). Denney, M. C.; Pons, V.; Hebden, T. J.; Heinekey, D. M.; Goldberg, K. I., *J. Am. Chem. Soc.* **2006,** 128, 12048-12049.
(15). Dorner, R. W.; Hardy, D. R.; Williams, F. W.; Davis, B. H.; Willauer, H. D., *Energ. Fuels* **2009,** 23, 4190-4195.
(16). Gnanamani, M. K.; Jacobs, G.; Hamdeh, H. H.; Shafer, W. D.; Liu, F.; Hopps, S. D.; Thomas, G. A.; Davis, B. H., *ACS Catal.* **2016,** 6, 913-927.
(17). Gnanamani, M. K.; Hamdeh, H. H.; Jacobs, G.; Shafer, W. D.; Hopps, S. D.; Thomas, G. A.; Davis, B. H., *ChemCatChem* **2017,** 9, 1303-1312.
(18). Xie, C.; Chen, C.; Yu, Y.; Su, J.; Li, Y.; Somorjai, G. A.; Yang, P., *Nano Lett.* **2017,** 17, 3798-3802.
(19). Lee, S.-C.; Jang, J.-H.; Lee, B.-Y.; Kim, J.-S.; Kang, M.; Lee, S.-B.; Choi, M.-J.; Choung, S.-J., *J. Mol. Catal. A: Chem.* **2004,** 210, 131-141.
(20). Rongxian, B.; Yisheng, T.; Yizhuo, H., *Fuel Process. Technol.* **2004,** 86, 293-301.
(21). Pérez-Alonso, F. J.; Ojeda, M.; Herranz, T.; Rojas, S.; González-Carballo, J. M.; Terreros, P.; Fierro, J. L. G., *Catal. Commun.* **2008,** 9, 1945-1948.
(22). Hu, S.; Liu, M.; Ding, F.; Song, C.; Zhang, G.; Guo, X., *J. CO2 Util.* **2016,** 15, 89-95.
(23). Ding, F.; Zhang, A.; Liu, M.; Zuo, Y.; Li, K.; Guo, X.; Song, C., *Ind. Eng. Chem. Res.* **2014,** 53, 17563-17569.
(24). Nguyen, L. T. M.; Park, H.; Banu, M.; Kim, J. Y.; Youn, D. H.; Magesh, G.; Kim, W. Y.; Lee, J. S., *RSC Adv.* **2015,** 5, 105560-105566.

(25). Upadhyay, P. R.; Srivastava, V., *Catal. Lett.* **2017,** 147, 1051-1060.
(26). Hao, C.; Wang, S.; Li, M.; Kang, L.; Ma, X., *Catal. Today* **2011,** 160, 184-190.
(27). Filonenko, G. A.; Vrijburg, W. L.; Hensen, E. J. M.; Pidko, E. A., *J. Catal.* **2016,** 343, 97-105.
(28). Preti, D.; Resta, C.; Squarcialupi, S.; Fachinetti, G., *Angew. Chem. Int. Ed.* **2011,** 50, 12551-12554.
(29). Yu, Y.-M.; Fei, J.-H.; Zhang, Y.-P.; Zheng, X.-M., *Chin. J. Chem* . **2006,** 24, 840-844.
(30). Xu, Z.; McNamara, N. D.; Neumann, G. T.; Schneider, W. F.; Hicks, J. C., *ChemCatChem* **2013,** 5, 1769-1771.
(31). McNamara, N. D.; Hicks, J. C., *ChemSusChem* **2014,** 7, 1114-1124.
(32). Zhang, Z.; Hu, S.; Song, J.; Li, W.; Yang, G.; Han, B., *ChemSusChem* **2009,** 2, 234-238.
(33). Zhang, Z.; Xie, Y.; Li, W.; Hu, S.; Song, J.; Jiang, T.; Han, B., *Angew. Chem.* **2008,** 120, 1143-1145.

5.6 References

1. Klankermayer, J.; Wesselbaum, S.; Beydoun, K.; Leitner, W., Selective Catalytic Synthesis Using the Combination of Carbon Dioxide and Hydrogen: Catalytic Chess at the Interface of Energy and Chemistry. *Angewandte Chemie International Edition* **2016,** *55* (26), 7296-7343.
2. Wang, W.-H.; Himeda, Y.; Muckerman, J. T.; Manbeck, G. F.; Fujita, E., CO2 Hydrogenation to Formate and Methanol as an Alternative to Photo- and Electrochemical CO2 Reduction. *Chemical Reviews* **2015,** *115* (23), 12936-12973.
3. Himeda, Y.; Miyazawa, S.; Hirose, T., Interconversion between Formic Acid and H2/CO2 using Rhodium and Ruthenium Catalysts for CO2 Fixation and H2 Storage. *ChemSusChem* **2011,** *4* (4), 487-493.
4. Ertem, M. Z.; Himeda, Y.; Fujita, E.; Muckerman, J. T., Interconversion of Formic Acid and Carbon Dioxide by Proton-Responsive, Half-Sandwich Cp*IrIII Complexes: A Computational Mechanistic Investigation. *ACS Catalysis* **2016,** *6* (2), 600-609.
5. Hull, J. F.; Himeda, Y.; Wang, W.-H.; Hashiguchi, B.; Periana, R.; Szalda, D. J.; Muckerman, J. T.; Fujita, E., Reversible hydrogen storage using CO2 and a proton-switchable iridium catalyst in aqueous media under mild temperatures and pressures. *Nat Chem* **2012,** *4* (5), 383-388.
6. Schaub, T.; Paciello, R. A., A Process for the Synthesis of Formic Acid by CO2 Hydrogenation: Thermodynamic Aspects and the Role of CO. *Angewandte Chemie International Edition* **2011,** *50* (32), 7278-7282.
7. Bulushev, D. A.; Ross, J. R. H., Heterogeneous catalysts for hydrogenation of CO2 and bicarbonates to formic acid and formates. *Catalysis Reviews* **2018,** *60* (4), 566-593.
8. Álvarez, A.; Bansode, A.; Urakawa, A.; Bavykina, A. V.; Wezendonk, T. A.; Makkee, M.; Gascon, J.; Kapteijn, F., Challenges in the Greener Production of Formates/Formic Acid, Methanol, and DME by Heterogeneously Catalyzed CO2 Hydrogenation Processes. *Chemical Reviews* **2017,** *117* (14), 9804-9838.
9. Farlow, M. W.; Adkins, H., The Hydrogenation of Carbon Dioxide and a Correction of the Reported Synthesis of Urethans. *Journal of the American Chemical Society* **1935,** *57* (11), 2222-2223.
10. Shao, X.; Xu, J.; Huang, Y.; Su, X.; Duan, H.; Wang, X.; Zhang, T., Pd@C3N4 nanocatalyst for highly efficient hydrogen storage system based on potassium bicarbonate/formate. *AIChE Journal* **2016,** *62* (7), 2410-2418.
11. Lee, J. H.; Ryu, J.; Kim, J. Y.; Nam, S.-W.; Han, J. H.; Lim, T.-H.; Gautam, S.; Chae, K. H.; Yoon, C. W., Carbon dioxide mediated, reversible chemical hydrogen storage using a Pd nanocatalyst supported on mesoporous graphitic carbon nitride. *Journal of Materials Chemistry A* **2014,** *2* (25), 9490-9495.
12. Park, H.; Lee, J. H.; Kim, E. H.; Kim, K. Y.; Choi, Y. H.; Youn, D. H.; Lee, J. S., A highly active and stable palladium catalyst on a g-C3N4 support for direct formic acid synthesis under neutral conditions. *Chemical Communications* **2016,** *52* (99), 14302-14305.

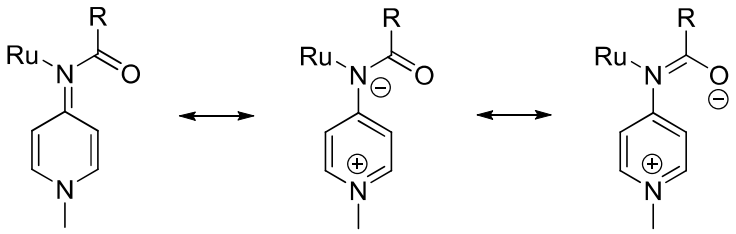
13. Nguyen, L. T. M.; Park, H.; Banu, M.; Kim, J. Y.; Youn, D. H.; Magesh, G.; Kim, W. Y.; Lee, J. S., Catalytic CO2 hydrogenation to formic acid over carbon nanotube-graphene supported PdNi alloy catalysts. *RSC Advances* **2015,** *5* (128), 105560-105566.
14. Preti, D.; Resta, C.; Squarcialupi, S.; Fachinetti, G., Carbon Dioxide Hydrogenation to Formic Acid by Using a Heterogeneous Gold Catalyst. *Angewandte Chemie International Edition* **2011,** *50* (52), 12551-12554.
15. Filonenko, G. A.; Vrijburg, W. L.; Hensen, E. J. M.; Pidko, E. A., On the activity of supported Au catalysts in the liquid phase hydrogenation of CO2 to formates. *Journal of Catalysis* **2016,** *343*, 97-105.
16. Upadhyay, P. R.; Srivastava, V., Selective hydrogenation of CO2 gas to formic acid over nanostructured Ru-TiO2 catalysts. *RSC Advances* **2016,** *6* (48), 42297-42306.
17. Krämer, J.; Redel, E.; Thomann, R.; Janiak, C., Use of Ionic Liquids for the Synthesis of Iron, Ruthenium, and Osmium Nanoparticles from Their Metal Carbonyl Precursors. *Organometallics* **2008,** *27* (9), 1976-1978.
18. Prechtl, M. H. G.; Scariot, M.; Scholten, J. D.; Machado, G.; Teixeira, S. R.; Dupont, J., Nanoscale Ru(0) Particles: Arene Hydrogenation Catalysts in Imidazolium Ionic Liquids. *Inorganic Chemistry* **2008,** *47* (19), 8995-9001.
19. Luska, K. L.; Bordet, A.; Tricard, S.; Sinev, I.; Grünert, W.; Chaudret, B.; Leitner, W., Enhancing the Catalytic Properties of Ruthenium Nanoparticle-SILP Catalysts by Dilution with Iron. *ACS Catalysis* **2016,** *6* (6), 3719-3726.
20. Rohmann, K.; Kothe, J.; Haenel, M. W.; Englert, U.; Hölscher, M.; Leitner, W., Hydrogenation of CO2 to Formic Acid with a Highly Active Ruthenium Acriphos Complex in DMSO and DMSO/Water. *Angewandte Chemie International Edition* **2016,** *55* (31), 8966-8969.
21. Zanatta, M.; Girard, A. L.; Marin, G.; Ebeling, G.; Dos Santos, F. P.; Valsecchi, C.; Stassen, H.; Livotto, P. R.; Lewis, W.; Dupont, J., Confined water in imidazolium based ionic liquids: a supramolecular guest@host complex case. *Phys. Chem. Chem. Phys.* **2016,** *18* (27), 18297-18304.
22. Zanatta, M.; Dos Santos, F. P.; Biehl, C.; Marin, G.; Ebeling, G.; Netz, P. A.; Dupont, J., Organocatalytic Imidazolium Ionic Liquids H/D Exchange Catalysts. *J. Org. Chem.* **2017,** *82* (5), 2622-2629.
23. Dupont, J.; Simon, N. M.; Zanatta, M.; Dos Santos, F. P.; Corvo, M. C.; Cabrita, E. J., Carbon dioxide capture by aqueous ionic liquid solutions. *ChemSusChem* **2017**, doi:10.1002/cssc.201701044

Chapter 6: Ru-pyridylamide complexes for CO_2 hydrogenation

6.1. Introduction

Pyridinylidene amide (PYA) and pyridinylidene amine (PYE) ligands display high donor flexibility.[1-2] For instance, the PYE scaffold can exist in two forms, a neutral and a zwitterionic resonance form. A similar behaviour can be assigned to PYA scaffolds.[3-4] A major difference between the PYA - and PYE scaffold is the enhanced coordinative flexibility induced by the oxygen in the amide moiety in the PYA moiety. Here a second zwitterionic structure can be drawn, see **figure 6.1**.[3]

a) PYA:



b) PYE:

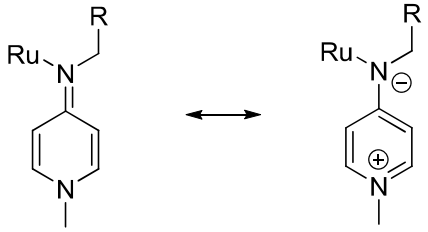


Figure 6.1 Resonance structures of PYA (a) and PYE (b) scaffolds.

Furthermore PYA ligands display similarities to N-heterocyclic carbene (NHC) ligands, i.e. a strong σ donation and a net overall charge of 0.[5] However, a

major difference between PYA's and NHC's is the bond polarity between the metal centre and the coordinative site. In the PYA, the metal nitrogen bond is strongly polarised, i.e. the N been negatively polarised, whilst the metal been positively polarised. This is in contrast to the more neutral bond between the metal centre and the carbon in NHC complexes,.[6]

This leads to a high susceptibility towards nucleophilic and electrophilic attacks with PYA's.[6] Consequently, PYA donor sites are often combined with a second donor site to hold the metal centre tightly to the ligand scaffold, prohibiting the decomposition of the active catalytic species.[3-4]

Bidentate complexes bearing PYA ligands have been employed in catalytic transformations such as olefin dimerization,[7] water oxidation,[8] dehydrogenations[3-4] and transfer hydrogenations.[4] However, as this thesis deals with the hydrogenation of CO_2 with Ru as the catalytic metal species, the focus is laid on reactions involving Ru-PYA's in dehydogenations and transfer hydrogenations.

A major feature of PYA-Ru complexes in dehydrogenations and transfer hydrogenation reactions is the flexibility of the N donor site. For instance, Ru-PYA complexes utilising triazolylidene as a wingtip (**4**), showed excellent activity for the transfer hydrogenation between isopropanol (IPA) and benzophenone.[4] Interestingly the addition of small amounts of dimethylacetamide (DMA) significantly increased the catalytic significantly and full conversion of benzophenone to diphenylmethanol was reached, **figure 6.2a**.[4] This finding is most likely due to the stronger contribution of the

zwitterionic resonance structure in polar environments, leading to a higher electron density at the metal centre.

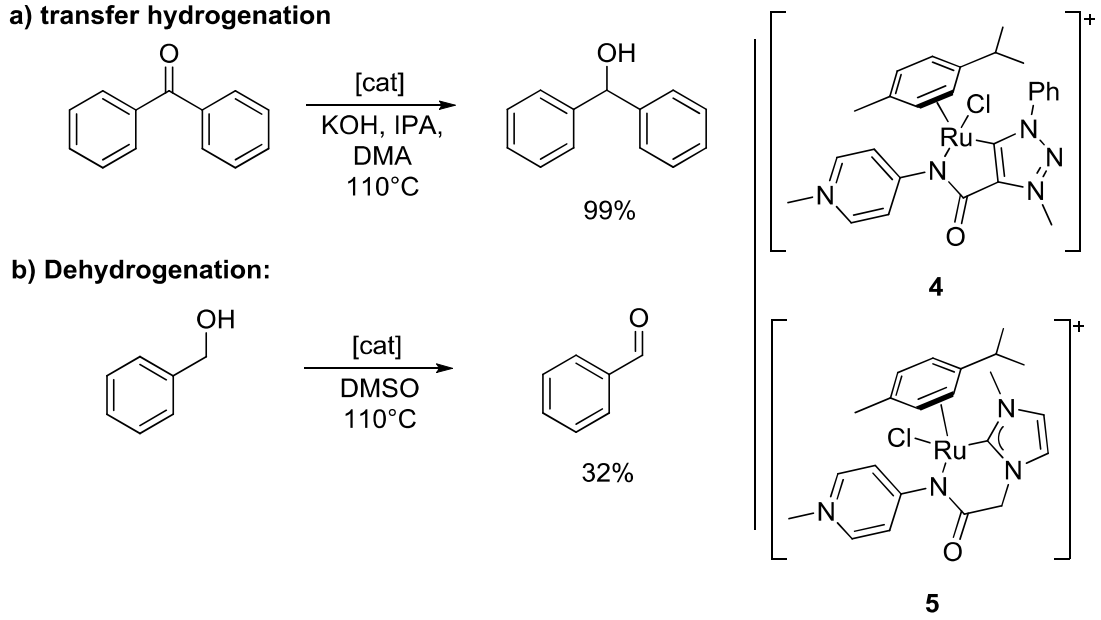


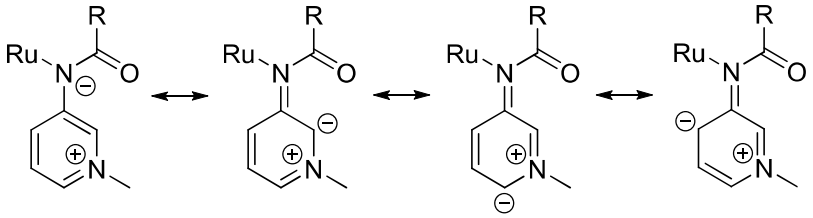
Figure 6.2 a) catalytic transfer hydrogenation between IPA and benzophenone to diphenylmethanol and b) dehydrogenation of benzylalcohol to benzaldehyde.

A similar trend was observed with a NHCs as a wingtip (**5**). Here, the catalytic activity in the dehydrogenation of benzylalcohol to benzaldehyde proceeded to a conversion of 32% in DMSO (**figure 6.2b**), whilst in more apolar solvents such as toluene only limited conversion is obtained. The reaction is limited further by the decomposition of the catalyst, observable as a black precipitate formed during the reaction.[3] This finding was attributed to the acidic CH_2 group next to the amide moiety in **5**, as in comparison no decomposition was observed with the triazolilydene derivative **4**.[3-4]

Upon switching the positional arrangement of the PYA scaffold to a meta positioned amide group (*meta*-PYA), the electron donating properties of the

PYA scaffold can be increased. This is due the lack of a neutral resonance structure in the *meta*-PYA scaffold, see **figure 6.3**.[9-10]

a) *meta*-PYA:



b) *para*-PYA:

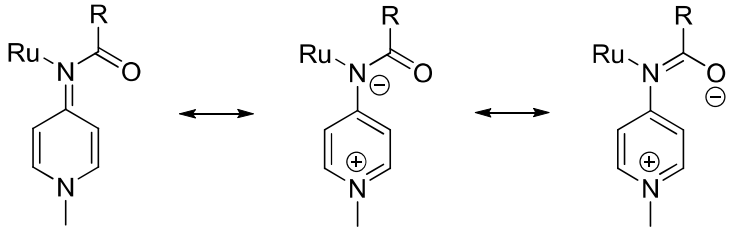


Figure 6.3 Possible resonance structure with meta-PYA ligands (a) and with para-PYA ligands (b).[3-4, 9-10]

Indeed, incorporating the meta-PYA scaffold into a pincer ligand platform combination with Ru, yielded a highly active transfer hydrogenation catalyst. With the *meta* complex derivative **6** a catalytic conversion of 97% in the transfer hydrogenation in between IPA and benzophenone, yielding diphenylmethanol, in the presence of 10 mol% KOH was achieved after 2h. In comparison with the *para* derivative **7** only 5% conversion was achieved after 6h. This observation was correlated to the higher electron density at the metal centre. Here a redox potential ($E_{1/2}$ (Ru^{II}/Ru^{III})) of 0.78 V with the para-scaffold (**30**) was observed whilst with the corresponding meta scaffold (**6**) a redox potential ($E_{1/2}$ (Ru^{II}/Ru^{III})) of 0.67 V was found.[10] The difference in the redox potential displays a higher electron density at the metal centre for the *meta* derivative (**6**), see **Figure 6.4**.

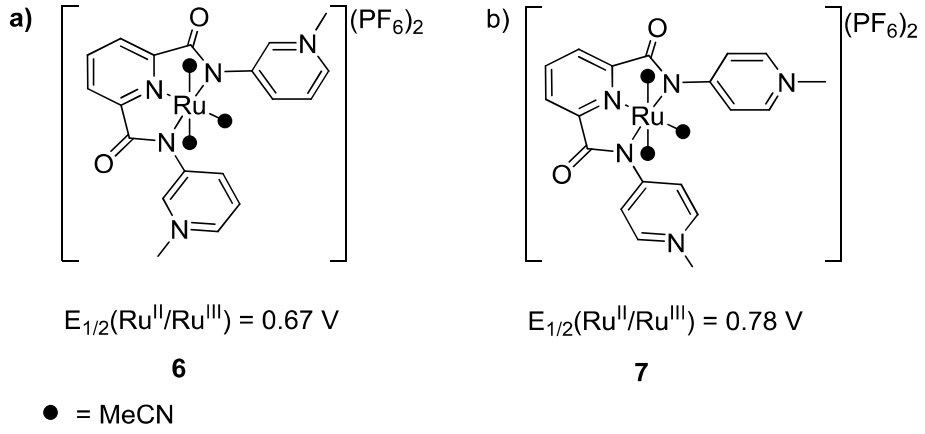


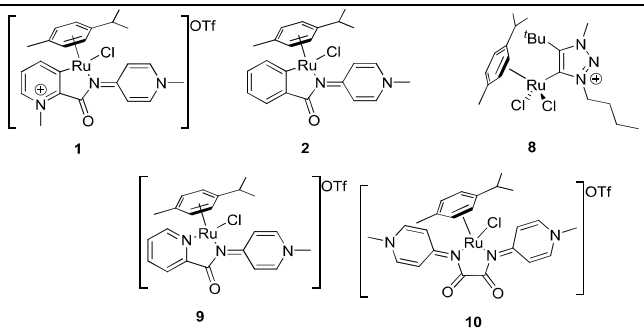
Figure 6.4 meta PYA pincer complex (a) and par PYA pincer complex (b).[10]

In the next part, the flexibility of PYA ligands onto the base free hydrogenation of CO_2 to formic acid was described. Here the aim was to gain fundamental insights for the design of catalysts under base free conditions, with a special emphasis on the effect of electron donation/withdrawal and sterical arrangement of the coordinative site.

6.2. Initial screening of homogeneous catalysts

In an initial screening, it was found that the most active catalysts contain a strong carbene donor as in the case of complexes **1, 2** and **8**. In the case of catalyst **1** an average TOF_{av} of 35 h^{-1} and a TON of 669 was achieved, giving a final concentration of 1.1M, hence reaching equilibrium, see ***section 4***. Complex **2** showed a TOF_{av} of 21 h^{-1} and a TON of 423, whilst complex **8** only achieved a TON of 308 and a TOF_{av} of 15 h^{-1}. Catalyst **9** and **10** do not possess a carbene donor and are less active than the catalysts **1, 2** and **8**.

Table 6.1 Pre-catalyst screening



Entry	Complex	[FA]/ M	TON	TOF / h^{-1}
1	**1**	1.1	669	35
2	**2**	0.7	423	21
3	**8**	0.5	309	15
4	**9**	0.2	119	6
5	**10**	0.1	82	4

Reaction conditions: 40 bar H_2, 20 bar CO_2, 6 mL DMSO:H_2O (5 v/v% water), reaction time: 24h, T=60°C, 3.3 mmol BMMI.OAc.

When complex **8** was employed, a black precipitate was formed which is likely due to the decomposition of the catalyst. Thus, catalyst **8** was discarded and further studies were focused onto catalysts **1** and **2** and their isomers.

6.3. Publication III: Catalyst design for highly efficient base-free carbon dioxide hydrogenation to formic acid

Contribution of the author: In this publication the author conducted all catalytic experiments, drew the research plan and synthesized all ionic liquids. The complexes investigated in this publication were prepared by collaborators. Manuscript preparation was undertaken in collaboration with all co-authors.

Reprinted with permission from

www.chemrxiv.org/articles/Catalyst_Design_for_Highly_Efficient_Base-Free_Carbon_Dioxide_Hydrogenation_to_Formic_Acid

Catalyst design for highly efficient base-free carbon dioxide hydrogenation to formic acid

Andreas Weilhard,[a] Kevin Salzmann,[b] Jairton Dupont,[c] Martin Albrecht,[b]* Victor Sans[a,d]*

a) Faculty of Engineering, University of Nottingham, Nottingham, NG7 2RD, UK
b) Department of Chemistry & Biochemistry, University of Bern, Freiestrasse 3, 3012 Bern, Switzerland
c) Institute of Chemistry – UFRGS – Av. Bento Gonçalves, 9500 Porto Alegre 91501-970 – RS Brazil
d) Institute of Advanced Materials (INAM), Universitat Jaume I, 12006, Castellon, Spain

Corresponding author e-mail: sans@uji.es, martin.albrecht@dcb.unibe.ch

Abstract

We report on new ruthenium complexes as catalysts for the efficient transformation of CO_2 into formic acid as a high-value chemical and fuel. Remarkably, these complexes catalyze the hydrogenation of CO_2 selectively and without employing any base, which improves the sustainability of the process when compared the common base-assisted technologies. The molecular catalyst design relies on donor-flexible and synthetically versatile pyridylidene amide (PYA) ligands which allows the ligand architecture to be varied in a controlled manner to gain valuable insights for the improvement of catalyst performance. Modification of the ligand properties directly

influence the catalytic process by shifting the turnover limiting step, the reaction mechanism and the stability upon the acidification of the reaction media and provide access to high-performance systems reaching turnover numbers of several thousands and turnover frequencies up to 350 h^{-1}.

Introduction

The transformation of carbon dioxide (CO_2) into chemicals and fuels is a key challenge of the 21st century and has gained a lot of interest in recent years.[1-2] Indeed, the synthesis of commodity chemicals, such as (poly)carbonates, hydrocarbons, methanol, formic acid and specialty chemicals[1] from CO_2 is highly desirable, as CO_2 represents a cheap, and virtually infinite source of C1 building blocks.[1-2] Except for the case of carbonates, CO_2 has to be reduced to a lower oxidation state. As reduced and synthetically useful product, formic acid (FA) represents formally the easiest target, requiring one dihydrogen molecule to react with one molecule of CO_2 to form FA and reducing formally the oxidation state of carbon from +IV to +II. Indeed the transformation of CO_2 to FA using H_2 *via* artificial photosynthesis has attracted high scientific and economic interest, also because CO_2 reduction is environmentally much more benign compared to the current production of FA by formal water carbonylation[3] at a megaton capacity per year.[4] Furthermore, FA has potential applications as a hydrogen storage vector.[5-9]

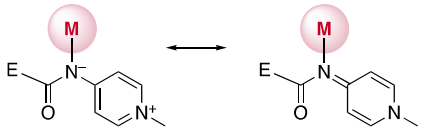
The hydrogenation of CO_2 is thermodynamically and kinetically challenging.[2] Indeed, the hydrogenation of CO_2 and H_2 in the gas phase yielding FA in liquid phase is entropically highly unfavourable and renders the reaction endergonic.[10-11] Most commonly the thermodynamic equilibrium is shifted to the product side by the addition of stoichiometric amounts of base. Under these conditions a plethora of noble metal catalyst formed by various types of ligands such as N-heterocyclic carbenes[12-13], half

sandwich,[5, 14-16] pincers[17-20] and phosphine[21-25] combined with a broad range of transition metals, including iron,[26-29] nickel,[30-31] copper and cobalt[34-36] have shown to be remarkably active (TON >10^6).[17] The key step in those processes is the formation of formate salts and adducts, which shifts the thermodynamic equilibrium to the product side. This increases the enthalpy and makes the reactions highly exothermic. Nevertheless, this energy has to be overcome during downstream processing to be able to utilize the formate salt synthesized in the presence of stoichiometric amounts of base. Currently, major strategies involve reactive distillation[10, 37-38] or utilization of $scCO_2$[39] as eluent phase to liberate formic acid from the reaction media, which is both economically and environmentally unattractive due to the energy involved as well as the huge quantities of waste produced.

In a more sustainable fashion, the reaction can be carried out in pure solvents without the addition of base. In this regard DMSO has found increased attention.[40-42] Here the basic properties of the solvent are exploited to stabilize the product by hydrogen bonding[41] and can be further enhanced by the addition of small amounts of water.[40] Furthermore, water[43-45] and ionic liquids (ILs)[46-48] have demonstrated to facilitate the formation of FA from CO_2 and H_2. However, in most cases the catalytic turnover[41-42] and concentrations of FA obtained[43-45] are relatively modest, with TONs<1000. Very recently, we have reported that ionic liquids can efficiently mediate the hydrogenation of CO_2 to formic acid by acting as a buffer.[46-47] Indeed, in the presence of ILs the reaction can be carried out in less basic solvents including THF, MeCN and MeTHF,[47] which are easier to separate than DMSO or water by stripping due to their relatively low boiling point.

In order to improve the catalytic performance and to benefit from the clear advantages of base-free FA synthesis, we designed ruthenium complexes containing an electronically flexible pyridylidene amide (PYA) ligand.[49-51] These ligands stabilize different electronic configurations at the metal center through unique toggling

between a limiting zwitterionic and neutral resonance structure (Scheme 1),[52-54] which is key for efficient redox catalysis.[55-57] Here, a set of neutral and cationic ruthenium complexes featuring PYA ligands are demonstrated to be efficient CO_2 reduction catalysts and produce FA in the absence of a base. Kinetic analysis, electrochemistry and spectroscopic analyses offer valuable insights into the catalyst reactivity, stability and activity under buffering conditions and provide structure-activity relationships for the sustainable CO_2 hydrogenation to formic acid.



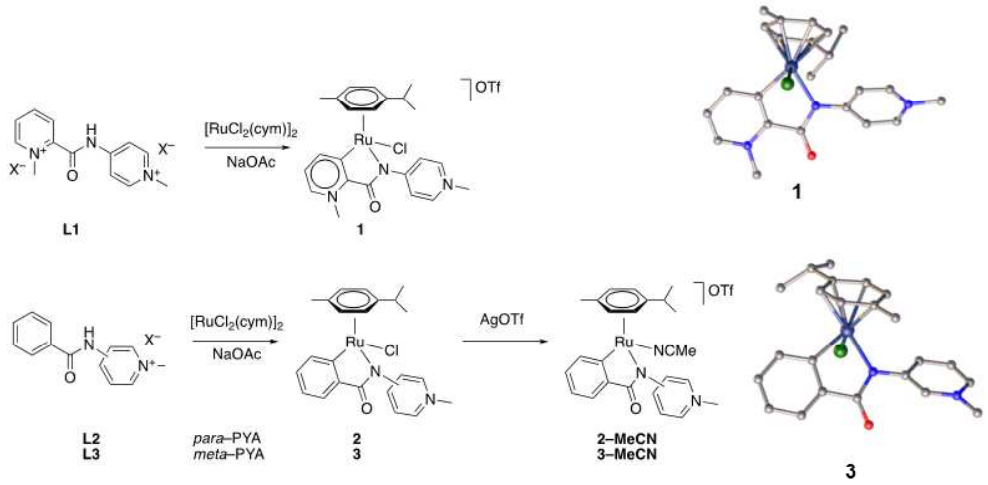
Scheme 1: Limiting resonance structures of PYA ligands featuring a zwitterionic amide (left) for stabilizing electron-poor (high-valent) metal centers, and the formally neutral limiting imine resonance form for stabilizing electron-rich (low-valent) metal centers (right); E may be a (non-)chelating functional group.

Results and discussion

Synthesis of the ruthenium complexes and evaluation of their catalytic activity in CO_2 reduction. Complexes **1–3** were synthesized by reaction of the known pyridinium salts **L1–L3** with $[Ru(cym)Cl_2]_2$ in the presence of NaOAc (Scheme 2).[58] This protocol afforded the cationic complex **1** containing a *para*-PYA ligand stabilized by a chelating pyridylidene unit in 61% yield, and the formally neutral complexes **2** and **3** in about 40% yield. These latter complexes were also prepared stepwise from the pyridinium salt by first deprotonating the pyridinium salt to form the free pyridylidene, followed by cycloruthenation. All complexes are air- and moisture-stable solids. Coordination of the PYA ligand site was indicated by the downfield shift of the PYA proton resonances (*e.g.* from = 9.25 (DMSO-d_6) in **L3** to 9.86 ($CDCl_3$) for Hα in complex **3**), and the loss of one aromatic signal with concomitant desymmetrization

of the remaining resonances established successful cyclometallation, see SI. Further evidence for the formation of complexes **1–3** was obtained from a single crystal X-ray diffraction analysis, which confirmed the anticipated connectivity pattern (Scheme 2). Further details on data collection and refinement parameters are compiled in Tables S1. Crystallographic data for the structure have been deposited with the Cambridge Crystallographic Data Centre (CCDC) as supplementary publication number 19182143098.

Complex **1** featuring a pyridylidene NHC ligand and a *para*-PYA ligand was cationic and featured an OTf^- anion. Notably, the donor properties of the three chelates is reflected in the electron density at the ruthenium center, quantified by cyclic voltammetry and revealing a shift of the Ru^{II}/Ru^{III} oxidation potential from $E_{1/2}$ = +0.83 V (for complex **1** with a formally neutral pyridylidene–PYA chelate) to lower potential for complexes **2** and **3** with an anionic phenyl-PYA chelating ligand ($E_{1/2}$ = +0.52 and +0.46 V *vs* SCE, all values in $MeNO_2$). This trend suggests stronger donor properties of the *meta*-PYA unit compared to the para-PYA analogue, in agreement with previous studies.[56]



*Scheme 2. A) Synthesis of complexes **1–3** and the solvent analogues **2-MeCN** and **3-MeCN.** B) X-ray structures of **1** and **3** (both 50% probability, OTf anion of **1** and all H atoms omitted for clarity)*

The neutral complexes **2** and **3** were readily transformed into their cationic species **2-MeCN** and **3-MeCN**, respectively, upon halide abstraction with AgOTf in MeCN (Scheme 2). Formation of the solvent complex is accompanied by an upfield shift of the PYA Hα protons and a downfield shift of the PYA Hβ protons in **2-MeCN** compared to **2**. These shifts are indicative for a larger relevance of the zwitterionic *vs* the charge-neutral limiting resonance form, in agreement with the lower electron density at the ruthenium center when bound to a MeCN ligand *vs* an anionic chloride. Interestingly, cyclic voltammetry does not suggest a change of the electronic configuration at the ruthenium center and the Ru^{II}/Ru^{III} redox potential of **2-MeCN** ($E_{1/2}$ = 0.52 V *vs* SCE, $MeNO_2$ solution) is identical to that of complex **2**, suggesting a very efficient compensation of the lower donor properties of MeCN *vs* Cl^- by the more zwitterionic PYA resonance form (see SI for further details).

For an initial evaluation of these complexes in CO_2 reduction catalysis, we chose DMSO:H_2O (19:1 v/v%) as the solvent system in combination with 1-butyl-2,3-dimethylimidazolium acetate (BMMI.OAc) as an additive. Under these conditions, the ionic liquid, BMMI.OAc, acts as a buffer during the formation of formic acid or the combination of IL and water may also catalyze the formation of carbonates.[47, 59-61] Further stabilization of the product is imparted by solvent cluster formation by FA, water and DMSO.[40-41] In the presence of H_2 and CO_2 ($P(H_2) = P(CO_2)$ = 30 bar, T = 70°C), all PYA ruthenium complexes catalyze the formation of FA without the need of an external base (Table 1).

*Table 1 Screening of catalytic activity of complexes **1-3-MeCN** in the base-free CO_2 hydrogenation to formic acid (FA)* [a)]

$$CO_2 + H_2 \xrightarrow{cat.\ [Ru]} HCOOH$$

entry	[Ru]	TON [b)]	TOF / h^{-1} [c)]	[FA] / M [b)]
1	**1**	4520±40	117±2.2	1.14±0.01
2	**2**	2190±40	55±3.6	0.55±0.01
3	**3**	1930±40	78±2.2	0.49±0.01
4	**2-MeCN**	1950±40	122±2.3	0.49±0.01
5	**3-MeCN**	1520±40	50±0.4	0.39±0.01

[a)] Reaction condtions: 6 mL DMSO:water (5 v/v% water), 3.3 mmol BMMI.OAc, 1.52 µmol [Ru] at 70°C, $P_{H2} = P_{CO2} = 30$ bar; [b)] determined by ^1H NMR spectroscopy after 72 h using BMMI.OAc as an internal standard, average of two independent runs; [c)] calculated by linear regression (see SI).

Variation of the ligand scaffold had a pronounced impact on the catalytic activity of the ruthenium complexes. Complex **1** displays a significantly higher catalyst stability than complexes **2, 3, 2-MeCN** according to the pertinent TON values, while **3-MeCN** produced the least stable system. The 4520 TONs achieved with complex **1** (Table 1, entry 1) are amongst the highest previously reported catalyst performance under base-free conditions and the final FA concentration of 1.14 M is very close to the predicted thermodynamic limit of FA concentration of 1.2 M under the conditions assayed.[40-41, 62] In contrast, complexes **2** and **3** achieved much lower FA concentrations around 0.5 M (entries 2–5), suggesting that these complexes have intrinsic catalytic limitations. While complex **1** is not the only cationic complex in this series, we note that this complex features a formally neutral pyridylidene–PYA ligand

scaffold, whereas the other four complexes evaluated here contain a formally anionic phenyl-PYA ligand.

Complexes **1** and **2-MeCN** reach an appreciable maximum turnover frequency (TOF_{max}) around 120 h^{-1} (entries 1,4). Interestingly, complex **2** achieved a significantly lower TOF value (TOF_{max} = 55 h^{-1}) than **2-MeCN** despite the same ligand scaffold. These complexes only differ in their ancillary ligand (Cl vs. MeCN). An inverse effect was observed for complexes **3** and **3-MeCN** (entries 3,5). Modification of the PYA unit from a *para* substituted system in **2** to the more electron-donating *meta* analogue (complex **3**) increases the rate from 55 h^{-1} to 78 h^{-1}, suggesting that electron donating effects are relevant for imparting higher catalytic activity.

These results clearly indicate that both the PYA-ligand and the ancillary ligand play an important role on the catalytic activity. In order to identify the effects determining the rate of catalytic conversion and stability, we investigated a series of parameters such as turnover limiting steps, effect of pressure, and activation energies for this base-free CO_2 hydrogenation process.

Analysis of turnover-limiting steps

In a first approximation, hydrogenation of CO_2 to FA can be divided into two steps. First CO_2 inserts into a metal hydride bond to yield a metal formate complex. In the second step H_2 reacts with this complex to release FA and regenerate the active hydride (Figure 1A). From this simplified mechanism three scenarios can arise: (i) either H_2 activation is the turnover limiting step (TLS) and the rate is solely dependent on the partial pressure of H_2, or (ii) CO_2 insertion is turnover limiting and thus the rate is dependent only on the partial CO_2 pressure, or (iii) both steps display similar rates and a dependence on both CO_2 and H_2 pressure is observed. In order to probe the nature of the TLS, we therefore evaluated complexes **1**, **2**, and **3** under varying partial pressures of CO_2 and H_2.

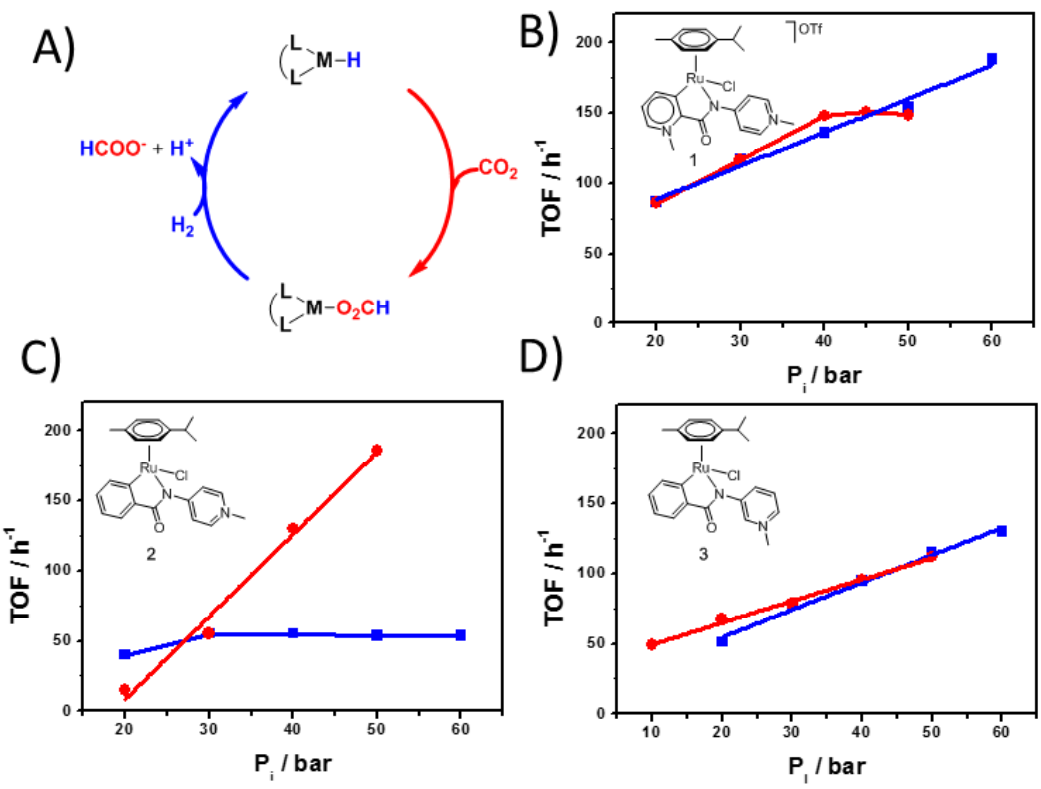


*Figure 1 Determination of the turnover limiting step (TLS) for complexes **1**, **2** and **3**. A) Schematic representation of a simplified mechanism of the hydrogenation of CO_2 to FA, divided into two main steps, the insertion of CO_2 (red) and H_2 activation (blue). B)-D) catalytic activity of complexes **1–3** upon variation of the partial pressure P_i of either CO_2 (red) or H_2 (blue), whilst keeping the pressure of the other reactant constant at 30 bar. Reaction conditions: T= 70°C, 6 mL DMSO:H_2O (5 v/v% H_2O), 3.3 mmol BMMI.OAc. and 1.52 µmol of ruthenium complex.*

With complex **1**, the catalytic activity is linearly dependent on the partial hydrogen pressure, whilst an increase in partial CO_2 pressure led to a plateau around 150 h^{-1} when reaching 40 bar CO_2 pressure, clearly indicating that the TLS is associated with the H_2 activation process (Figure 1B). The CO_2 dependence of the rate at low partial pressure of CO_2 has been attributed to the high solubility of H_2 in CO_2, which increases the effective concentration of H_2 in the reaction media.[63-64] A markedly different behavior was observed for complex **2**, as the rate is essentially independent of the H_2 pressure, yet directly correlates with changes in the partial CO_2 pressure

(Figure 1C), identifying CO_2 insertion as the TLS. The pressure-dependence of the catalytic activity of complex **2** is about three times stronger than that of complex **1** (ΔTOF ca. 5.9 h^{-1} ± 0.5 h^{-1} per bar CO_2 for **2** *vs* 2.4 h^{-1} ± 0.2 h^{-1} per bar H_2 for **1**).

Complex **3** showed a more complex behavior, with a linear dependence on both H_2 and CO_2 insertion (Figure 1D), suggesting that both steps are energetically closely related. Such a models are supported by catalytic runs for which the total pressure was kept constant at 60 bar, yet the partial pressures were varied (Figure 2). The rate is almost unaffected in this regime. The weakly positive dependence on H_2 pressure points to H_2 activation as the slightly more energetic and hence turnover-limiting step rather than CO_2 insertion.

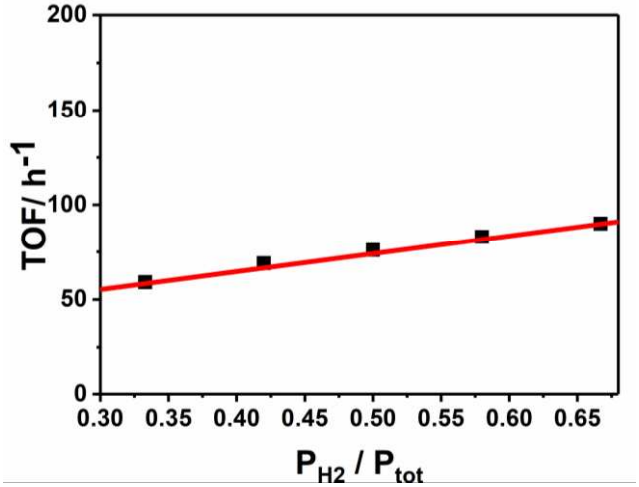


*Figure 2. Effect of gas composition on TOF for complex **3** by variation of gas composition at a constant total pressure (60 bar) with 1.52 µmol complex **3** and 3.3 mmol BMMI.OAc at 70°C in 6 mL DMSO:H_2O (5 v/v% H_2O).*

Interestingly, a change in the TLS as observed for complexes **1** and **2** has not been reported for Ru(II) complexes, even though computational studies have predicted that the activation for CO_2 and H_2 are energetically close for Ru(II)-catalysts.[65] Calculations on the thermodynamics of the hydrogenation process do not

identify any one step to be particularly facile, and therefore the insertion of CO2 may be endergonic or exergonic.[66-67] However, a change in TLS has been reported upon changing the active metal center. With complexes of Co and Ir, CO_2 insertion is rate limiting whilst for Ru and Fe the H_2 activation is generally considered as the limiting step. [43-44, 65, 68]

*Table 2 Optimized catalytic performance of complexes **1–3*** [a)]

Entry	[Ru]	P_{H2}:P_{CO2} / bar	TON [b)]	TOF_{max} / h^{-1} [b)]	[FA] / M [b)]
1	**1**	60:30	4520±40	188±8	1.15±0.01
2	**2**	30:50	2010±40	186±15	0.51±0.01
3	**3**	60:30	1930±40	130±5	0.49±0.01
4	**3**	30:50	1930±40	115±5	0.49±0.01
5	**2-MeCN**	30:50	1950±40	340±60 [c)]	0.49±0.01

[a)] Reaction conditions: 6 mL DMSO:water (5 v/v% water) *1.52 µmol [Ru],* 3.3 mmol BMMI.OAc at 70°C; [b)] determined by ^{1}H NMR spectroscopy after 72 h using BMMI.OAc as an internal standard, average of *two runs;* [c)] *Determined as* maxim*um* TOF *calculating the variation of FA* concentration *as a function of* time.

Identification of the TLS for each complex allows for tailoring the reaction conditions to enhance the catalytic performance of each complex. Under optimized conditions, *i.e.* in the presence of an excess of the turnover-limiting component, significantly higher TOF_{max} up to 340±60 h^{-1} are accessible (Table 2), even though the TON does not significantly change compared to the original conditions studied (*cf* Table 1). This observation indicates that the catalytically active species remain unchanged, even though considerably differing reaction conditions are applied.

The variable catalytic activity and the distinct turnover-limiting steps provide evidence that the nature of the ligand plays a significant role in the hydrogenation of CO_2 to FA.

Even relatively small modifications in the PYA ligand architecture lead to significant changes in the TLS. For example, with **1** containing a chelating pyridylidene unit with the PYA donor, the TLS is associated with H_2 activation, whilst substitution of this formally neutral carbene with an anionic phenyl chelating group as in complexes **2** and **2-MeCN** switches the TLS to CO_2 insertion. With **3**, both these steps are energetically close. Furthermore, the differences of complexes **2** and **3** indicate that the TLS is partially defined by the electron density at the metal center, as the *meta*-PYA unit induces a higher electron density at the metal center compared to the *para*-PYA analogue (see CVs Figure S7 in SI).

Modulation of the ancillary ligand in complex **2** from Cl to MeCN led to a more marked dependence of the catalytic activity on the pressure of CO_2 (Figure 3, (ΔTOF ca. 9.0 h^{-1} per bar CO_2). The stronger dependence is relevant because the TLS for both complexes is the insertion of CO_2. An increase of the partial CO_2 pressure up to 50 bar therefore leads to an outstanding TOF_{max} = 340 h^{-1} for complex **2-MeCN**. This complex is therefore the most active one of the series investigated here, and also one of the best reported to date for the base-free hydrogenation of CO_2 to FA. Higher rates are only observed under significantly higher pressures[40] or temperatures,, and only at very early stages, *i.e.* at very low concentrations of FA.[69]

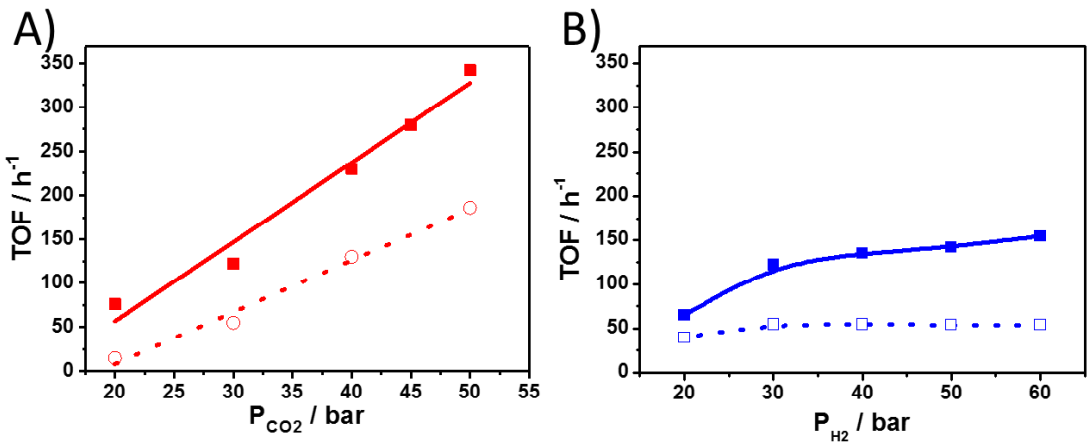


*Figure 3. Comparison of catalytic activity of **2** (dotted) and **2-MeCN** (solid) upon A) variation of partial CO_2 pressures (red) ($P(H_2)$ = 30 bar); and B) upon variation of the partial H_2 pressures (blue) ($P(CO_2)$ = 30 bar); General conditions: 1.52 µmol [Ru], 6 mL DMSO:H_2O (5 v/v% H_2O), 3.3 mmol BMMI.OAc, 70°C.*

Complex **2-MeCN** showed only small rate increases from 122 h^{-1} to 150 h^{-1} when the partial H_2 pressure was increased from 30 to 60 bar (Figure 3B), while complex **2** is completely insensitive to higher H_2 pressure (*cf* Figure 1C). The increasing rate at higher H_2 pressures with **2-MeCN** may be due to an increased concentration of reactant, favourable formation of the active hydride or alternatively a consequence of the higher overall physical pressure. In order to distinguish these effects, complexes **2** and **2-MeCN** were investigated at higher pressure entailed by Ar as an inert gas.

*Table 3 Effect of pressure on catalytic performance of **2** and **2-MeCN** [a)]*

Entry	Complex	T / °C	Ar / bar	[FA] / M	TON	TOF / h^{-1}	$\Delta V^{\ddagger}$ / M^{-1} [b)]
1	**2**	90	50	0.175 ± 0.01	695 ± 42	34.5 ± 3	≥ 0
2	**2**	90	-	0.195 ± 0.01	749 ± 42	37.5 ± 3	-
3	**2-MeCN**	80	50	0.185 ± 0.01	695 ± 42	37.5 ± 3	< 0
4	**2-MeCN**	80	-	0.14 ± 0.01	564 ± 42	31 ± 3	-

[a)] Reaction conditions: P_{CO2} = 20 bar, P_{H2} = 10 bar, 6 mL DMSO:water (5 v/v% water), 3.3 mmol BMMI.OAc, 1.52 µmol [Ru], 20 h, average of 2 runs; b) sign of $\Delta V^{\ddagger}$ estimated from ΔTOF between catalytic runs with and without Ar.

The addition of 50 bar of argon to the catalytic system based on complex **2** did not lead to any significant change in rate of catalytic CO_2 hydrogenation (Table 3, entry 1 *vs* 2). In contrast, a 20% increase of the TOF was observed when **2-MeCN** was used as the catalyst precursor (entry 3 *vs* 4). The increased rate noted for **2-MeCN** indicates a negative volume of activation according to Eq. 1 in the SI.

This negative value of $\Delta V^{\ddagger}$ suggests an associative process for **2-MeCN** in the TLS, while the TLS for the hydrogenation with complex **2** is volume-neutral. Two predominant mechanisms for the CO_2 insertion have been discussed which depend on the nucleophilicity and sterics around the metal center. Hence, strong nucleophiles such as metal amines, and metal hydrides with low steric demand generally proceed through a so-called inner sphere mechanism, involving coordination of CO_2 to the metal center and simultaneous hydride transfer to the CO_2 in a concerted, associative fashion.[70-71] With most metal hydrides and other weaker nucleophiles, an outer sphere mechanism is prevalent, consisting of an initial hydride transfer to CO_2 and formation of a zwitterionic intermediate comprised of a positively charged metal center and a formate anion. In a second step this zwitterionic intermediate rearranges to the formate complex (*cf.* Figure 1A).[70-71] According to this model, the negative volume of activation implies a concerted associative TLS for the **2-MeCN**-catalyzed process,

whilst with **2** the outer sphere mechanism with no significant volume change is dominant. Moreover, these data suggest that the ruthenium-hydride intermediate derived from **2-MeCN** has a lower steric demand or is a stronger nucleophile than the one derived from **2.** It has been shown that the inner sphere mechanism proceeds faster than the outer sphere mechanism,[71] in agreement with the twice higher rate of CO_2 hydrogenation observed with **2-MeCN** compared to **2** (340 *vs* 186 h^{-1},*cf* Table 2).

Ligand electronic effects on catalytic activity

The catalytic implications of varying electronic effects of the different PYA ligand scaffolds in complexes **1–3** has been quantified by determining the activation energy for CO_2 hydrogenation with each complex. An Arrhenius plot from rate measurements in the 60–90 °C temperature range is linear (Figure 3) and provides the activation energies (E_a) and pre-exponential factors (ln A) for the complexes (Table 4). To further probe the electronic flexibility of the PYA ligand, the activation energy for complex **2** was also determined in THF as a less polar solvent than DMSO. Lower polarity solvents were previously shown to favour the neutral PYA resonance structure more than the zwitterionic one (*cf.* Scheme 1),[52-54] which is also reflected in the higher Ru^{II}/Ru^{III} oxidation potential of complex **2** in THF than in polar solvents ($E_{1/2}$ = +0.63 V *vs* +0.52 V in $MeNO_2$ as proxy for DMSO). Activation energies in THF as the main solvent were measured in the presence of 1-decyl-2,3-dimethylimidazolium acetate (C_{10}MMI.OAc) rather than BMMI.OAc as IL media.

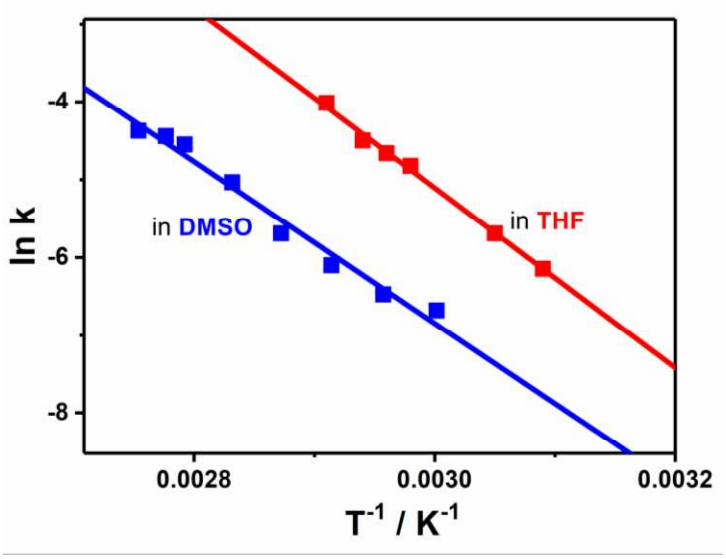


Figure 4 Arrhenius plot of **2** in DMSO:water with 3.3 mmol BMMI.OAc (blue), and in THF:water with 3.3 mmol C_{10}MMI.OAc (red) using 8 µmol catalyst and $P_{CO2} = P_{H2} = 20$ bar.

Complex **2** in polar and apolar media and complex **3** showed a direct correlation between the activation energy and the energy donation ability of the ligands. When compared to the *para*-PYA ligand system in complex **2** (ΔE_a = 86 kJ mol^{-1}; Table 4, entry 2), the *meta*-PYA ligand of complex **3** is stronger donating, which is also shown by the 60 mV easier $Ru^{II/III}$ oxidation. This increased electron density lowers the activation energy by 15 kJ mol^{-1} (entry 3). In contrast, the larger contribution of the neutral resonance structure of the *para*-PYA ligand in THF lowers the electron density at ruthenium (110 mV higher oxidation potential) which also imparts a 10 kJ mol^{-1} higher activation energy compared to the same complex in more polar DMSO solvent (entry 4). This observation suggests a relationship between the hydricity of the critical ruthenium hydride intermediate and the catalytic activity, as established previously for a wide range of catalysts. The hydricity has been shown to directly correlate with the electron density at the metal center, hence allowing to estimate the hydride transfer capability of metal complexes and to compare it to the hydride donor-ability of formate/formic acid.[30, 34-36, 66, 72-77] In general, higher hydride transfer capabilities lead to higher catalytic activities in the hydrogenation of CO_2. A relationship in

between the oxidation potential and the catalytic activity has been established previously with other Ru-catalysts in the hydrogenation of CO_2 under basic conditions.[78]

Table 4 Comparison of the redox potential, Arrhenius activation parameters [a)]

Entry	Complex	Solvent	Ionic liquid	ΔE_a / kJ mol^{-1}	lnA	$E_{1/2}$ / V
1	**1**	DMSO:water	BMMI.OAc	62 ± 4.2	18 ± 1.5	0.83
2	**2**	DMSO:water	BMMI.OAc	86 ± 5.1	24 ± 1.8	0.52
3	**3**	DMSO:water	BMMI.OAc	71 ± 4.5	19 ± 1.6	0.46
4	**2**	THF:water	C_{10}MMI.OAc	96 ± 3.1	30 ± 1.1	0.63

[a)] *Reaction conditions: 6 mL solvent with 5 v/v% H_2O, 3.3 mmol IL and $P(H_2) = P(CO_2) = 20$ bar and 8 µmol catalyst.*

While complex **2** and **3** follow the expected trend, complex **1** shows a distinct behavior and features the lowest activation energy (ΔE_a = 62 kJ mol^{-1}) despite having the lowest electron density at ruthenium according to cyclic voltammetry (entry 1). Furthermore, complex **1** generated a much higher concentration of FA and TONs were much higher than those of complexes **2** and **3**. These data indicate fundamental differences in the active species derived from **1** compared to those of **2** and **3**, suggesting a distinct reaction mechanism for complex **1**. This difference has been attributed to a beneficial effect of the overall neutral carbene donor ligand pyridylidene–PYA donor ligand in complex **1**, which imparts higher robustness of the catalytically active species than the anionic phenyl-PYA chelates in complexes **2** and **3**. Moreover, this neutral ligand entails less electron density at the ruthenium center of complex **1** compared to that of **2** and **3** (Figure 4B), which implies a less nucleophilic metal hydride for the catalysts derived from **1**. Accordingly, the catalytic hydride intermediate is more resistant to protonation and formation of the inactive ruthenium dihydrogen complex (Figure 4A). This catalyst passivation through protonation is

particularly relevant for highly nucleophilic metal hydride species as well as in the high turnover regime, where larger quantities of FA product impart increasingly more acidic conditions. Hence, the higher resistance to acidification of the hydride originating from complex **1** results in higher TON and FA concentrations compared to the performance of complexes **2** and **3** (Figure 4B).

The gas uptake kinetics for complexes **1–3** supported this hypothesis. An exponential decay, which fits very well with first order kinetics was observed for complex **1**, while the uptake curve with complexes **2** and **3** strongly deviate from an exponential fit (Figure 4C). This indicates that complexes **2** and **3** are deactivated before they reach the thermodynamic equilibrium. It is well established that one major deactivation path during the hydrogenation of CO_2 to FA involves the protonation of the active hydride species,[40] though with complexes **2** and **3,** deactivation may also involve protonation of the phenyl ligand due to the increased acidity, and subsequent ligand dissociation. Irrespective of the exact deactivation mechanism for those complexes, the results obtained here indicate that complex **1** represent an attractive lead complex to develop new high-turnover catalysts for the hydrogenation of CO_2 to FA under base-free conditions.

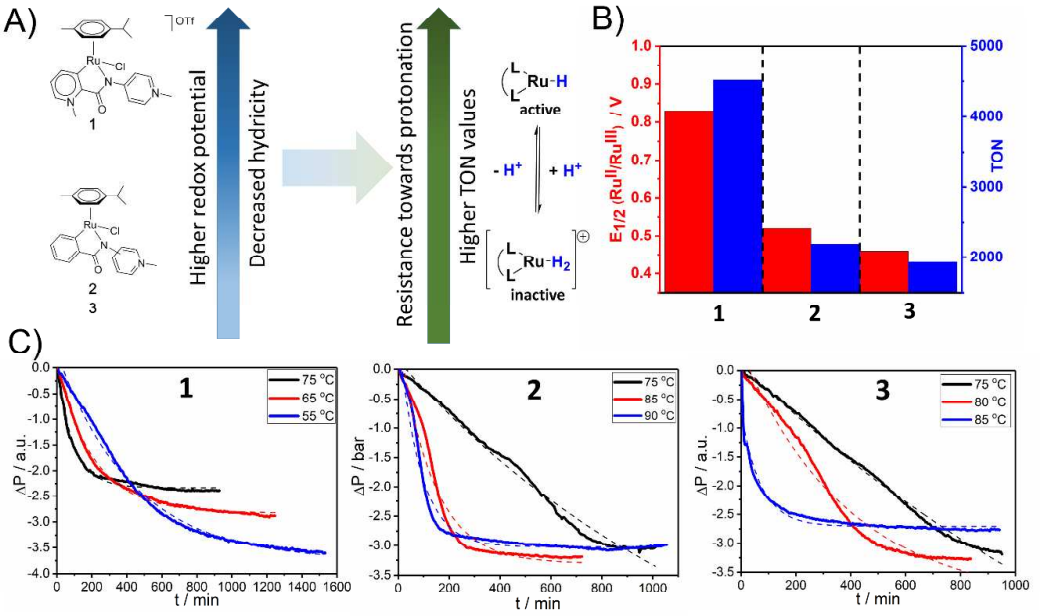


*Figure 5. A) Correlation between hydricity and catalyst robustness against acidification of the crucial ruthenium hydride intermediate. B) Correlation between redox potentials $E_{1/2}$ (Ru(II)/Ru(III)) values of complexes **1-3** in $MeNO_2$ as proxy for DMSO and the corresponding TON of the corresponding catalysts (Experimental conditions can be found in table 1). (C) Gas uptake kinetics for complexes **1-3,** solid lines represent experimental data obtained at P_{H2} = P_{CO2} = 20 bar in 6 mL DMSO:H_2O and 3.3 mmol BMMI.OAc with 8 µmol catalyst and dahed lines the best fit to an exponential decay function. Complex* **1** *shows a different behavior as gas uptake, fits an exponential decay, but not complexes* **2** *and* **3***.*

Conclusions

The base-free catalytic hydrogenation of CO_2 to form FA has a number of technical advantages and represents a more sustainable approach compared to the established base-assisted procedures. Direct hydrogenation has inherently a very high atom economy and therefore represents a sustainable alternative to generate chemicals and fuels from CO_2. Specific variation of the ligands bound to the catalytically active ruthenium center provided relevant insights into the mechanism of the reaction and the factors that influence the catalyst performance in terms of TON and TOF. Fine-tuning of the electron density at the metal center is key for catalyst

efficiency, with a dual effect observed: high-electron density facilitates CO_2 bonding and increases TOF, even though it also enhances the hydricity of the critical ruthenium hydride intermediate, which favours catalyst protonation due to the increasing acidity of the medium due to the formation of FA. Hence, while high electron density at the metal is beneficial for TOF optimization, low electron density favours the hydride-dihydrogen equilibrium to the catalytically active hydride side, thus enabling high TON values. This ambivalence of electron density emphasizes the relevance of fine-tuning the electronic configuration of the metal center. Moreover, the type of chelating PYA ligand has a direct influence on the nature of the TLS and depending on the set of ligands, either H_2 addition or CO_2 insertion have been observed as limiting step. Likewise, the ancillary ligand (Cl^- vs MeCN) modulates the mechanism of CO_2 insertion from inner to outer sphere.

Most interestingly, the catalyst precursor comprised of a formally neutral pyridylidene-PYA ligand showed unique activity. Specifically, the hydricity is markedly reduced and the catalytically active ruthenium hydride species stabilized, which prevents protonation even in the acidic product solution. As a consequence, these complex features results in high turnover frequency and also a two-fold increase in TON compared to the other complexes, hence representing an attractive lead for further catalyst development.

Acknowledgements

Dr Christof Jaeger is gratefully acknowledged for insightful discussions. The Faculty of Engineering from the University of Nottingham, the Generalitat Valenciana (CIDEGENT 2018/36), the European Research Council (CoG 615653) and the Swiss National Science Foundation (200020_182663) are gratefully acknowledged for funding.

References

1. Klankermayer, J.; Wesselbaum, S.; Beydoun, K.; Leitner, W., Selective Catalytic Synthesis Using the Combination of Carbon Dioxide and Hydrogen: Catalytic Chess at the Interface of Energy and Chemistry. *Angew. Chem. Int. Ed.* **2016,** *55* (26), 7296-7343.

2. Sordakis, K.; Tang, C.; Vogt, L. K.; Junge, H.; Dyson, P. J.; Beller, M.; Laurenczy, G., Homogeneous Catalysis for Sustainable Hydrogen Storage in Formic Acid and Alcohols. *Chem. Rev.* **2018,** *118* (2), 372-433.

3. Reutemann, W.; Kieczka, H., Formic Acid. In *Ullmann's Encyclopedia of Industrial Chemistry*, Wiley-VCH Verlag GmbH & Co. KGaA: 2000.

4. Mac Dowell, N.; Fennell, P. S.; Shah, N.; Maitland, G. C., The role of CO2 capture and utilization in mitigating climate change. *Nat. Clim. Chang.* **2017,** *7*, 243-249.

5. Hull, J. F.; Himeda, Y.; Wang, W.-H.; Hashiguchi, B.; Periana, R.; Szalda, D. J.; Muckerman, J. T.; Fujita, E., Reversible hydrogen storage using CO2 and a proton-switchable iridium catalyst in aqueous media under mild temperatures and pressures. *Nat. Chem.* **2012,** *4* (5), 383-388.

6. Loges, B.; Boddien, A.; Gärtner, F.; Junge, H.; Beller, M., Catalytic Generation of Hydrogen from Formic acid and its Derivatives: Useful Hydrogen Storage Materials. *Topics Catal.* **2010,** *53* (13), 902-914.

7. Grasemann, M.; Laurenczy, G., Formic acid as a hydrogen source - recent developments and future trends. *Energy Environ. Sci.* **2012,** *5* (8), 8171-8181.

8. Loges, B.; Boddien, A.; Junge, H.; Beller, M., Controlled Generation of Hydrogen from Formic Acid Amine Adducts at Room Temperature and Application in H2/O2 Fuel Cells. *Angew. Chem. Int. Ed.* **2008,** *47* (21), 3962-3965.

9. Johnson, T. C.; Morris, D. J.; Wills, M., Hydrogen generation from formic acid and alcohols using homogeneous catalysts. *Chem. Soc. Rev.* **2010,** *39* (1), 81-88.

10. Schaub, T.; Paciello, R. A., A Process for the Synthesis of Formic Acid by CO2 Hydrogenation: Thermodynamic Aspects and the Role of CO. *Angew. Chem. Int. Ed.* **2011,** *50* (32), 7278-7282.

11. Leitner, W., Carbon Dioxide as a Raw Material: The Synthesis of Formic Acid and Its Derivatives from CO2. *Angew. Chem. Int. Ed. Eng.* **1995,** *34* (20), 2207-2221.

12. Azua, A.; Sanz, S.; Peris, E., Water-Soluble IrIII N-Heterocyclic Carbene Based Catalysts for the Reduction of CO2 to Formate by Transfer Hydrogenation and the Deuteration of Aryl Amines in Water. *Chem. Eur. J.* **2011,** *17* (14), 3963-3967.

13. Sanz, S.; Azua, A.; Peris, E., '([small eta]6-arene)Ru(bis-NHC)' complexes for the reduction of CO2 to formate with hydrogen and by transfer hydrogenation with iPrOH. *Dalton Trans.* **2010,** *39* (27), 6339-6343.

14. Wang, W.-H.; Hull, J. F.; Muckerman, J. T.; Fujita, E.; Himeda, Y., Second-coordination-sphere and electronic effects enhance iridium(iii)-catalyzed homogeneous hydrogenation of carbon dioxide in water near ambient temperature and pressure. *Energy Environ. Sci.* **2012,** *5* (7), 7923-7926.

15. Himeda, Y.; Onozawa-Komatsuzaki, N.; Sugihara, H.; Kasuga, K., Simultaneous Tuning of Activity and Water Solubility of Complex Catalysts by Acid−Base Equilibrium of Ligands for Conversion of Carbon Dioxide. *Organometallics* **2007,** *26* (3), 702-712.

16. Himeda, Y.; Miyazawa, S.; Hirose, T., Interconversion between Formic Acid and H2/CO2 using Rhodium and Ruthenium Catalysts for CO2 Fixation and H2 Storage. *ChemSusChem* **2011,** *4* (4), 487-493.

17. Tanaka, R.; Yamashita, M.; Nozaki, K., Catalytic Hydrogenation of Carbon Dioxide Using Ir(III)−Pincer Complexes. *J. Am. Chem. Soc.* **2009,** *131* (40), 14168-14169.

18. Filonenko, G. A.; Hensen, E. J. M.; Pidko, E. A., Mechanism of CO2 hydrogenation to formates by homogeneous Ru-PNP pincer catalyst: from a theoretical description to performance optimization. *Catal. Sci. Technol.* **2014,** *4* (10), 3474-3485.

19. Filonenko, G. A.; Smykowski, D.; Szyja, B. M.; Li, G.; Szczygieł, J.; Hensen, E. J. M.; Pidko, E. A., Catalytic Hydrogenation of CO2 to Formates by a Lutidine-Derived Ru–CNC Pincer Complex: Theoretical Insight into the Unrealized Potential. *ACS Catal.* **2015,** *5* (2), 1145-1154.

20. Filonenko, G. A.; van Putten, R.; Schulpen, E. N.; Hensen, E. J. M.; Pidko, E. A., Highly Efficient Reversible Hydrogenation of Carbon Dioxide to Formates Using a Ruthenium PNP-Pincer Catalyst. *ChemCatChem* **2014,** *6* (6), 1526-1530.

21. Inoue, Y.; Izumida, H.; Sasaki, Y.; Hashimoto, H., CATALYTIC FIXATION OF CARBON DIOXIDE TO FORMIC ACID BY TRANSITION-METAL COMPLEXES UNDER MILD CONDITIONS. *Chem. Lett.* **1976,** *5* (8), 863-864.

22. Tsai, J. C.; Nicholas, K. M., Rhodium-catalyzed hydrogenation of carbon dioxide to formic acid. *J. Am. Chem. Soc.* **1992,** *114* (13), 5117-5124.

23. Fornika, R.; Gorls, H.; Seemann, B.; Leitner, W., Complexes [(P2)Rh(hfacac)](P2= bidentate chelating phosphane, hfacac = hexafluoroacetylacetonate) as catalysts for CO2 hydrogenation: correlations between solid state structures, 103Rh NMR shifts and catalytic activities. *J. Chem. Soc., Chem. Commun.* **1995,** (14), 1479-1481.

24. Graf, E.; Leitner, W., Direct formation of formic acid from carbon dioxide and dihydrogen using the [^{11}2]-Ph2P(CH2)4PPh2 catalyst system. *J. Chem. Soc., Chem. Commun.* **1992,** (8), 623-624.

25. Elek, J.; Nádasdi, L.; Papp, G.; Laurenczy, G.; Joó, F., Homogeneous hydrogenation of carbon dioxide and bicarbonate in aqueous solution catalyzed by water-soluble ruthenium(II) phosphine complexes. *Applied Catal. A* **2003,** *255* (1), 59-67.

26. Ziebart, C.; Federsel, C.; Anbarasan, P.; Jackstell, R.; Baumann, W.; Spannenberg, A.; Beller, M., Well-Defined Iron Catalyst for Improved

Hydrogenation of Carbon Dioxide and Bicarbonate. *J. Am. Chem. Soc.* **2012,** *134* (51), 20701-20704.

27. Robert, L.; Yael, D. P.; Gregory, L.; W., S. L. J.; Yehoshoa, B. D.; David, M., Low-Pressure Hydrogenation of Carbon Dioxide Catalyzed by an Iron Pincer Complex Exhibiting Noble Metal Activity. *Angew. Chem. Int. Ed.* **2011,** *50* (42), 9948-9952.

28. Zell, T.; Milstein, D., Hydrogenation and Dehydrogenation Iron Pincer Catalysts Capable of Metal–Ligand Cooperation by Aromatization/Dearomatization. *Acc. Chem. Res.* **2015,** *48* (7), 1979-1994.

29. Zhang, Y.; MacIntosh, A. D.; Wong, J. L.; Bielinski, E. A.; Williard, P. G.; Mercado, B. Q.; Hazari, N.; Bernskoetter, W. H., Iron catalyzed CO2 hydrogenation to formate enhanced by Lewis acid co-catalysts. *Chem. Sci.* **2015,** *6* (7), 4291-4299.

30. Burgess, S. A.; Kendall, A. J.; Tyler, D. R.; Linehan, J. C.; Appel, A. M., Hydrogenation of CO2 in Water Using a Bis(diphosphine) Ni–H Complex. *ACS Catal.* **2017,** *7* (4), 3089-3096.

31. Chakraborty, S.; Zhang, J.; Krause, J. A.; Guan, H., An Efficient Nickel Catalyst for the Reduction of Carbon Dioxide with a Borane. *J. Am. Chem. Soc.* **2010,** *132* (26), 8872-8873.

32. Ryo, W.; Yoshihito, K.; Shin-ichi, H.; Norio, M.; Takao, I., Hydrogenation of Carbon Dioxide to Formate Catalyzed by a Copper/1,8-Diazabicyclo[5.4.0]undec-7-ene System. *Adv. Synth. Catal.* **2015,** *357* (7), 1369-1373.

33. Zall, C. M.; Linehan, J. C.; Appel, A. M., A Molecular Copper Catalyst for Hydrogenation of CO2 to Formate. *ACS Catal.* **2015,** *5* (9), 5301-5305.

34. Burgess, S. A.; Appel, A. M.; Linehan, J. C.; Wiedner, E. S., Changing the Mechanism for CO2 Hydrogenation Using Solvent-Dependent Thermodynamics. *Angew. Chem. Int. Ed.* **2017,** *56* (47), 15002-15005.

35. Burgess, S. A.; Grubel, K.; Appel, A. M.; Wiedner, E. S.; Linehan, J. C., Hydrogenation of CO2 at Room Temperature and Low Pressure with a Cobalt Tetraphosphine Catalyst. *Inorg. Chem.* **2017,** *56* (14), 8580-8589.

36. Jeletic, M. S.; Hulley, E. B.; Helm, M. L.; Mock, M. T.; Appel, A. M.; Wiedner, E. S.; Linehan, J. C., Understanding the Relationship Between Kinetics and Thermodynamics in CO2 Hydrogenation Catalysis. *ACS Catal.* **2017,** *7* (9), 6008-6017.

37. Zhang, Z.; Hu, S.; Song, J.; Li, W.; Yang, G.; Han, B., Hydrogenation of CO2 to Formic Acid Promoted by a Diamine-Functionalized Ionic Liquid. *ChemSusChem* **2009,** *2* (3), 234-238.

38. Zhang, Z.; Xie, Y.; Li, W.; Hu, S.; Song, J.; Jiang, T.; Han, B., Hydrogenation of Carbon Dioxide is Promoted by a Task-Specific Ionic Liquid. *Angew. Chem. Int. Ed.* **2008,** *47* (6), 1127-1129.

39. Wesselbaum, S.; Hintermair, U.; Leitner, W., Continuous-Flow Hydrogenation of Carbon Dioxide to Pure Formic Acid using an Integrated scCO2 Process with Immobilized Catalyst and Base. *Angew. Chem.* **2012,** *124* (34), 8713-8716.

40. Rohmann, K.; Kothe, J.; Haenel, M. W.; Englert, U.; Hölscher, M.; Leitner, W., Hydrogenation of CO2 to Formic Acid with a Highly Active Ruthenium Acriphos Complex in DMSO and DMSO/Water. *Angew. Chem. Int. Ed.* **2016,** *55* (31), 8966-8969.

41. Moret, S.; Dyson, P. J.; Laurenczy, G., Direct synthesis of formic acid from carbon dioxide by hydrogenation in acidic media. *Nature Commun.* **2014,** *5*, 4017.

42. Sahoo, A. R.; Jiang, F.; Bruneau, C.; Sharma, G. V. M.; Suresh, S.; Roisnel, T.; Dorcet, V.; Achard, M., Phosphine-pyridonate ligands containing octahedral ruthenium complexes: access to esters and formic acid. *Catal. Sci. Technol.* **2017,** *7* (16), 3492-3498.

43. Hayashi, H.; Ogo, S.; Fukuzumi, S., Aqueous hydrogenation of carbon dioxide catalysed by water-soluble ruthenium aqua complexes under acidic conditions. *Chem. Commun.* **2004,** (23), 2714-2715.

44. Ogo, S.; Kabe, R.; Hayashi, H.; Harada, R.; Fukuzumi, S., Mechanistic investigation of CO2 hydrogenation by Ru(ii) and Ir(iii) aqua complexes under acidic conditions: two catalytic systems differing in the nature of the rate determining step. *Dalton Trans.* **2006,** (39), 4657-4663.

45. Zhao, G.; Joó, F., Free formic acid by hydrogenation of carbon dioxide in sodium formate solutions. *Catal. Commun.* **2011,** *14* (1), 74-76.

46. Qadir, M. I.; Weilhard, A.; Fernandes, J. A.; de Pedro, I.; Vieira, B. J. C.; Waerenborgh, J. C.; Dupont, J., Selective Carbon Dioxide Hydrogenation Driven by Ferromagnetic RuFe Nanoparticles in Ionic Liquids. *ACS Catal.* **2018,** *8* (2), 1621-1627.

47. Weilhard, A.; Qadir, M. I.; Sans, V.; Dupont, J., Selective CO2 Hydrogenation to Formic Acid with Multifunctional Ionic Liquids. *ACS Catal.* **2018,** *8* (3), 1628-1634.

48. Yasaka, Y.; Wakai, C.; Matubayasi, N.; Nakahara, M., Controlling the Equilibrium of Formic Acid with Hydrogen and Carbon Dioxide Using Ionic Liquid. *J. Phys. Chem. A* **2010,** *114* (10), 3510-3515.

49. Doster, M. E.; Johnson, S. A., Selective C□F Bond Activation of Tetrafluorobenzenes by Nickel(0) with a Nitrogen Donor Analogous to N-Heterocyclic Carbenes. *Angew. Chem. Int. Ed.* **2009,** *48* (12), 2185-2187.

50. Shi, Q.; Thatcher, R. J.; Slattery, J.; Sauari, P. S.; Whitwood, A. C.; McGowan, P. C.; Douthwaite, R. E., Synthesis, Coordination Chemistry and Bonding of Strong N-Donor Ligands Incorporating the 1H-Pyridin-(2E)-Ylidene (PYE) Motif. *Chem. Eur. J.* **2009,** *15* (42), 11346-11360.

51. Boyd, P. D. W.; Wright, L. J.; Zafar, M. N., Extending the Range of Neutral N-Donor Ligands Available for Metal Catalysts: N-[1-Alkylpyridin-4(1H)-ylidene]amides in Palladium-Catalyzed Cross-Coupling Reactions. *Inorg. Chem.* **2011,** *50* (21), 10522-10524.

52. Donnelly, K. F.; Segarra, C.; Shao, L.-X.; Suen, R.; Müller-Bunz, H.; Albrecht, M., Adaptive N-Mesoionic Ligands Anchored to a Triazolylidene for Ruthenium-Mediated (De)Hydrogenation Catalysis. *Organometallics* **2015,** *34* (16), 4076-4084.

53. Leigh, V.; Carleton, D. J.; Olguin, J.; Mueller-Bunz, H.; Wright, L. J.; Albrecht, M., Solvent-Dependent Switch of Ligand Donor Ability and Catalytic Activity of Ruthenium(II) Complexes Containing Pyridinylidene Amide (PYA)

N-Heterocyclic Carbene Hybrid Ligands. *Inorg. Chem.* **2014,** *53* (15), 8054-8060.

54. Navarro, M.; Smith, C. A.; Albrecht, M., Enhanced Catalytic Activity of Iridium(III) Complexes by Facile Modification of C,N-Bidentate Chelating Pyridylideneamide Ligands. *Inorg. Chem.* **2017,** *56* (19), 11688-11701.

55. Navarro, M.; Li, M.; Müller-Bunz, H.; Bernhard, S.; Albrecht, M., Donor-Flexible Nitrogen Ligands for Efficient Iridium-Catalyzed Water Oxidation Catalysis. *Chem. Eur. J.* **2016,** *22* (20), 6740-6745.

56. Navarro, M.; Smith, C. A.; Li, M.; Bernhard, S.; Albrecht, M., Optimization of Synthetically Versatile Pyridylidene Amide Ligands for Efficient Iridium-Catalyzed Water Oxidation. *Chem. Eur. J.* **2018,** *24* (24), 6386-6398.

57. Melle, P.; Manoharan, Y.; Albrecht, M., Modular Pincer-type Pyridylidene Amide Ruthenium(II) Complexes for Efficient Transfer Hydrogenation Catalysis. *Inorg. Chem.* **2018,** *57* (18), 11761-11774.

58. Navarro, M.; Li, M.; Bernhard, S.; Albrecht, M., A mesoionic nitrogen-donor ligand: structure, iridium coordination, and catalytic effects. *Dalton Trans.* **2018,** *47* (3), 659-662.

59. Simon, N. M.; Zanatta, M.; dos Santos, F. P.; Corvo, M. C.; Cabrita, E. J.; Dupont, J., Carbon Dioxide Capture by Aqueous Ionic Liquid Solutions. *ChemSusChem* **2017,** *10* (24), 4927-4933.

60. Zanatta, M.; Dupont, J.; Wentz, G. N.; dos Santos, F. P., Intermolecular hydrogen bonds in water@IL supramolecular complexes. *Phys. Chem. Chem. Phys.* **2018,** *20* (17), 11608-11614.

61. Zanatta, M.; Girard, A.-L.; Marin, G.; Ebeling, G.; dos Santos, F. P.; Valsecchi, C.; Stassen, H.; Livotto, P. R.; Lewis, W.; Dupont, J., Confined water in imidazolium based ionic liquids: a supramolecular guest@host complex case. *Phys. Chem. Chem. Phys.* **2016,** *18* (27), 18297-18304.

62. Weilhard, A.; Dupont, J.; Sans V., Carbon dioxide utilisation Vol 2. Berlin, De Gruyter: **2019**, 329-344. DOI: 10.1515/9783110665147-017

63. Hiraga, Y.; Sato, Y.; Smith, R. L., Development of a simple method for predicting CO2 enhancement of H2 gas solubility in ionic liquids. *J. Supercrit. Fluid* **2015,** *96*, 162-170.

64. Lopez-Castillo, Z. K.; Aki, S. N. V. K.; Stadtherr, M. A.; Brennecke, J. F., Enhanced Solubility of Hydrogen in CO2-Expanded Liquids. *Ind. Eng. Chem. Res.* **2008,** *47* (3), 570-576.

65. Mondal, B.; Neese, F.; Ye, S., Control in the Rate-Determining Step Provides a Promising Strategy To Develop New Catalysts for CO2 Hydrogenation: A Local Pair Natural Orbital Coupled Cluster Theory Study. *Inorg. Chem.* **2015,** *54* (15), 7192-7198.

66. Waldie, K. M.; Ostericher, A. L.; Reineke, M. H.; Sasayama, A. F.; Kubiak, C. P., Hydricity of Transition-Metal Hydrides: Thermodynamic Considerations for CO2 Reduction. *ACS Catal.* **2018,** *8* (2), 1313-1324.

67. Matsubara, Y.; Fujita, E.; Doherty, M. D.; Muckerman, J. T.; Creutz, C., Thermodynamic and Kinetic Hydricity of Ruthenium(II) Hydride Complexes. *J. Am. Chem. Soc.* **2012,** *134* (38), 15743-15757.

68. Mondal, B.; Neese, F.; Ye, S., Toward Rational Design of 3d Transition Metal Catalysts for CO2 Hydrogenation Based on Insights into Hydricity-Controlled Rate-Determining Steps. *Inorg. Chem.* **2016,** *55* (11), 5438-5444.

69. Lu, S.-M.; Wang, Z.; Li, J.; Xiao, J.; Li, C., Base-free hydrogenation of CO2 to formic acid in water with an iridium complex bearing a N,N[prime or minute]-diimine ligand. *Green Chem.* **2016,** *18* (16), 4553-4558.

70. Hazari, N.; Heimann, J. E., Carbon Dioxide Insertion into Group 9 and 10 Metal–Element σ Bonds. *Inorg. Chem.* **2017,** *56* (22), 13655-13678.

71. Heimann, J. E.; Bernskoetter, W. H.; Hazari, N.; Mayer, James M., Acceleration of CO2 insertion into metal hydrides: ligand, Lewis acid, and solvent effects on reaction kinetics. *Chem. Sci.* **2018,** *9* (32), 6629-6638.

72. Wiedner, E. S.; Chambers, M. B.; Pitman, C. L.; Bullock, R. M.; Miller, A. J. M.; Appel, A. M., Thermodynamic Hydricity of Transition Metal Hydrides. *Chem. Rev.* **2016,** *116* (15), 8655-8692.

73. Galan, B. R.; Schöffel, J.; Linehan, J. C.; Seu, C.; Appel, A. M.; Roberts, J. A. S.; Helm, M. L.; Kilgore, U. J.; Yang, J. Y.; DuBois, D. L.; Kubiak, C. P., Electrocatalytic Oxidation of Formate by [Ni(PR2NR′2)2(CH3CN)]2+ Complexes. *J. Am. Chem. Soc.* **2011,** *133* (32), 12767-12779.

74. Lilio, A. M.; Reineke, M. H.; Moore, C. E.; Rheingold, A. L.; Takase, M. K.; Kubiak, C. P., Incorporation of Pendant Bases into Rh(diphosphine)2 Complexes: Synthesis, Thermodynamic Studies, And Catalytic CO2 Hydrogenation Activity of [Rh(P2N2)2]+ Complexes. *J. Am. Chem. Soc.* **2015,** *137* (25), 8251-8260.

75. Waldie, K. M.; Brunner, F. M.; Kubiak, C. P., Transition Metal Hydride Catalysts for Sustainable Interconversion of CO2 and Formate: Thermodynamic and Mechanistic Considerations. *ACS Sustain. Chem. Eng.* **2018,** *6* (5), 6841-6848.

76. Pitman, C. L.; Brereton, K. R.; Miller, A. J. M., Aqueous Hydricity of Late Metal Catalysts as a Continuum Tuned by Ligands and the Medium. *J. Am. Chem. Soc.* **2016,** *138* (7), 2252-2260.

77. Kubas, G., *Metal-dihydrogen and σ-bond coordination: The consummate extension of the Dewar-Chatt-Duncanson model for metal-olefin π bonding*. *J. Organometal. Chem.* **2001**, *635* (1-2), 37-68.

78. Ono, T.; Qu, S.; Gimbert-Suriñach, C.; Johnson, M. A.; Marell, D. J.; Benet-Buchholz, J.; Cramer, C. J.; Llobet, A., Hydrogenative Carbon Dioxide Reduction Catalyzed by Mononuclear Ruthenium Polypyridyl Complexes: Discerning between Electronic and Steric Effects. *ACS Catal.* **2017,** *7* (9), 5932-5940.

6.4. Results and Discussion

In order to gain a broader understanding of the influence of different catalyst parameters influencing the reaction mechanism and the catalyst durability, catalyst **3** was added to the series investigated. Furthermore, the Cl ligand was replaced in the case of **2** and **3** by MeCN (giving **2-MeCN** and **3-MeCN**). An increased temperature (70°C) and pressure (60 bar total) led to the improvement in TON and TOF were reported for the catalyst series investigated here (**table 5)**.

The complexes behaved significantly differently under catalytic reaction conditions. Complex **2**, **2-MeCN**, **3** and **3-MeCN** displayed a significant induction period, whilst with **1** an induction period was not observed (for tabulated induction times the reader is referred to **publication III**, **SI table S4**). After the induction period all complexes enter a near linear regime for the formation of formic acid. This linear regime was used to calculate the rate of the reaction with the varying complexes and by dividing the obtained rate with the catalyst concentration the TOF was obtained, see **figure 6.5**.

Upon approaching the final concentration of formic acid the rate of formic acid formation most likely reduces till the achieved concentration plateaus, see **figure 6.5**. However, it is important to note that the reaction was not monitored continuously but rather the concentrations were determined by stopping individual reactions at different times, thus relatively low resolution of the reaction kinetics is obtained.

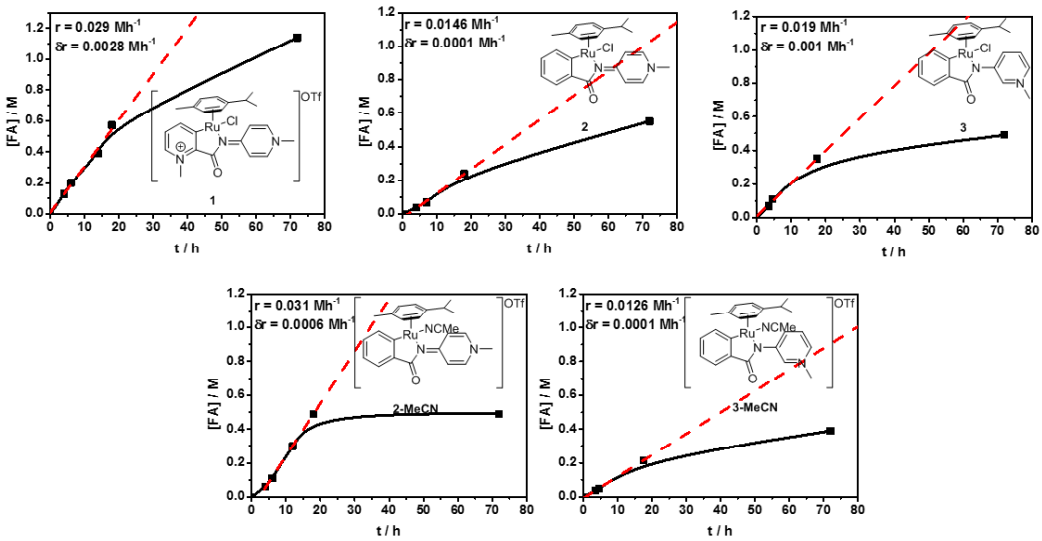
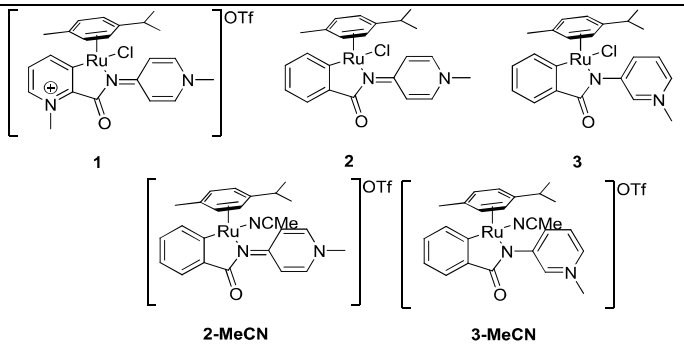


Figure 6.5 Observed concentrations of FA in dependence of time with catalysts **1 – 3-MeCN**. Black dots represent measured concentrations of FA, whilst the black line represents the curvature of FA formation (Note: Due to the high uncertainty of the measurement no fitting function is used), dashed red line represents the linear regression for the determination of the rate r and the error of the rate δr. Reaction conditions: 1.5 µmol catalyst and 3.3 mmol BMMI.OAc in 6 mL DMSO:H_2O (5 v/v% H_2O) under P(CO_2) P(H_2) = 30 bar at 70°C.

Beneath the aforementioned observations, it can determined that complex **1** displays a significantly higher catalyst stability, followed by complexes **2**, **3**, **2-MeCN** and **3-MeCN**. A TON of 4520 and a concentration of FA of 1.14 M (**table 6.2**, **entry 1** and **table 1, entry 1** in **publication III**) is achieved with **1**, which is very close to the thermodynamic predictable concentration of FA under the conditions assayed (thermodynamic equilibrium at [FA] = 1.2 M), see ***Part I*** and *Publication I*. On the other hand, the rest of complexes achieve FA concentrations of FA *ca.* 0.5 M (**Table 6.2**, **entries 2-5** and **table 1**, **entry 2-5** in **publication III**), suggesting that these complexes show limitations to the yield. The most remarkable feature of complex **1** to the rest of the series is a formally neutral pyridinium carbene wingtip, compared to the formally negative phenyl carbene wingtip.

In terms of catalytic activity, complexes **1** and **2-MeCN** (**table 6.2**, **entry 1** and **4**) showed distinctively higher values of TOF.

Table 6.2 Catalyst screening for the hydrogenation of CO_2 to FA; these tabulated results can also be found in **publication III table 1** & **2**.



Entry	Catalyst	P_{H2} : P_{CO2} / bar	TON[a]	TOF[b] / h^{-1}	[FA][a] / M
1	**1**	30:30	4515	117±11.1	1.14
2	**3**	30:30	1932	78.4 ± 2.2	0.49
3	**2**	30:30	2193	55 ± 3.6	0.55
4	**2-MeCN**	30:30	1953	122 ± 2.3	0.49
5	**3-MeCN**	30:30	1520	50 ± 0.4	0.39
6	**2-MeCN**	30:50	1905	342 ± 60	0.49
7	**2**	30:50	2010	180 ± 20	0.51
8	**3**	60:30	1930	136±4	0.49
9	**3**	30:50	1930	120±9	0.49
10	**1**	60:30	4520	192 ± 4	1.15

Reaction conditions: 6 mL DMSO:water (5 v/v% water) in the presence of 3.3 mmol BMMI.OAc at 70°C, P_{H2}:P_{CO2} = 30:30 (bar:bar). a) Determined after 72 h using BMMI.OAc as an internal standard; the average of two independent experiments with values within the certainty of quantitative ^{1}H-NMR measurements. B) calculated from the linear regression applied in the near linear regime.

Interestingly, complex **2** achieved a significantly lower TOF value than **2-MeCN,** even though the same ligand scaffold was employed, and they only differ in the substituents around the metal centre (Cl vs. MeCN). A reversed effect was observed in **3** and **3-MeCN** (**table 6.2**, **entries 2** and **5**). The substitution of the phenyl-*para*-PYA scaffold in **2** by the more electron donating phenyl-*meta*-PYA scaffold in **3** increases the rate from 55 h^{-1} to 78 h^{-1}, indicating the importance of electron donating effects on the catalytic activity observed.

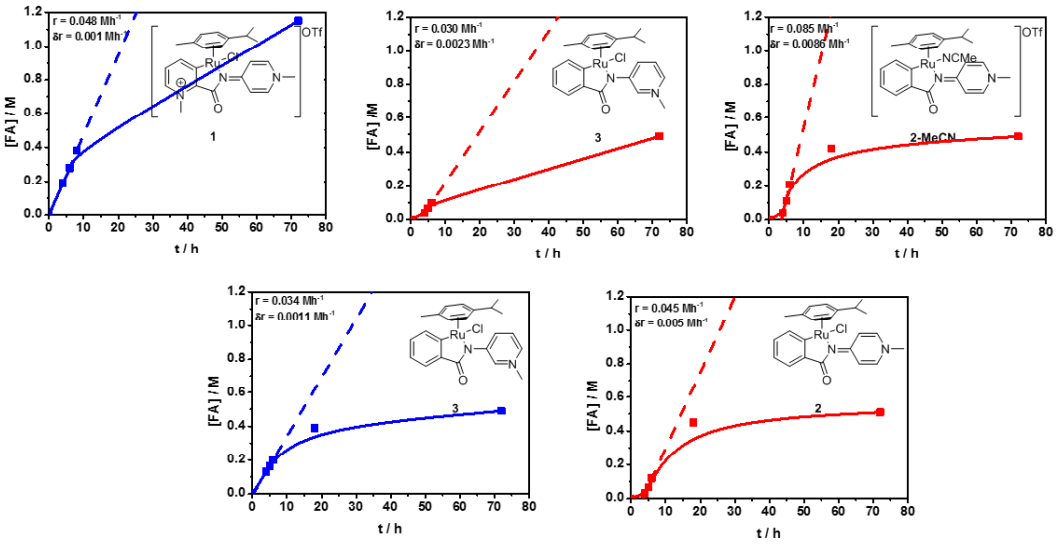


Figure 6.6 Observed concentrations of FA in dependence of time with catalysts **1 – 2-MeCN**. Dots represent measured concentrations of FA, whilst the red and blue line represent the curvature of FA formation under either excess pressure of H_2 or CO_2 (Note: Due to the high uncertainty of the measurement no fitting function is used), dashed red and line represents the linear regression for the determination of the rate r and the error of the rate δr. Reaction conditions: 1.5 µmol catalyst and 3.3 mmol BMMI.OAc in 6 mL DMSO:H_2O (5 v/v% H_2O) under P(CO_2) = 50 bar P(H_2) = 30 bar at 70°C (red lines) and 1.5 µmol catalyst and 3.3 mmol BMMI.OAc in 6 mL DMSO:H_2O (5 v/v% H_2O) under P(CO_2) = 30 bar P(H_2) = 60 bar at 70°C (blue lines).

Under optimised conditions, i.e. in the presence of excess amounts of the turnover limiting reagent, significantly higher TOFs are achieved, even though

the TON does not significantly change to un-optimised conditions, see **table 6.2 entry 6-11** and **figure 6.6**. This indicates that, the catalytically active species does not change even though considerably differing reaction conditions are applied. In the following differences in between the catalyst will be discussed, for further details the reader is referred to **publication III**, **table 1** & **2**.

6.4.1. Different turnover limiting steps

The first apparent difference between the complexes investigated here is the difference in the turnover limiting steps (TLS). In order to discuss the different TLS a simplified scheme to describe the transformation of CO_2 to formic acid with hydrogen will be given here.

In a first step CO_2 and H_2 must diffuse into the liquid phase. This was considered to proceed significantly faster than the following catalytic transformation of CO_2 and H_2 to formic acid and thus was not included in the development of the rate law. Also, it was assumed that neither the diffusion of the gases nor the solubility of the reactants in each other does play a significant role onto the observed rate. Accordingly, the concentration of reactants in the liquid phase was considered constant and the concentration of reactants could be calculated with Henry's law, **see section 1.2.1 equation 1.3**.

Despite the previous assumptions, it is important to note that diffusion and effective solubility might be significantly affected by cross effects, i.e. it is well

established that H_2 is highly soluble in (near-critical and supercritical) CO_2, thus increasing the partial pressure of CO_2 might alter the solubility of H_2 in the liquid phase.[33-35] Also, diffusion might be inhibited by the viscosity of the solvent system (the system DMSO:H_2O and BMMI.OAc is a highly viscous one). Therefore, increasing the concentration of a reactant with low viscosity might significantly alter the viscosity of the whole solvent system, and thereby having a beneficial role onto the diffusion coefficients of both reactants.

Indeed, cross effects concerning effective concentration and diffusion of H_2 with CO_2-expanded solvents has been described to affect the effective rate of CO_2 transformation to FA.[32] In order to evaluate the precise effect of alternating concentration of for example H_2 in CO_2 expanded solvents and the effect of diffusion onto the rate, further experiments would be necessary. Nonetheless, diffusion and alternating concentration of H_2 in CO_2-expanded can be expected to have only a minor effect onto the observed rate of reaction.

After diffusion of the gases into the liquid phase, CO_2 and H_2 are catalytically transformed to formic acid. In a simplistic model this step can be divided into two steps (see also ***section 1.2.2*** **figure 1.14**). First CO_2 inserts into the active metal hydride forming the formate complex. In the next step H_2 is activated, recovering the active hydride and releasing formic acid. This simplified mechanism is depicted in the **figure 6.7**.

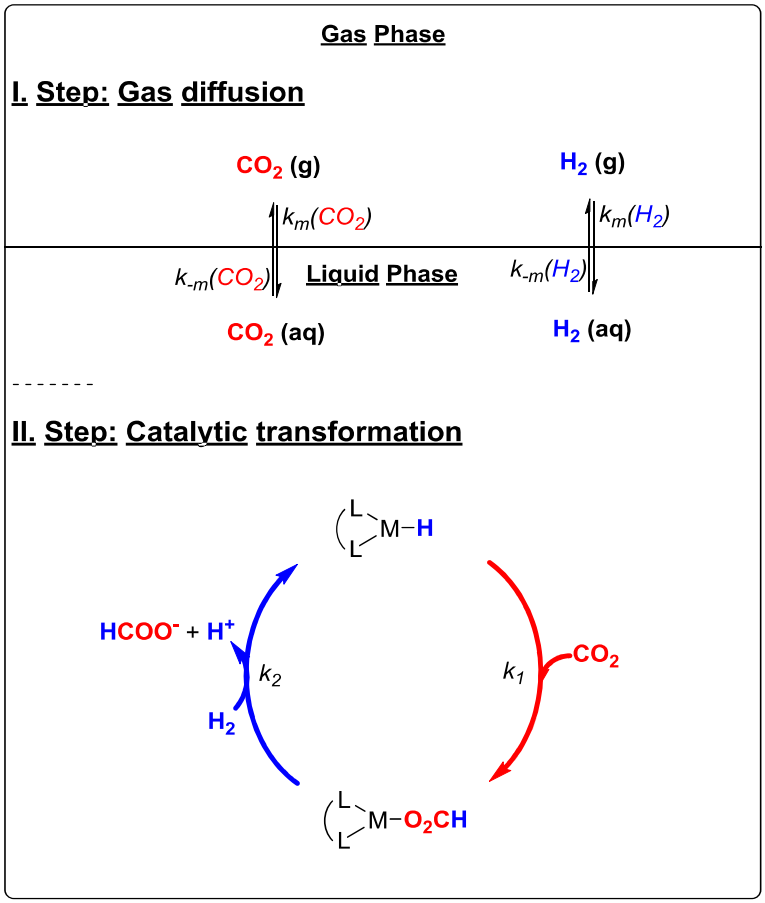


Figure 6.7 Process for the hydrogenation of CO_2 to formic acid. First CO_2 and H_2 are transferred from the gas phase to the liquid phase (I. step). Afterwards they are transformed in a catalytic cycle to formic acid (II. Step).

From this simplified mechanism two cases can already be envisioned. In the first case, the CO_2 insertion is much slower than the hydride recovery ($k_1 \ll k_2$). In the second case the hydride recovery is much slower than the CO_2 insertion ($k_1 \gg k_2$). Accordingly, two scenarios can already be derived. In the first scenario the rate is solely dependent on CO_2, in the second scenario on H_2. The rate laws for the first two scenarios are depicted in the equations below.

$$\frac{d[HCOOH]}{dt} = k_1[CO_2(aq)][M-H] \ for \ (k_1 \ll k_2) \quad (6.1)$$

$$\frac{d[HCOOH]}{dt} = k_2[H_2(aq)][M-O_2CH] \; for(k_2 \ll k_1) \qquad (6.2)$$

Furthermore, it can be assumed that if $k_1 \ll k_2$ or $k_1 \gg k_2$ only one intermediate species is present in the solution, as the other intermediate is immediately consumed after formation, hence $[M-H] \approx [Cat]$, respectively $[M-O_2CH] \approx [Cat]$ (with $[Cat]$ being the concentration of catalyst in solution).

However, in some cases $k_2 \approx k_1$ thus the assumption that only one catalytic intermediate is present is incorrect. In order to derive a rate law for this case a steady state approximation for the catalyst is assumed, see equation 6.3.

$$\frac{d[M-O_2CH]}{dt} = k_1[CO_2(aq)][M-H] - k_2[H_2(aq)][M-O_2CH] = 0 \quad (6.3)$$

From equation 6.3 equation 6.4 can be obtained.

$$\frac{[M-H]}{[M-O_2CH]} = \frac{k_2[H_2(aq)]}{k_1[CO_2(aq)]} \quad (6.4)$$

With the catalyst concentration defined here as $[CAT] = [M-O_2CH] + [M-H]$ equation 6.5 can be articulated.

$$[CAT] = [M-O_2CH]\left(1 + \frac{k_2[H_2(aq)]}{k_1[CO_2(aq)]}\right) \quad (6.5)$$

Resolving equation 17 towards $[M-O_2CH]$ and inserting the result into equation 6.2, equation 6.6 can be obtained.

$$\frac{d[HCOOH]}{dt} = \frac{k_2[H_2(aq)][\mathrm{Cat}]}{\left(1+\frac{k_2[H_2(aq)]}{k_1[CO_2(aq)]}\right)} \quad (6.6)$$

Here an increased concentration of either gas will lead to an increased rate if $k_2[H_2(aq)] \approx k_1[CO_2(aq)]$, thus a third case can be postulated in which the reaction rate is dependent on both reactants.

Indeed, all three cases can be found with the complexes investigated here. When complex **1** was employed as catalyst, the turnover limiting step (TLS) was clearly associated to the H_2 activation (see also **publication III**, **figure 1**). Indeed, **Figure 6.8b** shows a linear dependence on the partial pressure of H_2. In contrast the TOF plateaus at about 150 h^{-1} upon increasing the CO_2 pressure from 40 bar CO_2 to 50 bar CO_2. The initial increase in rate, when CO_2 partial pressure is increased (from 30 bar to 40 bar) can be explained by the high solubility of H_2 in CO_2, thus increasing the effective concentration of H_2 in the reaction media at higher CO_2 pressures, **Figure 6.8b**.

The TLS of **2** is associated with the CO_2 insertion. On the one hand complex **2** displays a linear relationship of partial pressure of CO_2 and measured TOF, reaching 186 h^{-1} at 50 bar CO_2, **Figure 6.8c**. On the other hand the TOF plateaued if the partial pressure of H_2 was increased above 30 bar. The same behaviour was observed with catalyst **2-MeCN** (see **publication III**, **Figure 3**).

With **3** the third case is observed, i.e. the CO_2 insertion and H_2 activation are energetically closely related. In this way, the change in activity as a function of partial pressure of H_2 and CO_2 did show a linear correlation in both cases (**Figure 6.8d**) and no plateauing was observed.

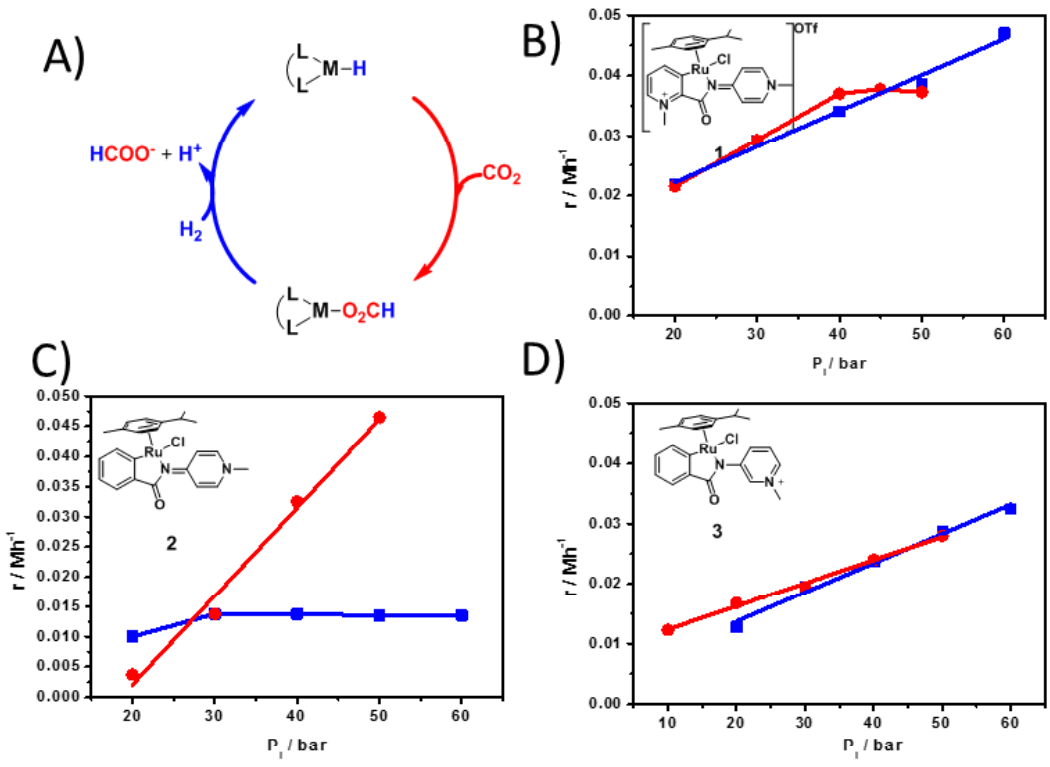


Figure 6.8 A)-D) variation of the partial pressure P_i of either CO_2 (red) or H_2 (blue), whilst keeping the pressure of the other reactant constant at 30 bar. Reaction conditions: T= 70°C, 6 mL DMSO:H_2O (5 v/v% H_2O), 3.3 mmol BMMI.OAc. and 1.52 µmol of complexes **1**-**3** respectively. Note: Points for the determination of the rate are either given in table 10 or are calculated from the achieved concentration of FA at at least 2 different times. Data for the calculation is given in **table S6**-**S9** in **publication III SI** and an exemplary calculation is given separately in the methods part of this chapter and this figure is also given in **publication III** as **figure 1**.

After determining the reaction rate in dependence of the reactants (CO_2 and H_2) with the complexes **1**-**2-MeCN**, the reaction order of the reactants can estimated. With the estimated reaction orders in hand, the rate constants for the hydrogenation of CO_2 to formic acid were determined (for precise procedures see experimental section). In general, a significantly higher rate constant is obtained for complexes, where the rate determining step was not (solely) dependent on the CO_2 partial pressure, see table below. This effect

can be attributed to the increased solubility of CO_2 in the reaction media compared to hydrogen.

Table 6.3 rate constants k calculated for complexes **1**-**2-MeCN**.

Complex	n(CO_2)	n(H_2)	k_{real}[a)]	$k_{first\ order}$[b)] / h^{-1}
1	0	1	0.9142 h^{-1}	0.9142
2	2	0	0.0013 M^{-1} h^{-1}	0.0044
3	1	1	0.1797 M^{-1} h^{-1}	0.5989
2-MeCN	2	0	0.0028 M^{-1} h^{-1}	0.0093
3-MeCN	n.a.	n.a.	n.a.	0.3972

a) calculated with the reactant order b) assuming first order dependency with the rate determining reactant.

Furthermore, a second reaction order can be derived for complexes **2** and **2-MeCN** in respect to CO_2, whilst complex **1** displayed a first order dependence towards H_2, whilst **3** displayed a first order towards both CO_2 and H_2. If a first order dependence is assumed for all the complexes, the rate constants derived with the here investigated complexes do change, although the overall catalytic activity remains in the same order (Note a first order dependence towards hydrogen is assumed for complex **3** and **3-MeCN**).

6.4.2. Parameters influencing the rate of catalytic transformation

In the next section focus was on the influence of different parameters on the observed rate. In the first step the electron donation of **2** and **3** was investigated, via the redox potential of the parent complexes. The redox potential is then compared to corresponding activation energy obtained for the investigated complex.

Electron donation and observed rate

In order to quantify the effect of electron density onto the rate the activation energy for complexes **2** and **3** in DMSO:water (5 v/v% water) with BMMI.OAc were determined. Furthermore, the group of Prof. Albrecht has demonstrated that the phenyl-*para*-PYA scaffold exists in two resonance structures (**figure 6.9**) that can be tuned by switching the polarity of the solvent.[3-4]

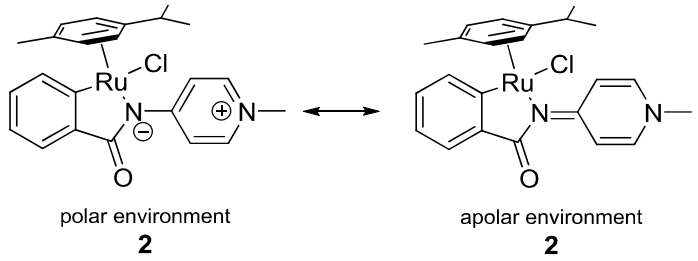


Figure 6.9 neutral vs zwitterion ionic form of **2**.[3-4]

The electron density at the metal centre can be tuned by shifting the distribution to one or the other resonance structure. This can be achieved by utilizing more apolar -, respectively more polar environment during a catalytic experiment.[3] The different electronic properties of the resonant structures were employed to study their effect on the activation energy of **2** in different solvent media. A relatively apolar medium (THF:water) in the presence of 1-Decyl-2,3-dimethylimidazolium acetate (C_{10}MMI.OAc) was chosen to mimic an apolar environment and compared to the results in DMSO: water employing BMMI.OAc as IL media.

It was found that, the oxidation potential of **2** increases from 0.52 V (in $MeNO_2$) to 0.63 V (THF), thus indicating a lower electron density at the metal centre if THF is employed as the solvent with **2**, see **table 6.3**, entry **2** and **3**. At the same time an increased activation energy for **2** is measured in THF (96 kJ mol-

[1] ± 3.1 kJ mol^{-1}), when compared to DMSO (86 kJ mol^{-1} ± 5.1 kJ mol^{-1}), see **table 6.3**. The highest electron density at the metal centre corresponded to complex **3**, evidenced by the lowest oxidation potential of the series (0.46 V). At the same time the lowest activation energy in this row was determined for **3** 71 kJ mol^{-1} ± 4.5 kJ mol^{-1}), see **table 6.3**, **entry 1**.

Table 6.4 Comparison of the redox potential, Arrhenius parameters, respectively **table 4** in **publication III**.

Entry	Cat.	Solvent	Ionic liquid	ΔE_a / kJ mol^{-1}	lnA	$E_{1/2}$ / V
1	**3**	DMSO:water	BMMI.OAc	71 ± 4.5	19 ± 1.6	0.46[a)]
2	**2**	DMSO:water	BMMI.OAc	86 ± 5.1	24 ± 1.8	0.52[a)]
3	**2**	THF: water	C_{10}MMI.OAc	96 ± 3.1	30 ± 1.1	0.63[b)]

Reaction conditions: catalyst amount 8 umol, 3.3 mmol IL, 6 mL solvent with 5 v/v% water, P(H_2) = P(CO_2) = 20 bar.a) measurement in DMSO is not possible due to solvent decomposition thus measurement was undertaken in $MeNO_2$, which has a similar polarity as DMSO; b) measured in THF

It is important to note that, a relationship in between the hydricity of the active catalytic species and the catalytic activity of a wide range of catalyst has been previously established.[12] The complex hydricity in turn has shown to correlate with the electron density at the metal centre, hence allowing to estimate the hydride transfer capability of metal complexes, and to compare to the hydride donor-ability of formate/formic acid.[12-22] In general, higher hydride transfer capabilities lead to higher catalytic activities in the hydrogenation of CO_2. In this regard complex **2** and **3** do follow an expected trend. Also, a relationship in between the oxidation potential and the catalytic activity has been

established previously with other Ru-catalysts in the hydrogenation of CO_2 under basic conditions.[23]

Furthermore, the increased electron density at the metal centre with **3** might even explain the change in the turnover limiting step when compared to **2**. Here the CO2 insertion might switch from being an endergonic reaction step ($\Delta G<0$), with **2**, to an exergonic one ($\Delta G>0$) with **3**.

However, the biggest change in catalytic activity (TOF) was not observed with an increased electron density at the metal centre but with the replacement of Cl^- in **2** with MeCN, giving **2-MeCN**. It is important to note that both complexes display the CO_2 insertion step as the turnover limiting, as shown in **figure 3a** and **b**.

Inner vs. outer sphere mechanism for the CO_2 insertion

Two mechanisms for the CO_2 insertion depending on nucleophilicity and sterics around the metal centre have been described. In the case of strong nucleophiles (such as metal amines) and metal hydrides with low sterical demand, an “inner sphere” mechanism is possible, where the approaching CO_2 simultaneously coordinates to the metal centre whilst the hydride is transferred onto the CO_2 in a concerted (associative) fashion.[24-25] In the case of weaker hydrides (such as most metal hydrides) an “outer sphere” mechanism is prevalent, where in the first step a hydride is transferred onto the approaching CO_2 molecule resulting in a zwitterionic intermediate with a positively charged metal center and a negatively charged formate moiety. In a second step this zwitterionic intermediate rearranges leading to a formate complex, **figure 6.10**.

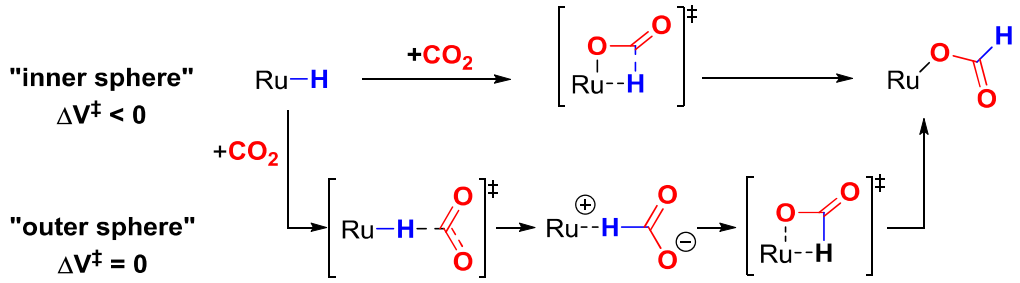


Figure 6.10 Inner (top) vs. outer sphere (bottom) mechanism during CO_2 insertion.

It is important to note that **2-MeCN** showed small increases in rate (from 122 h^{-1} to 150 h^{-1}) when the H_2 partial pressure was increased (see **publication III**, **Figure 3**), whilst this was not observed for complex **2**. In order to investigate whether the increasing rate observed under higher H_2 pressures with **2-MeCN** is due to an increased concentration of reactant, or whether other parameters such as physical pressure plays a significant role, a system containing **2**, respectively **2-MeCN** under additional pressure induced by the inert gas Ar.

The addition of 50 bar of Ar to the catalytic system led to an increase in the observed TOF of *ca.* 20% when **2-MeCN** was used as the catalyst (**table 6.4**, **entries 3** and **4** and **table 3**, **entry 3** and **4** in **publication III**). In contrast, no significant change in rate was observed when **2** was used as the catalyst (**table 6.4**, **entries 1** and **2** and **table 3**, **entry 1** and **2** in **publication III**). The increased rate with **2-MeCN** can be related a lowered volume of activation[26]:

$$\Delta V^{\ddagger} = -RT\left(\frac{dln\,k}{dP}\right)_T \quad (6.7)$$

where $\Delta V^{\ddagger}$ as volume of activation, R as the gas constant, T as the temperature P as the pressure. A negative value of $\Delta V^{\ddagger}$ suggests an associative process for **2-MeCN** as opposed to **2**. In the case of **2-MeCN** the TLS of CO_2 insertion proceeds most likely in a concerted (associative) fashion, thus resulting in a negative volume of activation, whilst with **2** the outer sphere mechanism is

dominant, thus no change in the volume of activation is observed. Furthermore, it has been shown that the inner sphere mechanism proceeds in a faster fashion as the outer sphere mechanism and thus might explain the significantly faster rate observed with **2-MeCN** compared to **2**.[25]

Table 6.5 Effect of pressure on catalytic performance of **2** and **2-MeCN,** see also **table 3** in **publication III**.

Entry	Complex	T / °C	Ar / bar	[FA] / M	r / M h^{-1}	k_{real} / M^{-1} h^{-1}	$\Delta V^{‡}$ /
1	**2**	90	50	0.175 ± 0.01	0.0088	0.0018	≥ 0
2	**2**	90	-	0.195 ± 0.01	0.0098	0.0020	-
3	**2-MeCN**	80	50	0.185 ± 0.01	0.0093	0.0019	< 0
4	**2-MeCN**	80	-	0.14 ± 0.01	0.0070	0.0014	-

Remarks: each entry corresponds to the average of 2 separate experiments that differed less than the confidence of the measurement. $\Delta V^{‡}$sign is estimated from Δk of the reactions comparing each catalyst with and without Ar. Reaction conditions: t = 20 h, P_{CO2} = 20 bar, P_{H2} = 10 bar, 6 mL DMSO:water (5 v/v% water), 3.3 mmol BMMI.OAc, 1.52 µmol catalyst.

Interestingly, **2** displays - as expected – a larger rate constant under the applied reaction conditions assayed in **table 6.5** (see **entry 2**, **table 6.5**) as in **table 6.3**. The higher rate constant is related to the higher temperature investigated in **table 6.5**. In contrast to **2**, **2-MeCN** displayed a smaller rate constant in **table 6.5**, which in turn might be related to the smaller volume of

activation, i.e. in **table 6.5**, **entry 4** only 30 bar total pressure are applied, whilst in **table 6.3** a total pressure of 60 bar are applied to the system.

6.4.3. Parameters influencing the resistance towards acidic conditions

In this part, the parameter found to influence the durability of the catalyst (TON and achieved concentration of FA) will be discussed. It is important to note that complex **1** was the only catalyst in this row of complexes, which achieved the thermodynamic equilibrium (see **table 6.2**, **entry 1**).

This observation was related to the lowered electron density at the metal centre compared to the other complexes ($E_{1/2}(Ru^{II}/Ru^{III})$ = 0.83 V for **1**), see **figure 6.11b**. Furthermore, the gas uptake kinetics with **1** followed a first order kinetics whilst with **2** and **3** a deviation from this kinetics were observed, see **figure 6.11c**. This behaviour indicated that **2** and **3** are deactivated prior reaching the thermodynamic equilibrium.

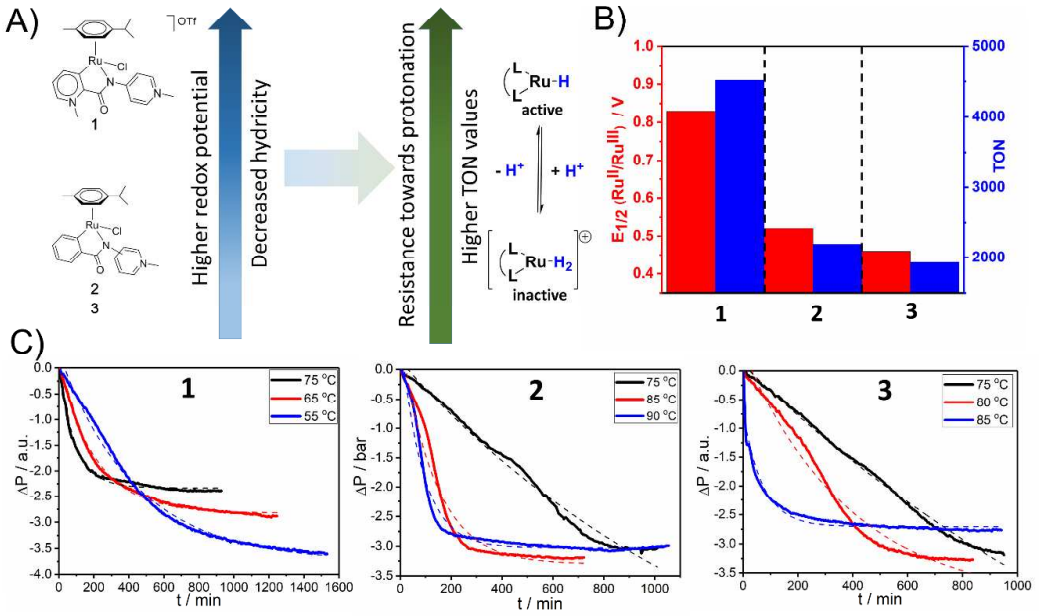


Figure 6.11 Correlation between hydricity/ redox potential and resistance towards protonation for the investigated complexes. B) Redox potentials $E_{1/2}$ (Ru(II)/Ru(III)) values of complexes **1**, **2** and **3** and the corresponding TON obtained with these catalysts, showing a correlation between redox potential and TON. (C) Observed gas uptake kinetics for complexes **1**, **2** and **3**. Complex **1**, shows a different behaviour, fitting to a exponential decay, see also **figure 5 publication III**.

The relationship in between the redox potential and hydricity, whereas a decreased hydricity (basicity of the hydride) leads to an increased resistance towards protonation, is schematically depicted in **figure 6.11a**. The resistance towards protonation leads consequently to higher TON values (and concentrations of formic acid), as the main changing parameter during the formation of formic acid is the pH (and thereby the concentration of protons in solution). This finding demonstrates the importance of a deeper understanding of deactivation mechanisms for the development of new, acid resistant catalysts in the future. Without a doubt future studies should focus onto this aspect.

6.5. Elucidating catalytic intermediates for the hydrogenation of CO_2

In order to investigate the formation and nature of plausible catalytic species, high pressure NMR (HP-NMR) experiments were undertaken with **3** in DMSO:D_2O under 60 bar H_2 pressure. For quantification purposes a capillary tube containing isopropanol was inserted in the HP-tube. In order to simplify analysis these experiments were performed in the absence of BMMI.OAc (for precise experimental details see Experimental section of this chapter).

Interestingly, prior to the formation of any hydridic species the release of p-cym ligand is observed (highlighted with a green star in **figure 6.12**). At the same time shifts in the bidentate PYA ligand scaffold is observed indicating the formation of a solvate complex **3-S**, which can be assumed to possess an octahedral structure.

It is noteworthy, that the precise nature of **3-S** is not known as Cl^- does not give a NMR shift, hence **3-S** might also constitute of a charged ionic species with Cl^- as a counter anion. Furthermore, a tetrahedral structure cannot be entirely dismissed for **3-S**, although the preferential structure for noble d_6 metals is an octahedral conformation.[27]

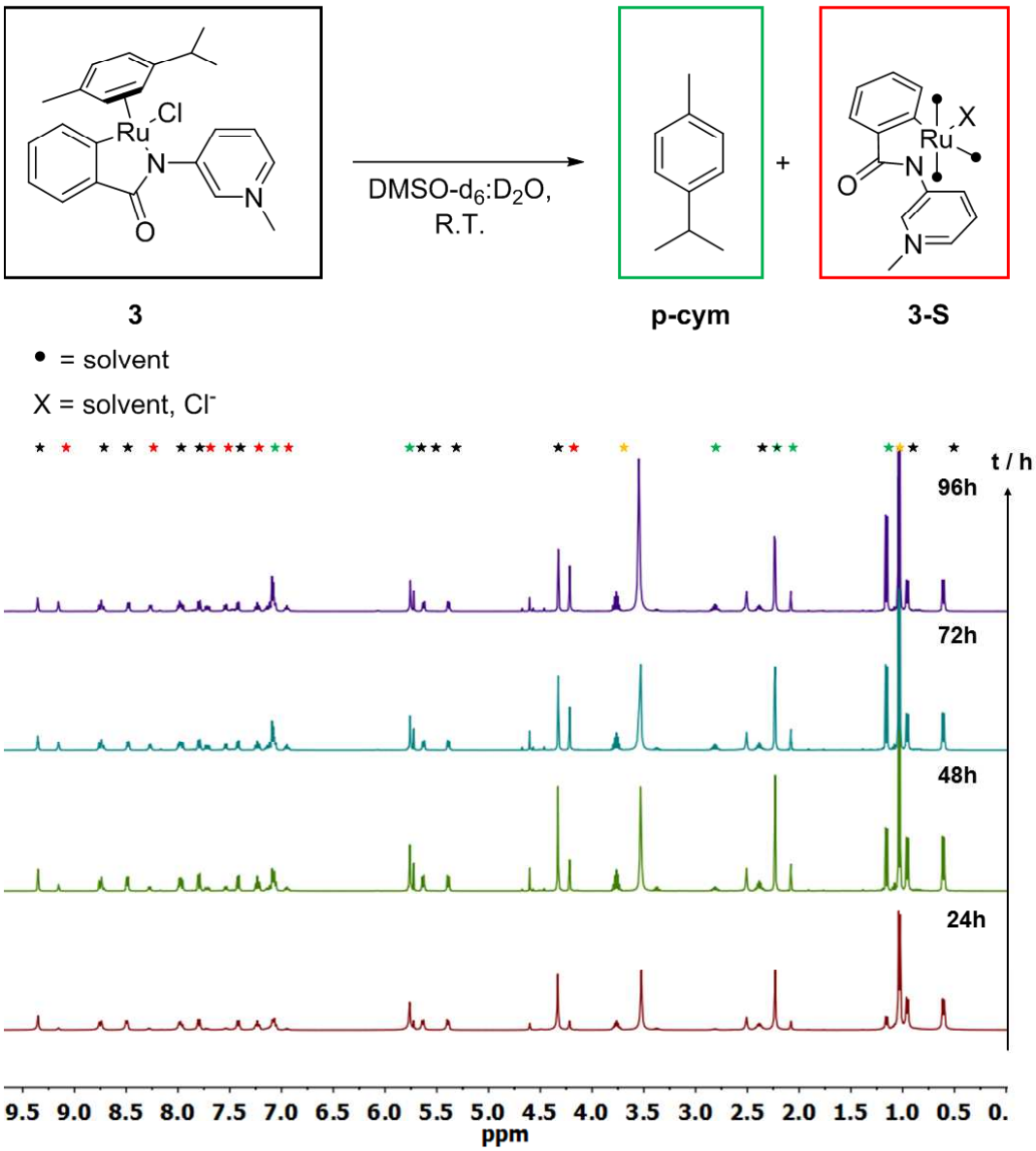


Figure 6.12 Initial dissociation of p-cym ligand from **3** giving **3-S** under 60 bar H_2 in DMSO-d6:D_2O (5 v/v% D_2O). Each measurement is undertaken after 24h. Green dots represent free p-cym ligand, red represent signals for **3-S** and black dots for **3**.

After this initial dissociation of the p-cym ligand, the formation of 3 hydrides can be observed at -11.06 ppm, -11.46 ppm and -14.46 ppm. Here the peaks at -11.06 ppm and -14.46 ppm appear as sharp signals, whilst the hydride species at -11.46 ppm appears broadened. The broadening of the signal at -11.46 ppm could be due to the formation of a M-H_2 complex, however a clear

determination *via* T1 determination is inhibited by the high melting point of DMSO-d_6 and D_2O, see **figure 6.13**.

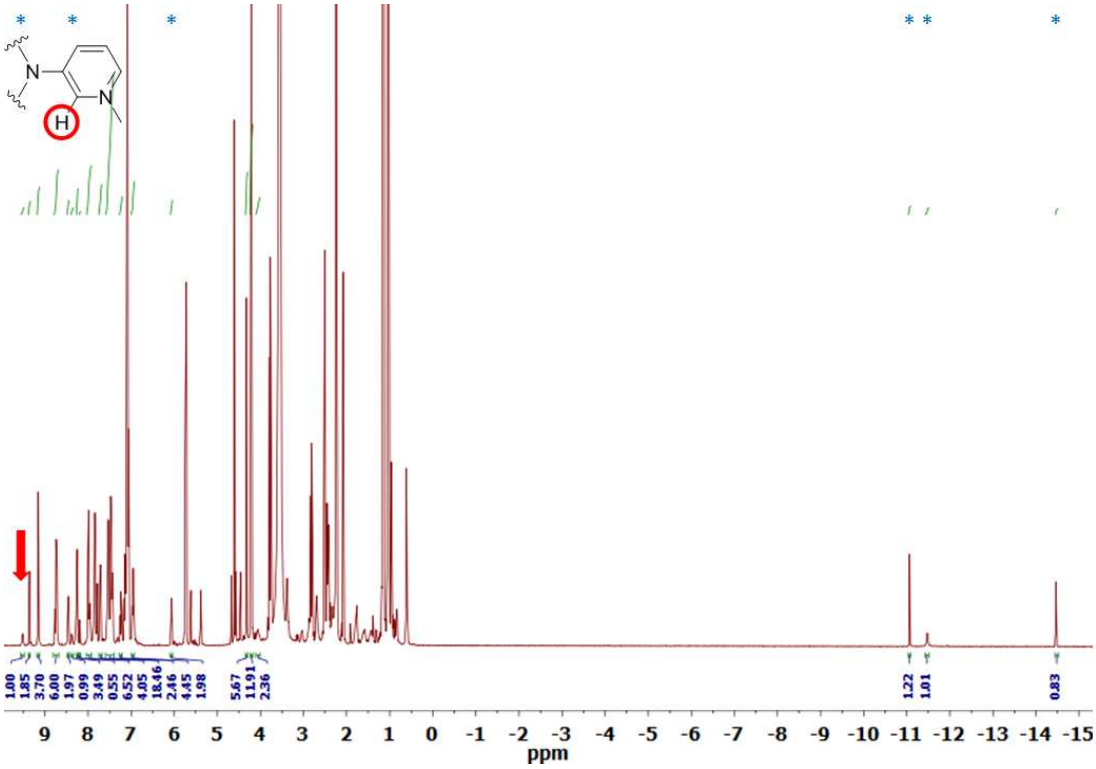


Figure 6.13 1H-NMR spectrum of 3 under 60 bar H2 after 192 h of incubation. Blue stars represent signals which can be unambiguously identified as signals corresponding to hydridic species.

As some peaks in the aromatic region appear at the same time as the hydridic species, bespoke peaks might be correlated to the hydridic signals discussed in the previous paragraph. These peaks include a singlet at 9.52 ppm, corresponding likely to the proton highlighted in red, and a duplet at 8.38 ppm. Furthermore, both signals can be correlated with a matching integral ratio, see **figure 6.13**. Other protons appearing in the aromatic region cannot be clearly assigned due to strong overlap of various species.

Beneath the aromatic signals an olefinic shift at 6.06 ppm can be associated to the hydridic species. It is worthwhile mentioning, that olefinic peaks are neither present in the starting material, nor in the solvato complex **3-S**. It is

very likely that the olefinic peak appears due to protonation or the hydride acceptation of the ligand.

Unfortunately, neither the integral ratios in the aromatic - nor in the olefinic region can be associated to the observed hydrides. In the region in between 0 ppm and 4 ppm all shifts appear strongly broadened and therefore a reasonable integration is challenging and was not undertaken here. A better resolution could be achieved at lower temperatures, but is inhibited here by the high melting point of DMSO.

Further assignments of the broadened peaks cannot be undertaken, as a clear multiplicity pattern cannot be detected. In order to resolve the spectrum the probe was heated, however this did not lead to any improvement (note cooling of the probe is inhibited but the high melting point of the solvent system), see **figure 6.14**.

Furthermore, 1D-NOESY experiments were undertaken with the hydridic species in order to clarify whether the broadened signals in positive ppm region can be assigned to bespoke hydrides. Here no dipole-dipole coupling can be detected with any of the hydrides and protons appearing in the positive ppm region. However, a chemical exchange in between the hydrides at -11.46 ppm and -14.46 ppm was observed. This indicates that at least these hydridic species are interconvertible. As the hydride at -11.46 ppm appears broadened, this observation could indicate either a deprotonation of a M-H_2 complex - although in this case a proton should be observable in the positive region, which was not detected - or an oxidative addition of H_2 onto the metal centre, giving two chemically equivalent hydrides at -14.46 ppm, see **figure 6.13**.

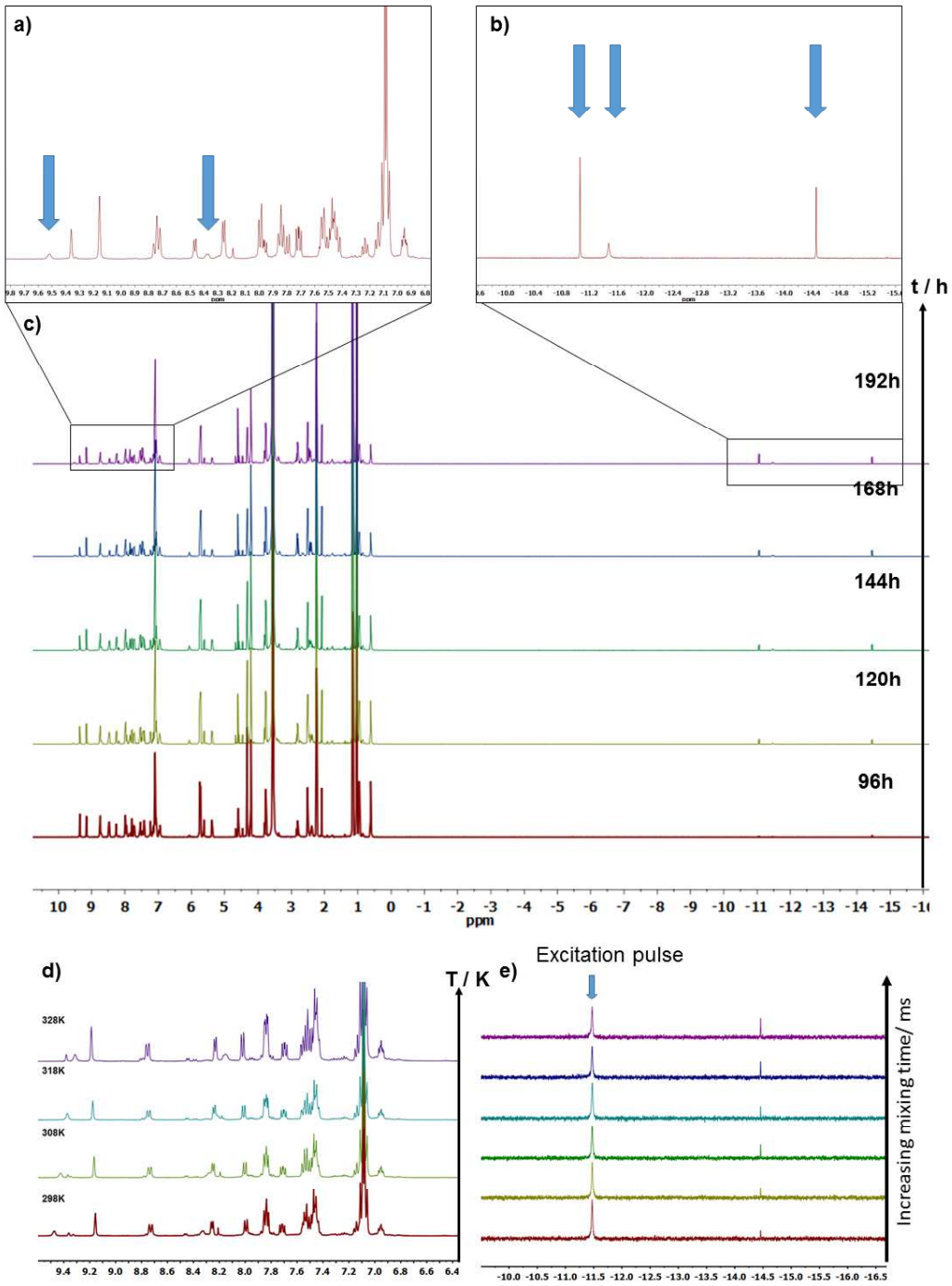


Figure 6.14 a) inset highlighting broadened signals in the positive ppm-region and b) inset highlighting three hydridic species. C) time dependant evolution of hydridic species with **3** after the dissociation of p-cym under 60 bar H_2 in DMSO-d6:D_2O (5 v/v% D_2O), each measurement is undertaken after 24h. d) VAT experiments with **3** and e) EXSY experiment displaying chemical exchange at various mixing times.

In general, the evolution of the catalytic intermediates required an extensive reaction time, thus the implication towards the reaction mechanism cannot be

clearly elucidated. However, the initial dissociation of the p-cym ligand followed by the formation of hydridic species is in line with the extensive induction period observed with the catalysts investigated in this chapter. In order to obtain improved NMR spectra, the investigation should be conducted in solvents with lower boiling points, i.e. THF-d8, which would allow the cooling of the probe. In this way a multiplicity pattern might be obtainable and a T1 determination for the broadened hydride at -11.46 ppm could be undertaken, giving information about the catalytically active species. Furthermore, studies should be conducted closer to the catalytic reaction conditions assayed initially.

6.6. Concluding remarks on the utilization of homogeneous catalysts

In this part it was demonstrated that the catalytic activity can, similar to basic conditions,[17, 23] be increased by the electron density at the metal centre. This leads to a catalyst with stronger hydride transfer capability, thus the thermodynamic difference in between the corresponding formate - and hydride complex is lowered, leading to higher catalytic activity, see ***section 6.4, table 6.3***. Similar effects have been described previously under basic conditions.[17]

At the same time an increased electron density at the metal centre led to change in the turnover limiting step. Interestingly, a change in the TLS has not been reported for Ru(II) complexes, even though computational studies predict that the activation for CO_2 and H_2 are energetically close for Ru(II)-catalysts.[28] Furthermore, the thermodynamics of the process don't have a predominant step and therefore the insertion of CO_2 can be ender or

exergonic.[12, 29] Furthermore, a change in TLS has been reported for other metals, like Co and Ir where the CO_2 insertion is rate determining whilst for Ru and Fe the H_2 activation has been considered the limiting step. [28, 30-32]

It was furthermore demonstrated that the mechanism for the CO2 insertion step can be switched in between an inner and outer sphere mechanism. This leads to a significantly enhanced catalytic activity as demonstrated with **2** and **2-MeCN**, see ***section 6.4***, ***table 6.4***.

However, the most significant new insight is the importance of the catalyst resistance towards the acidification of the reaction media. It was found that the lowered electron density at the metal centre with **1** significantly increased the catalyst durability. Without a doubt a catalyst with high acid resistance would be highly desirable for the studied reaction. However great care has to be taken here as a lowered electron density at the metal centre also leads to a lowered catalytic activity, i.e. on a certain point the catalyst might become inactive. Most likely the pyridinium scaffold as a carbene ligand might present here an attractive solution as catalyst **1** achieved, beneath the increased catalyst durability, acceptable catalytic activities, compared to the other complexes investigated here, see ***section 6.3***, ***table 6.2*** *and* ***section 6.4, figure 6.11***.

6.7. Experimental

6.7.1. General Information

NMR measurements were performed on a 400 MHz Bruker and ESI-MS analysis was performed on a Bruker microTOFII. HP-NMR measurements were undertaken using the High pressure NMR kit from Daedolus innovations. Deuterated solvents were supplied by Sigma Aldrich and were used without further purification.

6.7.2. Investigating hydride formation with 3

Catalyst **3** (15 mg, 31 µmol) was dissolved in 0.3 mL DMSO-d_6:D_2O (5 v/v% D_2O) and loaded into the ZrO_2 NMR tube. The tube was connected to an Xtreme Syringe Pump provided by Daedalus Innovative Technologies. Then 60 bar H_2 was led to the NMR tube, the tube was flushed and then left to equilibrate at the pressure source. The reaction was checked every 24h to determine the formation of hydrides.

6.7.3. Exemplary calculation for the rate of formation

In the cases where the concentration of formic acid was determined after less than three reaction times, the rate was determined by calculating the difference in between concentrations at each time point and dividing the difference by the difference in reaction time. An exemplary calculation is given for **2** at 40 bar CO_2 and 30 bar H_2 in 6 mL DMSO:H_2O (5 v/v% H_2O) in the presence of 3.3 mmol BMMI.OAc at 70°C (see also **figure 6.7.** and **Table S6** entry **15** & **16** in **publication III**, **Supporting Information**).

$$r = \frac{[FA]_{t1} - [FA]_{t2}}{t_1 - t_2} = \frac{0.09M - 0.02M}{7h - 5h} = 0.035\ Mh^{-1}$$

6.7.4. Determination of reactant order

The order of reactants with catalysts **1** to **2-MeCN** can be estimated in two ways. In the studies presented here, the relative change in rate is compared to the relative change in pressure of the rate determining reactant. An exemplary calculation is given below for complex **1**.

$$(\frac{P_{H2,2}}{P_{H2,1}})^x = \frac{r_2}{r_1}$$

$$(\frac{60\ bar}{30\ bar})^x = \frac{0.048\ Mh^{-1}}{0.029\ Mh^{-1}}$$

$$2^x = 1.66$$

$$\rightarrow\ x = 0.85\ \approx 1$$

In an alternative approach the observed rate can be plotted against the applied pressure of the rate determining reactant on a log-log scale. The slope of the linear regression displays the order of the investigated reactant.

6.7.5. Determination of rate constants

With the reaction order in hand, the reaction constant k can be calculated according to the equations below (here shown for complex **2**)

$$r = k[CO_2]^2$$

$$\frac{r}{[CO_2]^2} = k$$

The concentration of CO2 can be calculated using Henry's law. Henry constants were derived from reference 36a for CO_2 and 36b for H_2.

Alternatively, the concentration of the investigated reactant can be plotted on ln scale (with 1st order kinetics) against the time, respectively the inverse concentration of the reactant (for 2nd order kinetics). As the concentration of reactant in solution is not monitored during the reaction, this approach was not undertaken in these investigations. In the same way the, logarithmic concentration of FA (or inverse concentration if FA) can be plotted against time. In principle this plot will produce the same information as discussed with for the reactant concentration. However, as the concentration of FA in dependence of time was not continuously monitored, a poor resolution of the kinetic data is obtained, thus this approach was not undertaken either in this thesis.

6.8. Publication III, Supporting Information: Catalyst design for highly efficient base-free carbon dioxide hydrogenation to formic acid

Contribution of the author: In this publication the author conducted all catalytic experiments, drew the research plan and synthesized all ionic liquids. The complexes investigated in this publication were prepared by collaborators. Manuscript preparation was undertaken in collaboration with all co-authors.

Reprinted with permission from

www.chemrxiv.org/articles/Catalyst_Design_for_Highly_Efficient_Base-Free_Carbon_Dioxide_Hydrogenation_to_Formic_Acid

Catalyst design for highly efficient base-free carbon dioxide hydrogenation to formic acid

Andreas Weilhard,[a] Kevin Salzmann,[b] Jairton Dupont,[c] Martin Albrecht,[b]* Victor Sans[a,d]*

a) Faculty of Engineering, University of Nottingham, Nottingham, NG7 2RD, UK
b) Department of Chemistry & Biochemistry, University of Bern, Freiestrasse 3, 3012 Bern, Switzerland
c) Institute of Chemistry – UFRGS – Av. Bento Gonçalves, 9500 Porto Alegre 91501-970 – RS Brazil
d) Institute of Advanced Materials (INAM), Universitat Jaume I, 12006, Castellon, Spain

Supporting Information

Table of Contents

1. SYNTHESIS OF THE COMPLEXES 238

1.2. ^{1}H and $^{13}C^{1}$ NMR spectra of complexes 2-MeCN, 3, and 3-MeCN 245

1.3. Crystal-Structure Determination of complex 3 248

1.4. Electrochemical measurements ..... Error! Bookmark not defined.

2. CATALYTIC EXPERIMENTS 252

2.1. General procedure for CO_2 hydrogenation in the presence of BMMI.OAc 252

2.2. General procedure for CO_2 hydrogenation in the absence of BMMI.OAc 254

2.3. General procedure for determining TLS in the presence of BMMI.OAc 254

2.3.1. Variation of hydrogen pressure 254

2.3.2. Variation of CO_2 pressure 255

2.3.3. Variation of reactant ration with pre-catalyst 3 ..... **Error! Bookmark not defined.**

2.4. Determination of activation energy ..... Error! Bookmark not defined.

2.4.1. **2** in DMSO ..... **Error! Bookmark not defined.**

2.4.2. **2** in THF ..... **Error! Bookmark not defined.**

2.4.3. **3** in DMSO ..... **Error! Bookmark not defined.**

2.4.4. **1** in DMSO ..... **Error! Bookmark not defined.**

2.5. Inner vs outer sphere mechanism 269

2.5.1. Volume of activation ..... **Error! Bookmark not defined.**

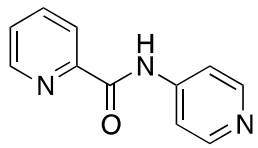
2.6. Representative 1H NMR spectrum for the hydrogenation of CO_2 to formic acid 270

3. REFERENCES 271

1. Synthesis of the complexes

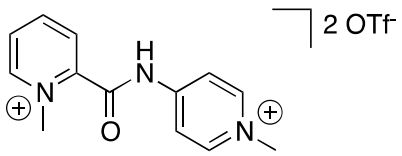
General: All reagents were commercially available and used as received. Unless specified otherwise, NMR spectra were recorded at 25°C on Bruker spectrometers operating at 300 or 400 MHz (^{1}H NMR) and 100 or 75 MHz (^{13}C NMR), respectively. Chemical shifts (δ in ppm, coupling constants J in Hz) were referenced to residual solvent signals. Assignments are based on homo- and heteronuclear shift correlation spectroscopy. Purity of bulk samples of the complexes has been established by NMR spectroscopy, and when possible by elemental analysis. Elemental analyses were performed at DCB Microanalytic Laboratory using a Thermo Scientific Flash 2000 CHNS-O elemental analyzer. High-resolution mass spectrometry was carried out with a Thermo Scientific LTQ Orbitrap XL (ESI-TOF) by the mass spectroscopy group of the Department of Chemistry and Biochemistry, University of Bern.

Synthesis of pre-L1: A slightly modified literature procedure was employed.[1]



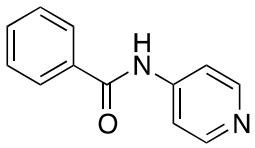
Picolinic acid (1.23 g, 10 mmol) and $SOCl_2$ (10 mL, 16.31 g, 137 mmol) were refluxed at 85 °C under N_2 for 3 h. The excess $SOCl_2$ was removed under reduced pressure and the resulting solid was washed with pentane. The pentane was removed under reduced pressure and the crude picolinoyl chloride was dissolved in THF (50 mL). 4-Aminopyridine (0.941 g, 10 mmol) and NEt_3 (2.51 mL, 1.82 g, 18 mmol) were added to the solution and stirred at room temperature for 72 h. The formed precipitate was removed by filtration and washed with THF (50 mL). All volatiles were removed from the filtrate solution under reduced pressure to give a brown solid, which was purified via column chromatography (SiO_2; EtOAc/pentane 7:3). The product fraction was concentrated and precipitated by addition of Et_2O. The white solid was collected by filtration and dried in vacuo to afford **pre-L1** as a white powder (1.111 g, 56%). Analytical data of this compound are in agreement with those reported.[1]

Syntheis of L1: Pre-L1 (200 mg, 1.0 mmol) was dissolved in dry 1,2-



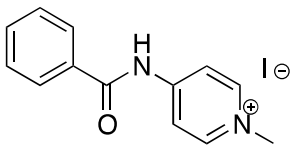
dichloroethane (DCE; 10 mL) and MeOTf (1.14 mL, 1.65 g, 10 mmol) was added. The solution was stirred at 100 °C for 18 h. After cooling to room temperature, the formed white precipitate was filtered off and washed with CH_2Cl_2 (100 mL). The solid was dissolved in MeCN (5 mL), precipitated with Et_2O (40 mL) and filtered to afford **L1** as a white solid (0.530 g, 82%). Analytical data of **L1** are identical with those reported.[2]

Synthesis of pre-L2: The synthesis of this precursor has been reported



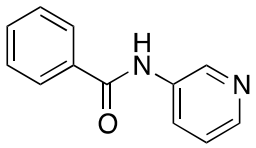
previously and was slightly modified.[1] 4-Aminopyridine (0.941 g, 10 mmol) and NEt_3 (1.5 mL, 1.089 g, 10.76 mmol) were dissolved in THF (30 mL). Benzoyl chloride (1.2 mL, 1.211 g, 10.34 mmol) was added dropwise to the pyridine solution. The resulting suspension was stirred at room temperature for 3 h. The formed precipitate was removed by filtration and washed with THF (50 mL). All volatiles were removed in vacuo and the residual white solid was dissolved in a 10% citric acid solution (10 mL). Addition of a saturated $NaHCO_3$ solution (100 mL) and subsequent filtration afforded **pre-L2** as a white solid (1.270g, 64%). Analytical data of this compound are in agreement with those reported.[1]

Synthesis of L2: Pre-L2 (396 mg, 2 mmol) was dissolved in MeCN (15 mL)

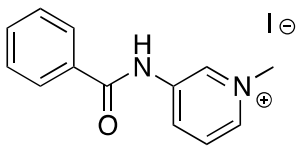


in a pressure tube and MeI (190 µL, 0.425 g, 3 mmol) was added. The mixture was stirred at 80 °C for 18 h. The solution was cooled to room temperature and the solvent was removed under reduced pressure. The resulting yellow solid was dissolved in MeCN (5 mL) and precipitated by addition of Et_2O (50 mL). The formed solid was collected by filtration and dried in vacuo to afford **L2** as an off-white solid (0.623 mg, 92%). Analytical data of this compound are in agreement with those reported.[3]

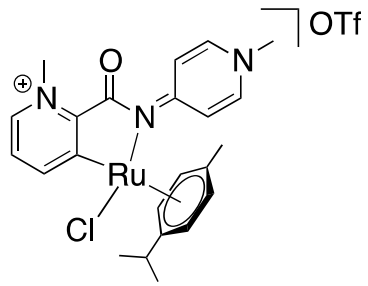
Synthesis of pre-L3: 3-Aminopyridine (0.941 g, 10 mmol) and NEt_3 (1.5 mL, 1.089 g, 10.76 mmol) were dissolved in THF (30 mL). Benzoyl chloride (1.2 mL, 1.211 g, 10.34 mmol) was added dropwise to the pyridine solution. The resulting suspension was stirred at 60 °C for 72 h. The mixture was filtered and the solid washed with THF (50 mL). The filtrates were combined and all volatiles removed in vacuo. The residual brown solid was purified by column chromatography (SiO_2; CH_2Cl_2/MeOH 95:5). The prduct fractions were concentrated and precipitated by addition of Et_2O to yield **pre-L3** as a brown solid (1.864 g, 94%). Analytical data of this compound are in agreement with those reported.[4]



Synthesis of L3: pre-L3 (396 mg, 2 mmol) was dissolved in MeCN (15 mL) and MeI (190 µL, 0.425 g, 3 mmol) was added. The mixture was stirred at 80 °C for 18 h in a pressure tube. The solution was cooled to room temperature and the solvent was removed under reduced pressure. The resulting yellow solid was dissolved in MeCN (5 mL) and precipitated by addition of Et_2O (50 mL). The formed solid was collected by filtration and dried in vacuo to afford **L3** as an off-white solid (0.647 mg, 95%). Analytical data of this compound are in agreement with those reported.[2]

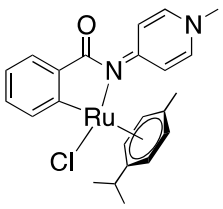


Synthesis of complex 1: The pyridinium salt **L1** (116 mg, 0.22 mmol), [Ru(*p*-cym)Cl_2]$_2$ (61 mg, 0.10 mmol) and NaOAc (180 mg, 2.20 mmol) were dissolved in dry CH_2Cl_2 (50 mL) and stirred at room temperature for 18 h. All volatiles were removed under reduced pressure and the crude solid was purified by column chromatography (SiO_2; CH_2Cl_2/MeOH 95:5). The red band was collected, concentrated, precipitated by addition of Et_2O, and collected by filtration. After drying in vacuo, complex **1** was obtained as a dark



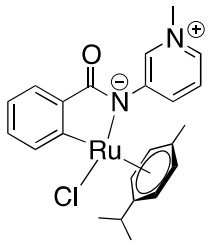
red solid (79 mg, 61%). Analytical data of this compound are in agreement with those reported.[2]

Synthesis of Complex 2: Pyridinium salt **L2** (0.647g, 1.9 mmol) was



dissolved in CH_2Cl_2 (50 mL) and transferred into a separation funnel. Aqueous NaOH (50 mL, 2M) was added. After vigorous mixing, the organic phase was collected. The aqueous layer was extracted with CH_2Cl_2 (3 x 50 mL), the combined organic layers were dried over anhydrous Na_2SO_4 and filtered through Celite. All volatiles were removed in vacuo to afford the neutral pyridylideneamide as an off-white solid (342 mg, 85%). Analytical data of this compound are in agreement with those reported.[3] This solid (200 mg, 0.94 mmol), [Ru(*p*-cym)Cl_2]$_2$ (300 mg, 0.49 mmol) and NaOAc (80 mg, 0.98 mmol) were dissolved in dry CH_2Cl_2 (50 mL) and stirred at room temperature for 3 h. All volatiles were removed under reduced pressure. The residue was dissolved in CH_2Cl_2 (20 mL) washed with brine. The aqueous layer was extracted with CH_2Cl_2 (3 x 20 mL). The combined organic layers were dried over anhydrous Na_2SO_4 and filtered through Celite. The filtrate was concentrated and purified by column chromatography (Al_2O_3; CH_2Cl_2/MeOH 98:2). The orange band was collected, concentrated, precipitated by addition of Et_2O, and collected by filtration, affording complex **2** as an orange solid (219 mg, 45%). Analytical data of this compound are in agreement with those reported.[2]

Synthesis of complex 3: The pyridinium salt **L3** (0.647g, 1.9 mmol) was

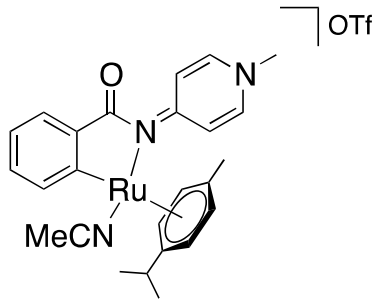


dissolved in CH_2Cl_2 (50 mL) and transferred into a separation funnel. Aqueous NaOH (50 mL, 2 M) was added. After vigorous mixing, the organic phase was collected. The aqueous layer was extracted with CH_2Cl_2 (3 x 50 mL). The combined organic layers were dried over anhydrous Na_2SO_4 and filtered through Celite. All volatiles were removed in vacuo to yield the free pyridylidene amide as a brown oil (342 mg, 85%). Analytical data of this compound are in agreement with those reported.[2] This oil (200 mg, 0.94

mmol), $[Ru(p\text{-cym})Cl_2]_2$ (300 mg, 0.49 mmol) and NaOAc (80 mg, 0.98 mmol) were dissolved in dry MeCN (50 mL) and refluxed for 3 h. The reaction mixture was cooled to room temperature and all volatiles were removed under reduced pressure. The residue was dissolved in CH_2Cl_2 (20 mL) and washed with a brine solution. The aqueous layer was extracted with CH_2Cl_2 (3 x 20 mL). The combined organic layers were dried over anhydrous Na_2SO_4 and filtered through Celite. The resulting filtrate was concentrated and purified by column chromatography (Al_2O_3; CH_2Cl_2/MeOH 98:2). The orange band was collected, concentrated, precipitated by addition of Et_2O, and isolated filtration. After drying in vacuo, complex **3** was obtained as a brown solid (259 mg, 43%).

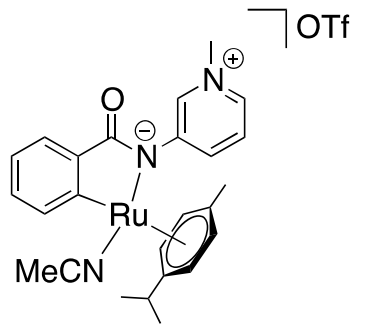
^{1}H NMR (400 MHz, CD_2Cl_2, 298K): δ = 9.86 (t, $^4J_{HH}$ = 1.4 Hz, 1H, C*H*$_{PYA}$), 9.46 (d, $^3J_{HH}$ = 8.7 Hz, 1H, C*H*$_{PYA}$), 8.02 (dd, $^3J_{HH}$ = 7.4 Hz, $^4J_{HH}$ = 0.9 Hz, 1H, C*H*$_{ph}$), 7.68 (td, $^3J_{HH}$ = 5.7 Hz, $^4J_{HH}$ = 1.4 Hz, 1H, C*H*$_{PYA}$), 7.57 (dd, $^3J_{HH}$ = 8.7, 5.8 Hz, 1H, C*H*$_{PYA}$), 7.46 (dd, $^3J_{HH}$ = 7.5 Hz, $^4J_{HH}$ = 1.6 Hz, 1H, C*H*$_{ph}$), 7.18 (dt, $^3J_{HH}$ = 7.4 Hz, $^4J_{HH}$ = 1.6 Hz, 1H, C*H*$_{ph}$), 6.95 (dt, $^3J_{HH}$ = 7.4 Hz, $^4J_{HH}$ = 0.9 Hz, 1H, C*H*$_{ph}$), 5.29 (dd, $^3J_{HH}$ = 5.7 Hz, $^4J_{HH}$ = 0.9 Hz, 1H, C*H*$_{cym}$), 5.12 (dd, $^3J_{HH}$ = 5.9 Hz, $^4J_{HH}$ = 0.9 Hz, 1H, C*H*$_{cym}$), 4.90 (dd, $^3J_{HH}$ = 5.9 Hz, $^4J_{HH}$ = 0.8 Hz, 1H, C*H*$_{cym}$), 4.86 (dd, $^3J_{HH}$ = 5.7 Hz, $^4J_{HH}$ = 0.8 Hz,1H, C*H*$_{cym}$), 4.17 (s, 3H, NC*H*$_3$), 2.25 (septett, $^3J_{HH}$ = 6.9 Hz, 1H, cym-C*H*Me$_2$), 1.99 (s, 3H, cym-C*H*$_3$), 0.96, 0.92 (2 x d, $^3J_{HH}$ = 6.9 Hz, 3H, C*H*$_{3\ iPr}$). $^{13}C^1$ NMR (100 MHz, CD_2Cl_2, 298K): δ = 178.49 (*C*O), 178.03 (*C*$_{ph}$), 156.51 (*C*$_{ph}$), 142.04 (*C*$_{PYA}$), 141.40 (*C*H$_{PYA}$), 141.28 (*C*H$_{PYA}$), 139.45 (*C*H$_{ph}$), 132.84 (*C*H$_{PYA}$), 130.40 (*C*H$_{ph}$), 127.70 (*C*H$_{ph}$), 126.50 (*C*H$_{PYA}$), 122.33 (*C*H$_{ph}$), 99.03, 98.20 (2 x *C*$_{cym}$), 91.61, 88.38, 83.36, 82.65 (4 x *C*H$_{cym}$), 48.90 (N*C*H$_3$), 31.31 (cym-*C*HMe$_2$), 23.03, 21.99 (2 x *C*H$_{3\ iPr}$), 18.90 (cym-*C*H$_3$). HR-MS: m/z calculated for $C_{23}H_{25}N_2ORu$ $[M–Cl]^+$ = 447.1010; found: 447.0997. Elem. Anal. Calcd. for $C_{23}H_{25}ClN_2ORu$ (482.07) x0.6 CH_2Cl_2: C 53.19; H 4.96; N 5.26; found: C 52.97; H 5.22; N 5.42%.

Synthesis of complex 2-MeCN: Complex **2** (50 mg, 0.10 mmol) were dissolved in MeCN (20 mL) and KOTf (38 mg, 0.20 mmol) was added. The mixture was stirred at room temperature for 18 h. The reaction mixture was filtered through Celite and concentrated. Precipitation by addition of Et_2O and subsequent filtration afforded complex **2-MeCN** as an orange-brown solid (30 mg, 47%).



^{1}H NMR (400 MHz, CD_3CN, 298K): δ = 8.44 (d, $^3J_{HH}$ = 7.5 Hz, 2H, C*H*$_{PYA}$), 8.01 (d, $^3J_{HH}$ = 7.5 Hz, 2H, C*H*$_{PYA}$), 8.00 (d, $^3J_{HH}$ = 7.4 Hz, 1H, C*H*$_{ph}$), 7.50 (dd, $^3J_{HH}$ = 7.4 Hz, $^4J_{HH}$ = 1.4 Hz, 1H, C*H*$_{ph}$), 7.25 (dt, $^3J_{HH}$ = 7.4 Hz, $^4J_{HH}$ = 1.4 Hz, 1H, C*H*$_{ph}$), 7.05 (dt, $^3J_{HH}$ = 7.4 Hz, $^4J_{HH}$ = 0.9 Hz, 1H, C*H*$_{ph}$), 5.62 (dd, $^3J_{HH}$ = 5.9 Hz, $^4J_{HH}$ = 1.0 Hz, 1H, C*H*$_{cym}$), 5.60 (dd, $^3J_{HH}$ = 6.0 Hz, $^4J_{HH}$ = 1.0 Hz, 1H, C*H*$_{cym}$), 5.40 (dd, $^3J_{HH}$ = 6.0 Hz, $^4J_{HH}$ = 0.9 Hz, 1H, C*H*$_{cym}$), 5.32 (dd, $^3J_{HH}$ = 5.9 Hz, $^4J_{HH}$ = 0.9 Hz, 1H, C*H*$_{cym}$), 4.00 (s, 3H, NC*H*$_3$), 2.23 (septett, $^3J_{HH}$ = 6.9 Hz, 1H, cym-C*H*Me_2), 2.17 (s, 3H, cym-C*H*$_3$), 0.98, 0.92 (2 x d, $^3J_{HH}$ = 6.9 Hz, 3H, C*H*$_{3\ iPr}$). $^{13}C^1$ NMR (100 MHz, CD_3CN, 298K): δ = 180.33 (*C*O), 171.87 (*C*$_{ph}$), 168.21 (*C*$_{PYA}$), 143.21 (*C*H$_{PYA}$), 142.84 (C$_{ph}$), 140.35, 131.80, 128.89, 124.14 (4 x *C*H$_{ph}$), 122.48 (*C*H$_{PYA}$), 102.00, 100.42 (2 x *C*$_{cym}$), 94.13, 92.24, 90.19, 86.49 (4 x *C*H$_{cym}$), 46.08 (N*C*H$_3$), 31.71 (cym-*C*HMe_2), 22.40, 22.33 (2 x *C*H$_{3\ iPr}$). HR-MS: m/z calculated for $C_{25}H_{28}N_3ORu$ [M–OTf]$^+$ = 488.1276; found: 488.1271. =

Synthesis of complex 3–MeCN: Complex **3** (75 mg, 0.15 mmol) was dissolved in MeCN (20 mL) and KOTf (58 mg, 0.31 mmol) was added. The mixture was stirred at room temperature for 18 h, filtered through Celite, and concentrated. Precipitation with Et_2O and filtration afforded complex **3–MeCN** as an orange-brown solid (91 mg, 91%).



^{1}H NMR (300 MHz, CD_3CN, 298K): δ = 9.30 (t, $^4J_{HH}$ = 1.4 Hz 1H, C*H*$_{PYA}$), 8.84 (dd, $^3J_{HH}$ = 8.6 Hz, $^4J_{HH}$ = 1.4 Hz, 1H, C*H*$_{PYA}$), 8.06 (d, $^3J_{HH}$ = 5.8 Hz, 1H,

C*H*$_{PYA}$), 8.00 (dd, $^3J_{HH}$ = 7.4, $^4J_{HH}$ =0.9 Hz, 1H, C*H*$_{ph}$), 7.77 (dd, $^3J_{HH}$ = 8.6, 5.8 Hz, 1H, C*H*$_{PYA}$), 7.45 (dd, $^3J_{HH}$ = 7.4, $^4J_{HH}$ = 1.5 Hz, 1H, C*H*$_{ph}$), 7.21 (dt, $^3J_{HH}$ = 7.4, 7.4 Hz, $^4J_{HH}$ = 1.5 Hz, 1H, C*H*$_{ph}$), 7.02 (td, $^3J_{HH}$ = 7.4, 7.4 Hz, $^4J_{HH}$ = 0.9 Hz, 1H, C*H*$_{ph}$), 5.61 (d, $^3J_{HH}$ = 5.8 Hz, 1H, C*H*$_{cym}$), 5.51, 5.26 (2 x d, $^3J_{HH}$ = 6.0 Hz, 1H, C*H*$_{cym}$), 5.22 (d, $^3J_{HH}$ = 5.8 Hz, 1H, C*H*$_{cym}$), 4.28 (s, 3H, NC*H*$_3$), 2.24 (septett, $^3J_{HH}$ = 6.9 Hz, 1H, cym-C*H*Me$_2$), 2.00 (s, 3H, cym-C*H*$_3$), 0.96, 0.92 (2 x d, $^3J_{HH}$ = 6.9 Hz, 3H, C*H*$_{3\ iPr}$). $^{13}C^1$ NMR (75 MHz, CD_3CN, 298K): δ = 178.29 (*C*O), 171.02 (*C*–Ru), 155.68 (*C*$_{ph}$), 142.91 (*C*$_{PYA}$), 142.50, 141.48, 140.03 (3 x *C*H$_{PYA}$), 136.34 (*C*H$_{ph}$), 131.07 (*C*H$_{PYA}$), 128.33, 127.46, 123.81 (3 x *C*H$_{ph}$), 101.32 (*C*$_{cym}$), 100.97 (*C*$_{OTf}$), 100.62 (*C*$_{cym}$), 93.39, 91.79, 89.32, 85.34 (4 x *C*H$_{cym}$), 66.27 (N*C*H$_3$), 49.15 (N*C*H$_{3\ PYA}$), 31.67 (cym-*C*HMe$_2$), 22.48, 22.29 (2 x *C*H$_{3\ iPr}$), 15.61 (cym-*C*H$_3$). HR-MS: m/z calculated for $C_{25}H_{28}N_3ORu$ $[M–OTf]^+$ = 488.1276; found: 488.1281.

1.2. ^{1}H and $^{13}C^{1}$ NMR spectra of complexes 2-MeCN, 3, and 3-MeCN

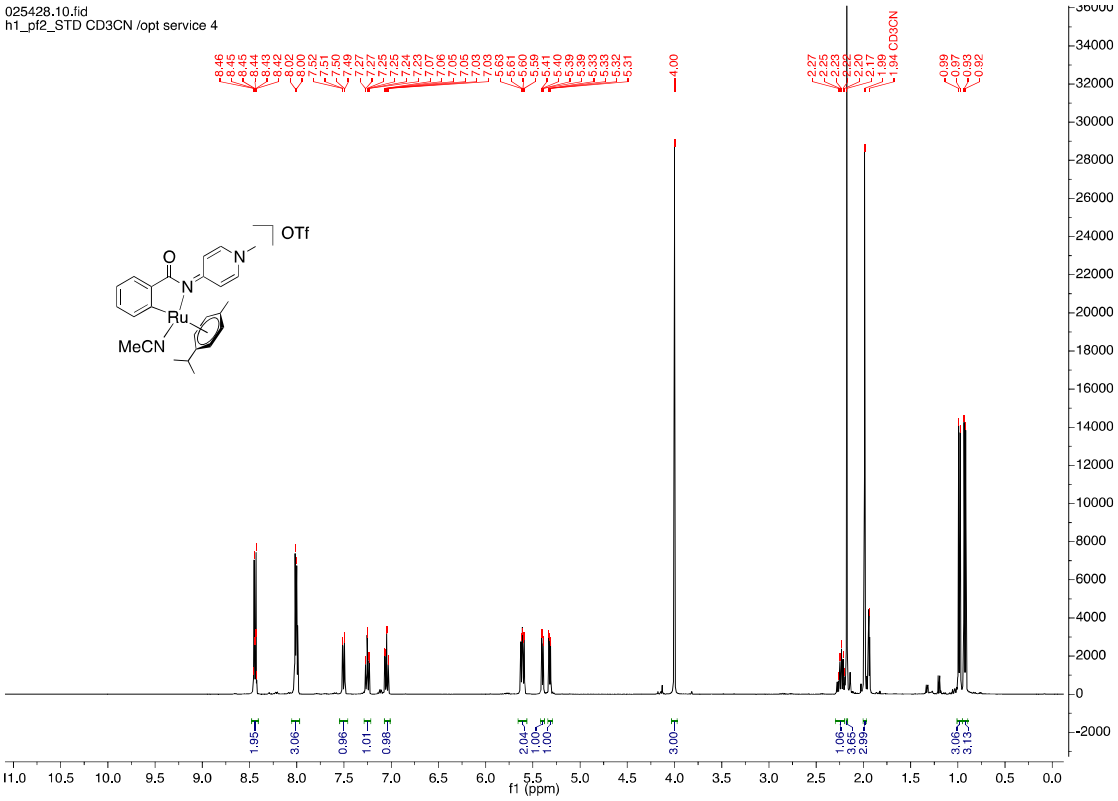


Figure S1 ^{1}H NMR spectrum of complex **2-MeCN** (CD_3CN, 298K, 400 MHz)

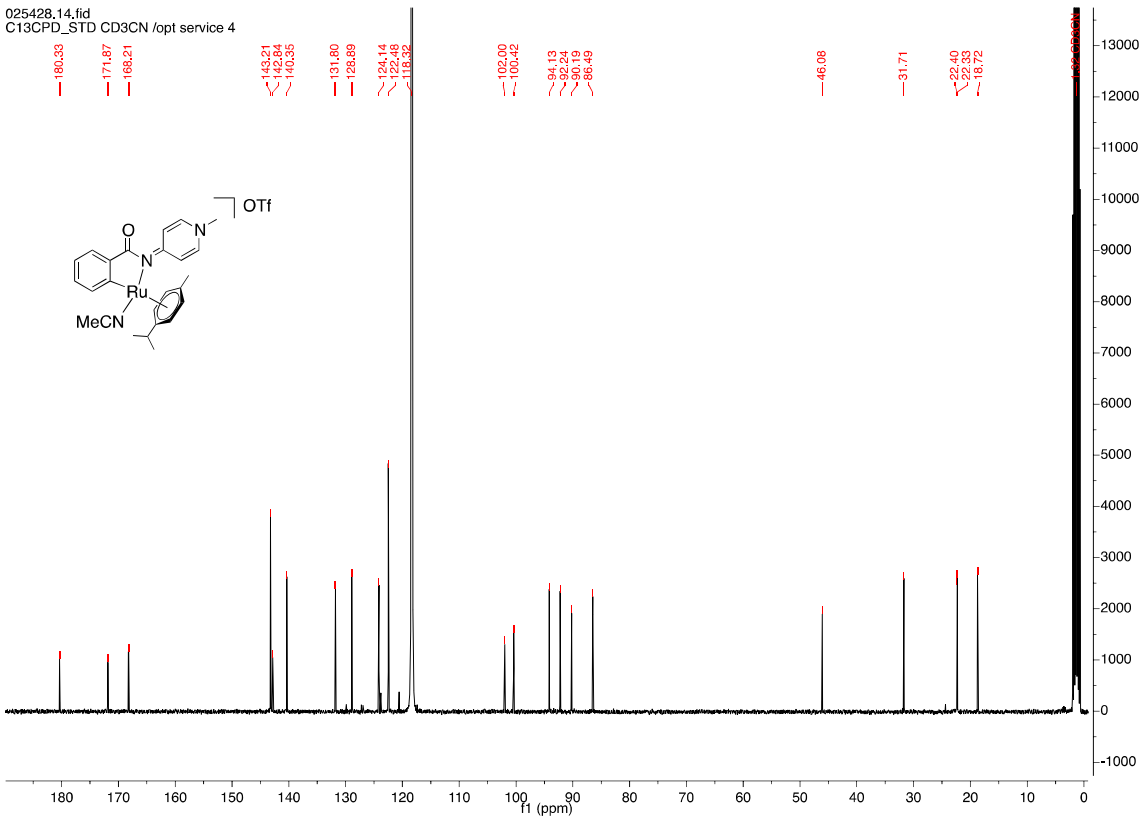


Figure S2 ^{13}C NMR spectrum of complex **2-MeCN** (CD_3CN, 298K, 100 MHz)

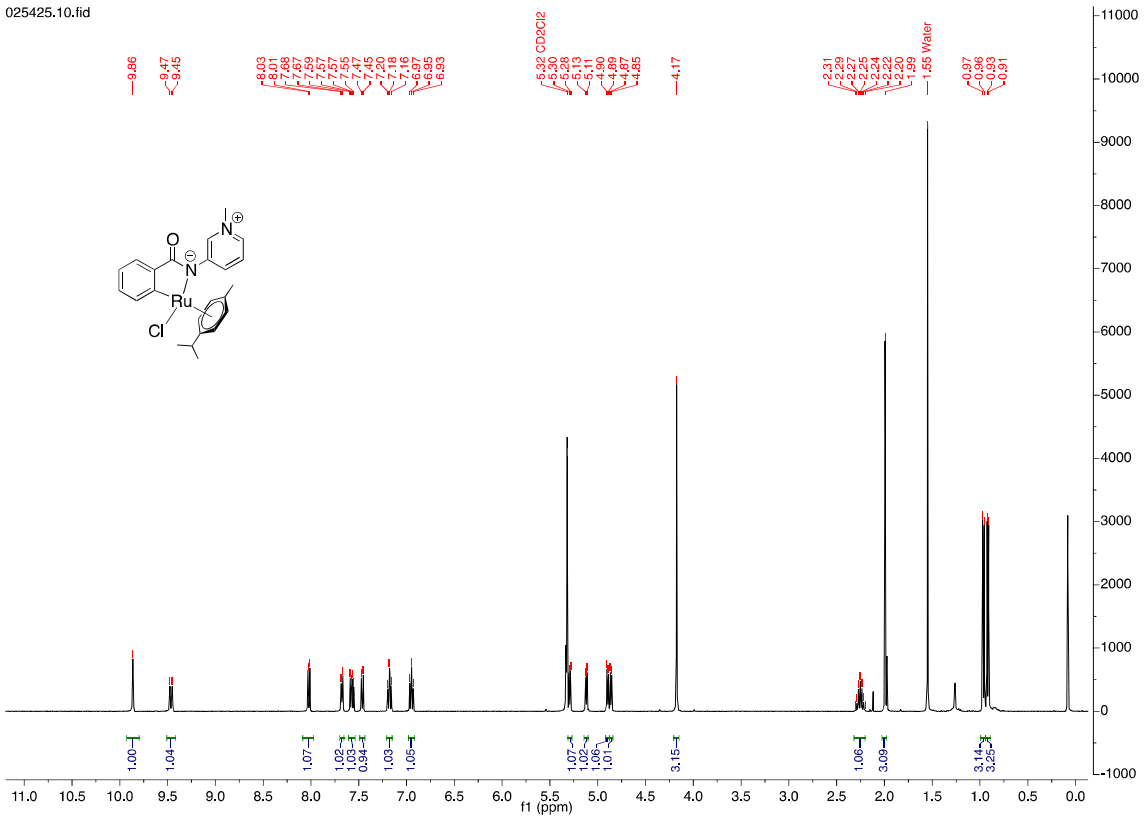


Figure S3 ^{1}H NMR spectrum of complex **3** (CD_2Cl_2, 298K, 400 MHz)

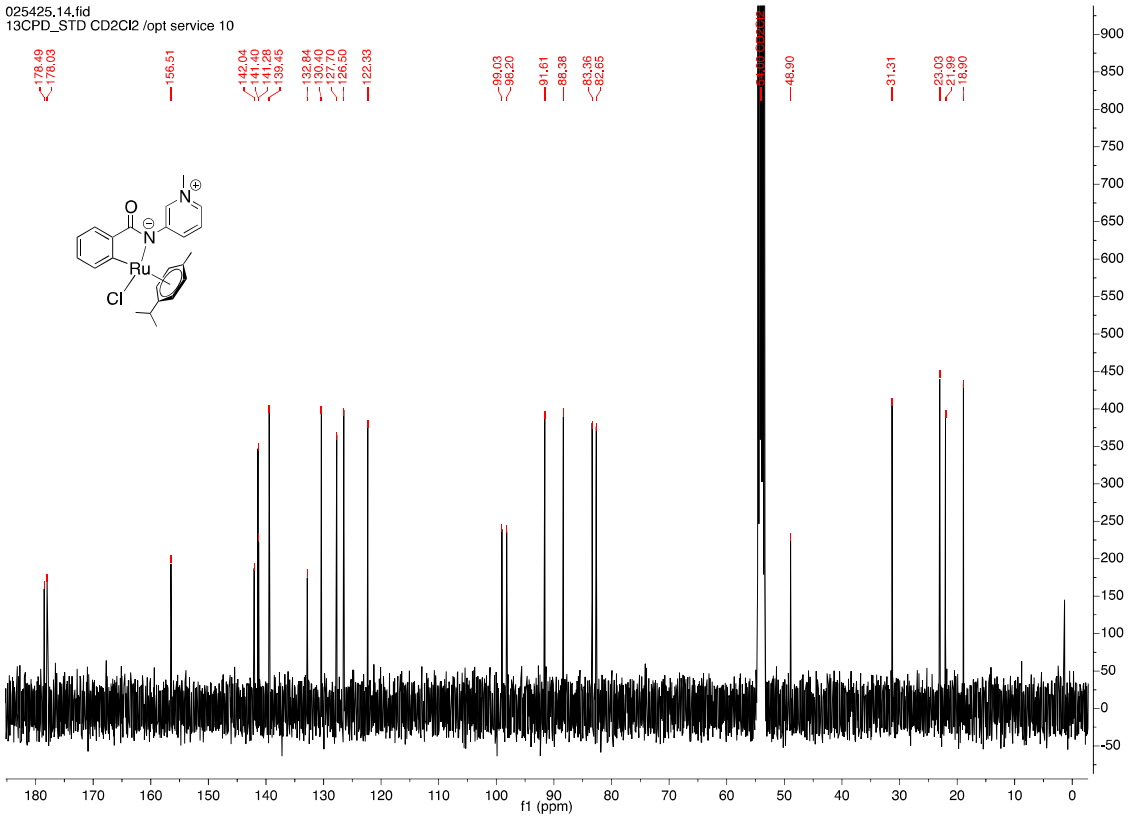


Figure S4 ^{13}C NMR spectrum of complex **3** (CD_2Cl_2, 298K, 100 MHz)

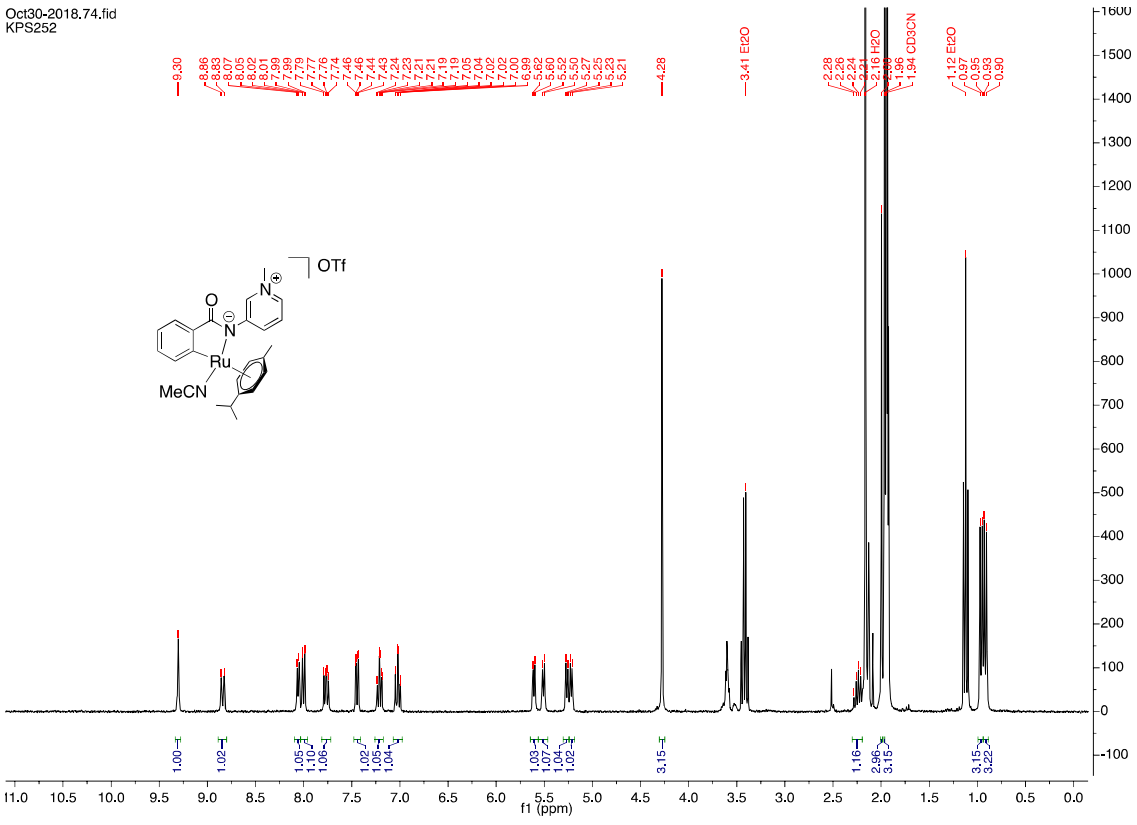


Figure S5 ^{1}H NMR spectrum of complex **3-MeCN** (CD_3CN, 298K, 300 MHz)

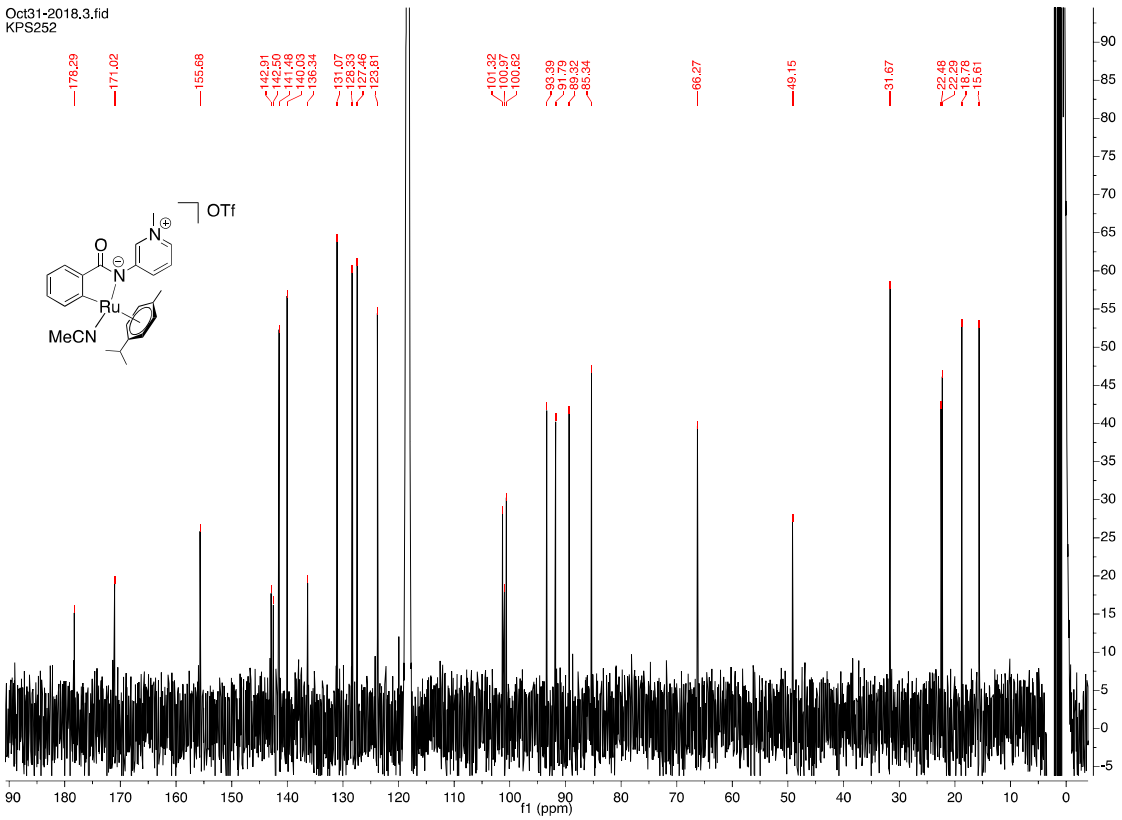


Figure S6 ^{13}C NMR spectrum of complex **3-MeCN** (CD_3CN, 298K, 75 MHz)

1.3. Crystal-Structure Determination of complex 3

Crystals suitable for single crystal X-ray diffraction were grown by slow evaporation of a saturated CH_2Cl_2 solution of complex **3**. A crystal of complex **3** was mounted in air at ambient conditions. All measurements were made on an *Oxford Diffraction SuperNova* area-detector diffractometer[5] using mirror optics monochromated Mo *K*α radiation (λ = 0.71073 Å) and Al filtered.[6] The unit cell constants and an orientation matrix for data collection were obtained from a least-squares refinement of the setting angles of reflections in the range 1.9° < θ < 25.0°. A total of 715 frames were collected using ω scans, with 60+60 seconds exposure time, a rotation angle of 1.0° per frame, a crystal-detector distance of 65.0 mm, at T = 123(2) K. Data reduction was performed using the *CrysAlisPro* program.[5] The intensities were corrected for Lorentz and polarization effects, and a numerical absorption correction based on gaussian integration over a multifaceted crystal model was applied. The structure was solved by direct methods using *SHELXT*,[7] which revealed the positions of all not disordered non-hydrogen atoms of the title compound. The non-hydrogen

atoms were refined anisotropically. All H-atoms were placed in geometrically calculated positions and refined using a riding model where each H-atom was assigned a fixed isotropic displacement parameter with a value equal to 1.2Ueq of its parent atom (1.5Ueq for methyl groups). The cymene ligand is disordered about two sites with different conformations of the isopropyl group. The geometries of the two moieties were with the SHELX SIMU and RIGU instructions. Refinement of the structure was carried out on F^2 using full-matrix least-squares procedures, which minimized the function $\Sigma w(F_o^2 - F_c^2)^2$. The weighting scheme was based on counting statistics and included a factor to downweight the intense reflections. All calculations were performed using the *SHELXL-2014/7* program.[8]

Table S1 Details of data collection and structure refinement of complex **3**

CCDC No	1918214	
Empirical formula	C23 H25 Cl N2 O Ru	
Formula weight	481.97	
Temperature	123(2) K	
Wavelength	0.71073 Å	
Crystal system	Monoclinic	
Space group	P 21/n	
Unit cell dimensions	a = 8.9158(3) Å	
	b = 13.7116(4) Å	β = 93.370(4)°.
	c = 16.4693(5) Å	
Volume	2009.89(11) Å^3	
Z	4	
Density (calculated)	1.593 Mg/m^3	
Absorption coefficient	0.929 mm^{-1}	
F(000)	984	
Crystal size	0.194 x 0.042 x 0.026 mm^3	
Theta range for data collection	1.934 to 25.349°	
Index ranges	-10<=h<=10, -16<=k<=16, -19<=l<=19	
Reflections collected	18559	
Independent reflections	3682 [R(int) = 0.0797]	
Completeness to theta = 25.242°	100 %	
Absorption correction	Gaussian	
Max. and min. transmission	1 and 0.833	
Refinement method	Full-matrix least-squares on F^2	
Data / restraints / parameters	3682 / 464 / 351	
Goodness-of-fit on F^2	1.148	
Final R indices [I>2σ(I)]	R1 = 0.0603, wR2 = 0.1144	
R indices (all data)	R1 = 0.089, wR2 = 0.1244	
Largest diff. peak and hole	0.774 and –1.03 e/Å^3	

1.4. Electrochemical measurements

General: Cyclic voltammograms were recorded using an Autolab PGSTAT101 from Metrohm with the corresponding complex (1mM) using

(nBu$_4$N)PF$_6$ (100 mM) as supporting electrolyte. Solutions were degassed with argon gas for 10 min prior to each run. Redox potentials were measured at 100 mV s^{-1} scan rate and the Fc$^+$/Fc couple was used as an internal reference ($E_{1/2}$ = +0.38 V *vs* SCE in $MeNO_2$; $E_{1/2}$ = +0.59 V *vs* SCE in THF).[9] A Pt disk with a 3.80 mm^2 surface area was used as working electrode and was polished before each measurement. The reference electrode was an Ag/AgCl electrode (SSCE); the counter electrode was a Pt wire. A 50 mL stock solution with 5 vol% H_2O and 1.935 g of electrolyte was prepared for each solvent. All data are collected in Table S2 and Figure S7.

Table S1 Oxidation potentials of complexes **1–3** and **2-MeCN** in $MeNO_2$ and THF [a]

Complex	$E_{1/2}$ ($Ru^{II/III}$) in $MeNO_2$ (ε = 35.87) [b]	$E_{1/2}$ ($Ru^{II/III}$) in THF (ε = 7.58) [b]
1	0.83 V	ca. 0.95 V [c]
2	0.52 V	0.63 V
2-MeCN	0.52 V	0.62 V
3	0.46 V	0.56 V

a) potentials in MeCN or THF vs. SCE at 100 mV s^{-1} scan rate using the Fc$^+$/Fc couple as standard; $E_{1/2}$ = +0.38 V in MeCN, +0.59 V in THF and nBu$_4$NPF$_6$ as electrolyte; b) dielectric constant ε from ref 10; c) ill-defined redox curves.

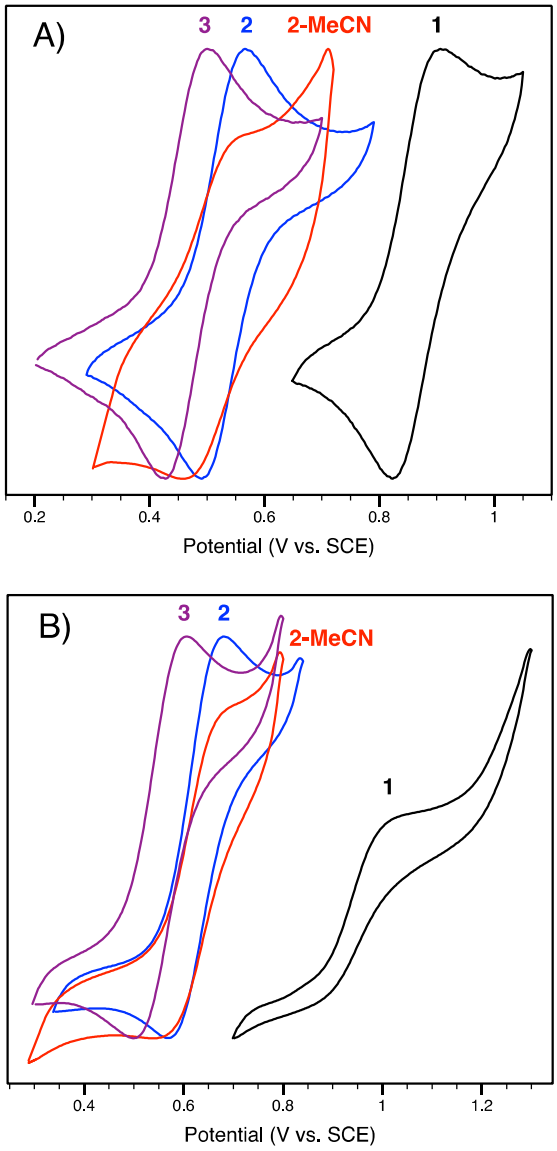


Figure S7 CV plots of complexes **1–3** and **2-MeCN** A) in $MeNO_2$ solution and B) in THF solution (1 mM complex, sweep rate 100 mV s^{-1}, potentials *vs* SCE referenced to Fc^+/Fc, $E_{1/2}$ = 0.38 V in $MeNO_2$ and 0.59 in THF; current normalized).

2. Catalytic experiments

Catalysis and ionic liquids: All the ionic liquids (1,2-dimethyl-3-butylimidazolium acetate and 1,2-dimethyl-3-decylimidazolium acetate) were prepared as described in literature.[11] 1,2-dimethylimidazole was purchased from IOLITEC while *n*-chlorbutane and *n*-chlorodecane, dimethylsulfoxide and deuterated dimethylsulfoxide were obtained from Sigma Aldrich,THF was purchased from Fischer chemicals. All the ILs were placed under vacuum at 50 °C for 2-3 h prior to use. NMR measurements were performed on a 400 MHz Bruker or 500 MHz Bruker and ESI-MS analysis was performed on a Bruker microTOFII. Headspace analysis was done on GC with (conditions column) with TCD detector for H_2 and a FID+methaniser for CO_2 and CO. Gas absorption curves were recorded with a house made pressure transducer connected to a 5512 Parr a compact stirred reactor using RealTeK software. Gas absorption curves were processes using a house made software using LabView programing platform and Origin software.

2.1. General procedure for CO_2 hydrogenation in the presence of BMMI.OAc

A Parr reactor (50 mL) was loaded with 1.0 mg (1.5 µmol) [Ru(p-cym)(pyr-p-PYA)Cl]OTf (**1**) or 1.0 mg (1.5 µmol) [Ru(p-cym)(phen-p-PYA)NCMe]OTf (**2-MeCN**) or 0.7 mg (1.5 µmol) [Ru(p-cym)(phen-m-PYA)Cl] (**3**) or 0.7 mg (1.5 µmol) [Ru(p-cym)(phen-p-PYA)Cl] (**2**) or 1.0 mg (1.5 µmol) [Ru(p-cym)(phen-m-PYA)NCMe]OTf (**3-MeCN**) and 700 mg BMMI.OAc (3.3 mmol). Then 6 mL of DMSO:water (5 v/v% water) from a stock solution was introduced into the reactor. The reactor was flushed with CO_2 gas in order to remove air. Afterwards, the reactor was filled with the desired amount of CO_2 and filled with H_2 gas, till the desired total pressure was reached at room temperature. The reaction was conducted at 70°C using a heating mantle under hard stirring. After the desired reaction time the reactor was cooled down to room temperature and carefully vented. The reaction mixture was analysed directly by ^{1}H NMR spectroscopy in DMSO-d_6 to determine the amount of formic acid formed, using BMMI.OAc as an internal standard.

The TOF was determined by linear regression as depicted in **Figure S4**.

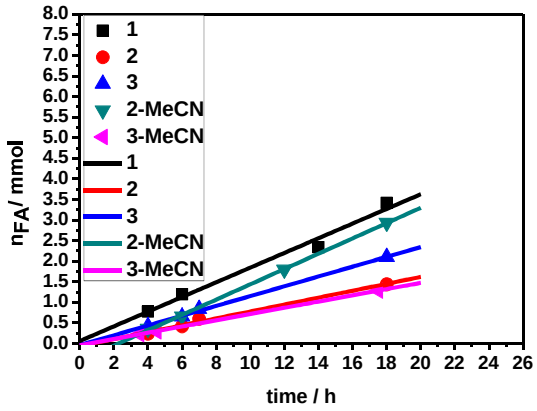


Figure S8 Determination of TOF at 70°C with P_{H2}=P_{CO2}= 30 bar

Table for TON determination under standard condtions:

Table S2 Table for the determination of TON.

Entry	Catalyst	[FA]/ M	TON
1	**1**	1.14	4505
2	**1**	1.15	4525
3	**2**	0.55	2190
4	**2**	0.55	2190
5	**3**	0.48	1902
6	**3**	0.49	1952
7	**2-MeCN**	0.49	1945
8	**2-MeCN**	0.49	1961
9	**3-MeCN**	0.39	1519

Reaction conditions: 3.3 mmol BMMI.OAc, 6 mL DMSO:H_2O (5 v/v% H_2O), P(H2) = P(CO2) = 30 bar, 1.5 µmol catalyst, t = 72h, T = 70°C.

From the intercept in **Figure S2** the induction period can be determined, which are tabulated in **table S3**.

Table S4 Induction period determined for the catalysts investigated here.

Entry	Catalyst	Induction period / min
1	**1**	0
2	**2**	20
3	**3**	47
4	**2-MeCN**	150

5	**3-MeCN**	31

Reaction conditions: 3.3 mmol BMMI.OAc, 6 mL DMSO:H_2O (5 v/v% H_2O), P(H2) = P(CO2) = 30 bar, 1.5 µmol catalyst, t = 72h, T = 70°C

2.2. General procedure for CO_2 hydrogenation in the absence of BMMI.OAc

A Parr reactor (50 mL) was loaded with 1.0 mg (1.5 µmol) [Ru(p-cym)(pyr-p-PYA)Cl]OTf (**1**) or 1.0 mg (1.5 µmol) [Ru(p-cym)(phen-p-PYA)NCMe]OTf (**2-MeCN**) or 0.7 mg (1.5 µmol) [Ru(p-cym)(phen-m-PYA)Cl] (**3**) or 0.7 mg (1.5 µmol) [Ru(p-cym)(phen-p-PYA)Cl] (**2**) or 1.0 mg (1.5 µmol) [Ru(p-cym)(phen-m-PYA)NCMe]OTf (**3-MeCN**).Then 6 mL of DMSO:water (5 v/v% water) from a stock solution was introduced into the reactor. The reactor was flushed with CO_2 gas in order to remove the air. Afterwards, the reactor was filled with desired amount of 30 bar CO_2 and filled with 30 bar H_2 gas, till the desired total pressure of 60 bar was reached at room temperature. The reaction was conducted at 70°C using a heating mantle under hard stirring. After 20h the reactor was cooled down to room temperature and carefully vented. The reaction mixture was analysed directly by ^{1}H NMR spectroscopy in DMSO-d_6 to determine the amount of formic acid formed, using NEt_3 as an external standard.

Table S3 Screening of catalyst 1-4 under additive free conditions.

Entry	Catalyst	Conc. FA	TON	TOF / h^{-1}
1	**3**	0.05	179	9
2	**1**	0.16	636	32
3	**2**	0.06	222	11
4	**2-MeCN**	0.06	245	12
5	**3-MeCN**	0.04	170	2.4

Reaction conditions 1 1.52 µmol catalyst, 6 mL DMSO:water (5 v/v% water), T=70°C, H_2 =CO_2 =30 bar, t = 20h.

2.3. General procedure for determining TLS in the presence of BMMI.OAc

2.3.1. Variation of hydrogen pressure

A Parr reactor (50 mL) was loaded with 1.0 mg (1.5 µmol) [Ru(p-cym)(pyr-p-PYA)Cl]OTf (**1**) or 1.0 mg (1.5 µmol) [Ru(p-cym)(phen-p-PYA)NCMe]OTf (**2-MeCN**), or 0.7 mg (1.5 µmol) [Ru(p-cym)(phen-p-PYA)Cl]OTf (**2-MeCN**) or 0.7 mg (1.5 µmol) [Ru(p-cym)(phen-m-PYA)Cl] (**3**) and 700 mg BMMI.OAc (3.3 mmol). Then 6 mL of DMSO:water (5 v/v% water) from a stock solution was introduced into the reactor. The reactor was flushed with CO_2 gas in order to remove the air. Afterwards, the reactor was filled with 30 bar CO_2 and filled with 20 bar – 60 bar H_2 gas at room temperature. The reaction was conducted at 70°C using a heating mantle under hard stirring. After the desired reaction time the reactor was cooled down to room temperature and carefully vented. The reaction mixture was analysed directly by ^{1}H NMR spectroscopy in DMSO-d_6 to determine the amount of formic acid formed, using BMMI.OAc as an internal standard.

2.3.2. Variation of CO_2 pressure

A Parr reactor (50 mL) was loaded with 1.0 mg (1.5 µmol) [Ru(p-cym)(pyr-p-PYA)Cl]OTf (**1**) or 1.0 mg (1.5 µmol) [Ru(p-cym)(phen-p-PYA)NCMe]OTf (**2-MeCN**) or 0.7 mg (1.5 µmol) [Ru(p-cym)(phen-m-PYA)Cl] (**3**) and 700 mg BMMI.OAc (3.3 mmol). Then 6 mL of DMSO:water (5 v/v% water) from a stock solution was introduced into the reactor. The reactor was flushed with CO_2 gas in order to remove the air. Afterwards, the reactor was filled with 10 bar - 50 bar CO_2 and filled with 30 bar H_2 gas at room temperature. The reaction was conducted at 70°C using a heating mantle under hard stirring. After the desired reaction time the reactor was cooled down to room temperature and carefully vented. The reaction mixture was analysed directly by ^{1}H NMR spectroscopy in DMSO-d_6 to determine the amount of formic acid formed, using BMMI.OAc as an internal standard.

Results

Table S4 Gas composition screening screening with catalyst **2**.

Entry	P_{H2}:P_{CO2}	t/ h	[FA] / M	TON	TOF / h^{-1}
1	60:30	18	0.23	890	49
2	60:30	7	0.09	347	50
3	60:30	5	0.06	239	47
4	50:30	5	0.06	239	47
5	50:30	7	0.09	347	50
6	40:30	4	0.05	195	48
7	40:30	7	0.09	360	51
8	30:30	18	0.24	955	53
9	30:30	6	0.07	276	46
10	30:30	4	0.04	157	39
11	20:30	18	0.18	720	40
12	20:30	24	0.24	960	40
13	30:20	18	0.07	270	15
14	30:20	24	0.09	370	15
15	30:40	5	0.02	87	22
16	30:40	7	0.09	347	50
19	30:50	4	0.03	108	27
20	30:50	6	0.12	480	80
21	30:50	18	0.45	1720	98
22	30:50	72	0.51	2010	28

Reaction conditions: 1.5 µmol **2**, 3.3 mmol BMMI.OAc, 6 mL DMSO:H_2O (5 v/v% H_2O), T = 70°C.

Table S7 Gas composition screening with catalyst **2-MeCN**.

Entry	P_{H2}:P_{CO2}	t/ h	[FA] / M	TON	TOF / h^{-1}
1[a)]	60:30	18	0.42	1658	92
2	60:30	6	0.15	587	74
3	60:30	5	0.11	432	86
4	50:30	6	0.13	513	86
5	50:30	5	0.09	370	74
6	40:30	6	0.12	490	82
7	40:30	4	0.06	217	54
8	30:30	18	0.49	1934	107
9	30:30	12	0.30	1184	99
10	30:30	6	0.12	480	80
11	30:30	4	0.06	240	59
12	20:30	6	0.09	347	58
13	20:30	4	0.03	217	27
14	30:20	6	0.07	260	43
15	30:20	5	0.05	180	36
16	30:40	6	0.14	564	94
17	30:40	5	0.08	330	67
18	30:45	5	0.13	521	104
19	30:45	6	0.20	798	133
21	30:50	4	0.04	171	42
22	30:50	5	0.11	434	86
23	30:50	6	0.21	830	138

Reaction conditions: 1.5 µmol **2-MeCN**, 3.3 mmol BMMI.OAc, 6 mL DMSO:H_2O (5 v/v% H_2O), T = 70°C a) not used for the calculation of TOF_{max} as the reaction already reached plateauing.

Table S5 Gas composition screening with catalyst **3.**

Entry	P_{H2}:P_{CO2}	t/ h	[FA] / M	TON	TOF / h^{-1}
1	60:30	18	0.39	1563	86
2	60:30	6	0.20	782	130
3	60:30	4	0.13	520	130
4	50:30	6	0.17	690	115
5	50:30	4	0.12	456	114
6	40:30	6	0.13	526	88
7	40:30	4	0.09	336	84
8	30:30	18	0.35	1368	76
9	30:30	6	0.11	430	75
10	30:30	4	0.07	274	69
11	20:30	4	0.05	204	51
12	20:30	6	0.08	309	52
13	30:10	4	0.05	196	49
14	30:10	6	0.07	294	49
15	30:20	4	0.06	234	58
16	30:20	6	0.10	368	61
17	30:40	3	0.05	192	64
18	30:40	5	0.10	380	76
19	30:50	4	0.04	168	42
20	30:50	6	0.10	392	65

Reaction conditions: 1.5 µmol **3**, 3.3 mmol BMMI.OAc, 6 mL DMSO:H_2O (5 v/v% H_2O), T = 70°C.

Table S6 Gas composition screening with catalyst **1.**

Entry	P_{H2}:P_{CO2}	t/ h	[FA] / M	TON	TOF / h^{-1}
1	60:30	8	0.38	1504	188
2	60:30	6	0.28	1110	185
3	60:30	4	0.19	760	190
4	50:30	6	0.23	924	154
6	40:30	6	0.21	816	136
7	30:30	18	0.57	2250	125
8	30:30	14	0.39	1539	110
9	30:30	6	0.20	789	132
10	30:30	4	0.13	513	128
11	20:30	6	0.13	522	87
13	30:20	6	0.13	516	86
14	30:40	6	0.22	888	148
15	30:40	4	0.15	590	148
16	30:40	6	0.22	888	148
17	30:45	4	0.16	616	154
18	30:45	6	0.23	900	150
19	30:50	4	0.15	590	148

Reaction conditions: 1.5 µmol **1**, 3.3 mmol BMMI.OAc, 6 mL DMSO:H_2O (5 v/v% H_2O), T = 70°C.

Table S7 Table for the determination of TON at improved reaction conditions.

Entry	Catalyst	P(H2):P(CO2)/ bar:bar	[FA]/ M	TON
1	**1**	60:30	1.15	4520
2	**1**	60:30	1.15	4520
3	**2**	30:50	0.51	2000
4	**2**	30:50	0.51	2020
5	**3**	60:30	0.49	1930
6	**3**	60:30	0.49	1930
7	**3**	30:50	0.48	1900
8	**3**	30:50	0.49	1960
9	**2-MeCN**	30:50	0.48	1885
10	**2-MeCN**	30:50	0.49	1925

Reaction conditions: 3.3 mmol BMMI.OAc, 6 mL DMSO:H_2O (5 v/v% H_2O), 1.5 µmol catalyst, t = 72h, T = 70°C

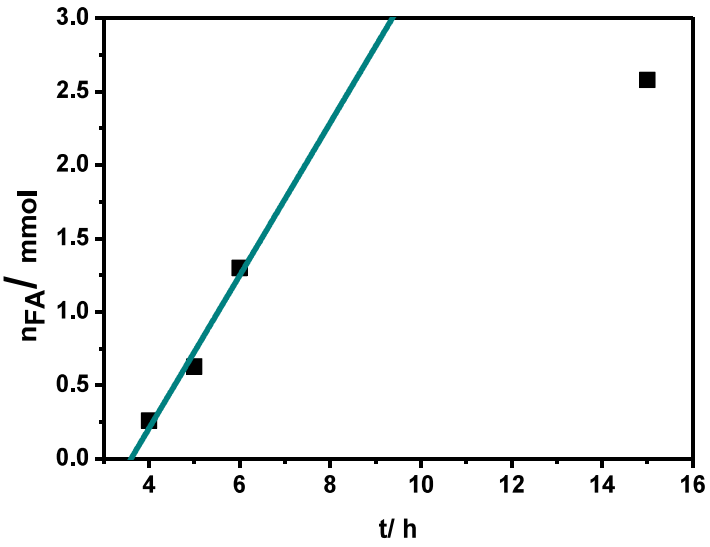


Figure S9 TOF determination with 2-MeCN under 50 bar CO_2 and 30 bar H_2 in 6 mL DMSO:H_2O (5 v/v% H_2O) in the presence of 3.3 mmol BMMI.OAc.

With **3** a clear dependence upon one reactant cannot be established, when only one reactant is varied, thus different reactant ratios were investigated.

2.3.3 Variation of reactant ratio with pre-catalyst 3

A Parr reactor (50 mL) was loaded with the 0.7 mg (1.5 µmol) [Ru(p-cym)(phen-m-PYA)Cl] (**3**) and 700 mg BMMI.OAc (3.3 mmol). Then 6 mL of DMSO:water (5 v/v% water) from a stock solution was introduced into the reactor. The reactor was flushed with CO_2 gas in order to remove the air. Afterwards, the reactor was filled with 10 bar to 40 bar CO_2 and filled with 20 bar – 40 bar H_2 gas giving a total pressure of 60 bar at room temperature. The reaction was conducted at 70°C using a heating mantle under hard stirring. After the desired reaction time the reactor was cooled down to room temperature and carefully vented. The reaction mixture was analysed directly by ^{1}H NMR spectroscopy in DMSO-d_6 to determine the amount of formic acid formed, using BMMI.OAc as an internal standard.

Table S8 Gas composition screening with catalyst **3** at constant pressure**.**

Entry	P_{H2}:P_{CO2}	t/ h	[FA] / M	TON	TOF / h^{-1}
1	40:20	5	0.11	450	90
2	40:20	6	0.14	540	90
3	35:25	5	0.09	374	75
4	35:25	6	0.12	457	76
5	35:25	7	0.14	540	77
5	25:35	5	0.07	276	55
6	25:35	6	0.09	345	58
7	20:40	5	0.06	221	44
8	20:40	6	0.07	280	47

Reaction conditions: 3.3 mmol BMMI.OAc, 6 mL DMSO:H_2O (5 v/v% H_2O), P(H2) = P(CO2) = 30 bar, 1.5 µmol **3**, t = 72h, T = 70°C.

2.4. Determination of activation energies

2.4.1. 2 in DMSO

A Parr reactor (50 mL) was loaded with 3.9 mg (8 µmol) [Ru(p-cym)(phen-p-PYA)Cl] and 700 mg (3.3 mmol) BMMI.OAc. Then 6 mL of DMSO:water (5 v/v% water) from a stock solution was introduced into the reactor. The reactor was flushed with CO_2 gas in order to remove the air. Afterwards, the reactor was filled with desired amount of 20 bar CO_2 and topped up with 20 bar H_2

gas, till the desired total pressure of 40 bar was reached at room temperature. The reaction was conducted at varying temperatures using a heating mantle under hard stirring. The pressure drop was measured using a pressure transducer connected to the reactor, whilst the recording was undertaken with an E725 RDS transducer indicator and the values were digitalised using Realtek software. After the gas uptake plateaued, the reactor was cooled down to room temperature and carefully vented. The reaction mixture was analysed directly by ^{1}H NMR spectroscopy in DMSO-d_6 to determine the amount of formic acid formed, using NEt_3 as an external standard.

2.4.2. 2 in THF

A Parr reactor (50 mL) was loaded with 3.9 mg (8 µmol) [Ru(p-cym)(phen-p-PYA)Cl] and 978 mg (3.3 mmol) DMMI.OAc. Then 6 mL of THF:water (5 v/v% water) from a stock solution was introduced into the reactor. The reactor was flushed with CO_2 gas in order to remove the air. Afterwards, the reactor was filled with the desired amount of 20 bar CO_2 and topped up with 20 bar H_2 gas, till the desired total pressure of 40 bar was reached at room temperature. The reaction was conducted at varying temperatures using a heating mantle under hard stirring. The pressure drop was measured using a pressure transducer connected to the reactor, whilst the recording was undertaken with a E725 RDS transducer indicator and the values were digitalised using Realtek software. After the gas uptake plateaued, the reactor was cooled down to room temperature and carefully vented. The reaction mixture was analysed directly by ^{1}H NMR spectroscopy in DMSO-d_6 to determine the amount of formic acid formed, using BMMI.OAc as an internal standard.

2.4.3. 3 in DMSO

A Parr reactor (50 mL) was loaded with 3.9 mg (8 µmol) [Ru(p-cym)(phen-m-PYA)Cl] and 700 mg (3.3 mmol) BMMI.OAc. Then 6 mL of DMSO:water (5 v/v% water) from a stock solution was introduced into the reactor. The reactor was flushed with CO_2 gas in order to remove the air. Afterwards, the reactor was filled with desired amount of 20 bar CO_2 and topped up with 20 bar H_2 gas, till the desired total pressure of 40 bar was reached at room temperature. The reaction was conducted at varying temperatures using a heating mantle

under hard stirring. The pressure drop was measured using a pressure transducer connected to the reactor, whilst the recording was undertaken with an E725 RDS transducer indicator and the values were digitalised using Realtek software. After the gas uptake plateaued, the reactor was cooled down to room temperature and carefully vented. The reaction mixture was analysed directly by ^{1}H NMR spectroscopy in DMSO-d_6 to determine the amount of formic acid formed, using BMMI.OAc as an internal standard.

2.4.4. 1 in DMSO

A Parr reactor (50 mL) was loaded with 3.9 mg (8 µmol) [Ru(p-cym)(phen-m-PYA)Cl] and 700 mg (3.3 mmol) BMMI.OAc. Then 6 mL of DMSO:water (5 v/v% water) from a stock solution was introduced into the reactor. The reactor was flushed with CO_2 gas in order to remove the air. Afterwards, the reactor was filled with desired amount of 20 bar CO_2 and topped up with 20 bar H_2 gas, till the desired total pressure of 40 bar was reached at room temperature. The reaction was conducted at varying temperatures using a heating mantle under hard stirring. The pressure drop was measured using a pressure transducer connected to the reactor, whilst the recording was undertaken with an E725 RDS transducer indicator and the values were digitalised using Realtek software. After the gas uptake plateaued, the reactor was cooled down to room temperature and carefully vented. The reaction mixture was analysed directly by ^{1}H NMR spectroscopy in DMSO-d_6 to determine the amount of formic acid formed, using BMMI.OAc as an internal standard.

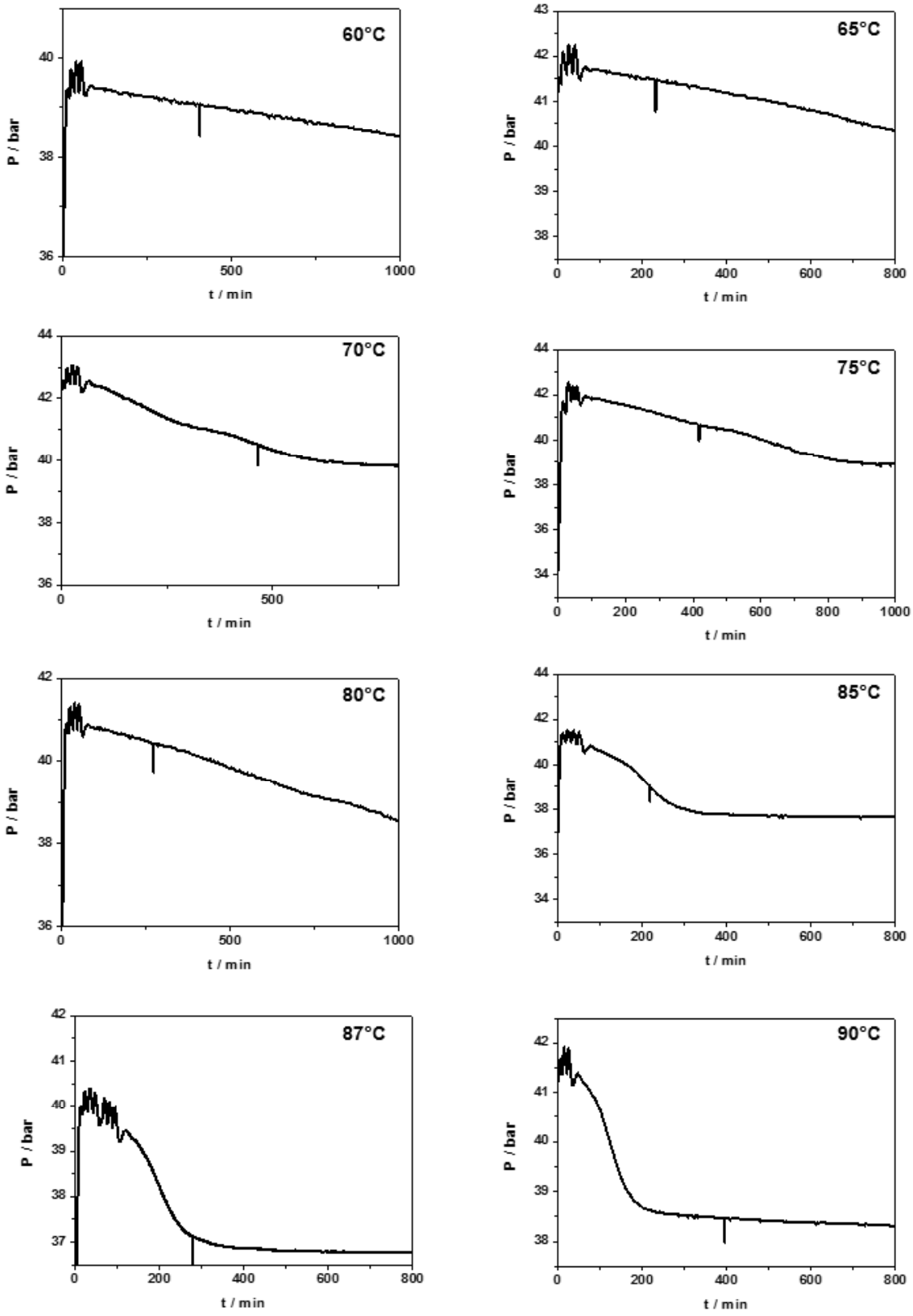
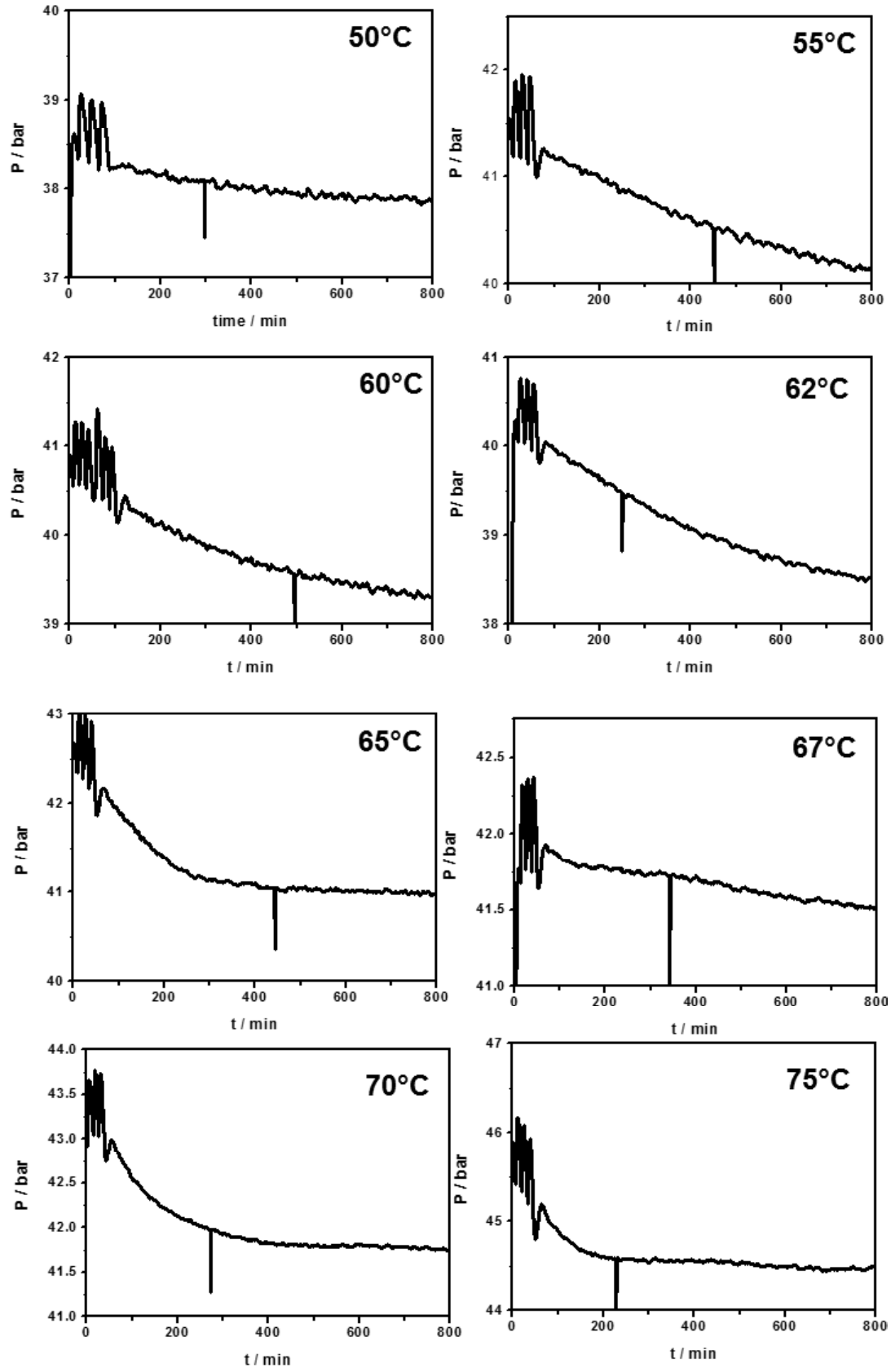


Figure S10 Gas absorption curves with **2** in DMSO. Reaction conditions: 8 µmol **2**, 3.3 mmol BMMI.OAc, P(H2) = P(CO2) = 20 bar, 6 mL DMSO:H_2O (5 v/v% H_2O).



.

Figure S11 Gas absorption curves **2** in THF. 8 µmol **2**, 3.3 mmol C_{10}MMI.OAc, P(H2) = P(CO2) = 20 bar, 6 mL THF:H_2O (5 v/v% H_2O).

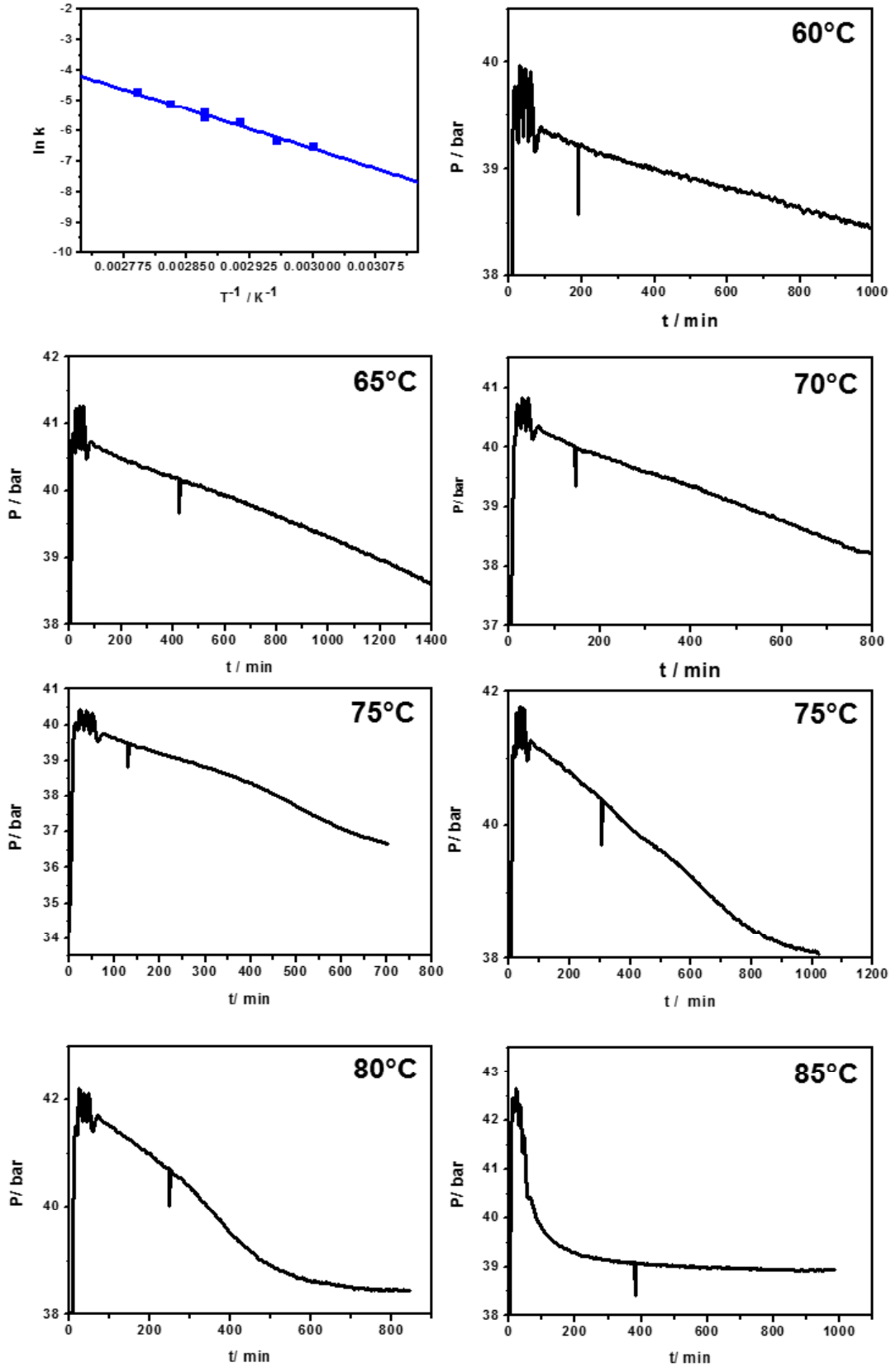


Figure S12 Gas absorption curves in of **3** in DMSO. 8 µmol **3**, 3.3 mmol BMMI.OAc, P(H2) = P(CO2) = 20 bar, 6 mL DMSO:H_2O (5 v/v% H_2O).

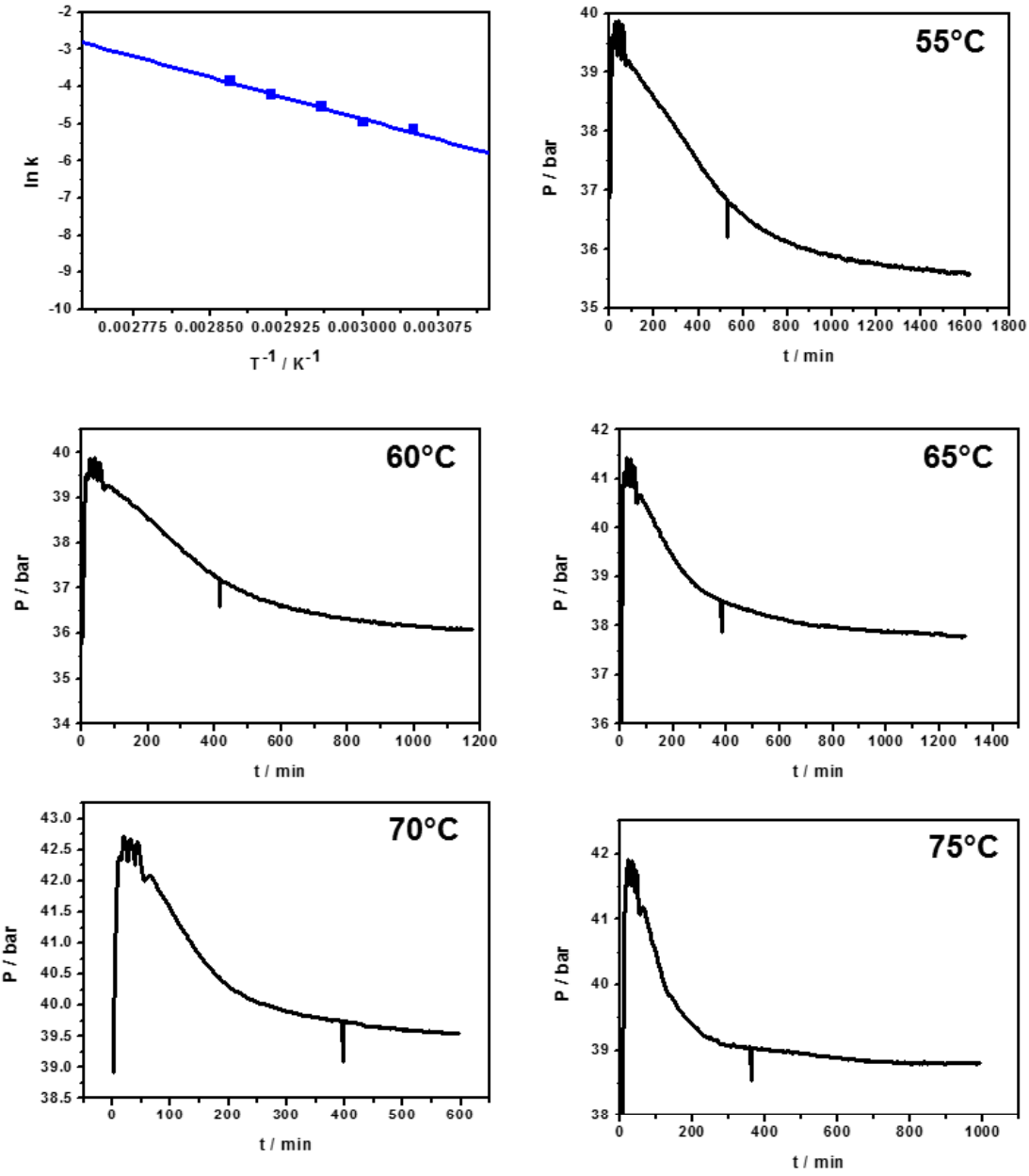


Figure S13 Arrhenius of **1** in DMSO with corresponding gas absorption curves. 8 µmol **1**, 3.3 mmol BMMI.OAc, P(H2) = P(CO2) = 20 bar, 6 mL DMSO:H_2O (5 v/v% H_2O).

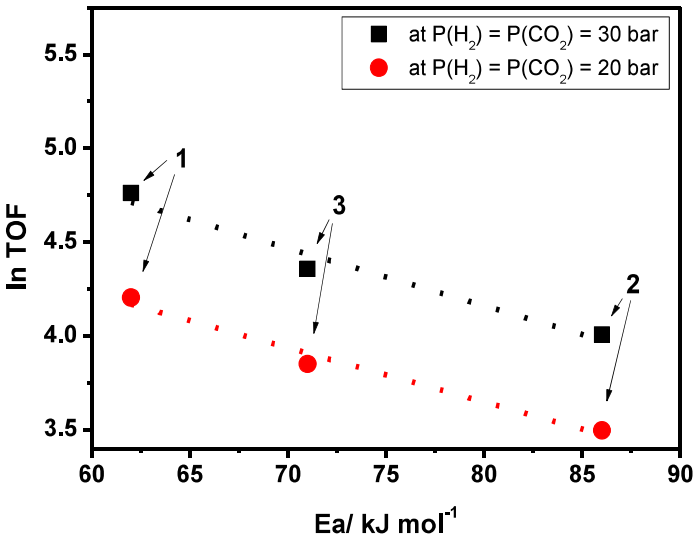


Figure S14 ln TOF vs Ea with **1**, **2** and **3** in DMSO. Red line indicates relationship in between ln(TOF_{av}) and E_a at $P(H_2) = P(CO_2) = 20$ bar and black line indicates relationship in between ln(TOF) vs E_a at $P(H_2) = P(CO_2) = 30$ bar. Note that at $P(H_2) = P(CO_2) = 20$ bar the average TOF was used whilst at $P(H_2) = P(CO_2) = 30$ bar was used.

2.5. Inner vs outer sphere mechanism

2.5.1. Volume of activation

A Parr reactor (50 mL) was loaded with 1.0 mg (1.5 µmol) [Ru(p-cym)(phen-p-PYA)NCMe]OTf (**2-MeCN**) or 0.7 mg (1.5 µmol) [Ru(p-cym)(phen-p-PYA)Cl] (**2**) and 700 mg (3.3 mmol) BMMI.OAc (3.3 mmol). Then 6 mL of DMSO:water (5 v/v% water) from a stock solution was introduced into the reactor. The reactor was flushed with CO_2 gas in order to remove the air. Afterwards, the reactor was filled with 20 bar CO_2 and filled with 10 bar H_2 gas, till the desired total pressure of 30 bar was reached. If desired, the reactor pressure was filled to 80 bar with Ar. The reaction was conducted at 80°C (**2-MeCN**), respectively 90°C (**2**), using a heating mantle under hard stirring. After the 18h (**2-MeCN**), respectively 20h (**2**), the reactor was cooled down to room temperature and carefully vented. The reaction mixture was analysed directly by ^{1}H NMR spectroscopy in DMSO-d_6 to determine the amount of formic acid formed, using BMMI.OAc as an internal standard.

Table S9 Experiments with additional Ar pressure to investigate inner vs outer sphere mechanism during CO_2 insertion with **2**, respectively **2-MeCN**.

Entry	Catalyst	Conc. Fa / M	TON	TOF / h^{-1}	Ar / bar
1[a]	**2**	0.18	716	36	50
2[a]	**2**	0.17	673	33	50
3[b]	**2**	0.20	782	39	
4[b]	**2**	0.19	716	36	
5[c]	**2-MeCN**	0.17	673	37	50
6[c]	**2-MeCN**	0.18	716	38	50
7[d]	**2-MeCN**	0.14	564	31	
8[d]	**2-MeCN**	0.14	564	31	

Reaction conditions: 1.5 µmol pre catalyst, 6 mL DMSO:water (5 v/v% water), 10 bar H_2, 20 bar CO_2, a) 50 bar Ar, T = 90°C, t =20 h b) T = 90°C, t =20 h, c) Ar = 50 bar, T = 80°C, t = 18 h, d) T = 80°C, t = 18 h.

The equation that explains the correlation between TOF, pressure and volume of activation is shown below:[12]

$$\Delta V^{\ddagger} = -RT\left(\frac{\partial ln\, k}{\partial P}\right)_T \qquad \text{Eq. 1}$$

where $\Delta V^{\ddagger}$ as volume of activation, R as the gas constant, T as the temperature P as the pressure.

2.6. Representative 1H NMR spectrum for the hydrogenation of CO_2 to formic acid

Reaction mixture analysis was undertake using the IL as an internal standard. The delays were set to d1 = 50s to ensure reproducibility. **Figure S15** depicts a representative ^{1}H NMR spectrum for the hydrogenation of CO_2 to formic acid in DMSO:H_2O (5 v/v% H_2O) and BMMI.OAc. Formic acid appears as a singlet at 8.44 ppm.

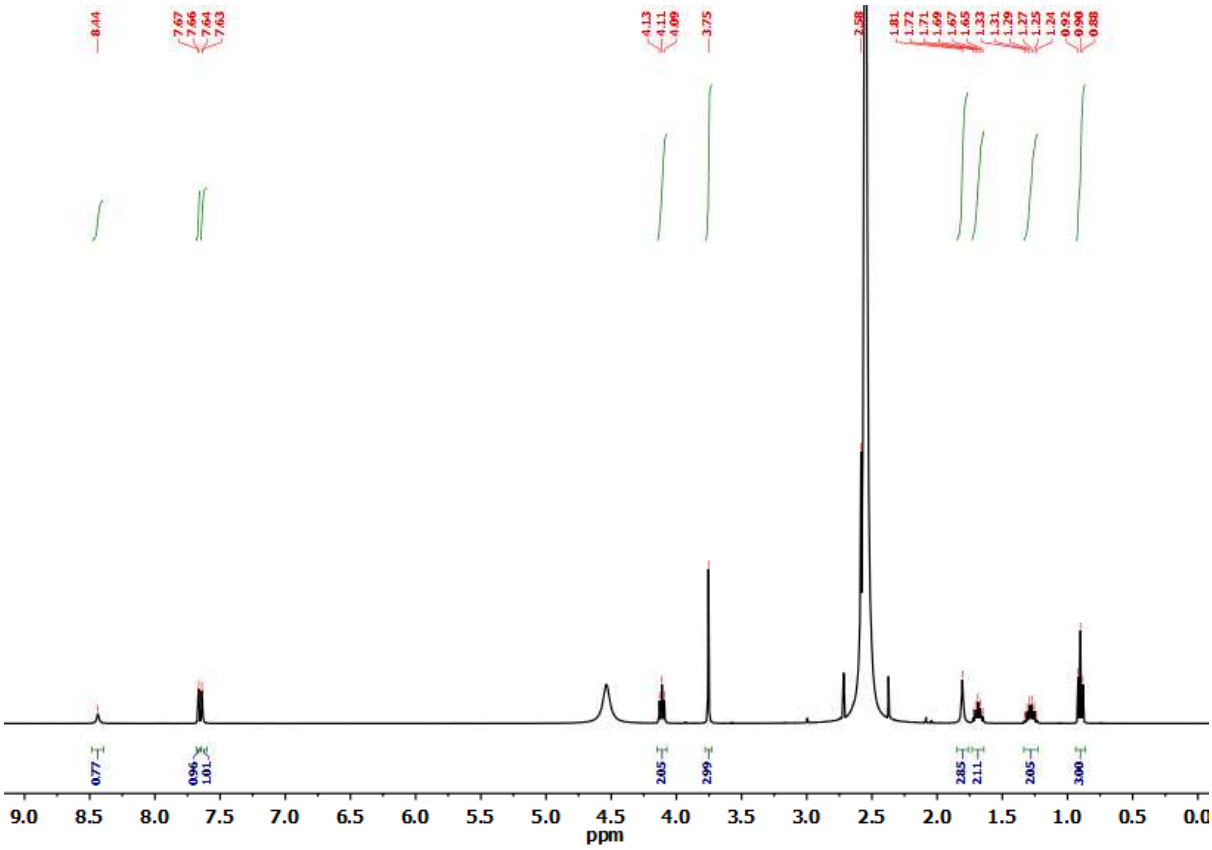


Figure S15 Representative ^{1}H NMR spectrum for the hydrogenation of CO2 to formic acid in the presence of BMMI.OAc in DMSO:H_2O (5 v/v% H_2O) with complex **2-MeCN** under 60 bar H_2 and 30 bar CO_2 (reaction time t = 18h).

3. References

1. Boyd, P. D. W.; Wright, L. J.; Zafar, M. N., Extending the Range of Neutral N-Donor Ligands Available for Metal Catalysts: N-[1-Alkylpyridin-4(1H)-ylidene]amides in Palladium-Catalyzed Cross-Coupling Reactions. *Inorganic Chemistry* **2011,** *50* (21), 10522-10524.
2. Navarro, M. Electronically Flexible Ligands for Transition Metal Catalysis. Universität Bern, 2017.
3. Navarro, M.; Li, M.; Müller-Bunz, H.; Bernhard, S.; Albrecht, M., Donor-Flexible Nitrogen Ligands for Efficient Iridium-Catalyzed Water Oxidation Catalysis. *Chemistry – A European Journal* **2016,** *22* (20), 6740-6745.
4. Vrijdag, J. L.; Delgado, F.; Alonso, N.; De Borggraeve, W. M.; Pérez-Macias, N.; Alcázar, J., Practical preparation of challenging amides from non-nucleophilic amines and esters under flow conditions. *Chemical Communications* **2014,** *50* (95), 15094-15097.
5. Oxford Diffraction (2010). *CrysAlisPro* (Version 1.171.38.41). Oxford Diffraction Ltd., Yarnton, Oxfordshire, UK.
6. Macchi, P. B., H.B.; Chimpri, A. S.; Hauser, J.; Gal, Z. , *J. Appl. Cryst.* **2011,** *44*, 763-771.
7. Sheldrick, G. M., *Acta Cryst.* **2015,** *A71*, 3-8.
8. Sheldrick, G. M., *Acta Cryst.* **2015,** *C71*, 3-8.
9. Connelly, N. G.; Geiger, W. E., Chemical Redox Agents for Organometallic Chemistry. *Chemical Reviews* **1996,** *96* (2), 877-910.
10. Welton, C. R. T., *Solvents and Solvent Effects in Organic Chemistry*. WILEY-VCH Verlag: 2011.
11. Zanatta, M.; dos Santos, F. P.; Biehl, C.; Marin, G.; Ebeling, G.; Netz, P. A.; Dupont, J., Organocatalytic Imidazolium Ionic Liquids H/D Exchange Catalysts. *The Journal of Organic Chemistry* **2017,** *82* (5), 2622-2629.
12. IUPAC, *Compendium of Chemical Terminology*. 2 ed.; Blackwell Scientific Publications: Oxford, 1997.

6.9. References

1. Shi, Q.; Thatcher, R. J.; Slattery, J.; Sauari, P. S.; Whitwood, A. C.; McGowan, P. C.; Douthwaite, R. E., Synthesis, Coordination Chemistry and Bonding of Strong N-Donor Ligands Incorporating the 1H-Pyridin-(2E)-Ylidene (PYE) Motif. *Chemistry – A European Journal* **2009,** *15* (42), 11346-11360.
2. Doster, M. E.; Hatnean, J. A.; Jeftic, T.; Modi, S.; Johnson, S. A., Catalytic C−H Bond Stannylation: A New Regioselective Pathway to C−Sn Bonds via C−H Bond Functionalization. *Journal of the American Chemical Society* **2010,** *132* (34), 11923-11925.
3. Leigh, V.; Carleton, D. J.; Olguin, J.; Mueller-Bunz, H.; Wright, L. J.; Albrecht, M., Solvent-Dependent Switch of Ligand Donor Ability and Catalytic Activity of Ruthenium(II) Complexes Containing Pyridinylidene Amide (PYA) N-Heterocyclic Carbene Hybrid Ligands. *Inorganic Chemistry* **2014,** *53* (15), 8054-8060.
4. Donnelly, K. F.; Segarra, C.; Shao, L.-X.; Suen, R.; Müller-Bunz, H.; Albrecht, M., Adaptive N-Mesoionic Ligands Anchored to a Triazolylidene for Ruthenium-Mediated (De)Hydrogenation Catalysis. *Organometallics* **2015,** *34* (16), 4076-4084.
5. Boyd, P. D. W.; Wright, L. J.; Zafar, M. N., Extending the Range of Neutral N-Donor Ligands Available for Metal Catalysts: N-[1-Alkylpyridin-4(1H)-ylidene]amides in Palladium-Catalyzed Cross-Coupling Reactions. *Inorganic Chemistry* **2011,** *50* (21), 10522-10524.
6. Slattery, J.; Thatcher Robert, J.; Shi, Q.; Douthwaite Richard, E., Comparison of donor properties of N-heterocyclic carbenes and N-donors containing the 1H-pyridin-(2E)-ylidene motif. In *Pure and Applied Chemistry*, 2010; Vol. 82, p 1663.
7. Navarro, M.; Rosar, V.; Montini, T.; Milani, B.; Albrecht, M., Olefin Dimerization and Isomerization Catalyzed by Pyridylidene Amide Palladium Complexes. *Organometallics* **2018,** *37* (20), 3619-3630.
8. Navarro, M.; Li, M.; Bernhard, S.; Albrecht, M., A mesoionic nitrogen-donor ligand: structure, iridium coordination, and catalytic effects. *Dalton Transactions* **2018,** *47* (3), 659-662.
9. Navarro, M.; Smith, C. A.; Li, M.; Bernhard, S.; Albrecht, M., Optimization of Synthetically Versatile Pyridylidene Amide Ligands for Efficient Iridium-Catalyzed Water Oxidation. *Chemistry – A European Journal* **2018,** *24* (24), 6386-6398.
10. Melle, P.; Manoharan, Y.; Albrecht, M., Modular Pincer-type Pyridylidene Amide Ruthenium(II) Complexes for Efficient Transfer Hydrogenation Catalysis. *Inorganic Chemistry* **2018,** *57* (18), 11761-11774.
11. Graf, E.; Leitner, W., Direct formation of formic acid from carbon dioxide and dihydrogen using the [{Rh(cod)Cl}2]-Ph2P(CH2)4PPh2 catalyst system. *Journal of the Chemical Society, Chemical Communications* **1992,** (8), 623-624.
12. Waldie, K. M.; Ostericher, A. L.; Reineke, M. H.; Sasayama, A. F.; Kubiak, C. P., Hydricity of Transition-Metal Hydrides: Thermodynamic Considerations for CO2 Reduction. *ACS Catalysis* **2018,** *8* (2), 1313-1324.

13. Wiedner, E. S.; Chambers, M. B.; Pitman, C. L.; Bullock, R. M.; Miller, A. J. M.; Appel, A. M., Thermodynamic Hydricity of Transition Metal Hydrides. *Chemical Reviews* **2016,** *116* (15), 8655-8692.
14. Burgess, S. A.; Appel, A. M.; Linehan, J. C.; Wiedner, E. S., Changing the Mechanism for CO2 Hydrogenation Using Solvent-Dependent Thermodynamics. *Angewandte Chemie International Edition* **2017,** *56* (47), 15002-15005.
15. Burgess, S. A.; Grubel, K.; Appel, A. M.; Wiedner, E. S.; Linehan, J. C., Hydrogenation of CO2 at Room Temperature and Low Pressure with a Cobalt Tetraphosphine Catalyst. *Inorganic Chemistry* **2017,** *56* (14), 8580-8589.
16. Burgess, S. A.; Kendall, A. J.; Tyler, D. R.; Linehan, J. C.; Appel, A. M., Hydrogenation of CO2 in Water Using a Bis(diphosphine) Ni–H Complex. *ACS Catalysis* **2017,** *7* (4), 3089-3096.
17. Jeletic, M. S.; Hulley, E. B.; Helm, M. L.; Mock, M. T.; Appel, A. M.; Wiedner, E. S.; Linehan, J. C., Understanding the Relationship Between Kinetics and Thermodynamics in CO2 Hydrogenation Catalysis. *ACS Catalysis* **2017,** *7* (9), 6008-6017.
18. Galan, B. R.; Schöffel, J.; Linehan, J. C.; Seu, C.; Appel, A. M.; Roberts, J. A. S.; Helm, M. L.; Kilgore, U. J.; Yang, J. Y.; DuBois, D. L.; Kubiak, C. P., Electrocatalytic Oxidation of Formate by [Ni(PR2NR′2)2(CH3CN)]2+ Complexes. *Journal of the American Chemical Society* **2011,** *133* (32), 12767-12779.
19. Lilio, A. M.; Reineke, M. H.; Moore, C. E.; Rheingold, A. L.; Takase, M. K.; Kubiak, C. P., Incorporation of Pendant Bases into Rh(diphosphine)2 Complexes: Synthesis, Thermodynamic Studies, And Catalytic CO2 Hydrogenation Activity of [Rh(P2N2)2]+ Complexes. *Journal of the American Chemical Society* **2015,** *137* (25), 8251-8260.
20. Waldie, K. M.; Brunner, F. M.; Kubiak, C. P., Transition Metal Hydride Catalysts for Sustainable Interconversion of CO2 and Formate: Thermodynamic and Mechanistic Considerations. *ACS Sustainable Chemistry & Engineering* **2018,** *6* (5), 6841-6848.
21. Pitman, C. L.; Brereton, K. R.; Miller, A. J. M., Aqueous Hydricity of Late Metal Catalysts as a Continuum Tuned by Ligands and the Medium. *Journal of the American Chemical Society* **2016,** *138* (7), 2252-2260.
22. Kubas, G., *Metal-dihydrogen and σ-bond coordination: The consummate extension of the Dewar-Chatt-Duncanson model for metal-olefin π bonding*. 2001; Vol. 635, p 37-68.
23. Ono, T.; Qu, S.; Gimbert-Suriñach, C.; Johnson, M. A.; Marell, D. J.; Benet-Buchholz, J.; Cramer, C. J.; Llobet, A., Hydrogenative Carbon Dioxide Reduction Catalyzed by Mononuclear Ruthenium Polypyridyl Complexes: Discerning between Electronic and Steric Effects. *ACS Catalysis* **2017,** *7* (9), 5932-5940.
24. Hazari, N.; Heimann, J. E., Carbon Dioxide Insertion into Group 9 and 10 Metal–Element σ Bonds. *Inorganic Chemistry* **2017,** *56* (22), 13655-13678.
25. Heimann, J. E.; Bernskoetter, W. H.; Hazari, N.; Mayer, James M., Acceleration of CO2 insertion into metal hydrides: ligand, Lewis acid, and solvent effects on reaction kinetics. *Chemical Science* **2018,** *9* (32), 6629-6638.
26. IUPAC, *Compendium of Chemical Terminology*. 2 ed.; Blackwell Scientific Publications: Oxford, 1997.

27. Crabtree, R. H., *The Organometallic Chemistry of the Transition Metals*. 6 ed.; Wiley VCH: 2014.
28. Mondal, B.; Neese, F.; Ye, S., Control in the Rate-Determining Step Provides a Promising Strategy To Develop New Catalysts for CO2 Hydrogenation: A Local Pair Natural Orbital Coupled Cluster Theory Study. *Inorganic Chemistry* **2015,** *54* (15), 7192-7198.
29. Matsubara, Y.; Fujita, E.; Doherty, M. D.; Muckerman, J. T.; Creutz, C., Thermodynamic and Kinetic Hydricity of Ruthenium(II) Hydride Complexes. *Journal of the American Chemical Society* **2012,** *134* (38), 15743-15757.
30. Mondal, B.; Neese, F.; Ye, S., Toward Rational Design of 3d Transition Metal Catalysts for CO2 Hydrogenation Based on Insights into Hydricity-Controlled Rate-Determining Steps. *Inorganic Chemistry* **2016,** *55* (11), 5438-5444.
31. Hayashi, H.; Ogo, S.; Fukuzumi, S., Aqueous hydrogenation of carbon dioxide catalysed by water-soluble ruthenium aqua complexes under acidic conditions. *Chemical Communications* **2004,** (23), 2714-2715.
32. Ogo, S.; Kabe, R.; Hayashi, H.; Harada, R.; Fukuzumi, S., Mechanistic investigation of CO2 hydrogenation by Ru(ii) and Ir(iii) aqua complexes under acidic conditions: two catalytic systems differing in the nature of the rate determining step. *Dalton Transactions* **2006,** (39), 4657-4663

33. Barghi, S. H.; Tsotsis, T. T.; Sahimi, M., Solubility and diffusivity of H2 and CO2 in the ionic liquid [bmim][PF6]. *International Journal of Hydrogen Energy* **2015,** *40* (28), 8713-8720.
34. Shi, W.; Sorescu, D. C.; Luebke, D. R.; Keller, M. J.; Wickramanayake, S., Molecular Simulations and Experimental Studies of Solubility and Diffusivity for Pure and Mixed Gases of H2, CO2, and Ar Absorbed in the Ionic Liquid 1-n-Hexyl-3-methylimidazolium Bis(Trifluoromethylsulfonyl)amide ([hmim][Tf2N]). *The Journal of Physical Chemistry B* **2010,** *114* (19), 6531-6541.
35. Jessop, P. G.; Stanley, R. R.; Brown, R. A.; Eckert, C. A.; Liotta, C. L.; Ngo, T. T.; Pollet, P., Neoteric solvents for asymmetric hydrogenation: supercritical fluids, ionic liquids, and expanded ionic liquids. *Green Chemistry* **2003,** *5* (2), 123-128.

36. a) Shokouhi, M.; Farahani, H.; Hosseini-Jenab, M., *Fluid Ph. Equilibria* **2014**, *367*, 29-37; b) Symons, E. A., *Can. J. Chem.* **1971**, *49* (24), 3940-3947.

Chapter 7: Ru-CNC pincer for CO_2 hydrogenation

7.1 Introduction

Based on the knowledge gained throughout this project, the last part of this thesis describes the design, synthesis, characterisation and application of an extremely active and stable catalyst to synthesise FA. In this case a NHC-CNC-pincer catalyst was selected for the hydrogenation of CO_2 to formic acid.

Pincer complexes have been employed extensively in the hydrogenation of CO_2 to formic acid, see ***section 1.3.2***. However, as shown in **figure 1.24**; ***section 1.3.2.***, the typical co-operative mechanism during H_2 activation is also the entry point for the deactivation of the catalyst.[1] Here the CO_2 is incorporated into the de-aromatized ligand scaffold, see **figure 1.24**; ***section 1.3.2.***.[1]

Furthermore, NHC donor ligands display certain similarities with the previously discussed N donation in PYA ligands. Here the NHC donation results in a stronger σ donation and weaker π acceptation, compared to the alkyl phosphines counterparts.[2] Sterically, the metal ligand bonds are shorter, compared to their alkyl phosphine counterparts and the ligand is thus deeply encroaching into the coordination sphere.[3] However, the functional groups are pointing towards the metal centre, creating space around the metal centre for substrate activation.[3] Synthetically, $C^{NHC}NC^{NHC}$ (CNC) pincer complexes can be synthesized *via* 3 main routes. These synthetic strategies involve the oxidative addition of the metal into the ligand scaffold, the deprotonation of the NHC ligands with strong bases and transmetallation routes with either Zr or Ag.[4]

Catalytic applications of Ru-CNC-pincer complexes involve hydrogen transfer reactions and the oxidative cleavage of olefins.[5] Ru-CNC-pincer complexes with an acidic CH_2 group have also been employed in the hydroboration of CO_2.[6] Lutidine derived CNC-Ru pincers (**7.1**) with an acidic CH_2 group are also active in the hydrogenation of CO_2 (under basic conditions), although the catalytic turnover in the hydrogenation of CO_2 was low.[7-8] However, these catalysts showed excellent activity in the hydrogenation of esters in contrast to their PNP counterparts (**7.2**).[7]

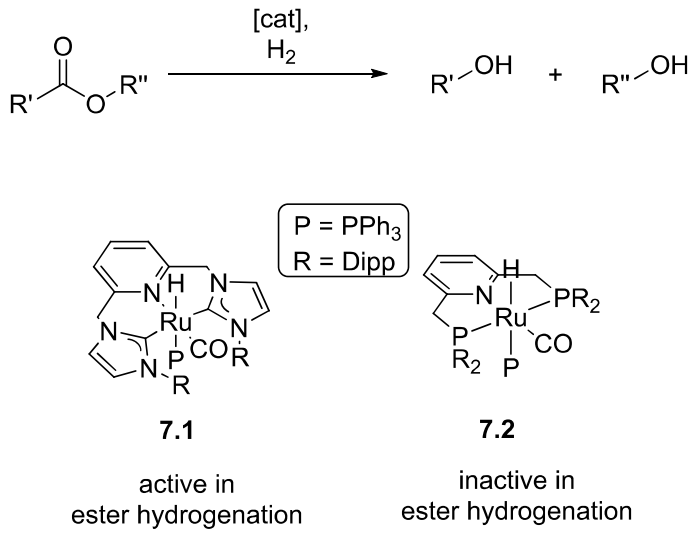


Figure 7.1 Comparison between lutidine derived CNC-Ru-pincer complex and the analogue PNP-pincer complex for ester hydrogenation reactions.[7]

Most likely the low turnover observed with the lutidine derived Ru CNC pincer complexes in the hydrogenation of CO_2 is due to the aforementioned incorporation CO_2 into the ligand scaffold.[1, 7] In order to avoid this reaction, the position of interest was blocked by the NHC donor, see **figure 7.2**. This feature also distinguishes the catalyst investigated in this thesis from the previously reported lutidine derived CNC-pincer in the hydrogenation of CO_2 to formic acid. Furthermore, as mentioned previously, the electron donating effects

observed in the PYA ligand scaffolds could be mimicked, leading to a facile CO_2 insertion into the Ru-H bond.

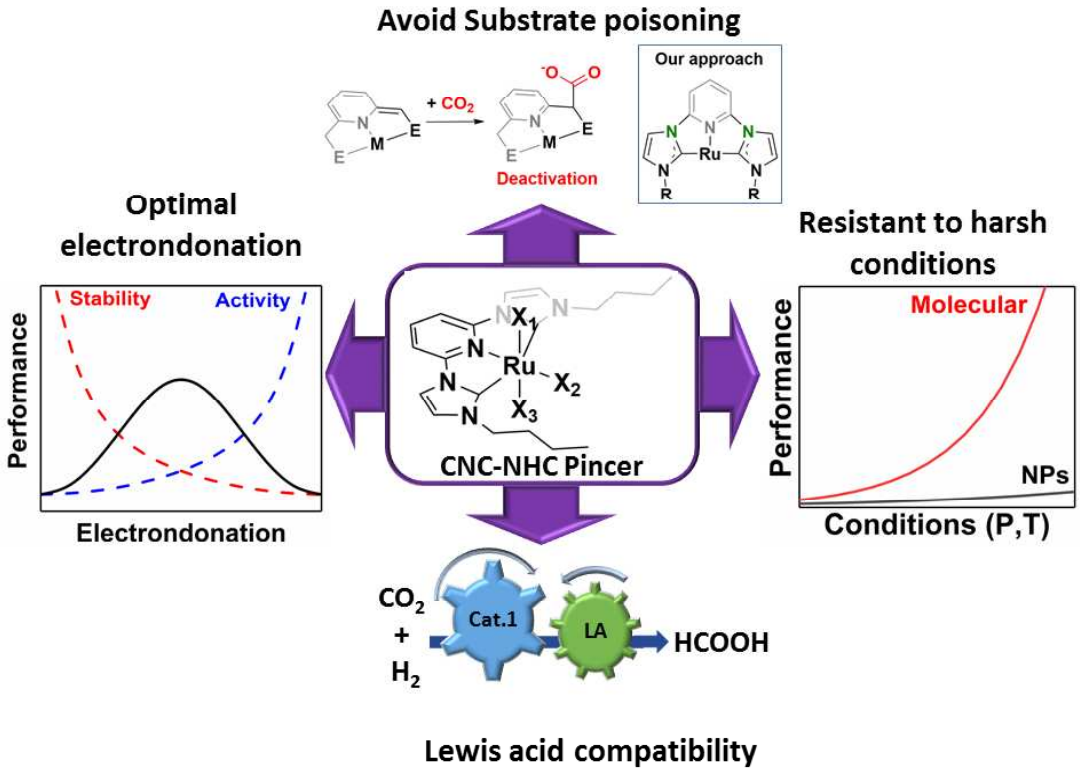


Figure 7.2 CNC pincer utilized in this thesis for the base free hydrogenation of CO_2 to formic acid. Beneficial ligand properties are highlighted in green.

7.2. Publicaiton IV: Highly efficient base-free synthesis of formic acid from carbon dioxide

Contribution of the author: In this publication the author designed the idea for the catalyst, planned the research in liaison with the PhD supervisors, and synthesized all complexes and ionic liquids undertook all the experiments, analysed and interpreted the data and wrote the manuscript in collaboration with all co-authors.

Reprinted with permission from www.chemrxiv.org/s/766685b107d9bca8418a

Highly efficient base-free synthesis of formic acid from carbon dioxide

Sustainable synthesis of formic acid from carbon dioxide

Andreas Weilhard,[a] Stephen Argent,[b] Victor Sans,[a,c]

[a] Faculty of Engineering, University of Nottingham, Nottingham, NG7 2RD, U.K

[b] School of Chemistry, University of Nottingham, Nottingham, NG7 2RD, U.K

[c] Institute of Advanced Materials (INAM), Universitat Jaume I, Castellon, 12071, Spain

Abstract

The efficient transformation of CO_2 into chemicals and fuels is a key challenge for the decarbonisation of the chemical synthetic production chain. The thermodynamic and kinetic stability of CO_2 however poses great challenges for the effective reduction to useful chemicals. The employment of bases is a typical strategy to overcome thermodynamic barriers in the synthesis of formic acid. However, it increases the amount of waste generated and requires post-processing of the formate salts. Here, we present a base-free methodology to catalytically transform CO_2 into formic acid (FA) with very high efficiency, with comparable performance to the base-assisted systems. The combination of basic ionic liquids that play multiple roles, including buffering the products of reaction, and catalyst design, achieves the synthesis of FA with unprecedented catalytic efficiency in TONs of $>8*10^5$ and TOFs $> 2.1*10^4$ h^{-1}, which represents a great step towards the development of cost-efficient catalytic systems.

Introduction

Formic acid (FA) is currently being discussed as a promising candidate for hydrogen storage and an important basic chemical.[1-3] Unfortunately, to date the synthesis is based on the indirect water carbonylation, using CO generated from fossil fuels.[4] Without a doubt a system using the greenhouse gas CO_2 as a carbon source would be environmentally preferential. However, the direct hydrogenation of CO_2 is thermodynamically unfavourable.[5] Bases are

commonly added to reaction mixture to shift the thermodynamic equilibrium by the consecutive consumption of formic acid in an acid base reaction to the product side.[5-7] Under these conditions a plethora of catalyst such as N-heterocyclic carbenes[8,9], half sandwich,[10-13] pincers[14-17] and phosphine[18-22] complexes of a broad range of transition metals, including iron,[23-26] nickel,[27,28] copper[29,30] and cobalt[31-33] have shown to be remarkably active (TON >10^6).[14]

However, an important limitation of these approaches is the formation of formate adducts and salts, which would need to be tediously purified in the consecutive steps.[6,34] Therefore, the direct hydrogenation of CO_2 would be preferential. Unfortunately, the hydrogenation under base free conditions is thermodynamically and kinetically difficult to operate.[5] As a consequence, considerably fewer systems have been reported for the hydrogenation of CO_2 to FA under base-free conditions. Furthermore, these systems typically operate under very high pressures[35] and the catalytic activity and concentration of FA achieved are significantly lower than under basic conditions.[36-41] We have demonstrated that basic ionic liquids can effectively buffer the reaction, stabilise the catalysts, and they can be immobilised onto supported phases, thus facilitating the separation of the FA at the end of the process, thus shifting the thermodynamic equilibrium to the product side and in the presence of IL the reaction can be operated at relatively low pressures.[42] In our previous studies we have established the thermodynamic parameters for this transformation employing basic ILs, and therefore we can understand the maximum concentration of FA achievable as a function of the reaction conditions. Furthermore, we previously studied the effect of ligand modifications onto the hydrogenation of CO_2 in the presence of ILs. Key parameters effecting the catalyst activity and stability were identified in this study.[1]

Here, we present a catalytic system for the base free hydrogenation of CO_2 specifically designed to work under a wide range of temperatures. This enables optimising the catalyst performance according to the thermodynamic limitations imposed by the reaction and consequently high catalytic efficiency

[1] Currently under review

is achieved. The robustness of the catalyst enables the addition of lewis acids, which increase the performance of the catalyst in terms of activity and stability. The results obtained here are comparable to those obtained with base containing systems and represent a huge leap forward for base-free systems.

Results and Discussion

The design of the catalysts plays a key role in the development of efficient catalytic systems. Very recently, we have demonstrated that basic ionic liquids provide a buffering environment that enables the efficient synthesis of FA, but with much lower enthalpy than when a base (leading to a salt formation) is employed.[43,44] Under these conditions, optimal electrondonation properties of the ligand are key to balance reactivity and the resistance to deactivation via protonation of the catalyst (Figure 1). Furthermore, complexes with high chemical and thermal stability lead to catalysts with large operational windows and an increased compatibility with other components, such as co-catalysts. NHC based pincer architectures fulfil all these criteria, hence being ideal candidates for this transformation.[45] Furthermore, pincer ligand architecture have already been demonstrated to be active in the hydrogenation of CO_2. However, pincers normally exhibit a co-operative mechanism in the activation of hydrogen[25,46] which leads to the deactivation of the catalyst (Figure 1, substrate poisoning).[15] Consequently, a suitable catalyst should prevent the coordination of substrates in undesired positions. In this study this was achieved by a direct connection of the aromatic pyridine with the imidazole side arms.

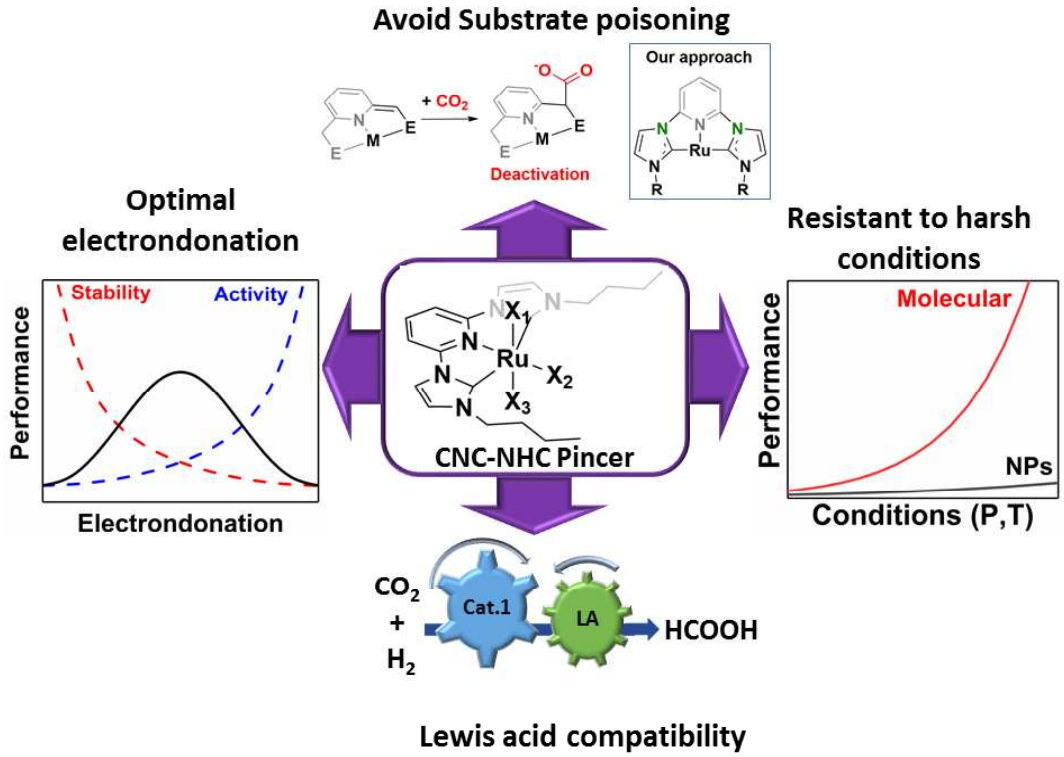


Figure 1 Catalyst design strategy. The molecular catalyst should be resistant to deactivation by the substrates, the increasingly acid media, the strong reductive conditions and compatible with other catalysts (e.g. Lewis acids).

The silver trans metalation route employing $[Ru(CO)_2(Cl)_2]_n$ as the Ru source, and **L-1** as the ligand was chosen to synthesize the desired Ru-CNC-complex. The reaction was followed by the disappearing signal for the C_2-H in the ^{1}H-NMR spectra and the appearance of a new peak at 181 ppm in the ^{13}C spectra (see ESI, Figure S1 and Figure S2). In the IR spectra two significant bands at 1993 cm^{-1} and 2051 cm^{-1} (see ESI, Figure S3), corresponding to two asymmetric CO stretching vibrations can be observed. The general structure was confirmed with Single X-ray crystal analysis. Minor scrambling is observed with Cl^- bond to Ru, i.e. replacement of Br^-. In a similar fashion the counterion distributed 1:1 (Br:Cl), giving an overall molecular sum formula of $C_{21}H_{25}Br_{0.63}Cl_{1.29}N_5O_2Ru$. The major halide bond to the metal centre was chloride, as confirmed with ESI-ms. ESI-ms analysis gave a mass of 516 m/z and a minor product with 562 m/z confirming (see ESI, Figure S4).

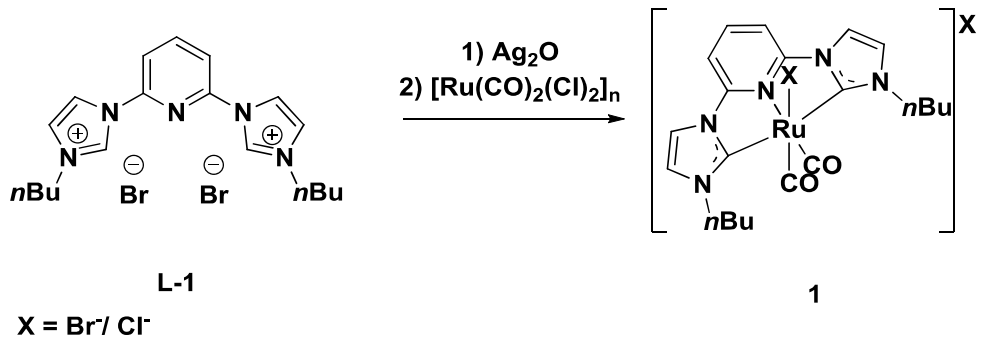


Figure 2 Synthetic strategy for the formation of **1** from **L-1** and $[Ru(CO)_2(Cl)_2]_n$.

The single crystal analysis indicated an average molecular mass of 578.11 g/mol, distributing to complexes with the sum formulas of $C_{21}H_{25}Cl_2N_5O_2Ru$ and $C_{21}H_{25}BrCl\ N_5O_2Ru$. This in bromide to chloride ratio of 30:70. Indeed, the observed mass peaks for the M-Cl^+ to M-Br^+ of ca. 73:27 indicate that the ratio determined by single crystal analysis is valid. Further evidence for this ratio was found by ICP-OES analysis. Here a Ru content of 19.2 mg L^{-1} was found in a 0.199 mM solution (for 100% Cl expected Ru content is 20.8 mg L^{-1} and for 100% Br expected Ru content is 18.2 mg L^{-1}), which indicate a molar ratio between **1-Br** and **1-Cl** of 70:30. In this way a molecular mass of 578.11 g/mol was used to determine the amount of catalyst in solution. Furthermore neither Cl^- nor Br^- showed a difference in catalytic activity or durability can be found in comparison to a non-modified system, indicating that the halide plays an insignificant role onto the catalytic activity, see ESI.

In an initial screening of catalytic activity, it was demonstrated that **1** achieves a concentration of 0.5 M solution of FA at 80°C in DMSO: water (5 v/v% water) in the presence of 1-butyl-2,3-dimethylimidazolium acetate (BMMI.OAc) under 60 bar pressure (H_2:CO_2 = 1:1). According to the thermodynamic parameters previously calculated for this system,[42] the concentration of FA observed is close to the thermodynamic equilibrium at approximately 120°C (see ESI Figure S5). Above 80°C the decomposition of DMSO was observed. Fortunately, when BMMI.OAc is employed as an additive the reaction can be performed in a broad range of solvents.[44] Furthermore the crucial role of BMMI.OAc is highlighted by the fact that **1** is inactive in the absence of BMMI.OAc. In dioxane the catalytic system achieves similar performance than in DMSO (0.54 M at 100°C).

It is important to note that no nanoparticle formation was observed under the reaction conditions assayed. Even at high temperatures and pressures (120°C and 60 bar (H_2:CO_2 = 30 bar)), TEM and DLS analysis showed no evidence of nanoparticles (see ESI for more details). Furthermore, the catalyst was not active in the hydrogenation of benzene at 120°C under 50 bar H_2 in the presence of BMMI.OAc even when high catalyst loadings are used, see ESI. It is important to note that the hydrogenation of benzene reaction is known to be catalysed by Ru nanoparticles.[47-50]

In the next step the catalyst activity and stability was explored. Lowering the concentration of catalyst showed that increasing the temperature led to increased kinetics, represented by increasing TOF values. However, this comes at the expense of reduced achievable concentration of FA (and consequently TON) due to the thermodynamic limitations at temperatures above 120°C, see table 1 entry 4 and 5.

Table 1 Temperature dependant results obtained with catalyst.

Entry	T / °C	[FA] / M	TON[a)]	TOF[b)] / h^{-1}
1	100	0.22	77550	1080
2	110	0.29	100580	1750
3	120	0.49	162900	4360
4	130	0.40	141000	10620
5	140	0.29	100862	16500

Reaction conditions: 6 mL dioxane;water (5 v/v% water), 3.3 mmol BMMI.OAc, 0.017 µmol catalyst. a) determined after 72 h, b) determined after 4h.

Plotting the concentration of FA generated after 72 h allows (Figure 3A) allows for a better understanding of the efficiency of the catalytic system. Here a maximum concentration of FA can be observed at 120 °C. Below that temperature, the system is controlled by kinetic limitations of the catalyst, whilst at higher temperatures the reaction is limited by approaching the thermodynamic equilibrium inherent to the reaction under the studied conditions.

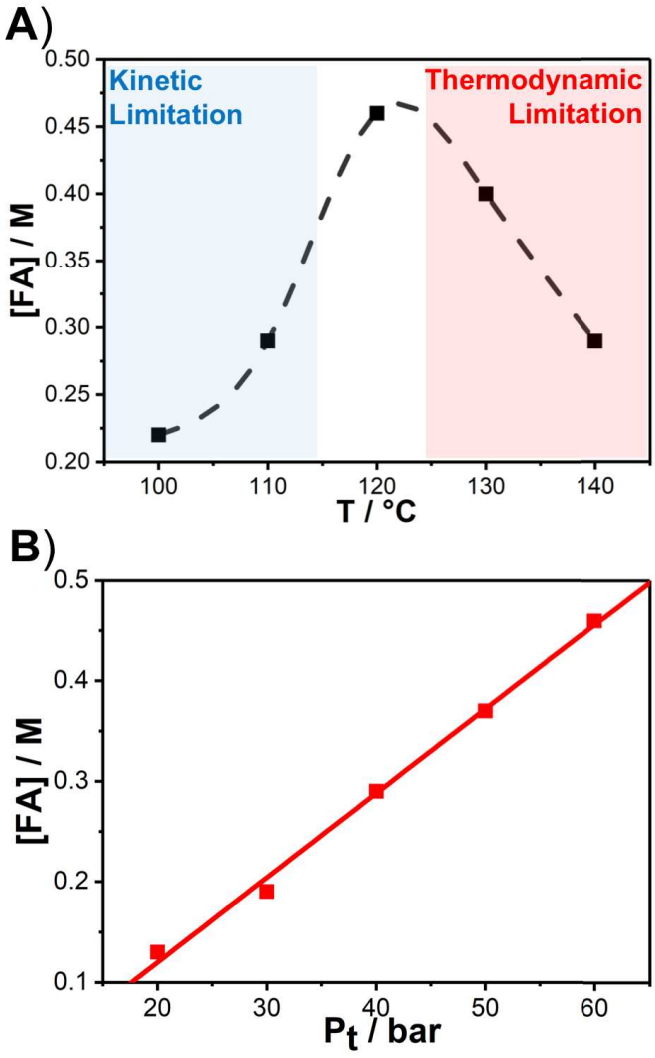


Figure 2 A) Optimal catalytic performance as a function of temperature, where kinetic and thermodynamic limitations are observed. B) Concentration of FA observed as a function of the total gas pressure.

In the next step the effect of pressure was investigated. Here a linear correlation in between the achieved concentration of FA and pressure can be observed (Figure 3B). This in consistent with the Henry's law, predicting a linear relationship in between the amount of dissolved gas and the applied pressure of the bespoke gases. As the gases represent the reactive species a reduced pressure leads inevitably to a lower concentration of FA (Figure 3B).

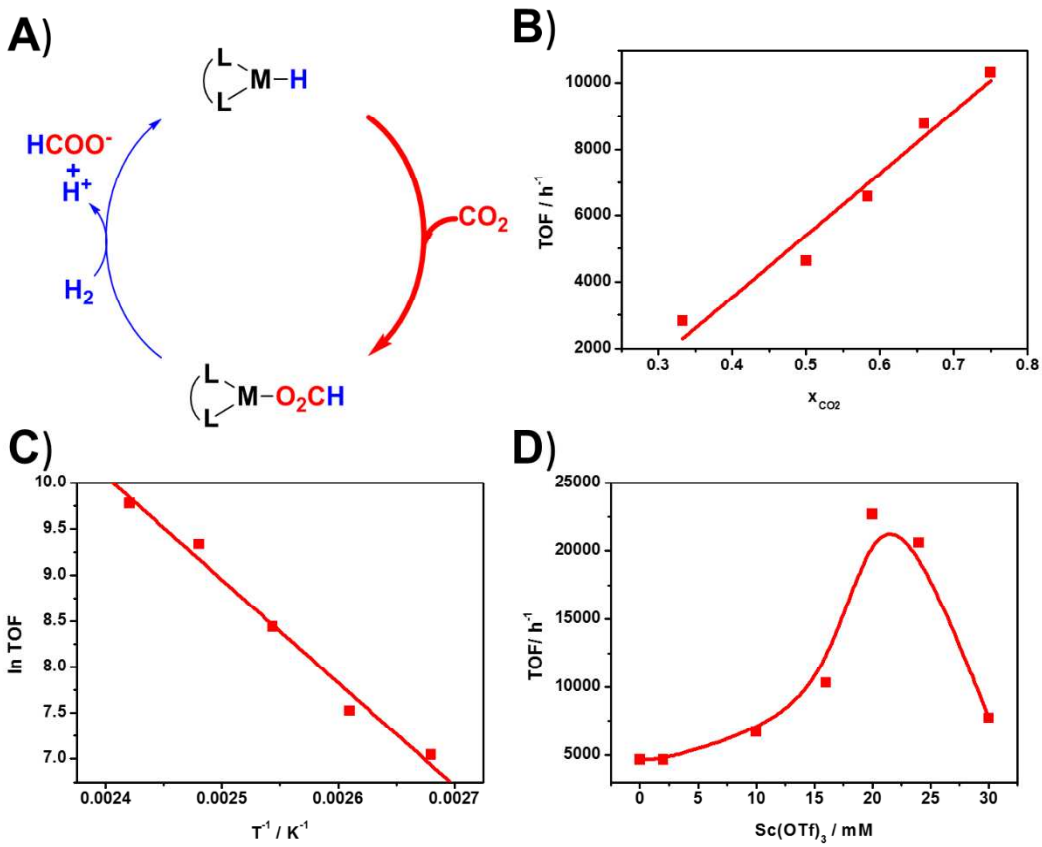


Figure 36 A) Simplified reaction mechanism with the rate determining step (CO_2 insertion) highlighted. B) Kinetic dependence of transformation on the partial pressure of CO_2. C) Arrhenius. D) effect of $Sc(OTf)_3$ on observed catalyst activity.

Mechanistically, the hydrogenation of CO_2 to FA can be divided into two main steps. In the first step, a hydride is transferred onto CO_2. In the second step, H_2 is activated releasing a proton and formate, with a simultaneous regeneration of the active hydride (figure 4A). In order to determine the rate determining step, various gas compositions were tested (maintaining constant the total pressure). The observed reaction rate decreased significantly at low partial pressure of CO_2 (Figure 4B). Indeed, at 20 bar CO_2 and 40 bar H_2 a TOF of 2700 h^{-1} was obtained. On the contrary an increased partial pressure of CO_2 led to increased rates, i.e. at 45 bar CO_2 and 15 bar H_2 a TOF of 9700 h^{-1} is determined, (c.f. 4360 h^{-1} at $P_{CO2} = P_{H2} = 30$ bar). These experiments clearly show a strong dependence on CO_2, thus indicating the CO_2 insertion to be rate determining steps.

An activation energy of 93 kJ mol^{-1} ± 6.7 kJ mol^{-1} was determined from the Arrhenius plot (figure 4C). The activation energy can either be decreased by increasing the electron donation onto the metal, leading to a more nucleophilic

hydride, decreasing hydricity (ΔG_{H^-}).[33] Based on our recent studies, great care has to be taken as a to low ΔG_{H^-} will ultimately lead to a more nucleophilic/ basic hydride, possibly rendering the catalyst prone to depletion of the active hydride species, *via* protonation.

Alternatively charged intermediates and transition state formed during the CO_2 insertion can be stabilised with lewis acids.[26,51-53] Therefore $Sc(OTf)_3$ was tested due to its high solubility in organic solvents, tolerance towards water and due to its relatively soft nature.[54] It was found that $Sc(OTf)_3$ significantly increased the reaction rate. However, smaller amounts have only a minor effect on the rate (Figure 4D). An optimal concentration of 20 mM for $Sc(OTf)_3$ was found. Above this concentration a drop in rate was observed, presumably due to catalyst poisoning as already observed in previous studies.[55] It is also important to note that in the absence of 1 no catalytic turnover was observed. Under optimised conditions a significant increase in TOF (21200 h^{-1}) was observed compared to reactions carried out in the absence of additional lewis acid. However, in the presence of $Sc(OTf)_3$ the concentration of FA generated decreased slightly to 0.32 M, yielding a TON of 114400, see table 2 entry 2. Increasing, the hydrogen to carbon dioxide ratio the achieved did not show any pronounced effects. Under these conditions, the amount of catalyst was reduced to 1.6 nmol, which led to an unprecedented TON of 833800, while the TOF was maintained at 20600 h^{-1} (table 3, entry 4).

Table 2 Optimised conditions for the hydrogenation of CO_2 to FA.

Entry	P_{H2}:P_{CO2} / bar:bar	$Sc(OTf)_3$ / mmol	[FA] / M	TON	TOF / h^{-1}
1	30:30	0	0.46	162900	4360
2	30:30	0.12	0.32	114400	21200
3	45:15	0.12	0.36	126000	22000
4[a]	45:15	0.12	0.26	833800	20600

Reaction conditions 0.017 µmol catalyst, T = 120°C in 6 mL 1,4-dioxane:H_2O (5 v/v% H_2O) in the presence of 3.3 mmol BMMI.OAc; TON and [FA] determined after 72h using BMMI.OAc as an internal standard, TOF determined after 4h; a) 0.0017 µmol catalyst, TON and [FA] determined after 5d using BMMI.OAc as an internal standard, TOF determined after 18h.

In summary we have developed a catalyst system, which has an up to a 50 times higher value in TON and 23 times higher value in TOF in the

hydrogenation of CO_2 to FA then ever reported under base free conditions.[35-37,40,42] Furthermore, the TON and TOF towards FA are comparable to values obtained under basic conditions.[14,17,58] Interestingly, the here reported CNC-Ru pincer outperforms its previously reported analogue with a six membered bite angle ring in terms of TON by >200 times, even though the previous complex was reported to operate under basic conditions.[59]

Beneath these findings the catalyst is active in the hydrogenation of CO_2 to C_1 compounds with lower oxidation state. We found that in the presence of $Sc(OTf)_3$ and nBuOH dialkoxymethane ether can be formed, representing the formaldehyde leve. The catalytic activity found for this transformation fall into the range of previously reported catalysts. [56,57]

Conclusions

To conclude, we have presented a catalytic system capable of highly efficiently transform CO_2 into FA under base-free conditions. The combination of basic ionic liquids, highly robust NHC CNC Ru based pincers and lewis acid catalysts showed high efficiency at 120 °C, achieving concentrations close to the thermodynamic equilibrium. The catalytic activity observed is the highest observed to date for base-free systems and comparable to literature reports employing base.

References

(1) Loges, B.; Boddien, A.; Junge, H.; Beller, M. *Angewandte Chemie International Edition* **2008**, *47*, 3962.
(2) Loges, B.; Boddien, A.; Gärtner, F.; Junge, H.; Beller, M. *Topics in Catalysis* **2010**, *53*, 902.
(3) Mellmann, D.; Sponholz, P.; Junge, H.; Beller, M. *Chemical Society Reviews* **2016**, *45*, 3954.
(4) Reutemann, W.; Kieczka, H. In *Ullmann's Encyclopedia of Industrial Chemistry*; Wiley-VCH Verlag GmbH & Co. KGaA: 2000.
(5) Klankermayer, J.; Wesselbaum, S.; Beydoun, K.; Leitner, W. *Angewandte Chemie International Edition* **2016**, *55*, 7296.
(6) Schaub, T.; Paciello, R. A. *Angewandte Chemie International Edition* **2011**, *50*, 7278.

(7) Leitner, W. *Angewandte Chemie International Edition in English* **1995**, *34*, 2207.
(8) Azua, A.; Sanz, S.; Peris, E. *Chemistry – A European Journal* **2011**, *17*, 3963.
(9) Sanz, S.; Azua, A.; Peris, E. *Dalton Transactions* **2010**, *39*, 6339.
(10) Hull, J. F.; Himeda, Y.; Wang, W.-H.; Hashiguchi, B.; Periana, R.; Szalda, D. J.; Muckerman, J. T.; Fujita, E. *Nat Chem* **2012**, *4*, 383.
(11) Wang, W.-H.; Hull, J. F.; Muckerman, J. T.; Fujita, E.; Himeda, Y. *Energy & Environmental Science* **2012**, *5*, 7923.
(12) Himeda, Y.; Onozawa-Komatsuzaki, N.; Sugihara, H.; Kasuga, K. *Organometallics* **2007**, *26*, 702.
(13) Himeda, Y.; Miyazawa, S.; Hirose, T. *ChemSusChem* **2011**, *4*, 487.
(14) Tanaka, R.; Yamashita, M.; Nozaki, K. *Journal of the American Chemical Society* **2009**, *131*, 14168.
(15) Filonenko, G. A.; Hensen, E. J. M.; Pidko, E. A. *Catalysis Science & Technology* **2014**, *4*, 3474.
(16) Filonenko, G. A.; Smykowski, D.; Szyja, B. M.; Li, G.; Szczygieł, J.; Hensen, E. J. M.; Pidko, E. A. *ACS Catalysis* **2015**, *5*, 1145.
(17) Filonenko, G. A.; van Putten, R.; Schulpen, E. N.; Hensen, E. J. M.; Pidko, E. A. *ChemCatChem* **2014**, *6*, 1526.
(18) Inoue, Y.; Izumida, H.; Sasaki, Y.; Hashimoto, H. *Chemistry Letters* **1976**, *5*, 863.
(19) Tsai, J. C.; Nicholas, K. M. *Journal of the American Chemical Society* **1992**, *114*, 5117.
(20) Fornika, R.; Gorls, H.; Seemann, B.; Leitner, W. *Journal of the Chemical Society, Chemical Communications* **1995**, 1479.
(21) Graf, E.; Leitner, W. *Journal of the Chemical Society, Chemical Communications* **1992**, 623.
(22) Elek, J.; Nádasdi, L.; Papp, G.; Laurenczy, G.; Joó, F. *Applied Catalysis A: General* **2003**, *255*, 59.
(23) Ziebart, C.; Federsel, C.; Anbarasan, P.; Jackstell, R.; Baumann, W.; Spannenberg, A.; Beller, M. *Journal of the American Chemical Society* **2012**, *134*, 20701.
(24) Robert, L.; Yael, D. P.; Gregory, L.; W., S. L. J.; Yehoshoa, B. D.; David, M. *Angewandte Chemie International Edition* **2011**, *50*, 9948.
(25) Zell, T.; Milstein, D. *Accounts of Chemical Research* **2015**, *48*, 1979.
(26) Zhang, Y.; MacIntosh, A. D.; Wong, J. L.; Bielinski, E. A.; Williard, P. G.; Mercado, B. Q.; Hazari, N.; Bernskoetter, W. H. *Chemical Science* **2015**, *6*, 4291.
(27) Burgess, S. A.; Kendall, A. J.; Tyler, D. R.; Linehan, J. C.; Appel, A. M. *ACS Catalysis* **2017**, *7*, 3089.
(28) Chakraborty, S.; Zhang, J.; Krause, J. A.; Guan, H. *Journal of the American Chemical Society* **2010**, *132*, 8872.
(29) Ryo, W.; Yoshihito, K.; Shin-ichi, H.; Norio, M.; Takao, I. *Advanced Synthesis & Catalysis* **2015**, *357*, 1369.
(30) Zall, C. M.; Linehan, J. C.; Appel, A. M. *ACS Catalysis* **2015**, *5*, 5301.

(31) Burgess, S. A.; Appel, A. M.; Linehan, J. C.; Wiedner, E. S. *Angewandte Chemie International Edition* **2017**, *56*, 15002.

(32) Burgess, S. A.; Grubel, K.; Appel, A. M.; Wiedner, E. S.; Linehan, J. C. *Inorganic Chemistry* **2017**, *56*, 8580.

(33) Jeletic, M. S.; Hulley, E. B.; Helm, M. L.; Mock, M. T.; Appel, A. M.; Wiedner, E. S.; Linehan, J. C. *ACS Catalysis* **2017**, *7*, 6008.

(34) Wesselbaum, S.; Hintermair, U.; Leitner, W. *Angewandte Chemie* **2012**, *124*, 8713.

(35) Rohmann, K.; Kothe, J.; Haenel, M. W.; Englert, U.; Hölscher, M.; Leitner, W. *Angewandte Chemie International Edition* **2016**, *55*, 8966.

(36) Moret, S.; Dyson, P. J.; Laurenczy, G. **2014**, *5*, 4017.

(37) Sahoo, A. R.; Jiang, F.; Bruneau, C.; Sharma, G. V. M.; Suresh, S.; Roisnel, T.; Dorcet, V.; Achard, M. *Catalysis Science & Technology* **2017**, *7*, 3492.

(38) Hayashi, H.; Ogo, S.; Fukuzumi, S. *Chemical Communications* **2004**, 2714.

(39) Ogo, S.; Kabe, R.; Hayashi, H.; Harada, R.; Fukuzumi, S. *Dalton Transactions* **2006**, 4657.

(40) Lu, S.-M.; Wang, Z.; Li, J.; Xiao, J.; Li, C. *Green Chemistry* **2016**, *18*, 4553.

(41) Zhao, G.; Joó, F. *Catalysis Communications* **2011**, *14*, 74.

(42) Weilhard, A.; Qadir, M. I.; Sans, V.; Dupont, J. *ACS Catalysis* **2018**.

(43) Qadir, M. I.; Weilhard, A.; Fernandes, J. A.; de Pedro, I.; Vieira, B. J. C.; Waerenborgh, J. C.; Dupont, J. *ACS Catalysis* **2018**, *8*, 1621.

(44) Weilhard, A.; Qadir, M. I.; Sans, V.; Dupont, J. *ACS Catalysis* **2018**, *8*, 1628.

(45) Peris, E. *Chemical Reviews* **2018**, *118*, 9988.

(46) Friedrich, A.; Drees, M.; Käss, M.; Herdtweck, E.; Schneider, S. *Inorganic Chemistry* **2010**, *49*, 5482.

(47) Dupont, J.; Weilhard, A.; Abarca, G. A.; Viscardi, J.; Prechtl, M. H. G.; Scolten, J. D.; Bernardi, F.; Baptista, D. L. *ChemCatChem* **2016**, n/a.

(48) Dyson, P. J. *Dalton Transactions* **2003**, 2964.

(49) Martínez-Prieto, L. M.; Chaudret, B. *Accounts of Chemical Research* **2018**, *51*, 376.

(50) Chacón, G.; Dupont, J. *ChemCatChem* **2019**, *11*, 333.

(51) Spentzos, A. Z.; Barnes, C. L.; Bernskoetter, W. H. *Inorganic Chemistry* **2016**, *55*, 8225.

(52) Bernskoetter, W. H.; Hazari, N. *Accounts of Chemical Research* **2017**, *50*, 1049.

(53) Heimann, J. E.; Bernskoetter, W. H.; Hazari, N.; Mayer, James M. *Chemical Science* **2018**, *9*, 6629.

(54) Kobayashi, S. *European Journal of Organic Chemistry* **1999**, *1999*, 15.

(55) Huff, C. A.; Sanford, M. S. *Journal of the American Chemical Society* **2011**, *133*, 18122.

(56) Thenert, K.; Beydoun, K.; Wiesenthal, J.; Leitner, W.; Klankermayer, J. *Angewandte Chemie International Edition* **2016**, *55*, 12266.

(57) Schieweck, B. G.; Klankermayer, J. *Angewandte Chemie International Edition* **2017**, *56*, 10854.

(58) Schmeier, T. J.; Dobereiner, G. E.; Crabtree, R. H.; Hazari, N. *Journal of the American Chemical Society* **2011**, *133*, 9274.

(59) Filonenko, G. A.; Cosimi, E.; Lefort, L.; Conley, M. P.; Copéret, C.; Lutz, M.; Hensen, E. J. M.; Pidko, E. A. *ACS Catalysis* **2014**, *4*, 2667.

7.3. Results and Discussion

The silver transmetallation route was chosen as the synthetic strategy to form the aforementioned catalyst. Reaction monitoring can be undertaken by the ^{1}H-NMR and ^{13}C-NMR analysis. In the ^{1}H-NMR the C_2-H at 12 ppm disappears and a new peak in the ^{13}C NMR spectrum at 181 ppm is formed, indicating the carbene formation. The resulting pale yellow complex (**1**) was characterised by ESI-ms, ATR-IR, ICP-OES and the structural arrangement was determined by single crystal XRD analysis. It is important to note that **1** was obtained as a mixture, i.e. scrambling of the counter anion was observed, and thus a bromide to chloride ratio of 30:70 was used to calculate a molar mass of 578.11 g /mol. This molar mass was used to determine the amount of catalyst in solution. It is also important to note that poisoning experiments with NaBr or NaCl did not show any effect, indicating the minor role of the halides. For more information see publication IV.

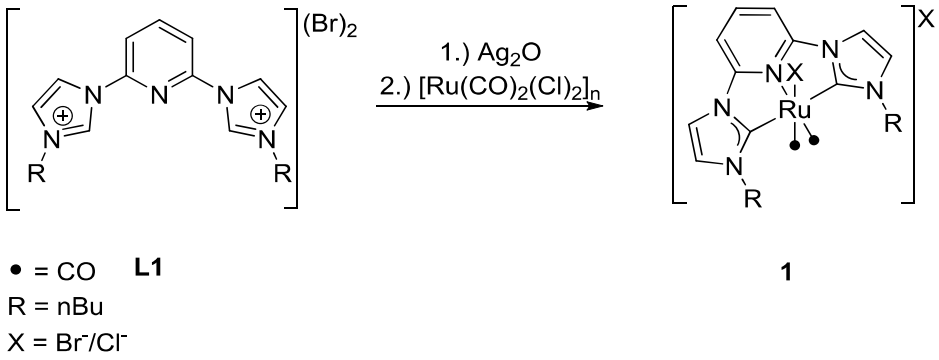


Figure 7.3. Depiction of the synthetic strategy for the CNC-pincer complex synthesised

An initial catalytic screening showed that **1** achieves a FA concentration of 0.5 M in DMSO:H_2O (5 v/v% H_2O) at 80°C under 60 bar pressure ($P(CO_2) = P(H_2)$ = 30 bar) in presence of 0.55 M 1-butyl-2,3-dimethylimidazolium acetate

(BMMI.OAc). It is important to note that **1** does not show catalytic activity in the absence of IL. Furthermore, with the thermodynamic parameter found in ***section 4.***, it can be predicted that the same concentration should be achievable at 120°C, see ***section 4***. However, upon increasing the reaction temperature to 100°C decomposition of DMSO was observed. Consequently, the solvent system was switched to 1,4-dioxane:H_2O (5 v/v% H_2O), keeping the other parameters constant.

Table 7.1 Temperature and $Sc(OTf)_3$ dependant results obtained with catalyst **1**.

Entry	$P(H_2):P(CO_2)$ / bar:bar	$Sc(OTf)_3$ / mmol	T / °C	[FA] / M	TON[a)]	TOF[b)] / h^{-1}
1	30:30	-	120	0.49	162900	4360
2	30:30	-	100	0.22	77550	1080
3	30:30	-	110	0.29	100600	1750
4	30:30	-	130	0.40	14100	10620
5	30:30	-	140	0.29	100860	16500
6	30:30	0.10	120	0.32	114400	21200
7	45:15	0.10	120	0.36	126000	22000
8[c]	45:15	0.10	120	0.26[d)]	833800[d)]	20600[e)]

Reaction conditions: 6 mL Dioxane;water (5 v/v% water), 3.3 mmol BMMI.OAc, 0.017 µmol catalyst a) determined after 72 h, b) determined after 4h; c) 0.0017 µmol catalyst; d) determined after 5d; e) determined after 24h.

Here the optimal performance was found at 120°C. Below 120°C the TOF decreased significantly whilst above 120°C the reaction is limited by the thermodynamic properties of the system, resulting in lower concentrations of

FA, compare **table 7.1**, **entry 1-5**. At 120°C a TOF of 4360 h^{-1} with a final concentration of FA of 0.49M was achieved, see **table 7.1**, **entry 1**.

Upon investigating the turnover limiting step (TLS), it was found that the rate is limited by the CO_2 insertion, see **publication IV figure 4b**. Consequently, the addition of lewis acids (here $Sc(OTf)_3$ was used) enhanced the rate of the reaction by stabilising charge intermediates (**1-Int**) and transition states formed during the insertion of CO_2 into the metal hydride bond (see **figure 67**). Furthermore, this hints toward a predominantly outer sphere mechanism.[9-10] Indeed, the TOF can be increased to >21,000 h^{-1} (compare **table 7.1**, **entry 1** & **6**). At very low catalyst concentrations the achieved TON was 833800 after 5d representing the highest catalytic activity and durability ever achieved under comparatively mildly basic conditions.[13-17]

In order to test the catalytic inactivity of the Sc^{3+} additive in the studied transformation[11-12] a reaction in the absence of **1** under elsewise identical reaction conditions (3.3 mmol BMMI.OAc, 0.1 mmol $Sc(OTF)_3$ $P(H_2) = P(CO_2)$ = 30 bar, T = 120°C and 6 mL Dioxane:H_2O) was conducted, which showed no activity towards the formation of FA.

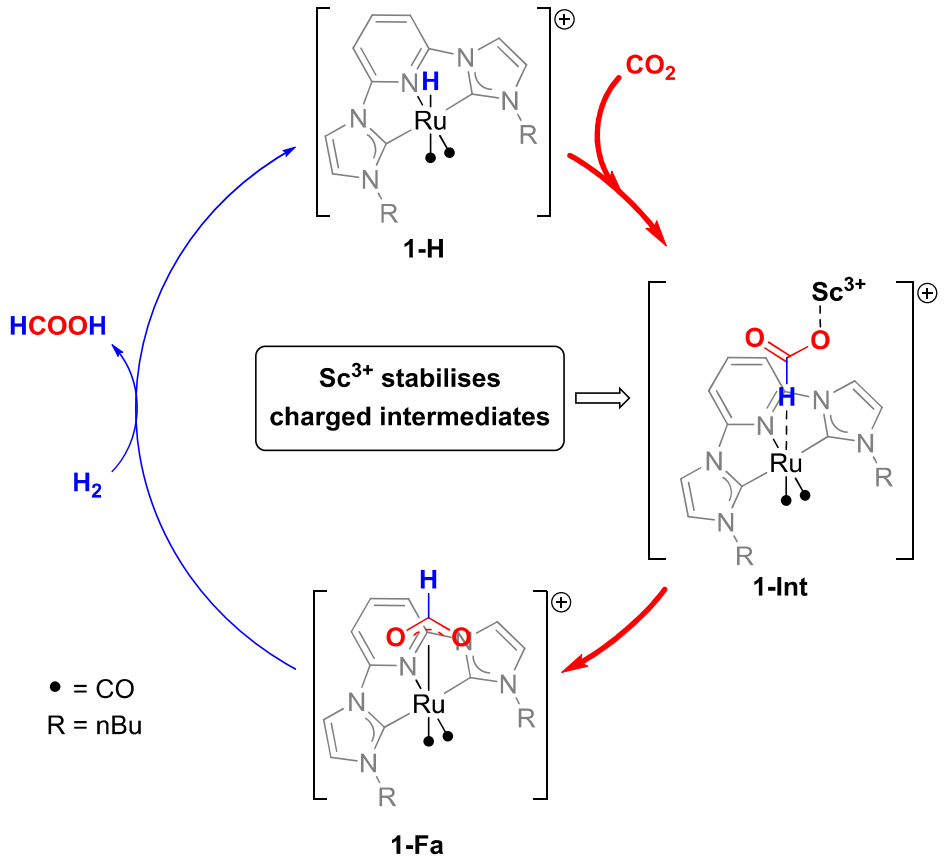


Figure 7.4 Graphical depiction of Sc^{3+} stabilising charge intermediates during the CO2 insertion, which represents the TLS in a hypothetical mechanism

Furthermore, in the absence of $Sc(OTf)_3$ an activation energy of 93 kJ mol^{-1} ± 6.7 kJ mol^{-1} was determined. This value falls into a similar range as already with catalyst **2** in ***section 6***. For a more detailed discussion the reader is referred to publication IV.

7.4. Concluding remarks about Ru-CNC pincer complexes in the hydrogenation of CO_2 to formic acid

The catalyst developed here (**1**) showed a *ca.* 50 times better performance in terms of catalytic durability and 22 times better catalytic activity (TOF) than the

best reported catalyst in the literature to date.[13] Interestingly the pincer complex developed in this part displayed similar properties to the catalyst **2** utilized for the CO_2 hydrogenation to FA in ***section 6.*** For instance both catalysts achieved similar concentrations of FA, the turnover limiting step was determined to be the CO_2 insertion step, which proceeds most likely in an outer sphere fashion and both have similar activation energies, i.e. with **1** 93 kJ mol^{-1} ± 6.7 kJ mol^{-1} and with **2** 96 kJ mol^{-1} ± 3.1 kJ mol^{-1} in THF. However, the pincer catalyst displayed a significantly increased catalyst durability compared to **2**.

7.5. Publicaiton IV Supporting Information: Highly efficient base-free synthesis of formic acid from carbon dioxide

Contribution of the author: In this publication the author designed the idea for the catalyst, planned the research in liaison with the PhD supervisors, and synthesized all complexes and ionic liquids undertook all the experiments, analysed and interpreted the data and wrote the manuscript in collaboration with all co-authors.

Reprinted with permission from www.chemrxiv.org/s/766685b107d9bca8418a

Supporting information

Andreas Weilhard,[a] Stephen Argent,[b] Victor Sans,[a,c]

[a] Faculty of Engineering, University of Nottingham, Nottingham, NG7 2RD, U.K

[b] School of Chemistry, University of Nottingham, Nottingham, NG7 2RD, U.K

[c] Institute of Advanced Materials (INAM), Universitat Jaume I, Castellon, 12071, Spain

Supporting information

Contents

GENERAL INFORMATION 300

SYNTHESIS OF 2,6-BIS(1-BUTYLIMIDAZOLIUM)PYRIDINE DIBROMIDE 300

SYNTHESIS OF RU-CNC PINCER 300

ICP-OES MEASUREMENT 304

PREPARATION OF STOCK SOLUTIONS 304

CL^-/BR^- POISONING EXPERIMENTS 305

INITIAL SCREENING 305

GENERAL PROCEDURE FOR THE HYDROGENATION OF CO_2 306

SCREENING OF THE EFFECT OF WATER ONTO THE HYDROGENATION OF CO_2 307

NANOPARTICLE FORMATION 307

Benzene test 307

DLS and TEM test 308

SCREENING OF THE EFFECT OF $SC(OTF)_3$ ONTO THE HYDROGENATION OF CO_2 308

DIALKOXYMETHANE ETHER ..... ERROR! BOOKMARK NOT DEFINED.

CRYSTAL STRUCTURE DETERMINATION OF 1 309

REFERENCES 318

General information

The ionic liquids 1,2-dimethyl-3-butylimidazolium acetate (BMMI.OAc) were prepared from literature methods.[1] $[Ru(Cl)_2(CO)_2]_n$ complex was synthesized according to a reported method.[2] 1,2-dimethylimidazole was purchased from IOLITEC while *n*-chlorbutane, dimethylsulfoxide, $Sc(OTf)_3$ and deuterated dimethylsulfoxide were obtained from Sigma Aldrich. Dioxane and ethylene glycol was provided by VWR. $RuCl_3 \cdot xH_2O$ was provided by Precious Metals Online. All the ILs were placed under vacuum at 50 °C for 2-3 h prior to use. NMR measurements were performed on a 400 MHz Bruker or 500 MHz Bruker with d1 = 50s and ESI-MS analysis was performed on a Bruker microTOFII.

Synthesis of 2,6-bis(1-butylimidazolium)pyridine dibromide

2,6-bis(1-butylimidazolium)pyridine dibromide was prepared according to a previously reported method.[3] 3.36 g (27 mmol, 2 eq) 1-butylimidazole and 3.2 g (13.5 mmol, 1 eq) 2,6-dibromopyridine are stirred at 150°C for 72h under argon. After cooling the reaction mixture to room temperature, the reaction mixture was dissolved in $CHCl_3$ and precipitated with Et_2O. The desired product is isolated as a white solid after repetitive precipitation from MeOH with Et_2O.

Yield: 4.1 g (8.37 mmol, 62%)

^{1}H-NMR and ^{13}C spectra match previously reported results.[3]

Synthesis of Ru-CNC pincer

In the dark under argon:

700 mg (1.55 mmol, 1 eq) 2,6-bis(1-butylimidazolium)pyridine dibromide and 400 mg (1.73 mmol, 1.12 eq) Ag_2O are dissolved in 10 mL dry and degassed DCM. The reaction mixture is stirred in the dark under an argon atmosphere for 24 h. Afterwards the solution is filtered through a celite pad, the solvent is removed in vacuum. The resulting white solid is washed with 3x15 mL Et_2O. The resulting white solid is directly used for the next step.

908 mg of the white precipitate obtained in the previous step and 300 mg (1.30 mmol, 1 eq) $[Ru(CO)_2(Cl)_2]$ are dissolved in 20 mL THF and stirred under argon in the dark for 48h at 55°C. The resulting reaction mixture is cooled to room temperature and filtered through a short celite pad and reduced under vacuum. The resulting yellow solid is re-dissolved in 5 mL MeOH and filtered. The product is obtained upon precipitation with Et_2O and finally washed with MeCN. Crystals are obtained by slow diffusion of Et_2O into MeOH.

Yield: 350 mg (0.61 mmol, 47%)

Sum Formula $C_{21}H_{25}Br_{0.6}Cl_{1.4}N_5O_2Ru$

^{1}H-NMR (DMSO-d6, 400 Mhz): δ 8.67 ppm (d, ^{3}J = 2.24 Hz, 2H), 8.62 ppm (t, ^{3}J = 8.2 Hz, 1H), 8.18 ppm (d, 3J = 8.24 Hz, 2H), 7.91 ppm (2 H, ^{3}J = 2.20 Hz, 2H), 4.52-5.13 ppm (m, 4H), 1.89 ppm (p, ^{3}J = 7.4 hz, 4H), 1.58-1.22 ppm (m, 4H), 0.95 ppm (t, ^{3}J = 7.4 Hz , 6H).

^{13}C-NMR (DMSO-d6, 126 MHz): δ 181 ppm, 151 ppm, 125 ppm, 120 ppm, 119 ppm, 109 ppm, 52 ppm, 33 ppm, 20 ppm, 14 ppm.

ESI-ms: 592 mz

ATR-IR: υ [cm^{-1}]: 3200 (C-H_{arom}), 3000 (C-H_{Im}), 2900 (C-H_{al}), 2051 (C=O), 1993 (C=O)

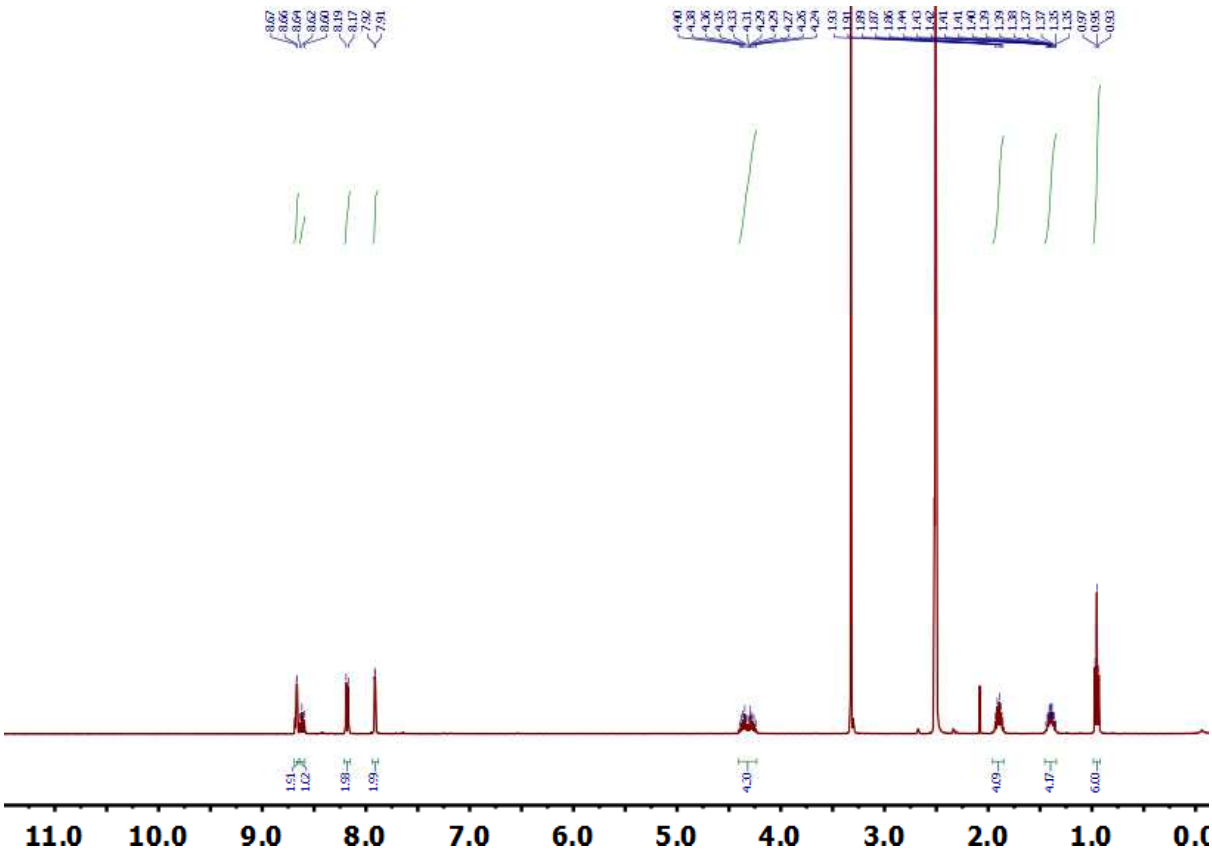


Figure S7 ^{1}H NMR spectrum of **1** in DMSO-d6.

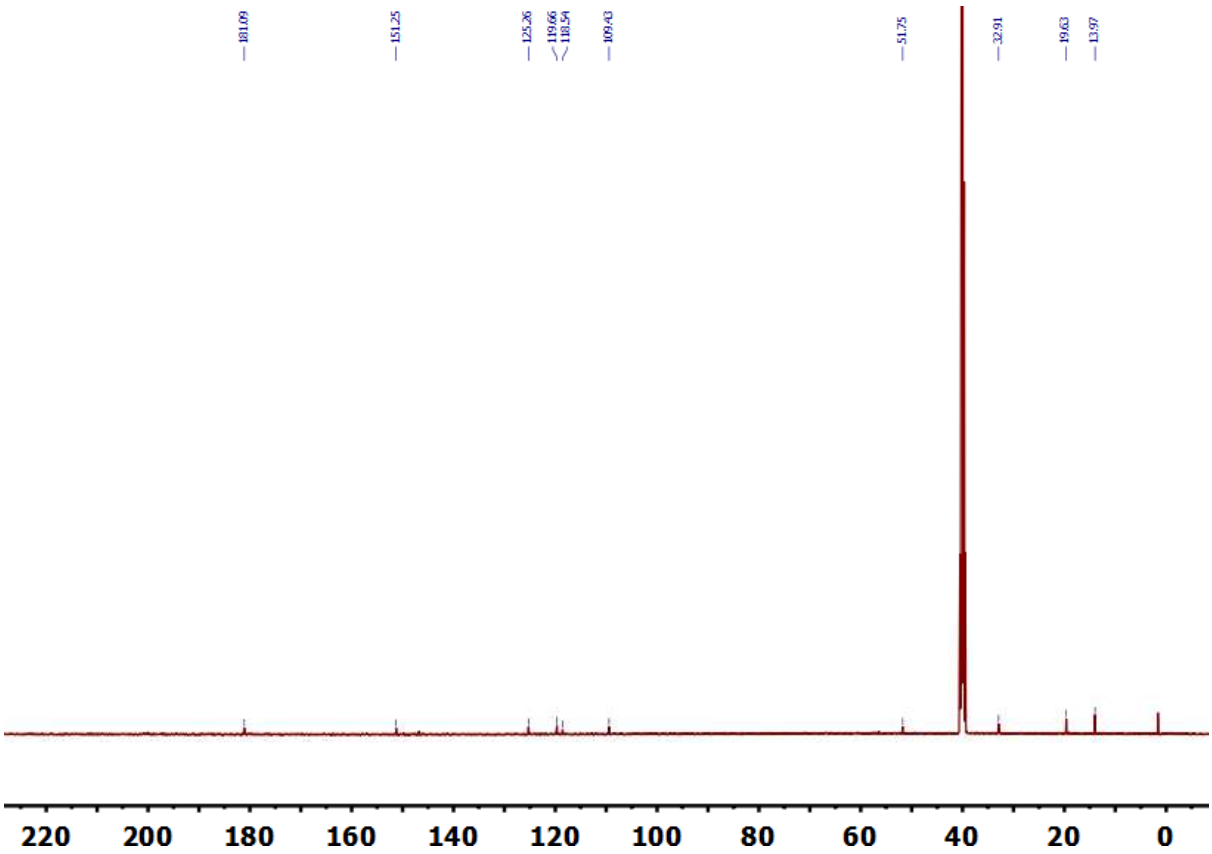


Figure S8 13C NMR of **1** in DMSO-d6.

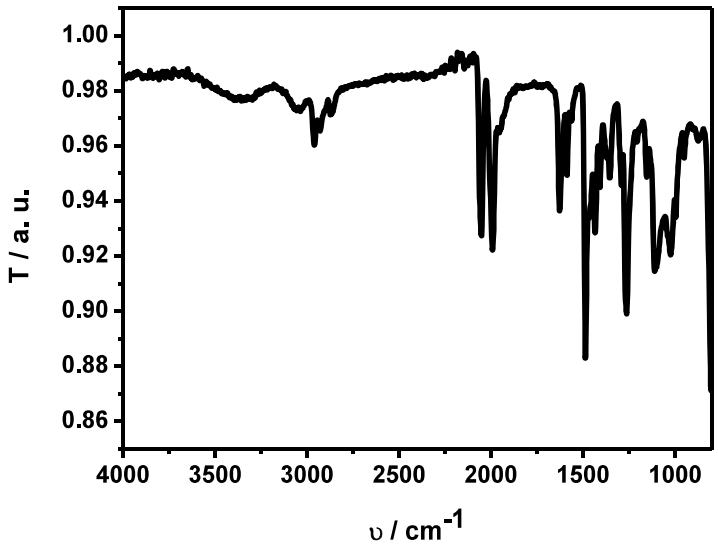


Figure S9 ATR-Ir of complex **1**.

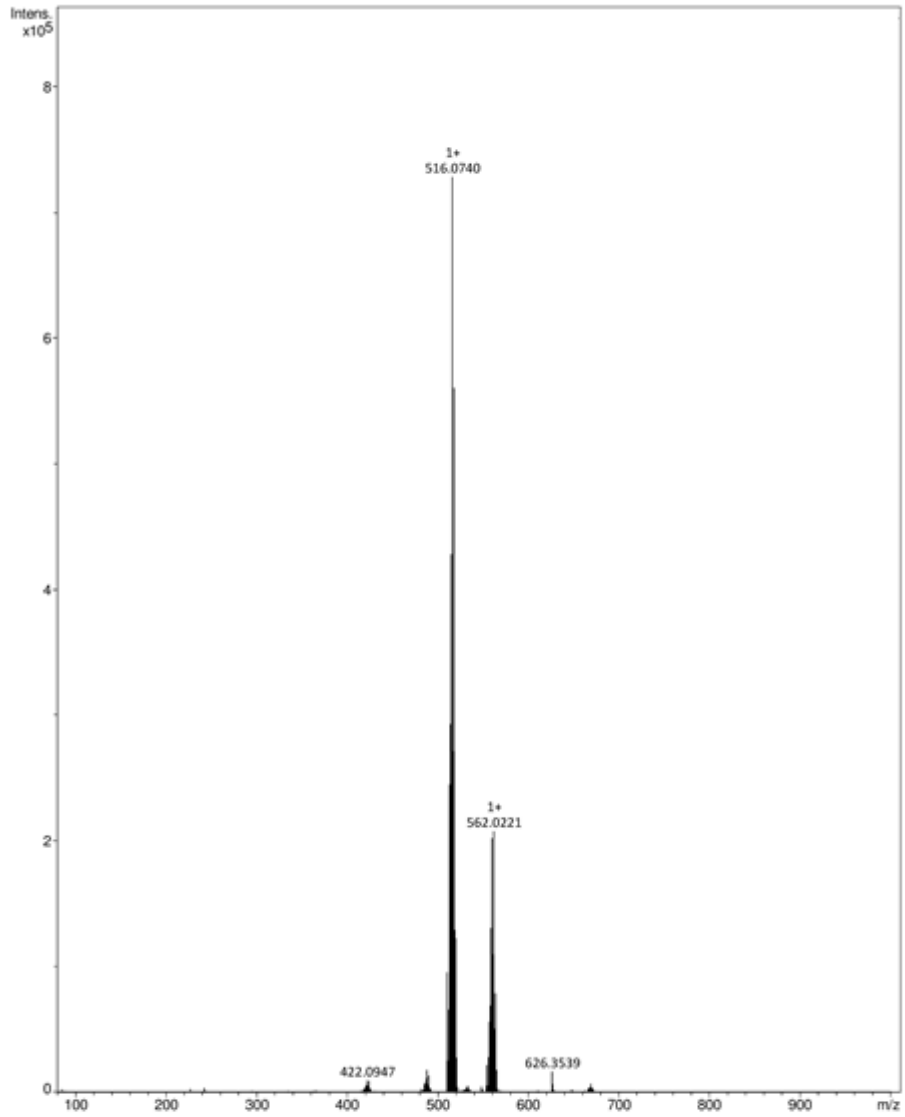


Figure S10 ESI-ms of **1**.

ICP-OES measurement

1.15 mg (1.85 µmol) of **1** are dissolved in 10 mL of 2 v/v% HCl solution and the Ru content is measured on a … ICP-OES. Expected concentration of Ru was 18,6 mg L^{-1}. Xxx mg L^{-1} was found confirming the expected sumformular.

Preparation of Stock solutions

For the calculation of the amount of catalyst the average mass obtained by the crystal structure was used (622.23 g/mol). 1 mg (1.7 µmol) of **1** is dissolved in

10 mL of the desired solvent system, giving a 0.17 mM catalyst stock solution. 1 mL of this solution (0.17 mM) is taken and diluted with 9 mL of the same solvent system to give a 0.017 mM solution. 1 mL of this solution (0.016 mM) is taken and diluted with 9 mL of the same solvent system to give a 0.0016 mM solution.

Cl^-/Br^- poisoning experiments

1 mg (1.7 µmol, 1 eq) **1** and 12 mg (116.6 µmol, 73 eq) NaBr, respectively 7 mg (116.6 µmol, 73 eq) NaCl, are mixed in 1 mL DMSO:H_2O (5 v/v% H_2O) and stirred for 24h. Afterwards, 5 mL DMSO:H_2O (5 v/v% H_2O) are added, the solution transferred together with 700 mg (3.3 mmol) BMMI.OAc to a Parr-reactor. Then the reactor is flushed with CO_2 to remove residual air contamination, pressurized with 30 bar CO_2 and filled with H_2 to 60 bar. The reactor was heated to 80°C using a heating mantle under hard stirring. After 4h (72h) the reactor was cooled down to room temperature and carefully vented. The reaction mixture was analysed directly by ^{1}H NMR spectroscopy in DMSO-d_6 to determine the amount of formic acid formed, using BMMI.OAc as an internal standard.

Table S1 catalyst comparison and poisoning experiments

Entry	Catalyst	Additive (mmol)	[FA]$^{a)}$ / M	TON$^{a)}$	TOF$^{b)}$ / h^{-1}
1	1	-	0.50	1763	58
2	1	NaCl (0.12 mmol)	0.50	1763	63
3	1	NaBr (0.12 mmol)	0.50	1763	56

Reaction conditions 1.6 µmol catalyst, 3.3 mmol BMMI.OAc, P(H_2) = P(CO_2) = 30 bar, 6 ml DMSO:H_2O (5 v/v% H_2O), T = 80°C, a) determined after 72h, b) determined after 4h.

Initial screening

1 mg (1.7 µmol, 1 eq) **1** is dissolved in 6 mL DMSO:H_2O (5 v/v% H_2O)/ 6 mL 1,4-dioxane:H_2O (5 v/v% H_2O). Then 700 mg (3.3 mmol) BMMI.OAc is added and the reaction mixture is transferred to a Parr-reactor. Then the reactor is flushed with CO_2 to remove residual air contamination, pressurized with 30 bar

CO_2 and filled with H_2 to 60 bar. The reactor was heated to the desired temperature using a heating mantle under hard stirring. After 4h (72h) the reactor was cooled down to room temperature and carefully vented. The reaction mixture was analysed directly by ^{1}H NMR spectroscopy in DMSO-d_6 to determine the amount of formic acid formed, using BMMI.OAc as an internal standard.

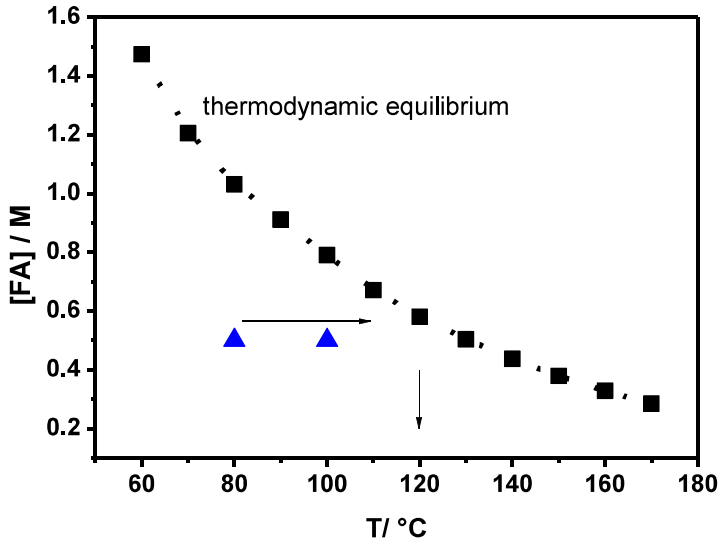


Figure S11 Curve for predicting optimal catalyst performance, showing the thermodynamic equilibrium for the applied reaction conditions (black) and results from the initial screening (blue).[4]

General procedure for the hydrogenation of CO_2

From a stock solution containing the catalyst (0.17 mM, 0.017 mM or 0.0017 mM) 1 mL is added to 700 mg (3.3 mmol) BMMI.OAc and then loaded into a Parr reactor (50 mL). Then 6 mL of Dioxane:water (5 v/v% water) from a stock solution was introduced into the reactor. The reactor was flushed with CO_2 gas in order to remove air. Afterwards, the reactor was filled with the desired amount of CO_2 and filled with H_2 gas, till the desired total pressure was reached at room temperature. The reactor was heated to the desired reaction temperature using a heating mantle under hard stirring. After the desired reaction time the reactor was cooled down to room temperature and carefully vented. The reaction mixture was analysed directly by ^{1}H NMR spectroscopy in DMSO-d_6 to determine the amount of formic acid formed, using BMMI.OAc as an internal standard.

Screening of the effect of water onto the hydrogenation of CO_2

From a stock solution containing the catalyst (0.017 mM) 1 mL is added to 700 mg (3.3 mmol) BMMI.OAc and then loaded into a Parr reactor (50 mL). Then 6 mL of Dioxane:water with varying amounts of water from a stock solution was introduced into the reactor. The reactor was flushed with CO_2 gas in order to remove air. Afterwards, the reactor was filled with the desired amount of CO_2 and filled with H_2 gas, till the desired total pressure was reached at room temperature. The reaction was conducted at 120°C using a heating mantle under hard stirring. After the desired reaction time the reactor was cooled down to room temperature and carefully vented. The reaction mixture was analysed directly by ^{1}H NMR spectroscopy in DMSO-d_6 to determine the amount of formic acid formed, using BMMI.OAc as an internal standard.

Table S2 Effect of water content onto the hydrogenation of CO_2 to FA.

Entry	Cat. amount/ µmol	T / °C	Water content / %	t / h	Conc. FA[a] / M	TON[a]	TOF[b] / h^{-1}
1	0.016	120	5	4	0.05	17500	4360
2	0.016	120	20	4	0.05	16600	4150
3	0.016	120	50	4	0.02	5800	1460
4	0.016	120	80	4	0.01	2000	500
5	0.016	120	30	4	0.03	11600	2900
6	0.016	120	5	72	0.46	162900	2260
7	0.016	120	20	72	0.36	127900	1780

Reaction conditions catalyst 0.017 µmol, 3.3 mmol BMMI.OAc, 6 mL solvent; a) determined after 72h, b) determined after 4h.

Nanoparticle formation

Benzene test

1 mg (1.6 µmol) of **1** is added to 700 mg (3.3 mmol) BMMI.OAc and then loaded into a Parr reactor (50 mL). Then 6 mL of Dioxane: H_2O (5 v/v% H_2O) and 1 mL benzene with were introduced into the reactor. The reactor was flushed with H_2 gas in order to remove air. Afterwards, the reactor was filled

with 50 bar H_2. The reaction was conducted at 120°C using a heating mantle under hard stirring. After 24h the reactor was cooled down to room temperature and carefully vented. The reaction mixture was analysed directly by ^{1}H NMR spectroscopy in DMSO-d_6 to determine the amount of formic acid formed, using BMMI.OAc as an internal standard.

DLS and TEM test

1 mg (1.6 µmol) of **1** is added to 700 mg (3.3 mmol) BMMI.OAc and then loaded into a Parr reactor (50 mL). Then 6 mL of Dioxane: H_2O (5 v/v% H_2O) was introduced into the reactor. The reactor was flushed with H_2 gas in order to remove air. Afterwards, the reactor was filled with 45 bar H_2 and 15 bar CO_2. The reaction was conducted at 140°C using a heating mantle under hard stirring. After 24h the reactor was cooled down to room temperature and carefully vented. The reaction mixture was analysed directly by ^{1}H NMR spectroscopy in DMSO-d_6 to determine the amount of formic acid formed, using BMMI.OAc as an internal standard. The reaction solution was screened for nanoparticles by Dynamic light scattering and TEM analysis. None of those experiments displayed nanoparticles under the investigated reaction conditions

Screening of the effect of $Sc(OTf)_3$ onto the hydrogenation of CO_2

From a stock solution containing the catalyst (0.016 mM) 1 mL is added to 700 mg (3.3 mmol) BMMI.OAc and then loaded into a Parr reactor (50 mL). Then 6 mL of Dioxane:water (5 v/v% water) from a stock solution was introduced into the reactor. Then the desired amount of $Sc(OTf)_3$ was added into the reactor. The reactor was flushed with CO_2 gas in order to remove air. Afterwards, the reactor was filled with the desired amount of CO_2 and filled with H_2 gas, till the desired total pressure was reached at room temperature. The reaction was conducted at 120°C using a heating mantle under hard stirring. After the desired reaction time the reactor was cooled down to room temperature and carefully vented. The reaction mixture was analysed directly

by ^{1}H NMR spectroscopy in DMSO-d_6 to determine the amount of formic acid formed, using BMMI.OAc as an internal standard.

Crystal structure determination of 1

Single crystals suitable for X-ray analysis were obtained by slow diffusion of toluene into methanol. This afforded pale yellow crystals suitable for structure determination. Crystals of **1** were mounted on MicroMounts (MiTeGen) using YR-1800 perfluoropolyether oil and cooled rapidly to 90 K / 120 K in a stream of cold nitrogen using an Oxford Cryosystems low-temperature device.[5] Data for compounds **1** were collected on an Oxford Diffraction SuperNova diffractometer equipped with a mirror-monochromated Cu Kα source (λ = 1.5418 Å). Gaussian grid face-indexed absorption corrections with a beam profile correction were applied in CrysAlisPro.[6] Data for compound **1** were collected on a Bruker SMART APEX diffractometer, equipped with a graphite-monochromated Mo Kα source (λ = 0.71073 Å). Absorption corrections were applied using multiscan methods implemented in SADABS.[7] Structure **1** was solved via olex2.solve.[8] All structures were refined by full matrix least-squares using SHELXL-2014.[9]

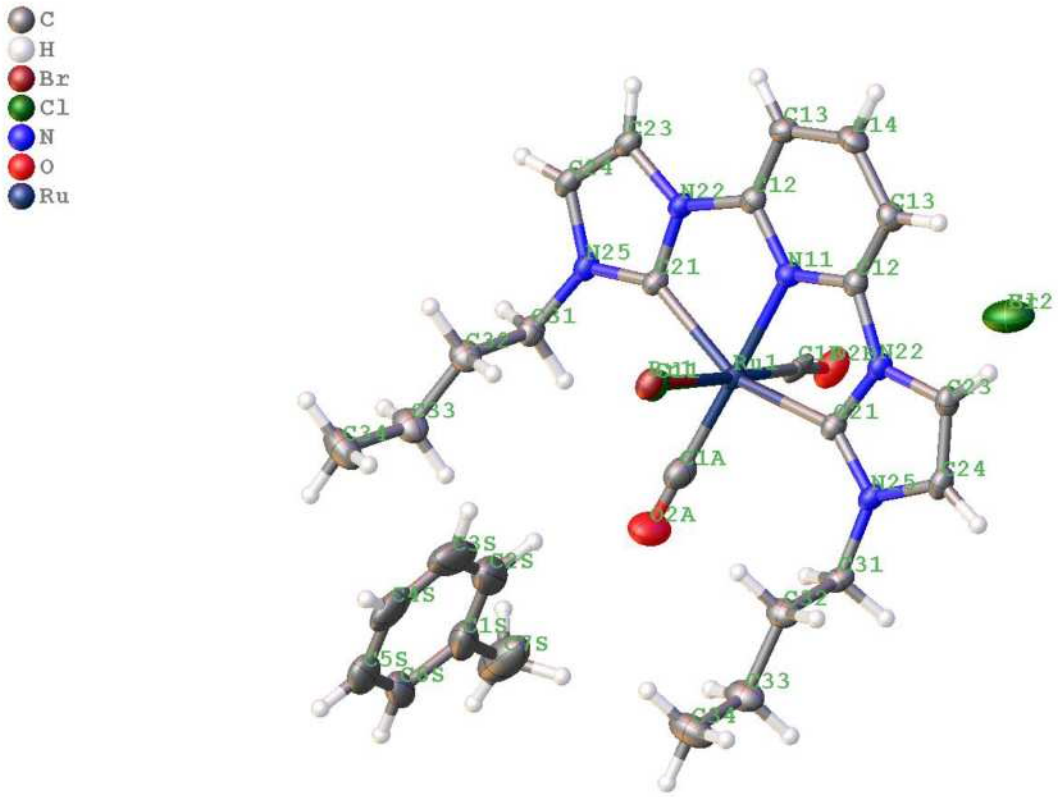


Figure S12 Crystal structure of **1**.

We observe that **1** crystallises with toluene. Structurally, the NHC **1** wingtips display identical bond lengths (2.075 Å), and the bonds in the NHC moiety are identical. Furthermore, **1** displays a symmetrical plane along the N11-Ru-C1A-O2A axis. The N11-Ru bond lengths is 2.011 Å long, which is identical to previously reported Ru-N(pyr) bond lengths in CNC-pincer complexes.[10] A significant trans-effect can be observed, i.e. the Ru-C1A (1.895 Å) bond is significantly shorter as the corresponding Ru-C1B (1.937 Å) bond lengths and the C1B-O1B (1.087 Å) bond is significantly shorter than the C1A-O1A (1.110 Å) bond length. Note that the Ru-C1A bond length is identical to Ru-CO bond lengths in similar Ru-CNC pincer complexes.[10] A Ru-Br1 bond length of 2.636 Å is found whilst the Ru-Cl1 bond length is comparatively compressed to 2.410 Å. Most bond angles display almost identical angles (90°). Exceptions are the NHC wingtips. Here compression of the C21-Ru-N11 (76°) bond and consequently stretching of the C21-Ru-C1A (103°) can be found. In general the structural arrangements are similar as already described for other complexes.[10]

Table S3 Crystal data and structure refinement for **1.**

Identification code	**1**
Empirical formula	$C_{24.5}H_{29}Br_{0.63}Cl_{1.29}N_5O_2Ru$
Formula weight	622.38
Temperature/K	120(2)
Crystal system	monoclinic
Space group	C2/m
a/Å	8.9075(3)
b/Å	13.6660(4)
c/Å	22.4967(7)
α/°	90
β/°	97.948(3)
γ/°	90
Volume/Å^3	2712.21(15)
Z	4
ρ_{calc}g/cm^3	1.524
μ/mm^{-1}	7.172
F(000)	1259.0
Crystal size/mm^3	0.397 × 0.194 × 0.071
Radiation	CuKα (λ = 1.54184)
2Θ range for data collection/°	7.936 to 149.108
Index ranges	$-10 \leq h \leq 10$, $-16 \leq k \leq 16$, $-21 \leq l \leq 27$
Reflections collected	10836
Independent reflections	2843 [R_{int} = 0.0387, R_{sigma} = 0.0241]
Data/restraints/parameters	2843/236/226
Goodness-of-fit on F^2	1.097
Final R indexes [I>=2σ (I)]	R_1 = 0.0338, wR_2 = 0.0840
Final R indexes [all data]	R_1 = 0.0340, wR_2 = 0.0841
Largest diff. peak/hole / e Å^{-3}	1.64/-0.95

Table S4 Fractional Atomic Coordinates ($\times 10^4$) and Equivalent Isotropic Displacement Parameters ($Å^2 \times 10^3$) for RUASWB. U_{eq} is defined as 1/3 of of the trace of the orthogonalised U_{IJ} tensor

Atom	*x*	*y*	*z*	U(eq)
Ru1	3063.9(3)	5000	2037.6(2)	19.13(11)
Cl1	5400(6)	5000	2721(4)	23.4(7)
O2A	1219(5)	5000	3059.7(17)	48.4(9)
O2B	124(4)	5000	1188.1(16)	37.3(7)
N22	4304(2)	3350.7(16)	1457.8(10)	19.5(4)
N25	3082(2)	2635.2(17)	2088.9(10)	20.1(5)
N11	4405(3)	5000	1364.2(14)	19.8(6)
C12	4882(3)	4151.1(19)	1165.4(11)	19.7(5)
C1B	1217(4)	5000	1471(2)	23.4(8)
C13	5881(3)	4112(2)	748.5(12)	23.4(5)
C14	6375(5)	5000	544.9(17)	26.1(8)
C21	3419(3)	3521.4(19)	1899.5(11)	19.2(5)
C23	4489(3)	2353(2)	1369.7(12)	22.1(5)
C24	3729(3)	1911(2)	1769.1(12)	23.4(5)
C31	2293(3)	2450(2)	2608.2(12)	22.6(5)
C1A	1912(5)	5000	2686(2)	32.0(9)
C32	3405(3)	2364(2)	3182.5(12)	27.1(6)
C33	2605(3)	2226(3)	3730.7(13)	32.9(7)
C34	3720(4)	2109(3)	4303.1(14)	45.5(9)
Br2	1686.0(13)	3328.7(10)	273.8(6)	50.3(5)
Cl2	1686.0(13)	3328.7(10)	273.8(6)	50.3(5)
C7S	2260(30)	4940(60)	4582(8)	89(9)
C1S	3910(20)	5010(40)	4860(5)	61(4)
C2S	5030(20)	5010(60)	4508(10)	74(6)
C3S	6510(30)	5090(60)	4757(10)	77(9)
C4S	6870(30)	5120(30)	5369(9)	63(8)
C5S	5750(20)	5130(30)	5723(7)	51(8)
C6S	4262(18)	5080(60)	5469(7)	45(7)
Br1	5648(16)	5000	2768(9)	23.4(7)

Table S5 Anisotropic Displacement Parameters ($Å^2 \times 10^3$) for 1. The Anisotropic displacement factor exponent takes the form: $-2\pi^2[h^2a^{*2}U_{11}+2hka^*b^*U_{12}+\ldots]$.

Atom	U_{11}	U_{22}	U_{33}	U_{23}	U_{13}	U_{12}
Ru1	19.53(16)	13.58(16)	25.85(17)	0	8.71(11)	0
Cl1	22(2)	18.5(4)	28.0(14)	0	-3.3(13)	0
O2A	57(2)	43(2)	53(2)	0	32.9(18)	0
O2B	33.6(15)	24.2(16)	51.8(19)	0	-2.4(13)	0
N22	21.1(10)	15.2(10)	22.3(10)	-0.7(8)	2.7(8)	0.8(9)
N25	19.2(10)	15.0(11)	25.7(11)	1.3(8)	1.6(8)	-1.1(8)
N11	19.0(15)	19.2(15)	21.8(15)	0	4.7(12)	0
C12	19.0(12)	18.9(13)	20.3(12)	-0.8(10)	-0.1(9)	0.4(10)
C1B	19.3(15)	7.9(16)	45(2)	0	10.2(14)	0
C13	23.9(13)	23.8(14)	22.8(12)	-1.5(10)	4.5(10)	3.7(11)
C14	25.1(19)	33(2)	22.1(18)	0	9.0(15)	0
C21	17.0(11)	16.3(12)	24.1(12)	-0.5(10)	1.9(9)	0.5(10)
C23	24.8(12)	17.1(13)	23.5(12)	-3.3(10)	-0.4(10)	3.2(10)
C24	25.6(13)	14.3(12)	28.6(13)	-2.0(10)	-2.0(10)	1.3(10)
C31	19.0(11)	19.6(13)	29.5(13)	3.8(10)	4.5(10)	-2.3(10)
C1A	34(2)	21(2)	42(2)	0	9.5(18)	0
C32	19.6(12)	33.6(16)	28.6(13)	2.1(12)	4.5(10)	-1.3(12)
C33	24.0(13)	43.9(18)	31.7(15)	3.3(13)	7.1(11)	-0.7(13)
C34	38.0(17)	72(3)	26.9(15)	8.4(16)	5.7(13)	-0.3(18)
Br2	37.7(7)	59.1(9)	55.6(8)	20.1(6)	11.7(5)	-4.7(5)
Cl2	37.7(7)	59.1(9)	55.6(8)	20.1(6)	11.7(5)	-4.7(5)
C7S	123(13)	62(18)	74(11)	20(20)	-18(9)	-40(30)
C1S	111(11)	32(8)	39(6)	-8(17)	10(5)	-20(20)
C2S	140(14)	36(11)	52(8)	-10(20)	37(8)	-20(20)
C3S	128(13)	30(20)	87(10)	5(14)	54(9)	-13(19)
C4S	83(11)	20(20)	96(10)	-10(12)	32(8)	-13(13)
C5S	81(8)	20(20)	51(7)	-5(8)	13(5)	-1(9)
C6S	78(9)	27(19)	33(5)	-7(13)	18(5)	1(13)
Br1	22(2)	18.5(4)	28.0(14)	0	-3.3(13)	0

Table S6 Bond Lengths for **1**.

Atom	Atom	Length/Å	Atom	Atom	Length/Å
Ru1	Cl1	2.410(5)	N11	C12[1]	1.334(3)
Ru1	N11	2.055(3)	N11	C12	1.334(3)
Ru1	C1B	1.937(4)	C12	C13	1.380(4)
Ru1	C21[1]	2.075(3)	C13	C14	1.390(3)
Ru1	C21	2.075(3)	C23	C24	1.342(4)
Ru1	C1A	1.895(5)	C31	C32	1.520(4)
Ru1	Br1	2.636(13)	C32	C33	1.519(4)
O2A	C1A	1.110(6)	C33	C34	1.522(4)
O2B	C1B	1.087(5)	C7S	C1S	1.52(2)
N22	C12	1.410(3)	C1S	C2S	1.358(17)
N22	C21	1.371(3)	C1S	C6S	1.366(17)
N22	C23	1.390(3)	C2S	C3S	1.36(3)
N25	C21	1.332(3)	C3S	C4S	1.37(2)
N25	C24	1.394(3)	C4S	C5S	1.357(18)
N25	C31	1.467(3)	C5S	C6S	1.37(2)

Table S7 Bond Angles for **1**.

Atom	Atom	Atom	Angle/°	Atom	Atom	Atom	Angle/°
N11	Ru1	Cl1	86.1(2)	C12	N11	Ru1	119.45(16)
N11	Ru1	C21[1]	76.91(7)	C12[1]	N11	Ru1	119.45(16)
N11	Ru1	C21	76.91(7)	C12	N11	C12[1]	120.9(3)
N11	Ru1	Br1	85.0(5)	N11	C12	N22	111.4(2)
C1B	Ru1	Cl1	178.5(2)	N11	C12	C13	121.8(3)
C1B	Ru1	N11	92.43(15)	C13	C12	N22	126.8(2)
C1B	Ru1	C21[1]	91.98(7)	O2B	C1B	Ru1	174.8(4)
C1B	Ru1	C21	91.98(7)	C12	C13	C14	117.0(3)
C1B	Ru1	Br1	177.4(5)	C13[1]	C14	C13	121.6(4)
C21[1]	Ru1	Cl1	87.69(8)	N22	C21	Ru1	112.88(18)
C21	Ru1	Cl1	87.69(8)	N25	C21	Ru1	142.38(19)
C21[1]	Ru1	C21	153.66(14)	N25	C21	N22	104.7(2)
C21	Ru1	Br1	87.45(12)	C24	C23	N22	105.4(2)
C21[1]	Ru1	Br1	87.45(12)	C23	C24	N25	107.9(2)
C1A	Ru1	Cl1	91.2(3)	N25	C31	C32	111.3(2)
C1A	Ru1	N11	177.26(16)	O2A	C1A	Ru1	179.0(4)
C1A	Ru1	C1B	90.31(19)	C33	C32	C31	112.1(2)
C1A	Ru1	C21[1]	103.00(7)	C32	C33	C34	112.1(2)
C1A	Ru1	C21	103.00(7)	C2S	C1S	C7S	120.5(14)
C1A	Ru1	Br1	92.3(5)	C2S	C1S	C6S	119.9(19)
C21	N22	C12	119.3(2)	C6S	C1S	C7S	119.5(13)
C21	N22	C23	111.2(2)	C1S	C2S	C3S	120.5(19)
C23	N22	C12	129.5(2)	C2S	C3S	C4S	120(2)
C21	N25	C24	110.7(2)	C5S	C4S	C3S	120(2)
C21	N25	C31	124.5(2)	C4S	C5S	C6S	120.0(18)
C24	N25	C31	124.5(2)	C1S	C6S	C5S	119.8(15)

Table S8 Torsion Angles for **1**.

A	B	C	D	Angle/°	A	B	C	D	Angle/°
Ru1	N11	C12	N22	2.0(3)	C23	N22	C12	C13	-5.5(4)
Ru1	N11	C12	C13	-174.8(2)	C23	N22	C21	Ru1	-178.73(17)
N22	C12	C13	C14	-176.1(3)	C23	N22	C21	N25	1.0(3)
N22	C23	C24	N25	0.6(3)	C24	N25	C21	Ru1	179.0(2)
N25	C31	C32	C33	177.0(3)	C24	N25	C21	N22	-0.6(3)
N11	C12	C13	C14	0.2(4)	C24	N25	C31	C32	83.4(3)
C12	N22	C21	Ru1	1.3(3)	C31	N25	C21	Ru1	-7.6(4)
C12	N22	C21	N25	-179.0(2)	C31	N25	C21	N22	172.8(2)
C12	N22	C23	C24	179.0(2)	C31	N25	C24	C23	-173.4(2)
$C12^1$	N11	C12	N22	176.8(2)	C31	C32	C33	C34	178.3(3)
$C12^1$	N11	C12	C13	0.0(5)	C7S	C1S	C2S	C3S	179(3)
C12	C13	C14	$C13^1$	-0.4(6)	C7S	C1S	C6S	C5S	179(3)
C21	N22	C12	N11	-2.2(3)	C1S	C2S	C3S	C4S	3(5)
C21	N22	C12	C13	174.5(2)	C2S	C1S	C6S	C5S	-1(5)
C21	N22	C23	C24	-1.0(3)	C2S	C3S	C4S	C5S	-3(6)
C21	N25	C24	C23	0.0(3)	C3S	C4S	C5S	C6S	1(6)
C21	N25	C31	C32	-89.1(3)	C4S	C5S	C6S	C1S	1(6)
C23	N22	C12	N11	177.9(3)	C6S	C1S	C2S	C3S	-1(4)

Table S9 Hydrogen Atom Coordinates (Å×10^4) and Isotropic Displacement Parameters (Å^2×10^3) for **1**.

Atom	*x*	*y*	*z*	U(eq)
H13	6215.49	3505.7	607.07	28
H14	7068.31	5000.01	259.51	31
H23	5037.55	2049.86	1086.61	27
H24	3645.84	1224.44	1824.26	28
H31A	1702.18	1836.29	2542.86	27
H31B	1575.41	2990.65	2649.05	27
H32A	4087.69	1801.66	3148.17	33
H32B	4034.15	2963.24	3234.43	33
H33A	1951.09	1638.11	3673.36	39
H33B	1946.48	2798.05	3772.31	39
H34A	4338.94	1522.9	4272.31	68
H34B	3161.09	2043.64	4646.72	68
H34C	4379.52	2685.39	4358.79	68
H7SA	2032.31	5449.43	4277.55	134
H7SB	1602.59	5022.92	4894.74	134
H7SC	2065.56	4293.85	4393.84	134
H2S	4780.54	4958	4084.52	88
H3S	7285.4	5120.49	4507.47	93
H4S	7903.09	5143	5545.4	76
H5S	6005.52	5165.82	6147.18	61
H6S	3479.38	5087.12	5716.35	54

Atom	*Occupancy*	Atom	*Occupancy*	Atom	*Occupancy*
Cl1	0.830(4)	Br2	0.188(4)	Cl2	0.312(4)
C7S	0.25	H7SA	0.25	H7SB	0.25
H7SC	0.25	C1S	0.25	C2S	0.25
H2S	0.25	C3S	0.25	H3S	0.25
C4S	0.25	H4S	0.25	C5S	0.25
H5S	0.25	C6S	0.25	H6S	0.25
Br1	0.170(4)				

References

(1) Zanatta, M.; dos Santos, F. P.; Biehl, C.; Marin, G.; Ebeling, G.; Netz, P. A.; Dupont, J. *The Journal of Organic Chemistry* **2017**, *82*, 2622.

(2) Anderson, P. A.; Deacon, G. B.; Haarmann, K. H.; Keene, F. R.; Meyer, T. J.; Reitsma, D. A.; Skelton, B. W.; Strouse, G. F.; Thomas, N. C. *Inorganic Chemistry* **1995**, *34*, 6145.

(3) Loch, J. A.; Albrecht, M.; Peris, E.; Mata, J.; Faller, J. W.; Crabtree, R. H. *Organometallics* **2002**, *21*, 700.

(4) Weilhard, A.; Qadir, M. I.; Sans, V.; Dupont, J. *ACS Catalysis* **2018**, *8*, 1628.

(5) Cosier, J.; Glazer, A. M. *J. Appl. Crystallogr.* **1986**, *19*, 105−107.

(6) **2014**, *Agilent Technologies: Yarnton, UK*

(7) Sheldrick, G. M. *SADABS Program for Area Detector Absorption Correction;* **1996**, *University of Göttingen, Germany*.

(8) Dolomanov, O. V., Bourhis, L. J., Gildea, R. J, Howard, J. A. K. & Puschmann, H. *J. Appl. Crystallogr. 2009, 42, 339−341.*

2009, *42*, 339.

(9) Sheldrick, G. M. *Acta Crystallogr., Sect. A: Found. Crystallogr.* **2008**, *64*, 112.

(10) Poyatos, M.; Mata, J. A.; Falomir, E.; Crabtree, R. H.; Peris, E. *Organometallics* **2003**, *22*, 1110.

7.6. References

1. Filonenko, G. A.; Hensen, E. J. M.; Pidko, E. A., Mechanism of CO2 hydrogenation to formates by homogeneous Ru-PNP pincer catalyst: from a theoretical description to performance optimization. *Catalysis Science & Technology* **2014,** *4* (10), 3474-3485.
2. Dröge, T.; Glorius, F., The Measure of All Rings—N-Heterocyclic Carbenes. *Angewandte Chemie International Edition* **2010,** *49* (39), 6940-6952.
3. Andrew, R. E.; González-Sebastián, L.; Chaplin, A. B., NHC-based pincer ligands: carbenes with a bite. *Dalton Transactions* **2016,** *45* (4), 1299-1305.
4. Benhamou, L.; Chardon, E.; Lavigne, G.; Bellemin-Laponnaz, S.; César, V., Synthetic Routes to N-Heterocyclic Carbene Precursors. *Chemical Reviews* **2011,** *111* (4), 2705-2733.
5. Poyatos, M.; Mata, J. A.; Falomir, E.; Crabtree, R. H.; Peris, E., New Ruthenium(II) CNC-Pincer Bis(carbene) Complexes: Synthesis and Catalytic Activity. *Organometallics* **2003,** *22* (5), 1110-1114.
6. Ng, C. K.; Wu, J.; Hor, T. S. A.; Luo, H.-K., A binary catalyst system of a cationic Ru–CNC pincer complex with an alkali metal salt for selective hydroboration of carbon dioxide. *Chemical Communications* **2016,** *52* (79), 11842-11845.
7. Filonenko, G. A.; Cosimi, E.; Lefort, L.; Conley, M. P.; Copéret, C.; Lutz, M.; Hensen, E. J. M.; Pidko, E. A., Lutidine-Derived Ru-CNC Hydrogenation Pincer Catalysts with Versatile Coordination Properties. *ACS Catalysis* **2014,** *4* (8), 2667-2671.
8. Filonenko, G. A.; Smykowski, D.; Szyja, B. M.; Li, G.; Szczygieł, J.; Hensen, E. J. M.; Pidko, E. A., Catalytic Hydrogenation of CO2 to Formates by a Lutidine-Derived Ru–CNC Pincer Complex: Theoretical Insight into the Unrealized Potential. *ACS Catalysis* **2015,** *5* (2), 1145-1154.
9. Bernskoetter, W. H.; Hazari, N., Reversible Hydrogenation of Carbon Dioxide to Formic Acid and Methanol: Lewis Acid Enhancement of Base Metal Catalysts. *Accounts of Chemical Research* **2017,** *50* (4), 1049-1058.
10. Heimann, J. E.; Bernskoetter, W. H.; Hazari, N.; Mayer, James M., Acceleration of CO2 insertion into metal hydrides: ligand, Lewis acid, and solvent effects on reaction kinetics. *Chemical Science* **2018,** *9* (32), 6629-6638.
11. Ibarra, I. A.; Yang, S.; Lin, X.; Blake, A. J.; Rizkallah, P. J.; Nowell, H.; Allan, D. R.; Champness, N. R.; Hubberstey, P.; Schröder, M., Highly porous and robust scandium-based metal–organic frameworks for hydrogen storage. *Chemical Communications* **2011,** *47* (29), 8304-8306.
12. Castellani, C. B.; Perotti, A.; Scrivanti, M.; Vidari, G., Scandium Trifluoromethanesulfonate as Catalyst in the Hydrogen/Deuterium Exchange of 1,3,5-Trimethoxybenzene: Evidence for a Direct Interaction of Scandium with the Aromatic Ring. *Tetrahedron* **2000,** *56* (41), 8161-8166.
13. Rohmann, K.; Kothe, J.; Haenel, M. W.; Englert, U.; Hölscher, M.; Leitner, W., Hydrogenation of CO2 to Formic Acid with a Highly Active

Ruthenium Acriphos Complex in DMSO and DMSO/Water. *Angewandte Chemie International Edition* **2016,** *55* (31), 8966-8969.
14. Moret, S.; Dyson, P. J.; Laurenczy, G., Direct synthesis of formic acid from carbon dioxide by hydrogenation in acidic media. **2014,** *5*, 4017.
15. Zhao, G.; Joó, F., Free formic acid by hydrogenation of carbon dioxide in sodium formate solutions. *Catalysis Communications* **2011,** *14* (1), 74-76.
16. Hayashi, H.; Ogo, S.; Fukuzumi, S., Aqueous hydrogenation of carbon dioxide catalysed by water-soluble ruthenium aqua complexes under acidic conditions. *Chemical Communications* **2004,** (23), 2714-2715.
17. Ogo, S.; Kabe, R.; Hayashi, H.; Harada, R.; Fukuzumi, S., Mechanistic investigation of CO2 hydrogenation by Ru(ii) and Ir(iii) aqua complexes under acidic conditions: two catalytic systems differing in the nature of the rate determining step. *Dalton Transactions* **2006,** (39), 4657-4663.

8. Conclusions and Outlook

The work carried out during this thesis investigated the intermediate regime in between strongly basic (see ***section 1.3***) and additive free conditions (see ***section 1.4***). It was shown that basic ILs, such as 1-butyl-2,3-dimethylimidazolium acetate (BMMI.OAc), can be used to shift the thermodynamic equilibrium to the product side by acting as a buffer, whilst avoiding the formation of formate salts and - adducts. The subtle stabilisation of formic acid facilitates the separation of the product from the ionic liquid immobilised onto a solid support, in this case a Merrifield resin. Hereby, the thermodynamic stabilising forces compromise in between disfavouring extraction efficiencies as would be expected under strongly basic conditions (see ***section 1.6***) and fast catalyst deactivations as observed under additive free conditions (see ***section 1.4***). These findings are especially interesting if the reaction should be conducted in an economically feasible fashion, i.e. the product separation is facilitated. However, one major task remains unsolved – the immobilisation of the catalyst.

In a first attempt to find a suitable catalyst, which could be immobilised, heterogeneous catalysts (RuFe-nanoparticles) were investigated for the hydrogenation of CO_2 to formic acid. It was clearly demonstrated that by diluting Ru-nanoparticles with Fe, the catalytic activity can be accelerated. However, the catalytic activity was far from satisfying. Here homogeneous catalysts seem to be superior for the investigated reaction.

In order to elucidate homogeneous catalyst for the hydrogenation of CO_2 to formic acid, a collaboration with Prof. Albrecht was started. Here a wide range of homogeneous catalysts were investigated. It was found that the catalytic activity depends on the electron density at the metal centre and the mechanism of the CO_2 insertion. However, the most important factor is the resistance towards low pH. This can be achieved with a pyridinium scaffold, leading to a twofold increase in turnover number (TON). However, a major improvement point with the complexes investigated in this part still remained to be the durability of the catalysts, although the achieved TON were in the range of other catalysts reported in literature for the base free hydrogenation of CO_2 to formic acid, see ***section 1.4***.

Therefore, the final part of this thesis investigated Ru-CNC-pincers complexes for the hydrogenation of CO_2 to formic acid. These complexes prohibit a ligand architecture which does not allow for a catalyst deactivation as described initially in ***section 1.3.2. Figure 1.24***. Furthermore, they displayed a high thermal - and chemical robustness, combined with a high electron density at the metal centre. Consequently, an astonishing rate of up to 22,000 h^{-1} and a TON of up to 833,800 can be achieved. These results demonstrate the plausible utilization of pincer type carbenes for the hydrogenation of CO_2 to formic acid.

In general this work studied the thermodynamic regime in between strongly basic conditions and additive free conditions for the hydrogenation of CO_2 to FA. This regime enables the separation of FA from an IL immobilised onto a Merrifield resin, due to the relatively weak thermodynamic stabilisation of FA

by the IL compared to additive free conditions. At the same time rapid catalyst deactivations as observed under base free conditions can be avoided and related to structural features in the coordination sphere of the catalysts. Hereby, the investigation of varying catalysts displayed, that the product tolerance (protons and FA) of the active species is crucial to achieve high concentrations of FA (see ***section 6***).

Consequently, future studies should focus on fine tuning the electronic properties of homogeneous pincer complexes using NHC moieties as ligating groups, with emphasis on the product resistance (formic acid and protons). As a starting point could be the here developed CNC-Ru-pincer used, whilst modifying ligating groups surrounding the active metal centre. Initially the effect of pyridylidene carbenes should be explored, as the corresponding complex displaying this functional group exhibited high tolerance towards the acidic media generated by formic acid (see ***section 6***, complex **1**).

These studies should be encompassed with thorough kinetic and mechanistic analysis using in-situ methods such as IR and NMR spectroscopy. Especially with in situ IR techniques the CO groups at the Ru centre could be “tapped” into to investigate the possible shift in catalyst distribution in the catalytic circle. These studies could lead to a thorough understanding of catalytic stability and activity during the hydrogenation of CO_2 to FA, similar to studies regarding thermodynamic hydricity and CO_2 activation as laid out in the introduction, see ***section 1.2.2***. As a final result the parametrisation of ligand groups towards the resistance of an increasingly acidifying reaction media could be achieved, facilitating the rapid development of novel catalyst which on turn can open a

gateway for the production of formic acid under completely additive free conditions.

Another string of study should be aimed at the immobilisation of homogeneous catalyst onto a support which at the same time should buffer the reaction media at favourable pH. These studies would continue investigating the separation of FA from a Merrifield resin as demonstrated in ***section 4***. However, it is important to note that in order to increase separation efficiencies, the thermodynamic interactions in between the support and FA should be further reduced. This could be achieved by using less basic counteranions such as formates, or by removing the ionic liquid support entirely. However, less basic environments, will inevitably lead to more demanding reaction conditions, thus these studies should be encompassed with the investigation of catalyst designs, favouring the product tolerance of bespoke catalysts, see also previous paragraph.

The final aim should be the development of a catalyst system which would encompass both, a facile and effective separation of FA from a support matrix and a catalyst immobilised onto the bespoke matrix which can tolerate strongly acidic conditions. In this way an effective flow process for the synthesis of FA from CO_2 could be achieved.